ABSTRACT

Title of Dissertation: THERMODYNAMIC AND INFORMATION ENTROPY-BASED PREDICTION AND DETECTION OF FATIGUE FAILURES IN METALLIC AND COMPOSITE MATERIALS USING ACOUSTIC EMISSION AND DIGITAL IMAGE CORRELATION

Seyed Fouad Karimian, Doctor of Philosophy, 2021

Dissertation directed by: Professor Mohammad Modarres, Department of Mechanical Engineering

Professor Hugh A. Bruck, Department of Mechanical Engineering

Although assumed to be identical, manufactured components always present some variability in their performance while in service. This variability can be seen in their degradation path and time to failure as they are tested under identical conditions. In engineering structures and some components, fatigue is among the most common degradation mechanisms and has been under extensive study over the past century. A common characteristic of the fatigue life models is to rely on some observable or measurable markers of damage, such as crack length or modulus reduction. However, these markers become more pronounced and detectable toward the end of the component or structure's life. Therefore, more advanced techniques would be needed to better account

for a structure's fatigue degradation. Several methods based on non-destructive testing techniques have developed over the past decades to decrease the uncertainty in fatigue degradation assessments. These methods seek to exploit the data collected by sensors during the operational life of a structure or component. Hence, the assessment of the health state can be constantly updated based on the operational conditions that allow for condition-based monitoring and maintenance. However, these methods are mostly context-dependent and limited to specific experimental conditions. Therefore, a method to effectively characterize and measure fatigue damage evolution at multiple length scales based on the fundamental concept of entropy is studied in this dissertation. The two entropic-based indices used are: Thermodynamic entropy, and, Information entropy.

The objectives of this dissertation are to develop new methods for fatigue damage detection and failure prediction in metallic and FRP laminated composite materials by using AE and DIC techniques and converting them to information and thermodynamic entropy gains caused by fatigue damage.

1. Develop and experimentally validate fatigue damage detection, failure prediction, and prognosis approaches based on the information entropy of AE signal waveforms in both metallic and FRP laminated composite materials.

2. Develop and experimentally validate fatigue damage detection, failure prediction, and prognosis approaches based on thermodynamic entropy using the DIC technique in both metallic and FRP laminated composite materials.

3. Develop a framework for RUL estimation of metallic and FRP laminated composite structures based on the two entropic measures.

THERMODYNAMIC AND INFORMATION ENTROPY-BASED PREDICTION AND DETECTION OF FATIGUE FAILURES IN METALLIC AND COMPOSITE MATERIALS USING ACOUSTIC EMISSION AND DIGITAL IMAGE CORRELATION

by

Seyed Fouad Karimian

Dissertation submitted to the Faculty of the Graduate School of the
University of Maryland, College Park, in partial fulfillment
of the requirements for the degree of
Doctor of Philosophy
2021

Advisory Committee:
Professor Mohammad Modarres, Advisor and Chair
Professor Hugh Bruck, Co-Advisor
Professor Aris Christou
Professor Abhijit Dasgupta
Professor Katrina Groth
Professor Norman Wereley, Dean's Representative

Dedication

To my parents who always supported me

&

To my beloved wife,

who stood by me every step of the way

Acknowledgements

First and foremost, I like to express my sincere gratitude to my advisor, Dr. Mohammad Modarres, for his guidance, encouragement, and support, both personally and professionally, during these years. It is hard for me to imagine such an enjoyable journey I had without his help.

I would like to thank my co-advisor, Dr. Hugh Bruck, for giving me new perspectives and pushing me toward excellence in my work. I am also grateful for the feedbacks and challenges I received from my dissertation committee: Dr. Katrina Groth, Dr. Abhijit Dasgupta, Dr. Aris Christou, and Dr. Norman Wereley, that helped me improve my work. I would like to extend my thanks to the former student at our laboratory, Dr. Huisung Yun, for assisting me with my early tests and helping me with laboratory troubleshooting even after graduation.

It was a pleasant journey with ups and downs, and it could not be possible without the love and support I received from my wife, Maral. We grew together in these years. I am also grateful for all the love and support I received from my parents and my family. They have always been a source of inspiration to me.

Finally, this work would have not been possible without the financial support of the various sources, including the Naval Air Systems Command under grant STTR N14A-T002, through the Technical Data Analysis, Inc., Ann G. Wylie Dissertation Fellowship provided by the Graduate School and The American Society for Nondestructive Testing (ASNT) Fellowship Award. On behalf of myself and the University of Maryland, thank you for your generous support.

Table of Contents

List of Tables

List of Figures

Chapter 1: Introduction

1.1. Background

Although assumed to be identical, manufactured components always present some variability in their performance while in service. This variability can be seen in their degradation path and time to failure as they are tested under identical conditions. In engineering structures and some components, fatigue is among the most common degradation mechanisms [1]. The fatigue failure mechanism has been under extensive study over the past century [2]. Structural elements of engineered systems are prone to degradation and catastrophic failures may occur if not properly maintained. Failure due to fatigue occurs under fluctuating loading conditions, even for loadings at much lower than the nominal yield strength of the material. During the operation of most engineered systems and structures, random variable loads result in fatigue-induced changes in component materials on scales much smaller than observed with the naked eye. These small changes accumulate during the operational life of components and eventually result in visible damage and failure. Fatigue is a scale- and load-dependent phenomenon starting from small scale (microscale) to macroscale. Depending on the material, 50% to 90% of fatigue life is spent before a small (and often challenging to detect) crack initiates [3].

In metals, accumulated damage usually leads to the formation of macro-cracks that grow in size until the final fracture. The fatigue damage modeling and life prediction in metals encompass a rich history of research, mainly focused on damage mechanisms and damage accumulation models [4]. Fatigue life prediction in metals is usually divided into two main regimes: crack initiation and crack propagation. Models that describe crack initiation

typically consider the stress and strain applied to materials for crack initiation time prediction, such as the widely accepted model developed by Smith, Watson, and Topper [5]. On the other hand, fracture mechanics models focus on crack length estimation based on the applied stress and other factors such as geometry. One of the most widely accepted models in fracture mechanics is the Paris Law [6]. A common characteristic of the fatigue life models is to rely on some observable or measurable markers of damage, such as crack length or modulus reduction. Unfortunately, these markers become more pronounced and detectable toward the end of the component or structure's life. Therefore, more advanced techniques would be needed to better account for a structure's fatigue assessment and remaining useful life estimation.

In composites, two or more components are combined to achieve properties superior to each of them individually. These materials offer a wide variety of properties regarding their constituent parts and manufacturing processes. Some of their properties and characteristics have motivated industries, such as the aerospace industry, to replace structures using conventional metallic alloys with composites. Fiber-reinforced polymer (FRP) composites have been the most prevalent due to their superior stiffness, strength, corrosion resistance, density, and fatigue life. While fatigue damage modeling of metals has a rich history and is far more developed than composites, fatigue damage modeling of FRP materials is a more complex and less understood problem. Various damage mechanisms such as matrix cracking, fiber/matrix debonding, delamination, and fiber breakage are present in FRP laminated composites [7]. These damage mechanisms happen in different length scales, and the synergy between them ultimately leads to fracture. Therefore, fatigue life analysis of FRP materials is a more complicated task and requires complex analysis.

Fatigue damage quantification and remaining useful life (RUL) estimation of structures and components made from either metallic or FRP laminated composites typically focus on techniques developed based on available (usually metal-based) physics-based models. The flexibility to adapt to unseen situations and the available historical information on physics-based models make them a reliable tool for fatigue life prediction [8]. However, they are mostly context-dependent, limited to specific experimental conditions, and associated with high uncertainties. Due to the stochastic nature of fatigue and the need to decrease the uncertainty in degradation processes' predictions of sensitive structures, several non-destructive evaluation (NDE) methods based on non-destructive testing (NDT) techniques have been developed over the past years [9], [10]. These methods seek to exploit and interpret high volumes of data collected by sensors during the operational life of a structure or component. Hence, the assessment of the health state can be constantly updated based on the operational conditions that allow for condition-based monitoring and maintenance. For instance, the inspection of airframe structure is an expensive, labor-intensive, and slow process that requires grounding and downtime that results in a considerable increase (by as much as 50%) in the operational cost of airplanes [11]. Therefore, the industry is moving toward using structural health monitoring (SHM) techniques to detect defects and damages that reduce the need for routine scheduled maintenance, minimizes human intervention, and increases the reliability of damage detection.

Among all the available NDT methods, the unique advantages of acoustic emission and digital image correlation (DIC) have made them among fatigue damage detection techniques. Acoustic emission (AE) is a well-known NDT technique that only requires

small sensors that detect activity inside the material with high sensitivity and no need to disassemble and clean the sensor. The AE technique can detect all the fatigue damage mechanisms in FRP materials [12]. Digital image correlation is a widely accepted and commonly used NDT technique to measure full-field displacement and strain map on object surfaces in the field of experimental mechanics [13]. Comparing to strain gauges and extensometers, DIC provides a full-field measurement and does not suffer surface slipping.

1.2. Motivation

Although the use of NDT techniques has been employed for fatigue damage assessment in the case of both metallic [14], [15] and FRP laminated composite [16], [17] materials, the available models usually depend on experimental setup or subjective parameter selection. As such, there is a gap in the fundamental fatigue damage modeling to detect and measure fatigue damage that is independent of experimental conditions. A method to effectively characterize and measure damage evolution at multiple length scales is based on the fundamental concept of entropy rather than markers of damage, as noted earlier. Therefore, this dissertation focuses on developing fatigue life estimation in metallic and FRP laminated composite materials based on entropy measurement when they undergo fatigue damage. As a measure of disorder, entropy has shown to be an appropriate fatigue damage index [18]. Two entropic-based indices to measure fatigue damage and predict fatigue failure is proposed in this dissertation:

- Thermodynamic entropy, and,
- Information entropy.

In thermodynamics, fatigue damage is seen as an irreversible process that dissipates energy and thus generates entropy. Thermodynamic entropy as a measure of irreversibility in processes is shown to be a promising damage index of fatigue [19]. On the other hand, comparing to the conventional threshold-dependent features of AE signals [20], information entropy of AE signal waveforms is a more integral measure of damage that removes the dependence on the subjectively selected thresholds by using the entire content of an AE waveform distribution and convert it to its equivalent information entropy to quantify the damage [21]. Measurement and modeling accumulation of the information entropy that measures the information content of the AE signal waveforms, and the thermodynamic entropy that measures the strain energies dissipated during the fatigue process, constitute the core of the research presented in this dissertation. This fundamental entropic-based research further closes the gaps and offers the promise of scale-independent, early fatigue failure detection, enhanced RUL estimation, and improved structural health management and prognostics.

1.3. Research objectives

This dissertation aims to develop new methods for fatigue damage detection and failure prediction in metallic and FRP laminated composite materials using AE and DIC techniques based on entropic measurements. Objectives are summarized as:

1. Develop and experimentally validate fatigue damage detection, failure prediction, and prognosis approaches based on the information entropy of AE signal waveforms in both metallic and FRP laminated composite materials.

2. Develop and experimentally validate fatigue damage detection, failure prediction, and prognosis approaches based on thermodynamic entropy using the DIC technique in both metallic and FRP laminated composite materials.
3. Develop a framework for RUL estimation of metallic and FRP laminated composite structures based on the two entropic measures.

The defined objectives are studied on metallic material first, then on FRP laminated composites, and the results are reported in separate chapters in this dissertation.

1.4. Brief overall literature review

The use of entropy in fatigue damage analysis has been addressed in the literature. In this section, some of the available literature is briefly presented. However, a far more comprehensive and detailed literature review on the focused topics covered in this dissertation appears at the beginning of each chapter.

The second law of thermodynamics explains thermodynamic entropy generation, and it is proposed as a natural fatigue damage index by Bryant et al. [22]. Naderi et al. [23] studied the thermodynamic entropy generation in two metallic alloys under various bending, torsional, and tension-compression fatigue testing. Results showed that regardless of the geometry, load, and frequency, cumulative thermodynamic entropy in each material at the point of fracture converges to a relatively constant level called fatigue fracture entropy, FFE (4 MJ m^{-3} K^{-1} for Al 6061-T6 and 60 MJ m^{-3} K^{-1} for SS 304). However, the study on notched aluminum specimens under cyclic loading by Ontiveros et al. [24] shows that stress amplitude is inversely related to thermodynamic entropy generation and cumulative entropy almost linearly increases with the number of cycles to failure. The discrepancy in

the results of the two studies is explained through the experimental setup difference in them. Naderi and Khonsari [25] studied glass/epoxy laminated composites under tension-tension and bending fatigue loading in different directions and amplitudes, and measured the thermodynamic entropy generation. It is shown that FFE is independent of frequency, load, and fiber orientation. Further, the effect of different terms such as thermal dissipation and damage energy in the hysteresis loop and the associated entropy generation is not considered. In another study by Naderi and Khonsari [26] on glass/epoxy laminated composites under tension-tension fatigue testing, it is concluded that degradation induced from internal damage energy generates considerable entropy and should not be neglected.

Information entropy is a measure of uncertainty or missing information [27] of the distribution of a random variable. According to information entropy, distributions with less bias toward a specific value are associated with higher uncertainties about the random variable. Hence, they have a higher value of entropy. Therefore, uniform distribution for a random variable is expected to have the highest information entropy since it is not biased toward any value. Kahirdeh and Khonsari [28] studied AE signals emitted from aluminum and glass/epoxy laminated composites under bending fatigue. Information entropy is calculated using the distribution of AE signal counts (random variable) based on the arrival times. It is observed that the final value of accumulated information entropy in the same material and under different testing conditions reached the same value and the final value of entropies in the two materials was about equal. However, AE count is an AE threshold-dependent feature that limits the scope of conclusion in the study. The selection of voltage values within a signal waveform as the random variable results in the information entropy analysis to become independent of the threshold settings. Sauerbrunn et al. [21] measured

the information entropy of AE signals under fatigue based on the waveform voltage distribution. They concluded that waveform information entropy is a better index of damage than count and energy. Chai et al. [29], [30] studied stainless steel under fatigue loading and used voltage values of AE waveform signal and the random variable for information entropy measurement. It is shown that cumulative energy, counts, and entropy evolve similarly with time.

1.5. Approach

This dissertation is divided into two parts with regard to the materials used. In the first part, the applications of information entropy and thermodynamic entropy on metallic material are discussed. The material selected for this part is Aluminum Alloy 7075-T6. The application of information entropy to detect crack initiation and measure crack growth is discussed in Chapter 2 and Chapter 3. The application of thermodynamic entropy on crack initiation detection is discussed in Chapter 4. Chapter 5 discusses a framework to fuse the two entropic indices for better RUL estimation using a dynamic Bayesian network.

The second part of the dissertation is focused on the application of information entropy and thermodynamic entropy on the FRP composites. Carbon FRP (CFRP) laminated composite is selected for this part. Chapter 6 discusses a new approach for AE signal clustering based on waveform characteristics that directly influence information entropy measurement and analysis. In Chapter 7, the application of information entropy in fatigue testing on CFRP laminated composites is discussed. Chapter 8 studies the thermodynamic entropy generation in fatigue testing of CFRP laminated composites. Finally, Chapter 9 summarizes the findings in the overall conclusions of the dissertation, presents the main contributions of this research, and provides recommendations for future work.

Chapters 2-8 are reproductions of the same papers that have already been published in various archival journals and conferences. Figure 1 shows a flowchart of the subjects covered and the relationship between the dissertation chapters to attain the overall objectives of the dissertation.

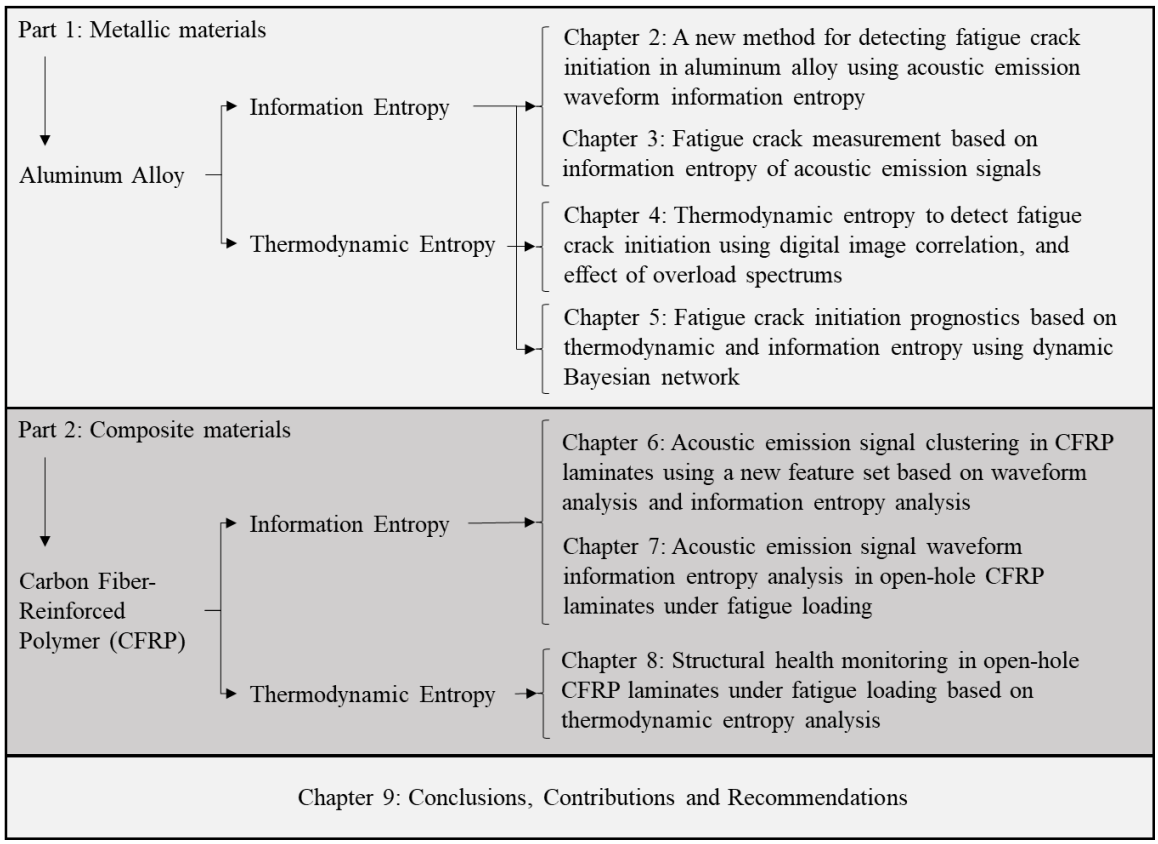

Figure 1-1 - Overview of the dissertation

1.6. References

[1] Md. T. A. Ansari, K. K. Singh, and M. S. Azam, "Fatigue damage analysis of fiber-reinforced polymer composites—A review," *Journal of Reinforced Plastics and Composites*, vol. 37, no. 9, pp. 636–654, May 2018, doi: 10.1177/0731684418754713.

[2] W. Cui, "A state-of-the-art review on fatigue life prediction methods for metal structures," *Journal of Marine Science and Technology*, vol. 7, no. 1, pp. 43–56, Jun. 2002, doi: 10.1007/s007730200012.

[3] J. A. Bannantine, J. J. Comer, and J. L. Handrock, *Fundamentals of metal fatigue analysis*. Englewood Cliffs, NJ: Prentice Hall, 1990.

[4] E. Santecchia *et al.*, “A Review on Fatigue Life Prediction Methods for Metals,” *Advances in Materials Science and Engineering*, vol. 2016, pp. 1–26, 2016, doi: 10.1155/2016/9573524.

[5] K. Smith, “A stress-strain function for the fatigue of metals.,” *Journal of materials*, vol. 5, pp. 767–778, 1970.

[6] P. Paris and F. Erdogan, “A Critical Analysis of Crack Propagation Laws,” *Journal of Basic Engineering*, vol. 85, no. 4, pp. 528–533, Dec. 1963, doi: 10.1115/1.3656900.

[7] A. P. Vassilopoulos, “The history of fiber-reinforced polymer composite laminate fatigue,” *International Journal of Fatigue*, vol. 134, p. 105512, May 2020, doi: 10.1016/j.ijfatigue.2020.105512.

[8] Y. Hu, S. Liu, H. Lu, and H. Zhang, “Remaining Useful Life Model and Assessment of Mechanical Products: A Brief Review and a Note on the State Space Model Method,” *Chin. J. Mech. Eng.*, vol. 32, no. 1, p. 15, Dec. 2019, doi: 10.1186/s10033-019-0317-y.

[9] M. Rabiei and M. Modarres, “A recursive Bayesian framework for structural health management using online monitoring and periodic inspections,” *Reliability Engineering & System Safety*, vol. 112, pp. 154–164, Apr. 2013, doi: 10.1016/j.ress.2012.11.020.

[10] N. Eleftheroglou, D. Zarouchas, T. Loutas, R. Alderliesten, and R. Benedictus, “Structural health monitoring data fusion for in-situ life prognosis of composite structures,” *Reliability Engineering & System Safety*, vol. 178, pp. 40–54, Oct. 2018, doi: 10.1016/j.ress.2018.04.031.

[11] A. P. Mouritz, *Introduction to Aerospace Materials*. Reston, VA: Woodhead Publishing, 2012.

[12] P. Duchene, S. Chaki, A. Ayadi, and P. Krawczak, “A review of non-destructive techniques used for mechanical damage assessment in polymer composites,” *Journal of Materials Science*, Jan. 2018, doi: 10.1007/s10853-018-2045-6.

[13] B. Pan, K. Qian, H. Xie, and A. Asundi, “Two-dimensional digital image correlation for in-plane displacement and strain measurement: a review,” *Measurement Science and Technology*, vol. 20, no. 6, p. 062001, Jun. 2009, doi: 10.1088/0957-0233/20/6/062001.

[14] P. A. Vanniamparambil, U. Guclu, and A. Kontsos, “Identification of Crack Initiation in Aluminum Alloys using Acoustic Emission,” *Experimental Mechanics*, vol. 55, no. 5, pp. 837–850, Jun. 2015, doi: 10.1007/s11340-015-9984-5.

[15] J. Payne, G. Welsh, R. J. Christ Jr., J. Nardiello, and J. M. Papazian, “Observations of fatigue crack initiation in 7075-T651,” *International Journal of Fatigue*, vol. 32, no. 2, pp. 247–255, Feb. 2010, doi: 10.1016/j.ijfatigue.2009.06.003.

[16] T. P. Philippidis and T. T. Assimakopoulou, “Strength degradation due to fatigue-induced matrix cracking in FRP composites: An acoustic emission predictive model,”

Composites Science and Technology, vol. 68, no. 15–16, pp. 3272–3277, Dec. 2008, doi: 10.1016/j.compscitech.2008.08.020.

[17] W. R. Broughton, M. R. L. Gower, M. J. Lodeiro, G. D. Pilkington, and R. M. Shaw, "An experimental assessment of open-hole tension–tension fatigue behaviour of a GFRP laminate," *Composites Part A: Applied Science and Manufacturing*, vol. 42, no. 10, pp. 1310–1320, Oct. 2011, doi: 10.1016/j.compositesa.2011.05.014.

[18] H. Yun and M. Modarres, "Measures of Entropy to Characterize Fatigue Damage in Metallic Materials," *Entropy*, vol. 21, no. 8, p. 804, Aug. 2019, doi: 10.3390/e21080804.

[19] A. Imanian and M. Modarres, "A thermodynamic entropy-based damage assessment with applications to prognostics and health management," *Structural Health Monitoring*, vol. 17, no. 2, pp. 240–254, Mar. 2018, doi: 10.1177/1475921716689561.

[20] C. Barile, C. Casavola, G. Pappalettera, and V. P. Kannan, "Application of different acoustic emission descriptors in damage assessment of fiber reinforced plastics: A comprehensive review," *Engineering Fracture Mechanics*, vol. 235, p. 107083, Aug. 2020, doi: 10.1016/j.engfracmech.2020.107083.

[21] C. Sauerbrunn, A. Kahirdeh, H. Yun, and M. Modarres, "Damage Assessment Using Information Entropy of Individual Acoustic Emission Waveforms during Cyclic Fatigue Loading," *Applied Sciences*, vol. 7, no. 6, p. 562, May 2017, doi: 10.3390/app7060562.

[22] M. D. Bryant, M. M. Khonsari, and F. F. Ling, "On the thermodynamics of degradation," *Proceedings of the Royal Society A: Mathematical, Physical and Engineering Sciences*, vol. 464, no. 2096, pp. 2001–2014, Aug. 2008, doi: 10.1098/rspa.2007.0371.

[23] M. Naderi, M. Amiri, and M. M. Khonsari, "On the thermodynamic entropy of fatigue fracture," *Proceedings of the Royal Society A: Mathematical, Physical and Engineering Sciences*, vol. 466, no. 2114, pp. 423–438, Feb. 2010, doi: 10.1098/rspa.2009.0348.

[24] V. Ontiveros, M. Amiri, A. Kahirdeh, and M. Modarres, "Thermodynamic entropy generation in the course of the fatigue crack initiation: Thermodynamic Entropy Generation in the Course of the Fatigue Crack Initiation," *Fatigue & Fracture of Engineering Materials & Structures*, vol. 40, no. 3, pp. 423–434, Mar. 2017, doi: 10.1111/ffe.12506.

[25] M. Naderi and M. M. Khonsari, "Thermodynamic analysis of fatigue failure in a composite laminate," *Mechanics of Materials*, vol. 46, pp. 113–122, Mar. 2012, doi: 10.1016/j.mechmat.2011.12.003.

[26] M. Naderi and M. M. Khonsari, "On the role of damage energy in the fatigue degradation characterization of a composite laminate," *Composites Part B: Engineering*, vol. 45, no. 1, pp. 528–537, Feb. 2013, doi: 10.1016/j.compositesb.2012.07.028.

[27] A. Ben-Naim, “Entropy, Shannon’s Measure of Information and Boltzmann’s H-Theorem,” *Entropy*, vol. 19, no. 2, p. 48, Jan. 2017, doi: 10.3390/e19020048.

[28] A. Kahirdeh and M. Khonsari, “Acoustic Entropy of the Materials in the Course of Degradation,” *Entropy*, vol. 18, no. 8, p. 280, Jul. 2016, doi: 10.3390/e18080280.

[29] M. Chai, Z. Zhang, Q. Duan, and Y. Song, “Assessment of fatigue crack growth in 316LN stainless steel based on acoustic emission entropy,” *International Journal of Fatigue*, vol. 109, pp. 145–156, Apr. 2018, doi: 10.1016/j.ijfatigue.2017.12.017.

[30] M. Chai, Z. Zhang, and Q. Duan, “A new qualitative acoustic emission parameter based on Shannon’s entropy for damage monitoring,” *Mechanical Systems and Signal Processing*, vol. 100, pp. 617–629, Feb. 2018, doi: 10.1016/j.ymssp.2017.08.007.

Chapter 2: A new method for detecting fatigue crack initiation in aluminum alloy using acoustic emission waveform information entropy[1]

2.1. Abstract

Sensitive structures, such as airframes, need careful inspection and maintenance to avoid fatigue failures. These activities are expensive, discrete and imperfect, since catastrophic failure may occur before cracks can be detected. This paper focuses on using information entropy of acoustic emission (AE) signals to identify precursors to fatigue crack initiation in AA7075-T6. The information entropy is investigated as a means to identify the conditions associated with nucleation and coalescence of microcracks that lead to crack initiation. The methodology is demonstrated using data from multiple fatigue tests on notched dog-bone specimens, under different loadings. It was determined that the information entropy reaches a minimum immediately before a macrocrack is formed, with values within an interval of 2.0 to 3.0 [nats], independent of loading condition. Following the minimum information entropy, the cumulative information entropy rapidly increased. Therefore, combining the minimum information entropy with the rapid increase in cumulative information entropy, the new method could be used to detect fatigue crack initiation reliably.

[1] The full-text of this chapter has been published in the Engineering Fracture Mechanics journal, Volume 223, January 2020. https://doi.org/10.1016/j.engfracmech.2019.106771

2.2. Introduction

Fatigue is the primary cause of structural failure [1]. Structural components are prone to degradation, and catastrophic failures may occur if not properly maintained. Failure due to fatigue occurs under fluctuating loading conditions at much lower than the nominal yield strength of the material. During operation, random variable loads result in fatigue-induced small changes in component materials on scales much smaller than observed with the naked eye. These small changes accumulate during the operational life of components, eventually resulting in observable damage, and consequently, failure. Fatigue is a scale- and load-dependent phenomenon starting from a small scale (microscale) to macroscale. Depending on the material, 50% to 90% of fatigue life is spent before crack initiation [2]. Specifically, for more brittle materials, such as Aluminum Alloy 7075-T6, crack propagation can occur rapidly and covers a relatively short period of the fatigue life. Because of this behavior, it has been challenging to use existing fatigue analyses to predict the lifetime of critical components, particularly aerospace structures, made from these materials when they are subjected to different fatigue loading conditions. Therefore, it is important to develop a method to detect crack initiation that results in a better estimate of the remaining useful life (RUL).

Acoustic emission (AE) is a well-known non-destructive evaluation technique that has been used extensively in the field of fatigue damage of metals [3]–[12] and composites [13]–[19]. Structural changes and internal redistribution of stress within the material result in energy release. Part of this energy is released in the form of AE signals [20]. These signals are recorded by AE sensors. The AE technique requires only small sensors that detect activity inside the material, while other non-destructive evaluation (NDE)

techniques examine the internal structure of the components [21]. Acoustic emission is used for NDE in many industrial applications such as pressure vessels [22], structural integrity [23] and chip formation assessment [24]. Studies based on AE usually use a combination of signal features such as count, peak levels, rise time, energy, duration and amplitude to draw conclusions. However, these features are heavily threshold-dependent and are affected by the wave propagation medium and attenuation characteristics. More recently, in addition to the features of the signal, waveform analysis of signals has been studied. For example, Vanniamparambil et. al. [3] have shown that discrete increases in waveform amplitudes associated with AE signals after crack initiation, in addition to increasing waveform frequency, can be considered as behaviors related to crack initiation. They also report signals with relatively high amplitude and peak frequencies after crack initiation, including a jump in the absolute energy of the waveform and an increase in the number of counts at crack initiation. Wisner et al. [25] have proposed a framework for AE signal processing in aluminum alloys. It is shown that AE signal feature selection and unsupervised data clustering methods make it possible to link the AE waveforms to potential fracture sources.

Another AE waveform analysis method recently used in fatigue damage studies is the use of AE waveform information (Shannon) entropy [26]–[32]. AE waveform information entropy is a more integral measure of damage, removing the dependence on threshold and signal features such as energy and count rate by using the signal distribution characteristics to quantify the damage. AE waveform information entropy relies on the information content of the distribution of emitted AE signals (described by the waveforms). It can quantify damage independent of AE characteristics that depend on experimental and

loading conditions. This method measures the information entropy of the signal waveform, using Shannon information entropy [33]. To calculate the information entropy, Sauerbrunn et al. [26] used non-parametric probability distribution based on voltage readings representing the AE signals for every 2048 data points. They suggested that waveform information entropy would be a better index of damage than count and energy. In a study by Chai et al. [27], a fatigue test and a three-point bending test was conducted, and the waveform of AE signal analysis showed that in both experiments, cumulative energy, counts and information entropy evolve similarly with time. In another study by the same group [28], AE information entropy during fatigue was used, where two distinct stages of evolution of information entropy were observed. The first stage was related to fatigue crack initiation and small crack growth, while the second stage was related to "plastic activities in plastic zone at the crack tip, the formation of micro voids and the ligaments shearing between these micro voids." It was shown that normalized cumulative AE information entropy and count have similar trends, suggesting cumulative information entropy can be regarded as an effective measure for fatigue damage evolution.

Previous studies on AE waveform information entropy use AE signals recorded by only a single sensor. Therefore, they fail to report the spatial dependence of AE features and waveform information entropy in addition to verifying the analysis results. Furthermore, they fail to offer a practical solution to employ AE waveform information entropy as a damage identification parameter under variable loading conditions. In this paper, AE signals are recorded by two independent sensors, which are used to verify each other to improve data collection and enhance noise reduction. A new method is developed for processing the waveform of the AE signal by selecting an optimum bin width after

removing the hit lockout time (HLT) and then calculating the waveform information entropy. The calculated waveform information entropy values of the AE signals are investigated as a means for identifying conditions associated with the nucleation and coalescence of microcracks that lead to fatigue crack initiation. Therefore, the method is applied to experimental data obtained under variable fatigue loading conditions to correlate with the formation of macroscale cracks. This method results in a reliable crack initiation detection using the information content of AE signals, which offers the capability of reliable real-time structural health monitoring for in-service structures.

2.3. Experimental setup and procedure

2.3.1. Procedure

A large AE signal database consisting of a total of 10 specimens fatigued under different loading conditions were generated. Loading conditions were defined as overload spectrum, high cyclic fatigue (HCF), programmed loading, and variable amplitude loading spectrum. Each test was monitored by 2 AE sensors attached to the specimen at a specific location. The overload spectrum was defined by fatigue cycling using stress ratio (R) equal to 0.1 with a maximum load of 12 [kN] and one cycle with a maximum load of 15.5 [kN] every 1,500 cycles. The maximum load in HCF loading spectrums was set to 8, 9.25 and 9.5 [kN] with R=0.1. Programmed loading was defined as a loading block of 37 cycles, all with a maximum load of 12 [kN] and different stress ratios: 20 cycles with R=0.1 followed by 10 cycles of R=0.25, 5 cycles of R=0.5, and 2 cycles of R=0.67. Variable amplitude loading was defined as a block of loading with 1,489 loading points, with a maximum of 15.5 [kN]. An 8 [MP] Point Grey Flea3 sensor with a 3.8–13 [mm] Fujinon lens was used to monitor the tests. Tests were paused once a crack became visible. Detected crack was then measured

and the crack initiation cycle was calculated using crack length at the termination cycle and material properties measured in monotonic tests. The definition of crack initiation is from the US Navy [34] described as a 0.25 [mm] crack length. Figure 1 shows an example of crack length measurement at the test termination cycle.

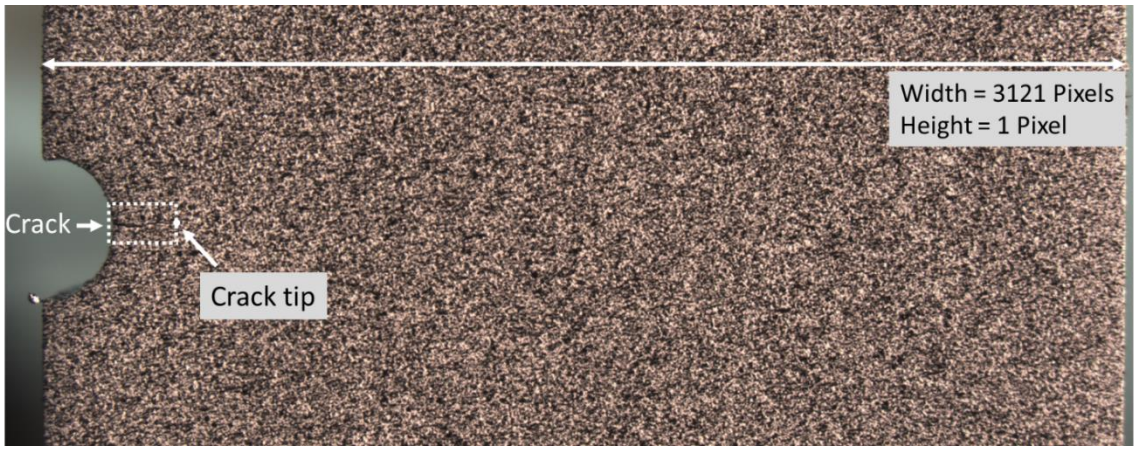

Figure 2-1 - Crack detection and measurement at the test termination cycle.

2.3.2. Specimens

All specimens were cut from the same sheet of AA7075-T6 material in the rolling direction and machined to dog-bone shape specimens with a notch at the center, following the ASTM E466 standard. A drawing of the specimen and its dimensions (in mm) is shown in Figure 2. The stress concentration factor around the notch area was calculated as 2.77. The yield strength of the material is measured as 506.9 [MPa]. Specimens were speckle patterned around the notch for further Digital Image Correlation (DIC) analysis to confirm crack initiation and strain map generation. Details of the DIC analysis and loading conditions can be found at [35].

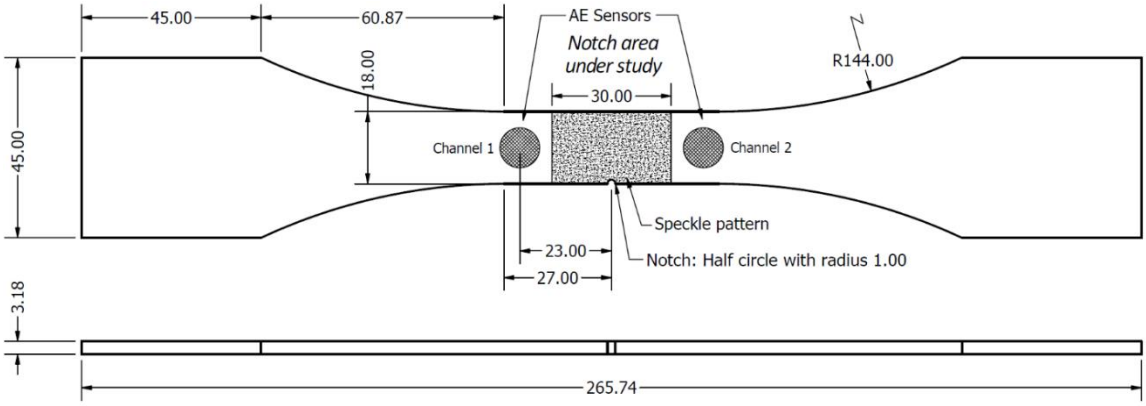

Figure 2-2 - Specimen geometry and AE sensor placement

2.3.3. Acoustic emission signal measurement

AE signals were recorded using two Physical Acoustics PCI-2 based resonant Micro-30s AE sensors (MISTRAS Group, Princeton Junction, NJ) with a frequency range of 150–400 [kHz] and a resonant frequency of 225 [kHz]. These sensors are proven to provide adequate results in our previous studies [26], [36] and cover the frequency range reported for crack initiation in other studies [3], [27], [28]. AE sensors were attached to the specimen using ultrasonic gel couplant. Sensors were placed symmetrically 23 [mm] away from the notch (as shown by Channel 1 and Channel 2 in Figure 2). The parameters used in AE recording—pre-trigger length, peak definition time, hit definition time and hit lockout time—were set to 256 [μs], 300 [μs], 600 [μs] and 1000 [μs], respectively. For each signal, hit length was set to 10960 points and sampling rate to 5 MSPS. Signals were passed through a 40 [dB] pre-amplifier before reaching the data acquisition module. The Physical Acoustics AEwin software (Physical Acoustic Corporation, Version E5.60, MISTRAS Group, Princeton Junction, NJ, 2007) was used to record AE signals. A servo-hydraulic material testing system machine retrofitted with an Instron 8800 controller was used to perform the fatigue tests.

2.3.4. Noise reduction

The presence of noise in AE acquisition is inevitable. The noise has different amplitude levels and sources, such as fretting of micro-crack surfaces, friction between the mechanical parts of the loading frame, and vibration of the fluid pump in the loading frame. Various signal processing approaches to increase the signal to noise ratio in AE signals such as using Discrete Wavelet Transform (DWT) [37] and Hilbert-Huang transform [38] are proposed in the literature. However, as demonstrated and explained by [27], no such denoising procedure is necessary when utilizing AE waveform information entropy. In this study, two approaches were used to reduce and remove noises: a pre-processing technique that reduces noise amplitude level and a post-processing method that eliminate noises in the AE dataset to be used for signal waveform analysis.

In the pre-processing technique, mechanical dampers were attached to the specimens to reduce noise amplitude levels by reducing the vibrations induced by the loading frame. The pre-processing technique enabled us to set a lower amplitude for the threshold. To set the threshold, the specimen was placed in the servo-hydraulic materials testing system frame, and the grips were closed to hold the specimen. Without applying any load, AE activity detected by the sensors was recorded. These AE activities were considered as background noises. The amplitude of the recorded signals showed the threshold level sufficient to eliminate noise. Figure 3 shows the threshold setting effect on noise reduction. It can be seen that after the mechanical dampers decreased the noise amplitudes to less than 52 [dB], the threshold eliminated them from being recorded in the AE database.

A post-processing method was applied to recorded signals. This filtering method had two steps and used the signals recorded in both channels to differentiate valid signals (hits

emitted from the notch area) and all other signals (either noise or hits emitted from other places). The first step was load filtering. Signals received in the upper portions of the tensile load were related to fatigue damage [4], [8], [10], [39], [40]. In this study, only signals received in the top 20% of the peak load were considered to be related to fatigue damage. The load filter was applied to raw AE data to remove the signals recorded below the top 20% peak load. The second step in the post-processing method was delta T filtering. In all tests, before applying any load, the delta T parameter was measured. Delta T was defined as the time it took for one AE signal to travel from one sensor to the other. This parameter was used to filter signals recorded from other locations rather than notch area. All the remaining signals in the AE dataset after post-processing were used for waveform information entropy analysis.

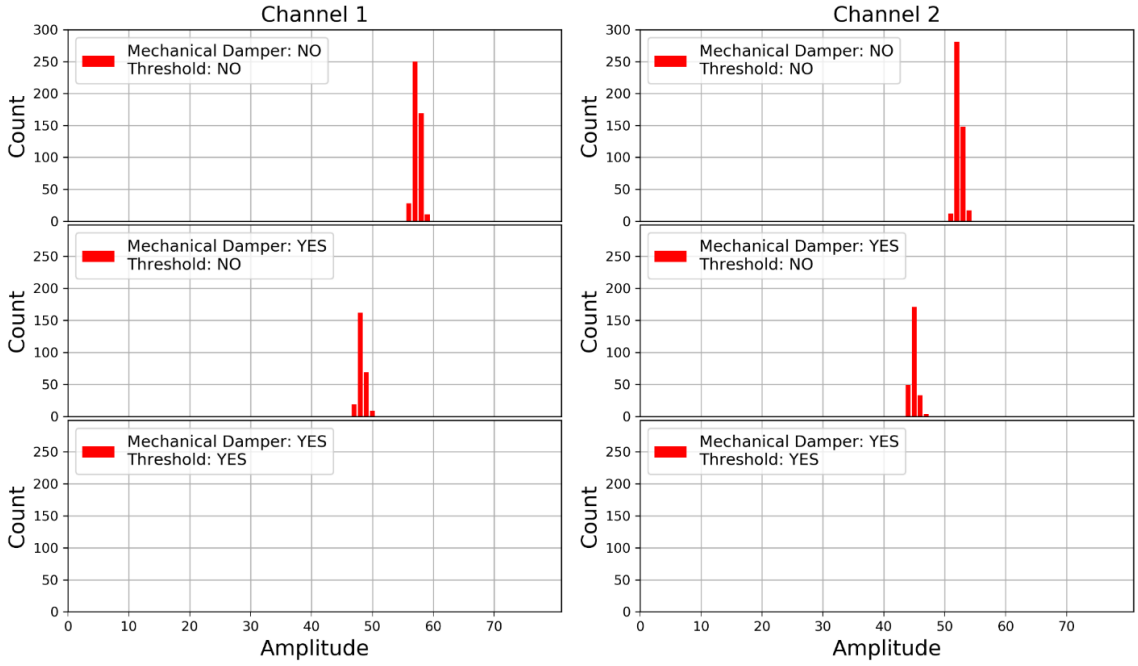

Figure 2-3 - Effect of mechanical dampers and threshold setting on noise recording elimination; Channel 1 is shown at left; Channel 2 is shown at right. The first row shows signals recorded at zero load with no threshold and mechanical damper. The second row shows noise amplitude reduction due to mechanical dampers. The third row shows the noise recorded after the threshold setting.

2.4. Acoustic emission waveform information entropy method

The information entropy of the AE signal waveforms emitted from the notch area under loading was measured as defined by Shannon [33]. Information entropy is a measure of uncertainty or information content from the probabilistic distribution of a random variable, such as the voltage in the AE waveform signals. According to the information entropy, distributions with less bias toward a specific value carry more information about the random variable; hence, they have a higher value of information entropy. Therefore, a uniform distribution for a random variable has the highest information entropy, since it is not biased toward any value. In other words, it has the highest uncertainty. Information entropy is used in this study to measure uncertainty associated with the AE signal waveforms emitted during the fatigue tests. The information entropy defined by Shannon [33] is expressed as:

$$I = c\sum_{i=1}^{n} P(X_i)\ln(1/P(X_i)) \qquad (1)$$

where $X_i = \{x_1, x_2, \dots, x_n\}$ is a random variable, $P(X_i)$ is the probability distribution of the random variable, I is the information entropy, and c is a constant considered to be unity in this study. The unit of AE information entropy used in this study is 'nats' since in Equation 1 the natural logarithm is used. The waveforms from valid signals remaining in the AE dataset after the post-processing method are used to calculate the information entropy using Equation 1. In this equation, voltage is the random variable. A histogram of the voltage values in each signal forms a nonparametric probability distribution of the random variable.

The choice of bin width is the most important parameter in developing a histogram, and selection of an appropriate bin width size is necessary to reveal the true shape of the underlying density of the variable. The ideal bin width should be able to reveal the essential structure of the data while avoiding too much detail. Histogram bin width choices are often related to the accuracy of the measured data. To study the optimum bin width for a histogram, the mean integrated squared error between the histogram and real density of the variable is minimized, which results in finding the optimum value for the bin width [41], [42]. Scott [41] proposes a simple approach to find an approximate optimum bin width, as expressed by Equation 2:

$$b_n = k\delta n^{-1/3} \qquad (2)$$

where k is a constant, given as $k = 3.49$, δ is the standard deviation of the data, and n is the number of data points. However, Equation 2 assumes that the true density function is a Gaussian distribution. To correct the bin widths for distributions violating this assumption, correction coefficients should be applied to the bin width. These coefficients are given based on the difference in skewness, kurtosis and bimodality of the true underlying density distribution. While Equation 2 gives an approximate estimate of the optimum bin width, Wand [42] proposes a more elaborate approach to find the optimum bin width. Bin widths found in the latter approach are computationally more expensive and provide only slightly smaller bin widths.

A bin width analysis was performed to determine the optimum width. Valid waveforms from both channels in one test were used. For each waveform, after removing the Hit Lockout Time (HLT), which is defined in the following paragraph, the optimum bin width

was calculated using Equation 2. These values were then corrected with the appropriate correction coefficients. All valid waveforms in Channels 1 and 2 were analyzed, and the optimum bin width for each of them was calculated. It is important to note that since HLT and amplitude of signals are different, each waveform has a unique δ and n values that result in a unique optimum bin width. The average optimum bin widths in Channels 1 and 2 are 0.0041 and 0.0038, respectively. Therefore, a bin width of 0.001 was selected for the AE waveform information entropy analysis that satisfied the bin width analysis and was slightly smaller than the suggested values. Figure 4 shows a bin width analysis of a HCF test using three different bin widths of 0.01, 0.001 and 0.0001. These bin widths were selected to highlight the sensitivity of the AE waveform information entropy to the choice of the bin width. As expected, sensitivity analysis shows all bin widths result in similar information entropy trends, with the smaller bin width having the higher information entropy values. However, selection of the optimum bin width will result in a higher scatter, and corresponding range, for the information entropy values of the AE signals. Figure 4 clearly shows this scatter, where a bin width of 0.001 results in the highest range in information entropy values comparing to the other two bin widths. The selection of the optimum bin width results in a better differentiation between AE signals that helps in relating them to their sources. Choice of other bin width can result in either a very rough histogram (in case of a too small bin width), or a very smooth histogram that might overlook important changes in the true underlying distribution. Both cases negatively affect relating AE signals to their sources.

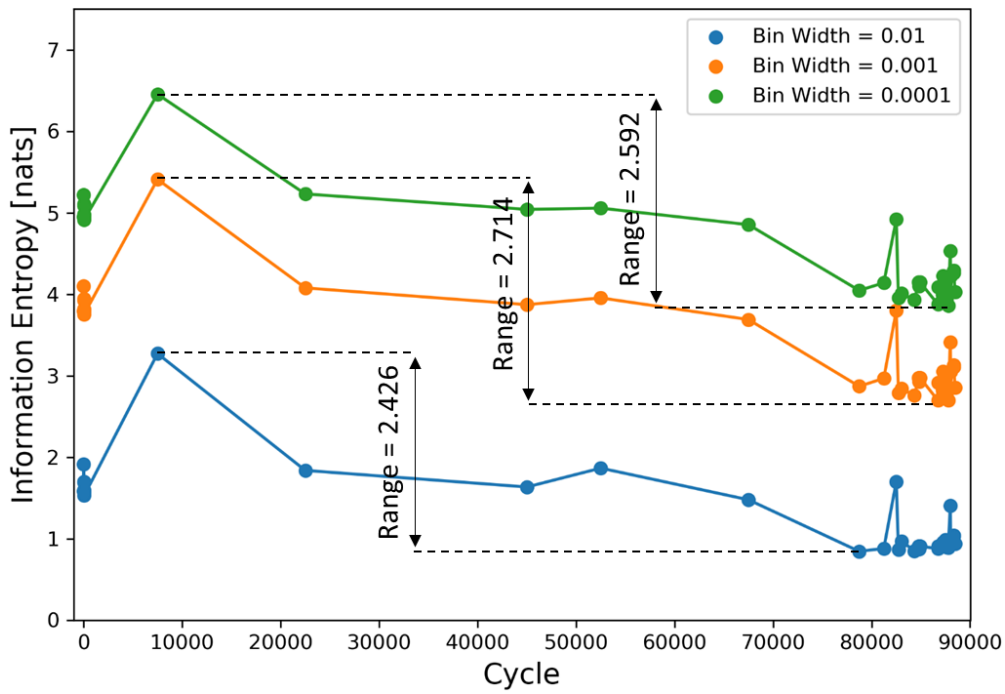

Figure 2-4 - Bin width sensitivity analysis on AE waveform entropies of one of the HCF tests.

Raw AE signal waveforms include the HLT, which is set in AE acquisition parameters. The HLT is defined as the time that should pass before the next signal is detected. During HLT, no signal passes the threshold, and voltage readings are zero. Therefore, HLT does not carry any information, and should be removed from the signal before calculating its information entropy. Failing to remove HLT would strongly affect the information entropy calculation results. Valid signals remaining in the AE dataset after filtering steps are selected and imported to Matlab, where the HLT is removed and the waveform information entropy is calculated for each signal using the bin width of 0.001. Figure 5 shows the effect of HLT on waveform information entropy calculation. It can be seen that failing to remove HLT causes the histogram to be biased toward zero and, consequently, falsely decreases the information entropy.

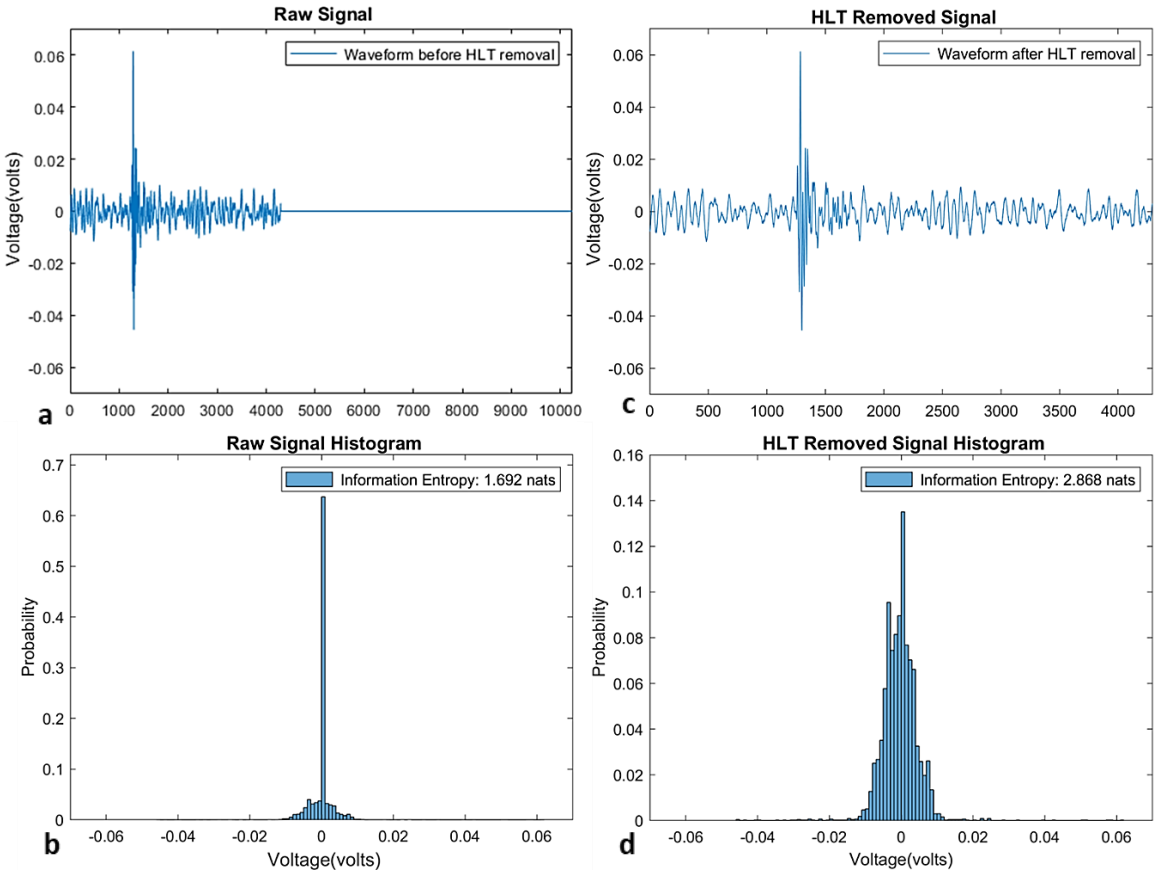

Figure 2-5 - Effect of HLT removal from signal and waveform information entropy calculation. Same signal before HLT removal (a) and after HLT removal (c) and its histogram in (b) and (d), respectively. It is seen that failing to remove HLT causes the histogram to be biased toward zero, which falsely decreases the calculated information entropy from 2.868 [nats] in (d) to 1.692 [nats] in (b)

2.5. Experimental results and discussion

An *in-situ* strain life analysis is performed to detect crack initiation in the AA7075-T6 specimens using AE signal waveform information entropy. Summing the information entropy values from individual waveforms results in the "cumulative information entropy". The cumulative information entropy can be compared to cumulative count and cumulative energy, which are commonly used in AE analysis. Results from both channels (sensors) are compared to study the spatial dependence of AE features. While the threshold is selected to remove features of the signals believed to be unrelated to damage, the

cumulative count and cumulative energy of AE signals are heavily threshold-dependent. However, waveform information entropy is independent of threshold setting. Figure 6 shows the cumulative count, cumulative energy, cumulative waveform information entropy (6a) and waveform information entropy (6b) of the same signals recorded in each channel in one of the overload spectrum tests. Ideally, the features of a specific signal (count, energy and waveform information entropy) recorded in both channels should be the same, resulting in the same final cumulative values. However, it is observed that while the cumulative waveform information entropies measured by the two channels are similar throughout the test and yield similar final values, cumulative energy and cumulative count show increasing trends but different final values. Each point in information entropy value plot (Figure 6b) represents waveform information entropy of a valid signal. As expected, toward the end of the test (time of crack initiation), the number of signals increase. This results in an increase in the difference between cumulative count and cumulative energy recorded in Channel 1 and 2. However, such difference is much less in cumulative information entropy. Figure 7 shows the same result for one of the HCF tests. In HCF tests, due to considerably lower load amplitude, AE activity is drastically lower comparing to other loading spectrums. Therefore, effects of the difference in cumulative AE features is more pronounced. In Figure 7, cumulative energy shows higher disparity in each channel comparing to cumulative count and cumulative information entropy. The small number of signals generated in this test shows that the difference between energy values of each AE signal is higher comparing to count and waveform information entropy.

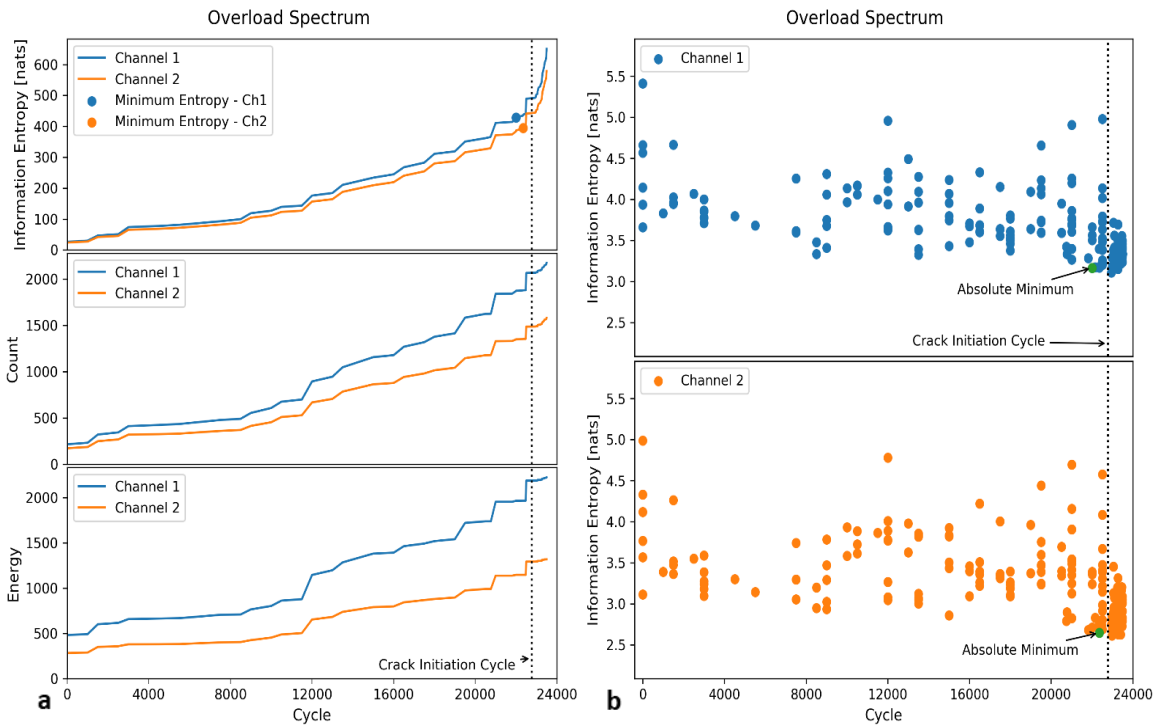

Figure 2-6 - Cumulative information entropy, cumulative count and cumulative energy (a) and information entropy (b) of valid signals in each channel – Overload spectrum

Decrease in signal amplitude caused by attenuation results in a signal partially fall below the threshold level in one channel while recorded fully in the other channel. Waveform information entropy is a measure of the signal waveform shape, and therefore, as long as the overall shape of the waveform signal is preserved, waveform information entropy value would not be affected heavily by attenuation. This is not seen in the case of count and energy. In addition to the attenuation, noise recordings affect the shape of signals, but their effects are more pronounced in the cumulative energy and cumulative count compared to the cumulative waveform information entropy. This is seen in the final values of cumulative energy, cumulative counts and cumulative information entropy in all tests. This is because energy is calculated as the rectified area under the waveform; therefore, if one signal emits closer to one channel, its waveform will have a higher amplitude for that channel. But due to the AE attenuation, the same signal might show a lower amplitude in

the other channel, which results in lower energy. The same phenomenon may apply to the counts recorded. That is, AE attenuation might cause a decrease in the amplitudes of the signal, resulting in part of the waveform being filtered by the threshold. Therefore, counts measured in each channel for the same AE event will be different. Figure 8 show the results for one of the tests with programmed loading spectrum. Higher AE activity in this loading spectrum better demonstrate the lower difference in cumulative information entropy comparing to cumulative count and cumulative energy in each channel, caused by attenuation and threshold setting.

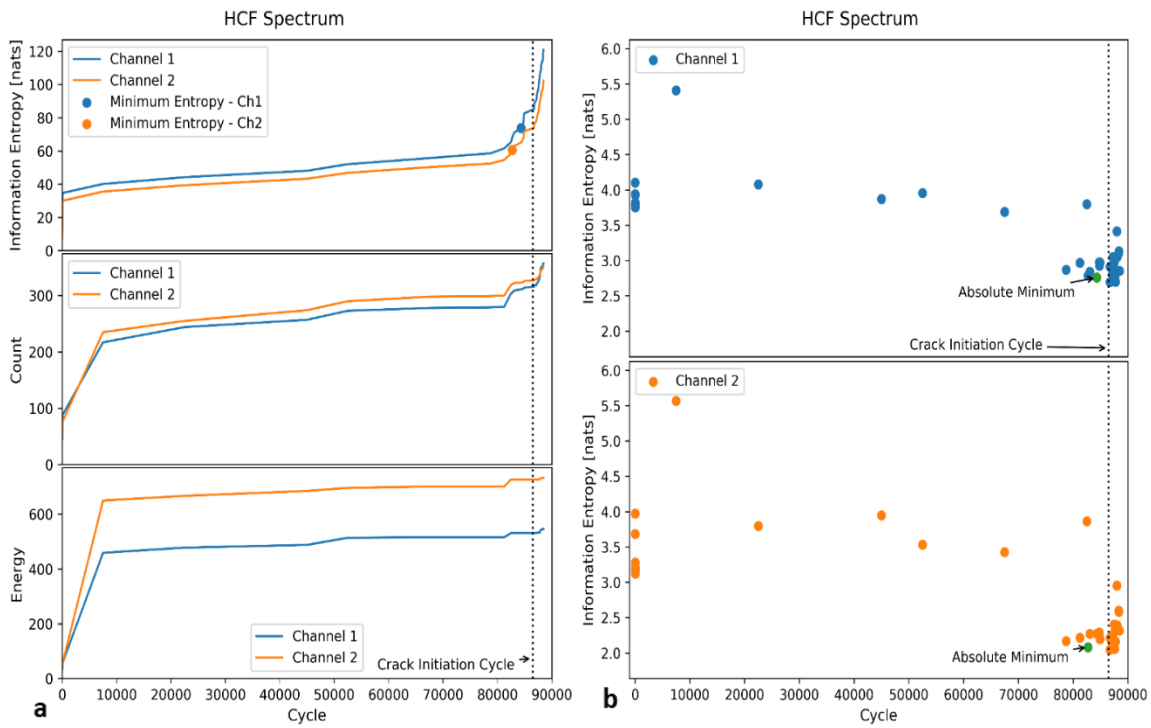

Figure 2-7 - Cumulative information entropy, cumulative count and cumulative energy (a) and information entropy (b) of valid signals in each channel – HCF spectrum

AE waveform recorded for a signal includes all the sounds emitted from the specimen at the time of recording. These sounds can be attributed to different sources and locations within the notch. When the sounds are combined, the waveform generated can result in a widely spread shape (resulting in high information entropy), or can be concentrated around

a specific value (leading to low information entropy). Immediately prior to the crack initiation cycle, most of the sounds are generated by crack nucleation; therefore, the waveforms are generated from a single source and consequently lead to a low value of information entropy. Figures 6-8 b, show examples of the waveform information entropy of valid AE signals up to test termination. It is evident from the waveform information entropy results that the minimum value of the information entropy in both channels shortly precedes crack initiation. Since the crack initiation (subjectively assumed as a 0.25 mm crack length) occurs after the time of the minimum information entropy observance, it can be surmised that the concentrated AE waveform generated is due to the initial crack generation in the matrix (crack nucleation). Crack generation starts with incubation, in which iron-bearing particles within the material crack first; then these microcracks nucleate and transfer to the matrix [43]. It is observed that the cumulative AE waveform information entropies show a sudden increase around the crack initiation cycle (Figure 6-8 a). This can be attributed to the increased number of AE signals emitted when the macroscale crack nucleates from the microcracked inclusions. Same trend is seen in all tests, regardless of number of cycles to crack initiation or number of AE signals. Figure 9 shows similar results for variable amplitude loading spectrum. This loading condition resembles a closer spectrum to in-service loading spectrum. Comparing to previous loading spectrums, it is more complex and generates considerably higher AE activity.

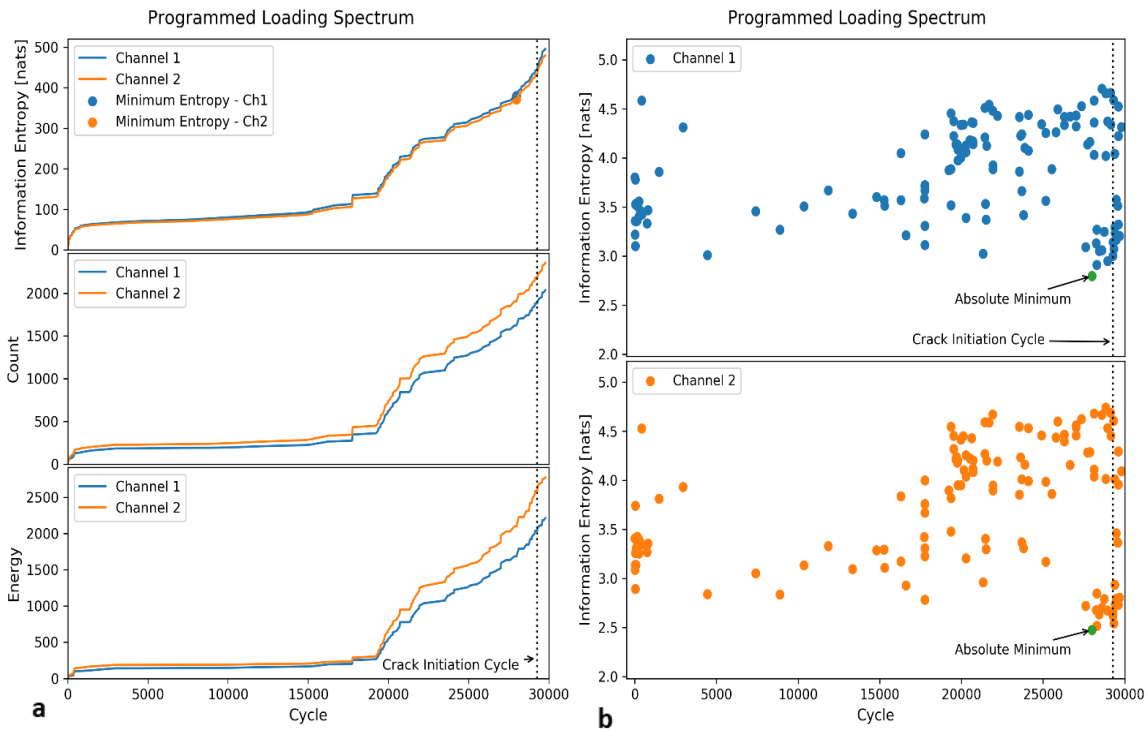

Figure 2-8 - Cumulative information entropy, cumulative count and cumulative energy (a) and information entropy (b) of valid signals in each channel – Programmed loading spectrum

In Figure 9 there is one exception in Channel 2 where the minimum waveform information entropy happened at around 75% of the fatigue life, comparatively earlier than other cases. The minimum value of waveform information entropy in this case is not associated with sudden increases in cumulative information entropy, and thus, not crack nucleation. Closer examination of the waveform information entropy value of this case revealed that its information entropy value were within 1% of the second minimum waveform information entropy value in the channel. In fact, it was the second minimum waveform information entropy value of the signals in this case that was associated with a sudden increase in the cumulative information entropy and subsequent crack initiation. Given that the waveform information entropy values for this case is only 1% less than the second minimum waveform information entropy value, it is reasonable to assume that noise recording in the waveform of this case resulted in voltages concentrating around specific values, resulting

in decreased information entropy. A possible source for the noise in the waveform is the vibration of actuators during dynamic loading. The noise that is present has a low amplitude, and its effects is mostly seen in low amplitude signals.

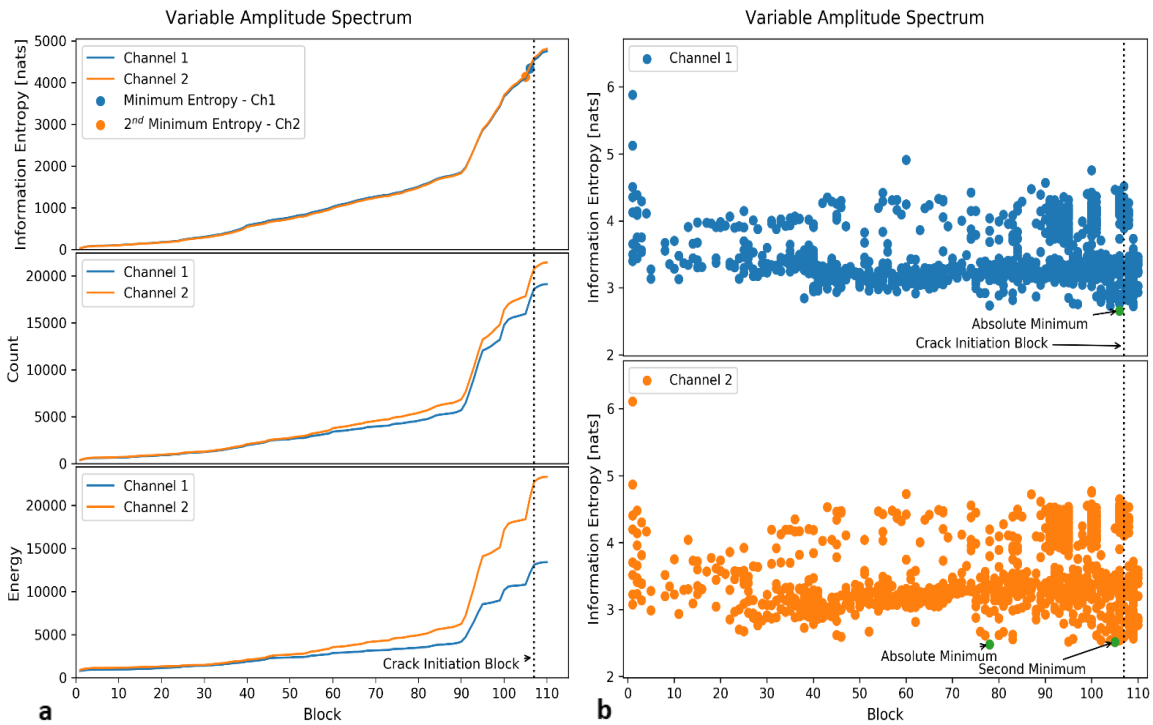

Figure 2-9 - Cumulative information entropy, cumulative count and cumulative energy (a) and information entropy (b) of valid signals in each channel – variable amplitude spectrum

The assumption that all signals with minimum waveform information entropy are emitted due to the crack nucleation is further studied by observing the range of amplitude (i.e., associated voltage) for these signals. It is assumed that all these minimum waveform information entropy signals are mainly affected by the same crack nucleation sources; therefore, they should result in the same range of amplitudes regardless of loading spectrum. To examine this assumption, the amplitudes of signals with minimum information entropy in all tests are compared. As an example, Figure 10 shows the minimum information entropy signal recorded in one of the programmed loading tests. The same range of amplitude is expected for all signals with minimum information entropy

values. To demonstrate the differences in amplitudes of minimum information entropy signals with other signals, the amplitude range of two other types of signals in each test is examined: a signal for which Channel 2 shows higher information entropy, and a signal for which the information entropy value of both channels is almost the same. It should be noted that waveform information entropies of Channel 2 are mostly lower than the waveform information entropies of Channel 1 in each test (as shown in Figure 6-9). In both scenarios, the same signal recorded in each channel is depicted, and the amplitude for the signal is found. The average and standard deviation of amplitude range for each of the signal types is calculated, and the results show that for the signals with minimum information entropy, average amplitude is 54 dB with standard deviation of 2 dB, while other signal types have an average amplitude of 68 dB with standard deviation of 8 dB and 67 dB with standard deviation of 12 dB, respectively. It is seen that the amplitude range in the minimum information entropy signals is very small, while the other signals examined are associated with big differences in their amplitude ranges. This reinforces the assumption that the minimum information entropy signals in all tests come from the same source (i.e., crack nucleation).

It is important to note that in some tests, the minimum value of the information entropy did not happen at the same cycle in both channels. However, differences in the cycle numbers were in the range of 1% of the fatigue life until crack initiation. The difference is due to the noise inherent to the AE signals. As explained previously, the voltage range of these signals is very short; therefore, small amounts of noise can make a difference and result in a change in the timing of the minimum waveform information entropy. Figures 6-9 b show that after crack initiation, more signals are associated with information entropy values of

the absolute minimum before crack initiation. This is expected since crack growth can be viewed as a series of crack nucleation. The further decrease in information entropy after crack initiation compared to the absolute minimum preceding it (in some cases) is very small and due to further concentration of emission generation source (i.e., crack nucleation).

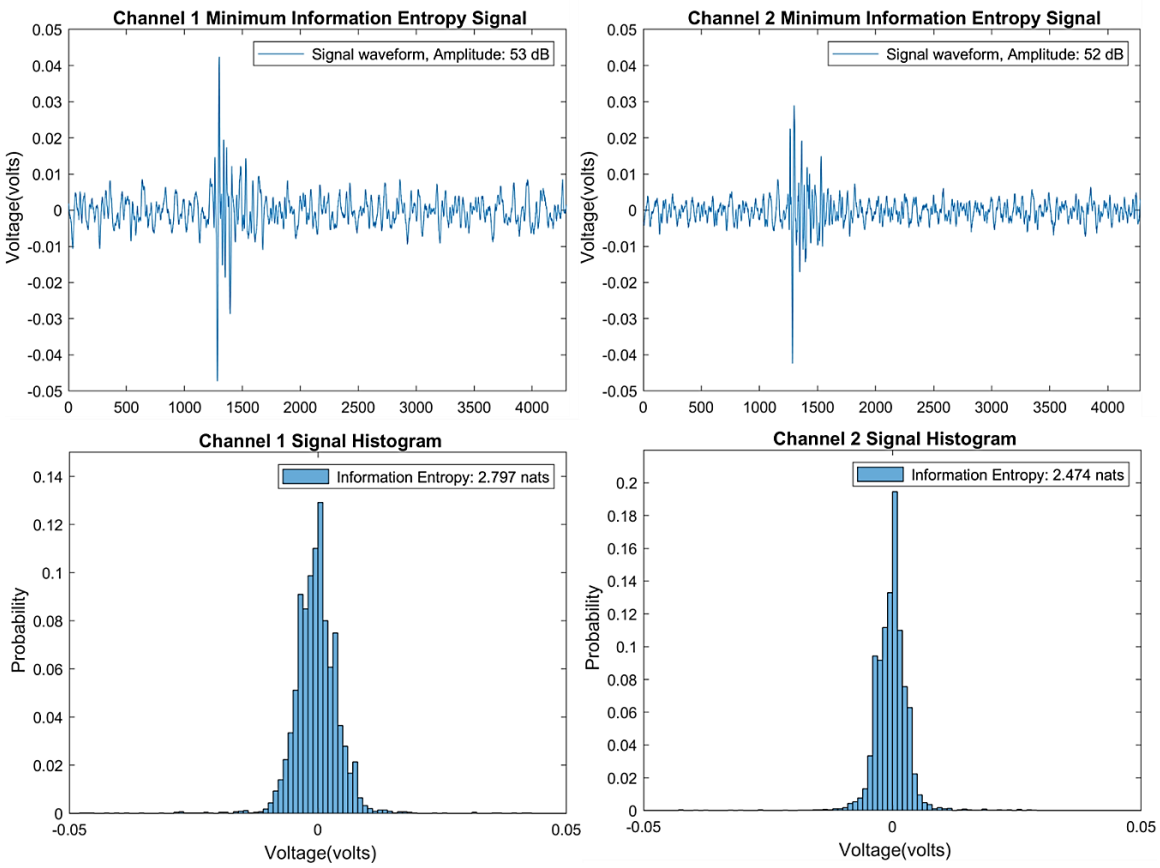

Figure 2-10 - Minimum information entropy signal, its amplitude, and histogram in Channel 1 (left) and Channel 2 (right). Amplitude and information entropy in Channels 1 and 2 are 53 [dB], 2.797 [nats], and 52 [dB] and 2.474 [nats], respectively.

The crack nucleation and initiation point cannot be readily distinguished by the other features of the AE signal, but due to the inherent properties of the signal, information entropy is capable of detecting them. The unique properties of the information entropy can reveal details of the crack nucleation and initiation. At crack nucleation, most of the sound

emitted from the notch area is due to nucleation, and therefore its waveform has low information entropy in both channels. The voltage range of the signal as well as the minimum information entropy value will fall within a short interval and is consistent in all tests with small changes related to other parameters, such as maximum load. After this point, a jump in cumulative information entropy is seen in both channels, indicating crack initiation. Figure 11 shows the minimum waveform information entropy value prior to crack initiation in both channels and its dependence on maximum load. It is evident from the plots in this figure that the linear dependence of minimum waveform information entropy value on maximum load in both channels has a mild increasing slope of 0.15 [nats/kN] of maximum load. Mean, standard deviation and coefficient of variation (CoV) for the minimum waveform information entropies of tests in each channel are reported in Table 1. It can be observed that the final values of the minimum information entropy in all tests fall within an interval of 2.0 to 3.0 [nats], where the mean value for channel 1 was 2.748 [nats] and the mean value for channel 2 was 2.375 [nats].

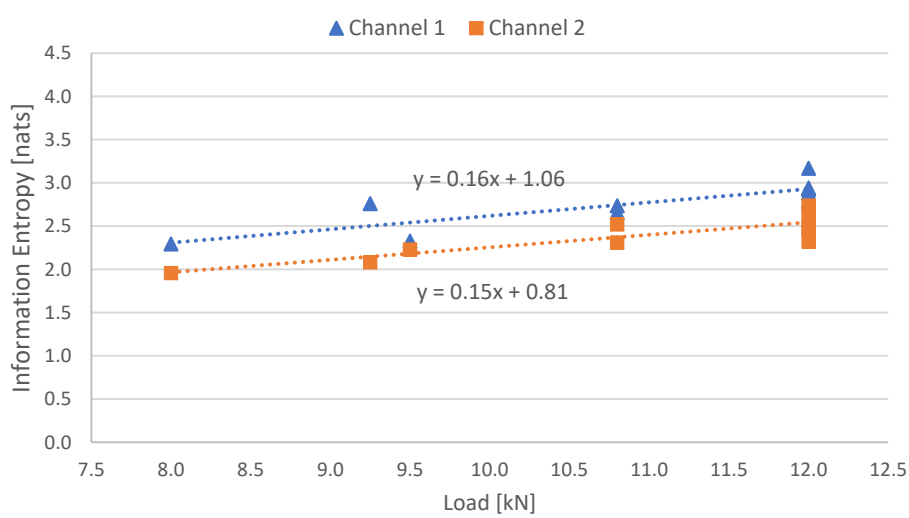

Figure 2-11 – Variation of the minimum waveform information entropy with maximum load for each sensor from each of the loading conditions. A linear fit to the data indicates an increase of 0.15 [nats/kN] of maximum load with a shift of approximately 0.35 [nats] between sensors.

Table 2-1 - Mean, STD and CoV of minimum waveform information entropies

	Mean	SD	CoV
Channel 1	2.748	0.257	9.34%
Channel 2	2.375	0.232	9.76%

2.6. Conclusions

A new method for detecting precursors to fatigue crack initiation using AE signals has been presented for *in-situ* fatigue life analysis in aluminum alloy structures. This method consists of taking the AE signal and processing it by removing hit lockout time and using an optimal bin width to calculate the waveform information (Shannon) entropy. Measurements of the information entropy associated with AE waveform signals were obtained from two independent AE sensors to enhance the filtering of the signals and to validate the calculated waveform information entropy. Compared to the conventional threshold-dependent AE features such as count and energy, waveform information entropy provides an earlier, more consistent, more reliable and threshold-independent detection of fatigue crack initiation in structural health monitoring.

The following conclusions were drawn from the AE waveform information entropies:

- The choice of bin width is an important step in developing histogram for a signal and consequently measuring its information entropy. Selection of the optimum bin width improves measurement and differentiation in signals information entropy values that yields in the detection of crack initiation.
- Information entropies of the AE waveform signal coming from the notch area reached minimum values preceding the formation of a macrocrack. Since most of the AEs are generated from nucleation of microcracks, the signals were centered

around specific values that were sharp and narrowly dispersed as the microcracks coalesce, thereby minimizing the information entropy. This contrasts with the time prior to crack nucleation, where AE signals are generated from multiple locations and sources at the notch, such as inclusions, leading to waveforms with wider spreads corresponding to higher waveform information entropies.

- Cumulative information entropy exhibits very little dependence on the spatial location of the measurement, unlike the cumulative count and cumulative energy, both of which showed significant variation. This is consistent with a previous observation that the normalized cumulative information entropy is a better representative of damage evolution [26].
- Cumulative information entropy also exhibited a sudden increase preceding propagation of the macrocrack. This property, when combined with the observation of minimum AE waveform information entropy values at macrocrack formation, provides a very reliable indicator of fatigue crack initiation.
- Study of the amplitudes of signals associated with minimum information entropy values showed they are independent of the loading condition, with all values falling within an interval of 2.0 to 3.0 [nats]. However, the minimum information entropy values themselves were found to increase slightly with the maximum load at a rate of 0.15 [nats/kN] of maximum load. There was also a slight shift of 0.35 [nats] between the two sensors.

2.7. References

[1] Md. T. A. Ansari, K. K. Singh, and M. S. Azam, “Fatigue damage analysis of fiber-reinforced polymer composites—A review,” *J. Reinf. Plast. Compos.*, vol. 37, no. 9, pp. 636–654, May 2018.

[2] J. A. Bannantine, J. J. Comer, and J. L. Handrock, *Fundamentals of metal fatigue analysis*. Englewood Cliffs, NJ: Prentice hall, 1990.

[3] P. A. Vanniamparambil, U. Guclu, and A. Kontsos, "Identification of Crack Initiation in Aluminum Alloys using Acoustic Emission," *Exp. Mech.*, vol. 55, no. 5, pp. 837–850, Jun. 2015.

[4] T. M. Roberts and M. Talebzadeh, "Acoustic emission monitoring of fatigue crack propagation," *J. Constr. Steel Res.*, vol. 59, no. 6, pp. 695–712, Jun. 2003.

[5] F. Hamel, J. P. Bailon, and M. N. Bassim, "Acoustic emission mechanisms during high-cycle fatigue," *Eng. Fract. Mech.*, vol. 14, no. 4, pp. 853–860, Jan. 1981.

[6] M. N. Bassim, S. St. Lawrence, and C. D. Liu, "Detection of the onset of fatigue crack growth in rail steels using acoustic emission," *Eng. Fract. Mech.*, vol. 47, no. 2, pp. 207–214, Jan. 1994.

[7] M. Biancolini, C. Brutti, G. Paparo, and A. Zanini, "Fatigue cracks nucleation on steel, acoustic emission and fractal analysis," *Int. J. Fatigue*, vol. 28, no. 12, pp. 1820–1825, Dec. 2006.

[8] T. M. Morton, R. M. Harrington, and J. G. Bjeletich, "Acoustic emissions of fatigue crack growth," *Eng. Fract. Mech.*, vol. 5, no. 3, pp. 691–697, Sep. 1973.

[9] A. Berkovits and D. Fang, "Study of fatigue crack characteristics by acoustic emission," *Eng. Fract. Mech.*, vol. 51, no. 3, pp. 401–416, Jun. 1995.

[10] A. Keshtgar and M. Modarres, "Detecting crack initiation based on acoustic emission," *Chem. Eng. Trans.*, pp. 547–552, Jul. 2013.

[11] G. La Rosa, C. Clienti, and F. L. Savio, "Fatigue Analysis by Acoustic Emission and Thermographic Techniques," *Procedia Eng.*, vol. 74, pp. 261–268, 2014.

[12] M. Mohammad, S. Abdullah, N. Jamaludin, and O. Innayatullah, "Predicting the fatigue life of the SAE 1045 steel using an empirical Weibull-based model associated to acoustic emission parameters," *Mater. Des. 1980-2015*, vol. 54, pp. 1039–1048, Feb. 2014.

[13] R. Unnthorsson, T. Runarsson, and M. Jonsson, "Acoustic emission based fatigue failure criterion for CFRP," *Int. J. Fatigue*, vol. 30, no. 1, pp. 11–20, Jan. 2008.

[14] T. P. Philippidis and T. T. Assimakopoulou, "Strength degradation due to fatigue-induced matrix cracking in FRP composites: An acoustic emission predictive model," *Compos. Sci. Technol.*, vol. 68, no. 15–16, pp. 3272–3277, Dec. 2008.

[15] M. R. Bhat, M. A. Majeed, and C. R. L. Murthy, "Characterization of fatigue damage in unidirectional GFRP composites through acoustic emission signal analysis," *NDT E Int.*, vol. 27, no. 1, pp. 27–32, Feb. 1994.

[16] D. G. Aggelis, N.-M. Barkoula, T. E. Matikas, and A. S. Paipetis, “Acoustic structural health monitoring of composite materials : Damage identification and evaluation in cross ply laminates using acoustic emission and ultrasonics,” *Compos. Sci. Technol.*, vol. 72, no. 10, pp. 1127–1133, Jun. 2012.

[17] D. Crivelli *et al.*, “Localisation and identification of fatigue matrix cracking and delamination in a carbon fibre panel by acoustic emission,” *Compos. Part B Eng.*, vol. 74, pp. 1–12, Jun. 2015.

[18] R. Gutkin, C. J. Green, S. Vangrattanachai, S. T. Pinho, P. Robinson, and P. T. Curtis, “On acoustic emission for failure investigation in CFRP: Pattern recognition and peak frequency analyses,” *Mech. Syst. Signal Process.*, vol. 25, no. 4, pp. 1393–1407, May 2011.

[19] D. E. Mouzakis and D. G. Dimogianopoulos, “Acoustic emission detection of damage induced by simulated environmental conditioning in carbon fiber reinforced composites,” *Eng. Fract. Mech.*, vol. 210, pp. 422–428, Apr. 2019.

[20] A. Kahirdeh and M. M. Khonsari, “Energy dissipation in the course of the fatigue degradation: Mathematical derivation and experimental quantification,” *Int. J. Solids Struct.*, vol. 77, pp. 74–85, Dec. 2015.

[21] Huang, Miinshiou, Liang Jiang, Peter K. Liaw, Charlie R. Brooks, Rodger Seeley, and Dwaine L. Klarstrom, “Using acoustic emission in fatigue and fracture materials research.,” *JOM*, vol. 50, no. 11, pp. 1–14, 1998.

[22] I. G. Palmer, “Acoustic emission measurements on reactor pressure vessel steel,” *Mater. Sci. Eng.*, vol. 11, no. 4, pp. 227–236, Apr. 1973.

[23] A. Keshtgar, C. Sauerbrunn, and M. Modarres, “Structural Reliability Prediction Using Acoustic Emission-Based Modeling of Fatigue Crack Growth,” *Appl. Sci.*, vol. 8, no. 8, p. 1225, Jul. 2018.

[24] B. Wang and Z. Liu, “Acoustic emission signal analysis during chip formation process in high speed machining of 7050-T7451 aluminum alloy and Inconel 718 superalloy,” *J. Manuf. Process.*, vol. 27, pp. 114–125, Jun. 2017.

[25] B. Wisner *et al.*, “Acoustic emission signal processing framework to identify fracture in aluminum alloys,” *Eng. Fract. Mech.*, Apr. 2018.

[26] C. Sauerbrunn, A. Kahirdeh, H. Yun, and M. Modarres, “Damage Assessment Using Information Entropy of Individual Acoustic Emission Waveforms during Cyclic Fatigue Loading,” *Appl. Sci.*, vol. 7, no. 6, p. 562, May 2017.

[27] M. Chai, Z. Zhang, and Q. Duan, “A new qualitative acoustic emission parameter based on Shannon’s entropy for damage monitoring,” *Mech. Syst. Signal Process.*, vol. 100, pp. 617–629, Feb. 2018.

[28] M. Chai, Z. Zhang, Q. Duan, and Y. Song, “Assessment of fatigue crack growth in 316LN stainless steel based on acoustic emission entropy,” *Int. J. Fatigue*, vol. 109, pp. 145–156, Apr. 2018.

[29] A. Kahirdeh, H. Yun, and M. Modarres, “Degradation Entropy: An Acoustic Emission Based Approach to Structural Health Assessment,” presented at the Structural Health Monitoring 2017 (shm), 2017.

[30] A. Kahirdeh, C. Sauerbrunn, H. Yun, and M. Modarres, “A parametric approach to acoustic entropy estimation for assessment of fatigue damage,” *Int. J. Fatigue*, vol. 100, pp. 229–237, Jul. 2017.

[31] M. Amiri, M. Modarres, and E. L. Droguett, “AE entropy for detection of fatigue crack initiation and growth,” in *2015 IEEE Conference on Prognostics and Health Management (PHM)*, 2015, pp. 1–8.

[32] R. Unnthorsson, T. P. Runarsson, and M. T. Jonsson, “AE Entropy for the Condition Monitoring of CFRP Subjected to Cyclic Fatigue,” *J. Acoust. Emiss.*, vol. 26, pp. 262–269, 2008.

[33] Shannon, Claude Elwood., “A Mathematical Theory of Communication,” *Bell Syst. Tech. J.*, vol. 27, no. 3, pp. 379–423, 1948.

[34] N. Iyyer, S. Sarkar, R. Merrill, and N. Phan, “Aircraft life management using crack initiation and crack growth models – P-3C Aircraft experience,” *Int. J. Fatigue*, vol. 29, no. 9–11, pp. 1584–1607, Sep. 2007.

[35] S. F. Karimian, H. A. Bruck, and M. Modarres, “Thermodynamic entropy to detect fatigue crack initiation using digital image correlation, and effect of overload spectrums,” *Int. J. Fatigue*, vol. 129, p. 105256, Dec. 2019.

[36] H. Yun and M. Modarres, “Measures of Entropy to Characterize Fatigue Damage in Metallic Materials,” *Entropy*, vol. 21, no. 8, p. 804, Aug. 2019.

[37] M. Kharrat, E. Ramasso, V. Placet, and M. L. Boubakar, “A signal processing approach for enhanced Acoustic Emission data analysis in high activity systems: Application to organic matrix composites,” *Mech. Syst. Signal Process.*, vol. 70–71, pp. 1038–1055, Mar. 2016.

[38] G. Siracusano *et al.*, “A framework for the damage evaluation of acoustic emission signals through Hilbert–Huang transform,” *Mech. Syst. Signal Process.*, vol. 75, pp. 109–122, Jun. 2016.

[39] T. C. Lindley, I. G. Palmer, and C. E. Richards, “Acoustic emission monitoring of fatigue crack growth,” *Mater. Sci. Eng.*, vol. 32, no. 1, pp. 1–15, Jan. 1978.

[40] A. Keshtgar and M. Modarres, “A Probabilistic Approach to Small Fatigue Crack Initiation and Sizing Using Acoustic Emission,” Feb. 2017.

[41] D. W. Scott, “On optimal and data-based histograms,” *Biometrika*, vol. 66, no. 3, pp. 605–610, 1979.

[42] M. P. Wand, “Data-Based Choice of Histogram Bin Width,” *Am. Stat.*, vol. 51, no. 1, pp. 59–64, 1997.

[43] J. Payne, G. Welsh, R. J. Christ Jr., J. Nardiello, and J. M. Papazian, “Observations of fatigue crack initiation in 7075-T651,” *Int. J. Fatigue*, vol. 32, no. 2, pp. 247–255, Feb. 2010.

Chapter 3: Fatigue crack measurement based on information entropy of acoustic emission signals[1]

3.1. Abstract

Fatigue crack detection and measurement play an essential role in the remaining useful life (RUL) estimation of sensitive structures. The current use of non-destructive testing (NDT) methods is usually limited to the out-of-service inspections and measurements. The ability to detect structural changes resulting from redistribution of the stress within components while in-service, makes acoustic emission (AE) a desirable NDT method for structural health monitoring (SHM). However, current approaches in AE signal analysis are usually based on some threshold-dependent features such as count and energy of the signals, which limit their utility. This research examines the potential of using a threshold-independent measure of AE signals based on the information content of the signals. The histogram of AE signals is studied to measure the Shannon information entropy. Cumulative information entropy of signals from two independent sensors placed in close vicinity of a crack is compared to two conventional threshold-dependent AE features. It is found that compared to cumulative energy and cumulative count, cumulative AE information entropy is less spatially dependent. The cumulative information entropy is shown to correlate well with crack length. This method provides a novel approach to measure the crack length in general, as shown specifically for aluminum alloy 7075-T6 material, using AE as a well-known NDT technique.

[1] The full-text of this chapter has been published in the Proceedings of ASNT Annual Conference, November 10-12 2020, Virtual. https://bit.ly/3elm4kH

3.2. Introduction

Machining induced damage in manufacturing processes, as well as imperfections in materials (such as voids), can cause fatigue crack growth (FCG) as early as during the first few cycles of the service life [1]. This is especially true when the stress level approaches the strength limit, typically at “hot spot” locations within airframes. The FGC rate will depend on various parameters, such as the specimen geometry and the loading conditions. In the case of variable amplitude loading, the FGC rate will be affected by phenomenological behaviors, such as crack-closure [2]. Other factors influencing the FCG rate, including the crack growth retardation due to crack-closure, and the comparison of the behavior in constant and variable amplitude loads are extensively studied by Newmans et. al. [3] and Lee et al. [4]. Iyyer et al. [5] demonstrated an example of an aircraft fatigue life management using crack initiation and crack growth models for the P-3C aircraft. However, despite over 170 years of research in metal fatigue cracking, there are still shortcoming in detection and measurement of fatigue cracks that result in unexpected development of fatigue cracks and part failure before the expected fatigue life [6]. The standard procedure of periodic maintenance of airframe structures is an expensive, labor-intensive and slow process which requires grounding and downtime for aircraft that results in a considerable increase (by as much as 50%) in the operational costs. As a result, the aerospace industry is moving toward relying on structural health monitoring (SHM) techniques to detect defects and damages in real-time, thereby reducing the need for routine maintenance and increases the integrity of the airframes [7].

Acoustic emission (AE) is one of the most well-known non-destructive testing (NDT) techniques used for SHM. This technique requires small AE sensors to be mounted on the

surface of components, and infers the material degradation process by passively monitoring the acoustic energy released due to the redistribution of stress in a material during FCG. Specific features extracted from the AE signals, such as the signal energy, amplitude, count, and duration are combined to study the material response behavior. Early studies on the FCG were focused on the sources of AE signals [8], while more recent papers focused on the relation between the AE signal features' and FCG rate. Rabiei and Modarres, for example, proposed a model to measure damage severity based on the AE count rate and estimated the crack size distribution [9]. Furthermore, they proposed a framework to recursively update the parameters of their model based on new crack size or crack growth rate observations in aluminum alloy 7076-T6 specimens, using a Bayesian framework [10]. Keshtgar et. al. [11] showed that the Rabiei-Modarres model holds in case of FCG in titanium alloys as well. Although these studies are promising, the use of conventional AE features suffers from the subjective selection of a threshold in the measurement of the features. Therefore, a new measure of AE signal, (Shannon) information entropy, has recently been studied that removes such a dependence. Information entropy is a more integral measure of damage, removing the reliance on the threshold and signal features, such as energy and count rate, by using the signal distribution characteristics. Sauerbrunn et. al. [12] have shown that AE information entropy better correlates with fatigue life in comparison to the energy or count. Chai et al. [13] have correlated the cumulative information entropy AE signals with fatigue crack length on stainless steel. They showed the correlation follows a two-stage behavior. Although many publications are available covering various aspects of AE, the number of publications reporting actual applications of the AE is limited [14]. In previous work, authors of this paper have shown the AE

information entropy can be used to readily detect fatigue crack initiation in aluminum alloy specimen regardless of the loading condition [15].

In this paper, we investigate the calculation of information entropy of AE signals emitted during multiple FCG tests on a 7076-T6 aluminum alloy (AA7075-T6). Two independent sensors record the signals and we show that the information entropy is less spatially dependent in comparison to energy and count. The values of information entropy of the AE signals are calculated, and then compared to the values of the AE signals that have been correlated with crack initiation, as previously reported in reference [15]. A model correlating information entropy to crack length is then developed, and parameters of the model are found using a maximum likelihood estimation (MLE) approach.

3.3. Experimental setup and procedure

3.3.1. Specimen geometry and setup

A total number of 9 compact tension (CT) specimens made of AA7075-T6 were used in this study. The geometry of specimens, its dimensions, and AE sensor placements are shown in Figure 1. Samples were pre-cracked at the V-notch before a loading spectrum was applied. The pre-crack was created by applying a relatively higher load compared to the test loading spectrum, following the ASTM E647 standard.

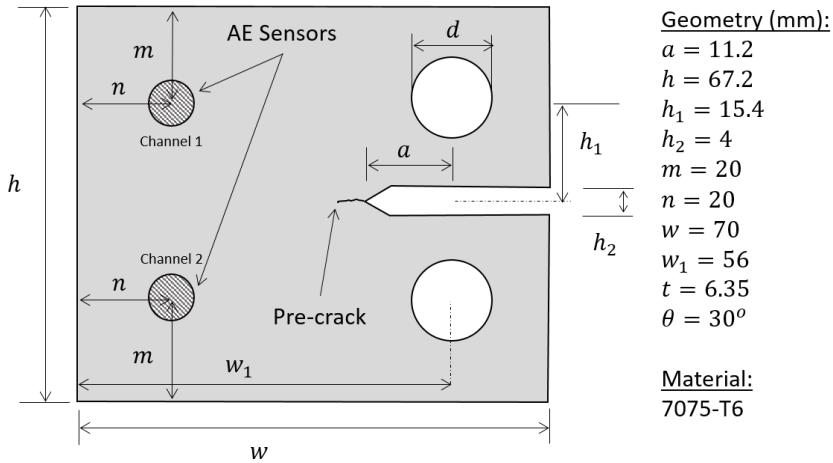

Figure 3-1 - Specimen geometry and dimension

A servo-hydraulic material testing system machine retrofitted with an Instron 8800 controller was used to perform the fatigue tests. Two pin-joint grips were used to hold specimens in the loading cell. Figure 2 shows the specimen setup. An 8 [MP] Point Grey Flea3 sensor with 3.8–13 [mm] Fujinon lens was used to record images in pre-determined intervals for crack length measurements.

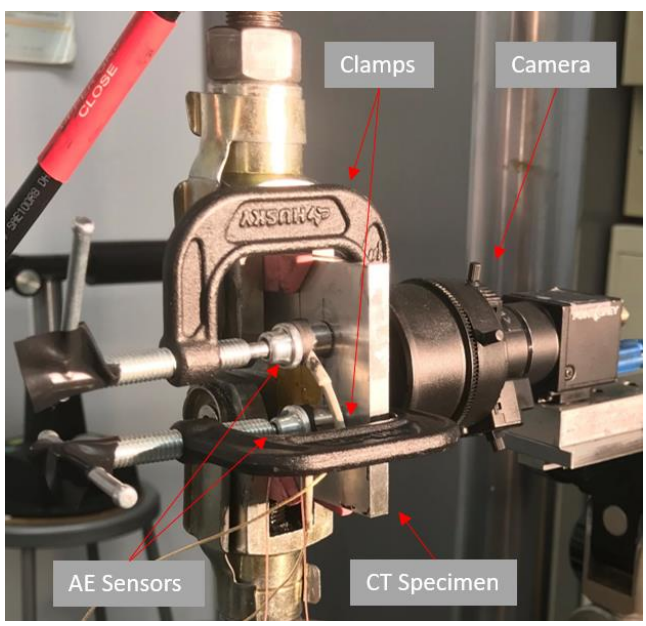

Figure 3-2 - Specimen setup.

3.3.2. Loading condition

Two different loading spectrums, constant load (CL) and variable load (VL), were applied on specimens, as shown in Figure 3. Three stress ratios of 0.1, 0.3 and 0.5 were used in the CL spectrum. In the CL spectrum, maximum load was selected such that the initial stress intensity factor yielded to $\Delta K_{init} = 7\ [MPa.m^{1/2}]$ for stress ratio of $R = 0.1$ and $R = 0.3$, and $\Delta K_{init} = 5\ [MPa.m^{1/2}]$ for $R = 0.5$. The VL spectrum was defined as a block of loading with 5000 cycles, with 1000 cycles of 0.667 [kN] maximum load followed by 1000 cycles of 1.334 [kN] maximum load, 1000 cycles of 2 [kN] maximum load, 1000 cycles of 2.668 [kN] maximum load, and 1000 cycles of 3.336 [kN] maximum load. Stress ratio in VL spectrum was kept constant as $R = 0.1$.

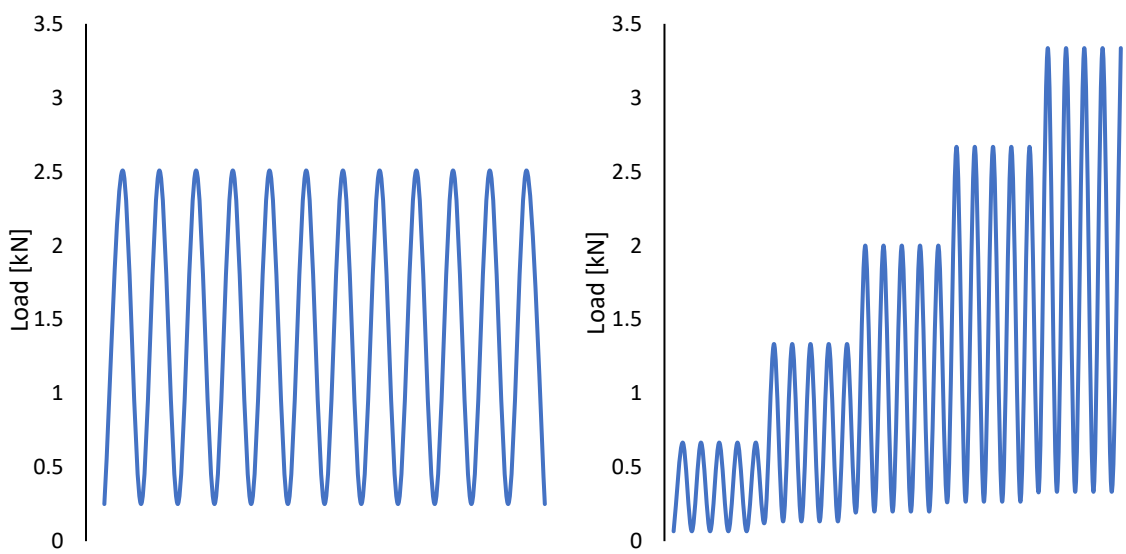

Figure 3-3 - Loading spectrums; constant load - R=0.1 (left), and variable load (right)

3.3.3. Acoustic emission measurement

Two Physical Acoustics PCI-2 based resonant Micro-30s AE sensors (MISTRAS Group, Princeton Junction, NJ) with a frequency range of 150–400 [kHz] and a resonant frequency of 225 [kHz] were used to record the AE signals. An ultrasonic gel coupling agent was

used to improve sensor attachment and the AE signal recording. Sensors were placed symmetrically 20 [mm] away from the specimen edges (as shown by Channel 1 and Channel 2 in Fig. 1). The parameters used in the AE recording—pre-trigger length, peak definition time, hit definition time and hit lockout time—were set to 256 [μs], 300 [μs], 600 [μs] and 1000 [μs], respectively. For each signal, hit length was set to 10,960 points and sampling rate to 5 mega samples per second (MSPS). Signals were passed through a 40 [dB] pre-amplifier before reaching the data acquisition module. The Physical Acoustics AEwin software (Physical Acoustic Corporation, Version E5.60, MISTRAS Group, Princeton Junction, NJ, 2007) was used to record the AE signals. Prior to performing the tests, specimens were placed in the testing rig and the AE signals were recorded while no loads were applied. This process resulted in the selection of a 40 [dB] threshold to remove background noises due to the testing system. Two clamps were used to attach the AE sensors to the specimens. As shown in Figure 2, vinyl electric tape was used to fix the clamp's screw handles in place to prevent noise generation.

3.4. AE signal analysis

The AE dataset recorded for each test was examined to only keep the signals emitted due to FCG. In FCG tests, it is known that the friction of the crack surfaces generates a high number of signals. These signals are known to happen in lower portions of the applied load [11]. Therefore, to eliminate them, a load filter was applied to the recorded signals that only kept the signals recorded within the top 20% of the maximum applied load. The second filter used to remove unwanted signals was the Delta-T filter. Delta-T is the time it takes for one signal to travel from one sensor to the other. Since the crack growth is not directly in the middle of two sensors, a Pythagoras relation was used to calculate a modified

Delta-T value. The modified Delta-T value was then used to detect valid signals within the collected AE dataset. A Matlab code was developed to apply load and Delta-T filtering steps. Only the signals left in the AE dataset after these two filtering actions are used for the remainder of the analysis.

The conventional AE signal analysis uses selective features extracted from signals. Some common features of signals used for analysis are amplitude, rise time, duration, count and energy. However, all these features depend on the subjective value of the threshold. A threshold is set to remove the assumed unrelated portions of the signal. In contrast, information entropy analysis of the AE signals does not depend on any threshold setting. Figure 4 shows a sample AE signal, the conventional threshold-dependent analysis and the threshold-independent analysis of the signal. Figure 4-b shows how the conventional analysis depends on the subjective level of threshold. On the contrary, the information entropy analysis uses all of the values of the AE signals that are recorded. As seen in Figure 4-c, in order to measure the information entropy of AE signals, all of the unique voltage values recorded first need to be extracted. Then, a histogram with appropriate bin width is used to describe the underlying shape of the signal. The histogram describes the probability distribution of voltage values in the signal. The choice of bin width to generate the histogram depends on the accuracy of the collected data. Following the bin width analysis discussed in [15], an optimum bin width of 0.001 was selected for this study. The probability of occurrence of each bin in histogram is then used with the Shannon information entropy equation [16] (Eq. 1) to measure the information content of the signal:

$$I = c\sum_{i=1}^{n} P(V_i)\ln(1/P(V_i)) \quad (1)$$

where, $V_i = \{v_1, v_2, \dots, v_n\}$ is AE signal voltage (considered a random variable), $P(V_i)$ is the probability distribution of the voltage values, I is the signal's information entropy, and c is a constant considered to be unity in this study. The unit of AE information entropy used in this study is 'nats' since in Eq. (1) the natural logarithm is used. The waveforms of the signals in the AE dataset are used to calculate the information entropy using Eq. (1). The voltage values in the waveforms of each signal, forms the histogram as a nonparametric probability distribution. Information entropy is a measure of uncertainty or information content from the probabilistic distribution of a random variable. According to the information entropy, distributions with less bias toward a specific value carry more information about the random variable; hence, they have a higher value of information entropy. Information entropy is used in this study to measure uncertainty as expressed by the histogram representing the AE signal waveforms emitted during the FCG tests.

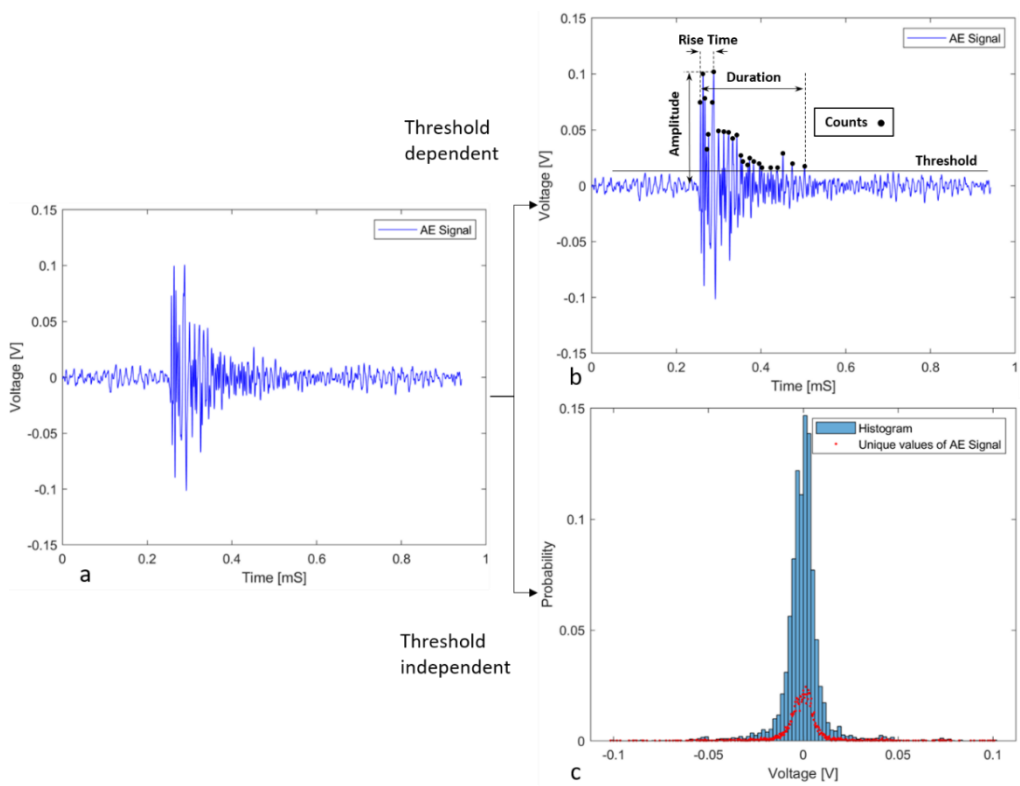

Figure 3-4 - Comparison of threshold dependent and threshold independent AE signal analysis

3.5. Results and discussions

The spatial dependence of the conventional AE signal features (i.e., energy and count), are compared to the information entropy of the same AE signals. Figure 5 shows the cumulative values of information entropy, count and energy of AE signals in one of the FCG tests. In this figure, the same signals recorded in both sensors (Channel 1 and Channel 2) are used to extract the features and measure the information entropy. Ideally, one signal should have the same values for all its descriptors in both channels (in our case of closely placed sensors). Therefore, it is expected that the cumulative figure of each descriptor (energy, count or information entropy) show the same values as a function of cycle (time) in both channels. However, as it is shown in Figure 5-b and 5-c, the cumulative count and cumulative energy of the same signals recorded in the two channels diverge as a function of the cycle number. This behavior is not seen in the case of information entropy values, as shown in Figure 5-a. This shows that information entropy is less spatially dependent compared to the threshold-dependent features. This behavior is described with regard to the information entropy being a more integral measure of the signal characteristics and less sensitive to the acoustic attenuations compared to the threshold-dependent descriptors [12][15].

Figure 6 shows the information entropy values of individual signals recorded in each channel during the FCG test shown in Figure 5. There are two important observations in this figure: 1- all the signals recorded in both channels approximately have the same values of information entropy during the entire test, and 2- except for the very end of the test, all of the information entropy values are within a short interval around 2.5 [nats]. This behavior is associated with the signals' emission source. It is expected that all the signals

kept in the AE dataset are emitted due to the FCG. Consequently, since all signals are emitted due to the same mechanism, their information entropy values would fall within a similar interval.

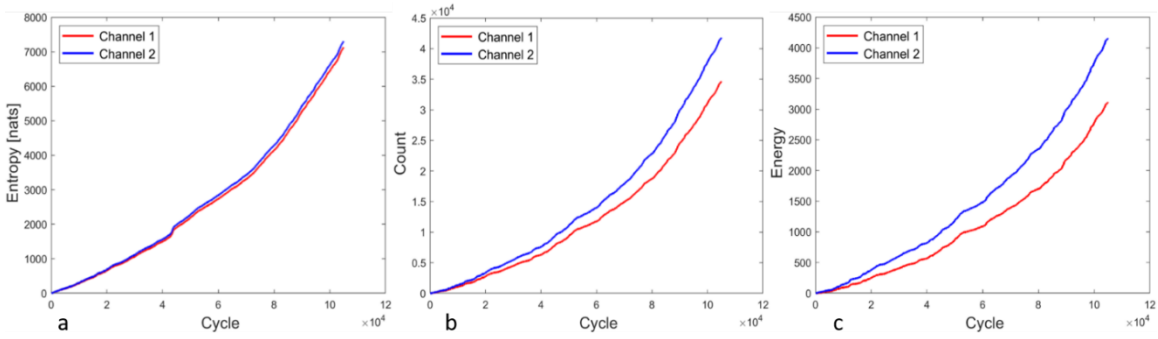

Figure 3-5 - Descriptors of same signals recorded in two sensors: information entropy (a), count (b) and energy (c).

FCG tests are associated with crack length increase, and, therefore, the constant generation of new crack faces. This behavior can also be defined as a repeated crack initiation mechanism, which results in the crack growth. Therefore, AE signals are expected to be emitted as a result of new crack initiations. A previous study of the crack initiation on the same material by the authors [15] has concluded that the minimum value of AE information entropy in a fatigue test, regardless of the loading condition, precedes macro-crack initiation (i.e., 0.25 [mm] crack) and is correlated with crack nucleation. The mean and coefficient of variation for the minimum entropy values are reported as 2.56 [nats] and 13.5% [15], respectively. Similar values are observed in information entropy values of FCG tests, as shown in Figure 6.

To further study the trends in information entropy values, the moving average of the descriptor as a function of cycles and crack length is calculated. Figure 7 shows the results for one of the tests. The moving average is calculated by dividing the cumulative information entropy to the number of AE signals at each instant. It is seen that the moving

average fluctuates in the beginning, but quickly converges to ~2.5 [nats], as the crack length reaches ~4 [mm]. A similar trend with similar values of convergence is seen in all tests, regardless of the loading condition. The convergence value for information entropy of signals in all tests is measured as 2.47 [nats] with 6% coefficient of variation. This value is within the interval of the information entropy value observed before crack initiation in [15], and further suggests that the information entropy value preceding crack initiation (i.e. crack nucleation) in AA7075-T6 falls in the defined interval.

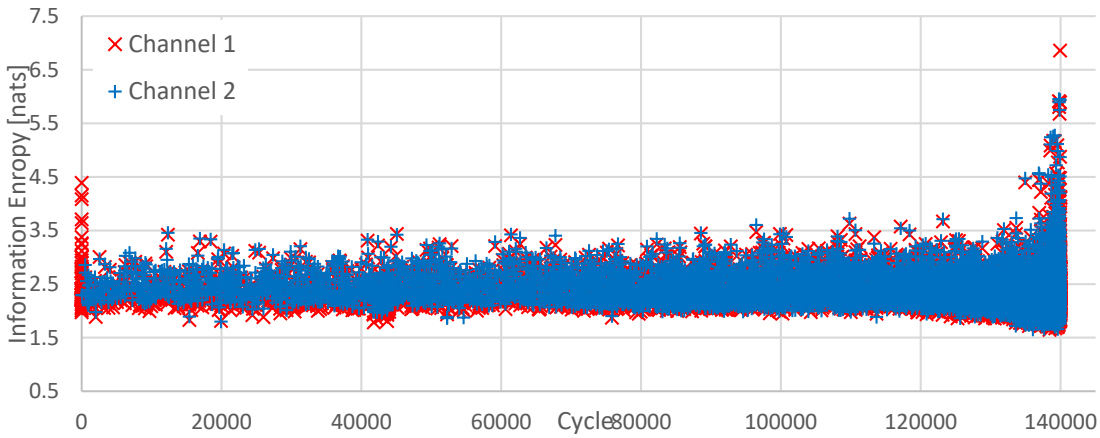

Figure 3-6 - Information entropy of individuals signals in each channel

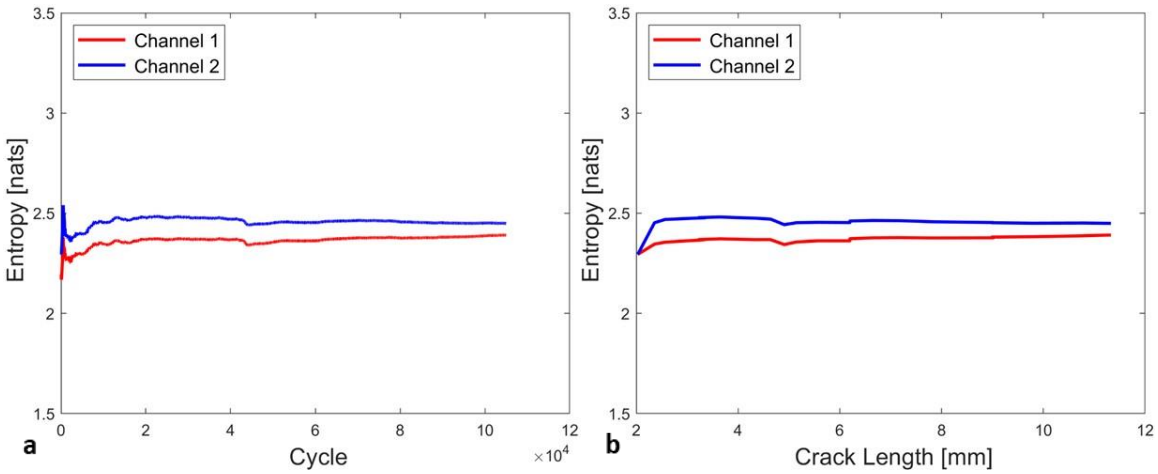

Figure 3-7 - Moving average of information entropy values as a function of cycle (a) and crack length (b).

The similarity in properties of individual information entropy values observed in all FCG tests, regardless of the loading conditions, suggests a strong relationship between the

cumulative values of information entropy and the crack length. However, the relation is not expected to be independent of the loading condition, due to the physics of crack growth response to overload cycles [17]. The overload cycles in VL loading condition result in a residual compressive stress field [18] that will eventually decrease the FCG rate [19]. Extensive experimental work on the subject is reported in Newman et al. [3] on the same material. Therefore, it is expected to observe a slower FCG rate in VL loading condition compared to CL. Figure 8 shows the cumulative information entropy versus crack length for the tests in both loading conditions. It can be seen in this figure that a 10 [mm] crack length is reached when the cumulative information entropy reaches ~6500 [nats] (Fig. 8–a) in case of CL spectrum and ~31622 [nats] in case of VL spectrum. The difference is due to the lower FCG rate in VL to reach to same crack length and higher AE activity. It should also be reminded that in the case of CL spectrum, there are three different stress ratios used. Therefore, it is expected to observe higher variability between tests in CL loading conditions as compared to the VL spectrum in which the same spectrum is used in all tests.

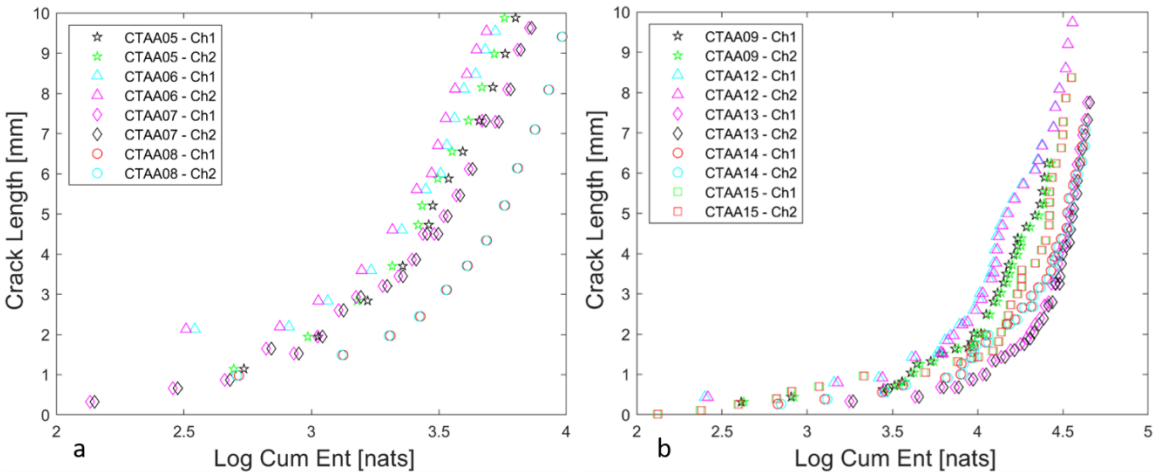

Figure 3-8 - Cumulative information entropy ($\log_{10}$) versus crack length for CL (a) and VL (b) spectrum.

The relationship between crack length and an AE signal descriptor, such as count rate [11], is usually described in the form of the Paris-Erdogan (power-law) equation. These

equations usually determine the FCG rate, given a specific descriptor of AE signals. Parameters of the equation are then determined by fitting the equation to experimental data. In this study, a power-law relationship is found to best fit the data in Figure 8, and is described as:

$$a = c_0(\log_{10} CE)^{c_1} \quad (2)$$

in which a $[mm]$ is crack length from the beginning of the FCG test, CE [nats] is the cumulative AE waveform entropy and c_1 and c_0 are the parameters of the equation. This equation correlates the crack length from an initial state (pre-crack length) to the calculated cumulative entropy. In order to find the parameters of Eq. (2) that best fits the trend, with respect to the loading spectrum, the following steps are taken:

- Parameters of Eq. (2) are first found for each individual test by minimizing the root mean square error (RMSE) using Nelder-Mead minimization method.
- The parameters are used to construct a continues cumulative entropy vs. crack length curve for each test.
- Information entropy value at multiple specific crack lengths are sampled.
- Using the samples, a maximum likelihood estimation (MLE) approach is used to fit a Weibull distribution over cumulative entropy values at specific crack lengths.
- The Weibull distributions are sampled at 5%, 63% and 95% and fit to Eq. (2) to determine the parameter values for each curve.

The results that were obtained after applying these steps, shown in Figure 9, indicate Eq. (2) fits well with the experimental data.

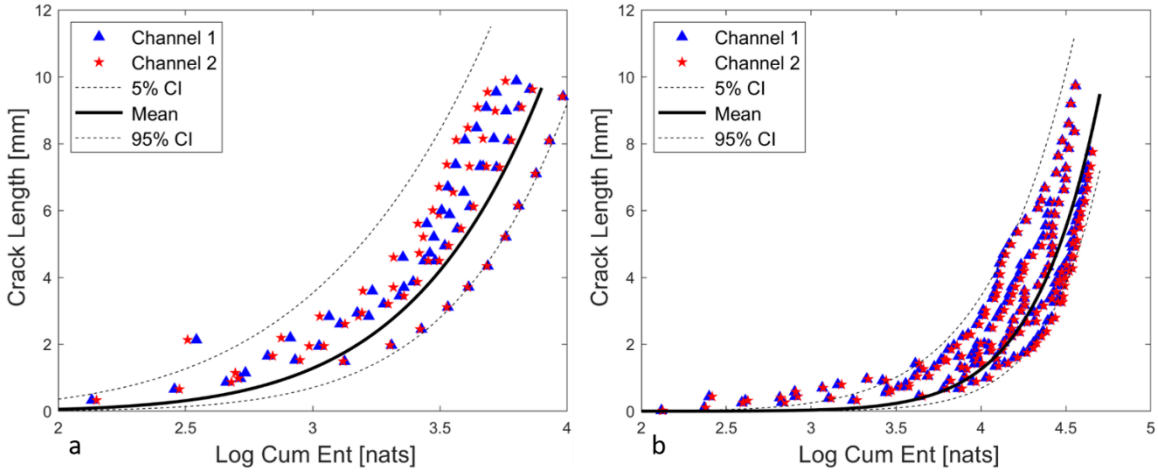

Figure 3-9 - Mean and confidence interval fits of Eq. 2 on experimental data with CL (a) and VL (b) spectrum.

3.6. Conclusions

This study provides a new method for crack length measurement based on a threshold-independent AE signal descriptor (i.e., information entropy). A series of FCG tests are performed on AA7075-T6 using constant and variable loading spectrum, and AE signals are recorded. Two threshold-dependent descriptors of AE signals (count and energy), and one threshold-independent descriptor of AE signals (information entropy), were extracted and compared. It is shown that information entropy is a better descriptor of the information content in the AE signals with less spatial dependence. Information entropy values of the generated AE signals in FCG tests are found to be similar to the information entropy values of AE signals related to crack initiation, which were previously reported by authors in [15]. The observation of the similarity in information entropy values when crack initiation occurs suggests this might be a material-dependent property. However, more experiments and analyses would be necessary to fully validate this assertion. Crack length as a function of cumulative information entropy values is found to follow a power-law equation. Parameters of the equation are found using an MLE approach, for cases involving either constant or variable loading spectrum.

3.7. References

[1] S. A. Barter, L. Molent, and R. J. H. Wanhill, "Typical fatigue-initiating discontinuities in metallic aircraft structures," *International Journal of Fatigue*, vol. 41, pp. 11–22, Aug. 2012, doi: 10.1016/j.ijfatigue.2011.10.017.

[2] E. Salvati, S. O'Connor, T. Sui, D. Nowell, and A. M. Korsunsky, "A study of overload effect on fatigue crack propagation using EBSD, FIB–DIC and FEM methods," *Engineering Fracture Mechanics*, vol. 167, pp. 210–223, Nov. 2016, doi: 10.1016/j.engfracmech.2016.04.034.

[3] J. C. Newman, E. L. Anagnostou, and D. Rusk, "Fatigue and crack-growth analyses on 7075-T651 aluminum alloy coupons under constant- and variable-amplitude loading," *International Journal of Fatigue*, vol. 62, pp. 133–143, May 2014, doi: 10.1016/j.ijfatigue.2013.04.020.

[4] E. U. Lee, G. Glinka, A. K. Vasudevan, N. Iyyer, and N. D. Phan, "Fatigue of 7075-T651 aluminum alloy under constant and variable amplitude loadings," *International Journal of Fatigue*, vol. 31, no. 11–12, pp. 1858–1864, Nov. 2009, doi: 10.1016/j.ijfatigue.2008.11.013.

[5] N. Iyyer, S. Sarkar, R. Merrill, and N. Phan, "Aircraft life management using crack initiation and crack growth models – P-3C Aircraft experience," *International Journal of Fatigue*, vol. 29, no. 9–11, pp. 1584–1607, Sep. 2007, doi: 10.1016/j.ijfatigue.2007.03.017.

[6] L. Molent and B. Dixon, "Airframe metal fatigue revisited," *International Journal of Fatigue*, vol. 131, p. 105323, Feb. 2020, doi: 10.1016/j.ijfatigue.2019.105323.

[7] A. P. Mouritz, *Introduction to Aerospace Materials*. Reston, VA: Woodhead Publishing, 2012.

[8] T. M. Morton, R. M. Harrington, and J. G. Bjeletich, "Acoustic emissions of fatigue crack growth," *Engineering Fracture Mechanics*, vol. 5, no. 3, pp. 691–697, Sep. 1973, doi: 10.1016/0013-7944(73)90047-7.

[9] M. Rabiei and M. Modarres, "Quantitative methods for structural health management using in situ acoustic emission monitoring," *International Journal of Fatigue*, vol. 49, pp. 81–89, Apr. 2013, doi: 10.1016/j.ijfatigue.2012.12.001.

[10] M. Rabiei and M. Modarres, "A recursive Bayesian framework for structural health management using online monitoring and periodic inspections," *Reliability Engineering & System Safety*, vol. 112, pp. 154–164, Apr. 2013, doi: 10.1016/j.ress.2012.11.020.

[11] A. Keshtgar, C. Sauerbrunn, and M. Modarres, "Structural Reliability Prediction Using Acoustic Emission-Based Modeling of Fatigue Crack Growth," *Applied Sciences*, vol. 8, no. 8, p. 1225, Jul. 2018, doi: 10.3390/app8081225.

[12] C. Sauerbrunn, A. Kahirdeh, H. Yun, and M. Modarres, “Damage Assessment Using Information Entropy of Individual Acoustic Emission Waveforms during Cyclic Fatigue Loading,” *Applied Sciences*, vol. 7, no. 6, p. 562, May 2017, doi: 10.3390/app7060562.

[13] M. Chai, Z. Zhang, Q. Duan, and Y. Song, “Assessment of fatigue crack growth in 316LN stainless steel based on acoustic emission entropy,” *International Journal of Fatigue*, vol. 109, pp. 145–156, Apr. 2018, doi: 10.1016/j.ijfatigue.2017.12.017.

[14] K. Ono, “Structural Health Monitoring of Large Structures Using Acoustic Emission–Case Histories,” *Applied Sciences*, vol. 9, no. 21, p. 4602, Oct. 2019, doi: 10.3390/app9214602.

[15] S. F. Karimian, M. Modarres, and H. A. Bruck, “A new method for detecting fatigue crack initiation in aluminum alloy using acoustic emission waveform information entropy,” *Engineering Fracture Mechanics*, vol. 223, p. 106771, Jan. 2020, doi: 10.1016/j.engfracmech.2019.106771.

[16] Shannon, Claude Elwood., “A Mathematical Theory of Communication,” *Bell system technical journal*, vol. 27, no. 3, pp. 379–423, 1948.

[17] J. A. Bannantine, J. J. Comer, and J. L. Handrock, *Fundamentals of metal fatigue analysis*. Englewood Cliffs, NJ: Prentice hall, 1990.

[18] A. Steuwer, M. Rahman, A. Shterenlikht, M. E. Fitzpatrick, L. Edwards, and P. J. Withers, “The evolution of crack-tip stresses during a fatigue overload event,” *Acta Materialia*, vol. 58, no. 11, pp. 4039–4052, Jun. 2010, doi: 10.1016/j.actamat.2010.03.013.

[19] L. P. Borrego, J. M. Ferreira, J. M. Pinho da Cruz, and J. M. Costa, “Evaluation of overload effects on fatigue crack growth and closure,” *Engineering Fracture Mechanics*, vol. 70, no. 11, pp. 1379–1397, Jul. 2003, doi: 10.1016/S0013-7944(02)00119-4.

Chapter 4: Thermodynamic entropy to detect fatigue crack initiation using digital image correlation, and effect of overload spectrums[1]

4.1. Abstract

Current approaches to fatigue life prediction are mostly based on classical fracture mechanics and it is difficult to predict lifetime under different loading conditions, particularly under overload spectrums. A thermodynamic entropy-based approach is less sensitive to variability in loading conditions and provides a dependable measure of damage. Volumetric thermodynamic entropy is utilized in this study to measure damage. Digital Image Correlation-DIC is used to measure plastic deformation in close vicinity of the notch in AA7075-T6 specimens. The plastic deformations are converted to a corresponding thermodynamic entropy, using a modified Clausius-Duhem inequality. A comparison of thermodynamic entropy generation using global measurement consisting of load frame data and Linear Variable Differential Transformer-LVDT extensometer, and local measurement using DIC data is done. The entropic-endurance level for fatigue crack initiation regardless of loading spectrums is shown to scatter within a short interval and is represented by a Weibull distribution.

4.2. Introduction

Fatigue is a major cause of failure in structural components [1]. Fatigue life of metallic components, in general, is divided into two phases: crack initiation and crack propagation. Depending on the material, nearly 50% to 90% of fatigue life is spent up to the time of

[1] The full-text of this chapter has been published in the International Journal of Fatigue, Volume 129, December 2019. https://doi.org/10.1016/j.ijfatigue.2019.105256

crack initiation [2]. The fatigue-induced changes in component materials, generally referred to as “damage”, occur at microscale as early as the first fatigue cycle [3] and accumulate during operational life of components. A review of microstructural damage assessment and modeling in metals in crack initiation is given by Sangid [4]. In thermodynamics, fatigue damage is seen as an irreversible process that dissipates energy and thus generates entropy. This irreversible process and entropy generation can be measured according to the thermal, strain and acoustic energies dissipated, while the system undergoes fatigue. In a thermodynamics context, failure occurs when the entropy reaches an entropic-endurance level, which is independent of the path to failure [5].

Thermodynamic entropy, as a measure of irreversibility in processes, is used as a promising damage index of fatigue [5]. Manufacturing components from raw materials reduces entropy. Entropy generation during fatigue results from the degradation of components tending to return to their natural state before they were manufactured [6]. Entropy generation in thermodynamics is explained by the second law of thermodynamics through the Clausius-Duhem inequality, which states that entropy production within a system must be non-negative. Thermodynamic entropy, as a measure for fatigue damage, is formulated based on continuum damage mechanics [7]. It is shown that widely used empirical equations to assess degradation in metals, such as Coffin-Manson equation, can be deducted from the 2nd law of thermodynamics [8]. A review of thermodynamic entropy studies of fatigue and wear damage mechanism assessment is given by Amiri and Modarres [9]. Dissipated energy from material in course of fatigue loading is expressed by different terms such as plastic deformation, thermal dissipation, internal damage energy and acoustic dissipation [10]. Thermodynamic entropy generation of each term is then measured

regarding energy dissipation of the term. However, the share of each terms is different, specifically in case of metallic and composite materials. For instance, while in metals entropy generation due to plastic deformation is dominant and entropy generation due to internal damage is often negligible [7], in polymer matrix composites, it accounts for 30-50% of plastic deformation entropy [11]. Degradation processes, in general, include different damage mechanisms with multiple rates, types, features and sequences. All of the damage mechanisms result in increase in entropy and failure occurs when the entropy reaches a critical level. Volumetric entropy generation in aluminum alloy and stainless steel subjected to bending, torsional and tension-compression fatigue tests reported in [12] show that regardless of geometry, load and frequency, cumulative entropy generation in each material converged to specific amount, named fatigue fracture entropy (FFE) with values of $4\frac{MJ}{m^3K}$ for Al 6061-T6 and $60\frac{MJ}{m^3K}$ for SS 304. However, in this study, global strain measurements are used to calculated hysteresis energy and consequently thermodynamic entropy generation. Full-field deformation measurement techniques, like Digital Image Correlation, provide us with the opportunity to directly quantify changes in the deformation field related to the irreversible mechanical processes locally, at much smaller length scales.

Digital image correlation (DIC) is a widely accepted and commonly used non-destructive technique (NDT) to measure full-field displacement and strain map on object surfaces in the field of experimental mechanics [13]. This technique, pioneered by Chu et. al. [14], generates displacement and strain maps by following changes of a random pattern applied on the surface, known as speckle pattern, before and after applying load. Bruck et. al. [15] introduced a faster approach for image correlation that leads to more practical use of DIC.

Comparing to interferometric optical techniques, DIC enjoys advantages of simple experimental setup and specimen preparation, low requirements in measurement environment and wide range of measurement sensitivity and resolution [16]. Furthermore, compared to strain gauges and extensometers, DIC provides a full-field measurement and does not suffer surface slipping. These advantages have made this technique to be widely used on composite and metallic materials [16]–[25]. For Metals, specifically in aluminum alloys, analysis of scanning electron microscope (SEM) images taken from aluminum 7075-T6 subjected to fatigue loading have revealed that constituent hard particles (iron-bearing phases) fracture relatively soon in the material and short crack growth (propagation in matrix away from the particle) follows these fractures after a noticeable delay [21]. Similar conclusion is made by Winser and Kontos [25] by analyzing strain maps around constituent particles in aluminum 2024-T3 under monotonic loading and reporting strain localization around the fractured particles to be nearly 4-5 times higher than within the fractured particle. The ability to extract strain maps with various spatial sizes makes DIC a desirable technique to evaluate plastic deformation at high stress concentrated areas.

Entropy generation due to plastic deformation during fatigue is a fundamental irreversible thermodynamic process [12]. Previous studies used global strain measurements to quantify hysteresis energy and use it as plastic deformation energy to find entropy generation. However, not all the hysteresis energy causes damage in materials. Part of it transforms to thermal energy resulting in temperature rise and dissipated through heat (convection and radiation) to the environment. This part should be neglected when measuring entropy generation due to plastic deformation, since it has no influence on the degradation of the material [7]. In fact, it is shown by Wong and Kirby [26] that most of the hysteresis energy,

specially until crack initiation, is dissipated through heat. Therefore, in this paper, DIC is used to solely measure plastic deformation and its corresponding entropy generation on aluminum alloy until fatigue crack initiation. A modified version of the Clasius-Duhem entropy equation is introduced to convert plastic deformation measurements to thermodynamic entropy. This method is applied to AA7075-T6 notched dog-bone specimens, fatigued under different loading conditions. Effect of overload is also studied. It is expected that an entropic endurance level can be found that results in crack initiation in the material, regardless of loading conditions.

4.3. Methods

4.3.1. Thermodynamic entropy

Thermodynamic entropy generation equation in fatigue testing is derived from continuum damage mechanics using the first and the second law of thermodynamics. A detailed derivation can be found in [7]. The second law of thermodynamics is described by the Clausius-Duhem inequality as

$$\dot{S} = \frac{1}{T}\left(\sigma : \dot{\varepsilon}_p - A_k \dot{V}_k - \frac{1}{T}\dot{q} \cdot \nabla T\right) \geq 0 \qquad (1)$$

where $\dot{S}$ is the entropy generation rate, T is the absolute temperature, σ is the stress tensor, $\dot{\varepsilon}_p$ is the plastic strain tensor, $\dot{V}_k$ is the change rate of any internal variable, A_k is the thermodynamic forces associated with the internal variable, $\dot{q}$ is the thermal flux and ∇T is the temperature gradient. Entropy generation defined by Equation 1 consists of three parts: entropy generation due to plastic deformation $\left(\frac{\sigma:\dot{\varepsilon}_p}{T}\right)$, entropy generation due to evolution of internal variables $\left(\frac{A_k \dot{V}_k}{T}\right)$ and entropy generation due to heat conduction $\left(\frac{1}{T^2}\dot{q} \cdot \nabla T\right)$. In

case of metals, entropy generation due to internal variables only accounts for 5-10% of the entropy generation due to plastic deformation and is often negligible [7], [12]. Furthermore, heat conduction is also assumed to be negligibly small [8]. Therefore, only thermodynamic entropy generation due to plastic deformation is measured and used in this study.

Local plastic strain measurement using DIC enables us to directly measure thermodynamic entropy generation due to plastic deformation. The plastic strain energy is estimated by using the yield strength of the material multiplied by the plastic strain of the area under study. Thus, the thermodynamic entropy generation due to uniaxial loading using DIC generated strains can be expressed as:

$$\mathrm{S} = \sum_{i=1}^{N} \sigma_y \, \varepsilon_i A_{pix} \frac{d}{T} \qquad (2)$$

where, N is the number of pixels at area of interest (AOI), σ_y is the yield strength of the material, A_{pix} is the area corresponding to a single pixel, ε_i is the plastic strain at the ith pixel, d is the thickness of the coupon, and T is the absolute temperature (in Kelvin). Equation 2 can be further simplified to:

$$S = \sigma_y \, \frac{d}{T} \sum_{contour} A_i \varepsilon_i = \sigma_y \, \frac{d}{T} A_{contour} \varepsilon_{avg} \qquad (3)$$

where, $A_{contour}$ is the area of the contour and ε_{avg} is the average of the measured strain of the contour. AOI is selected to cover all the vicinity of high stress concentrated area. Temperature rise showed an increase of 2~3 ℃ in all tests. The change in temperature results in a negligibly small difference in absolute temperature and thermodynamic entropy generation. Therefore, absolute room temperature at the time of each test is used in Equation 3.

4.3.2. Digital image correlation

DIC analysis is performed using VIC-2D software [27]. Parameters of the software that strongly affect strain map generation are subset size, step and filter size. Figure 1 shows these parameters on a speckle pattern. Subset size affects the ability of DIC to follow the speckle pattern and find deformations. Its value is mainly dependent on speckle pattern quality and speckle size. Smaller subset results in more detailed displacement maps, but less accuracy in matching process with reference image. A subset size study was performed on speckle pattern on each specimen using Grey Level Co-occurrence Matrix (GLCM) [28] and optimum value for the subset was selected. Step controls the number of data points for which displacement values are calculated. Lower values for step results in generation of more data in AOI, but too small step size adversely affects displacement map calculation by resulting in pseudo displacement generations. Filter size controls strain map calculation using displacement maps generated from images. Lower values of filter size result in more detailed strain maps, but if the values are too low, it generates noise. A sensitivity study was done on all of these parameters and optimum values were selected for each speckle pattern. Failure to select the appropriate value for each of the parameters would directly influence thermodynamic entropy measurement results.

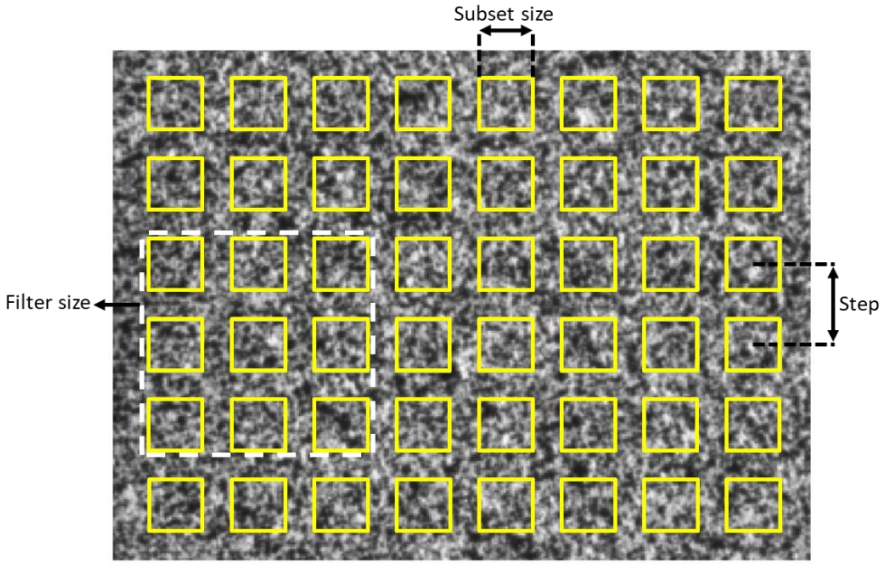

Figure 4-1 - DIC analysis parameters

4.4. Experimental setup and procedure

4.4.1. Procedure

A total of 8 specimens were fatigued under widely different loading conditions. Loading conditions were defined as high cyclic fatigue (HCF), overload spectrum, programmed loading and variable amplitude loading spectrum. Maximum load in HCF loading spectrum was set to 9.25 [kN] with R=0.1. Overload spectrum was defined by fatigue cycling using a stress ratio (R) of 0.1 with maximum load of 12 [kN] and one cycle with maximum load of 15.5 [kN] every 1,500 cycles. Programmed loading was defined as a loading block of 37 cycles, all with maximum load of 12 [kN] and different stress ratios: 20 cycles with R=0.1 followed by 10 cycles of R=0.25, 5 cycles of R=0.5, and 2 cycles of R=0.67. Variable amplitude loading was defined as a block of loading with 1,489 loading points, with maximum of 15.5 [kN]. All tests were paused after a crack was detected at the notch. Detected crack was then measured and crack initiation cycle was calculated. The definition for crack initiation is adopted from the US Navy [29] as a 0.25 mm crack length. A servo-

hydraulic material testing system machine retrofitted with an Instron 8800 controller was used to perform the fatigue tests. Figure 2 shows the loading spectrums and Figure 4 shows experiment setup.

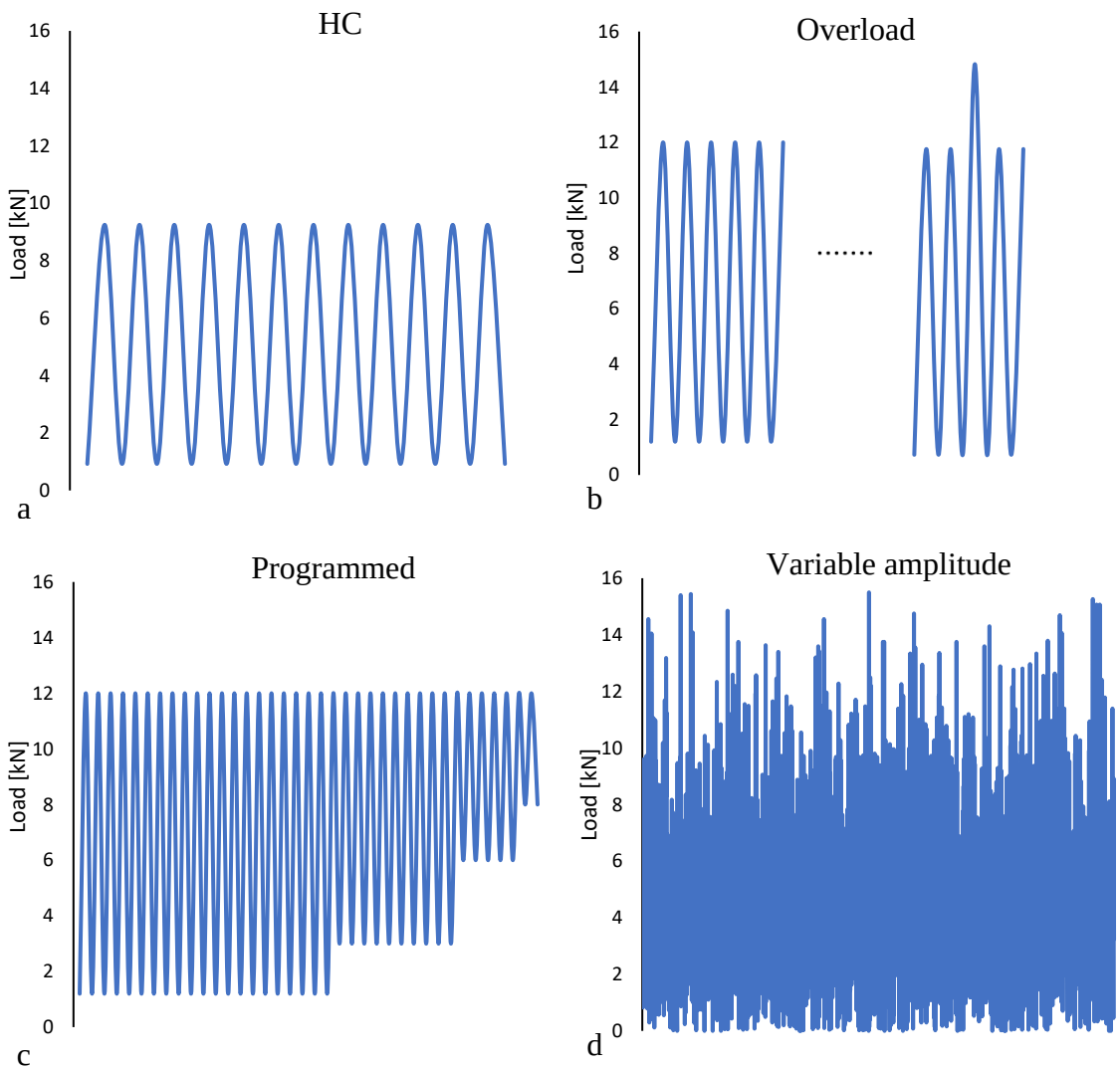

Figure 4-2 - Loading spectrums: HCF (a), overload (b), programmed loading (c) and variable amplitude loading-1 block (d).

4.4.2. Specimen

All specimens were cut from the same sheet of AA7075-T6 material in the grain boundary direction and machined in dog-bone shapes with a notch at the center, following ASTM E466 standard. A drawing of the specimen and its dimensions (in [mm]) is shown in Figure

3. Specimens were sanded around the notch area and guidelines for speckle paint were drawn. The stress concentration factor around the notch area was calculated as 2.77. Yield strength of material is measured as 506.9 [MPa].

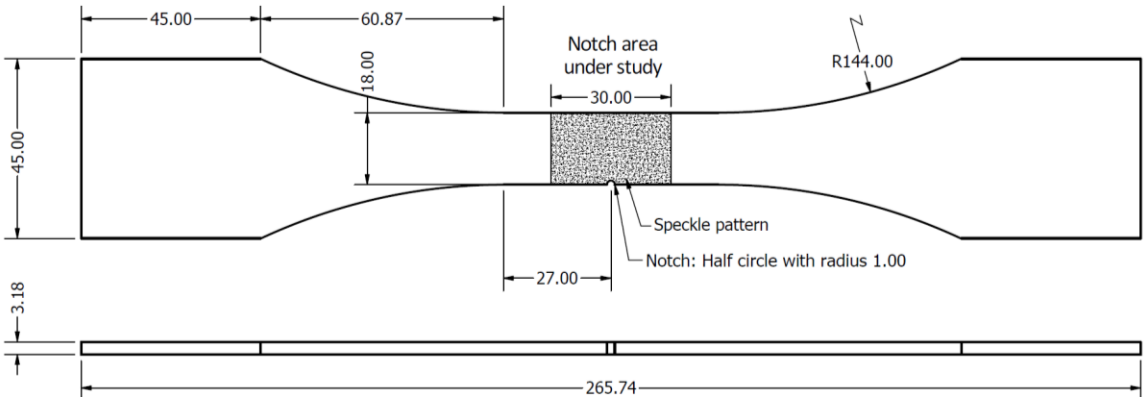

Figure 4-3 - Specimen geometry

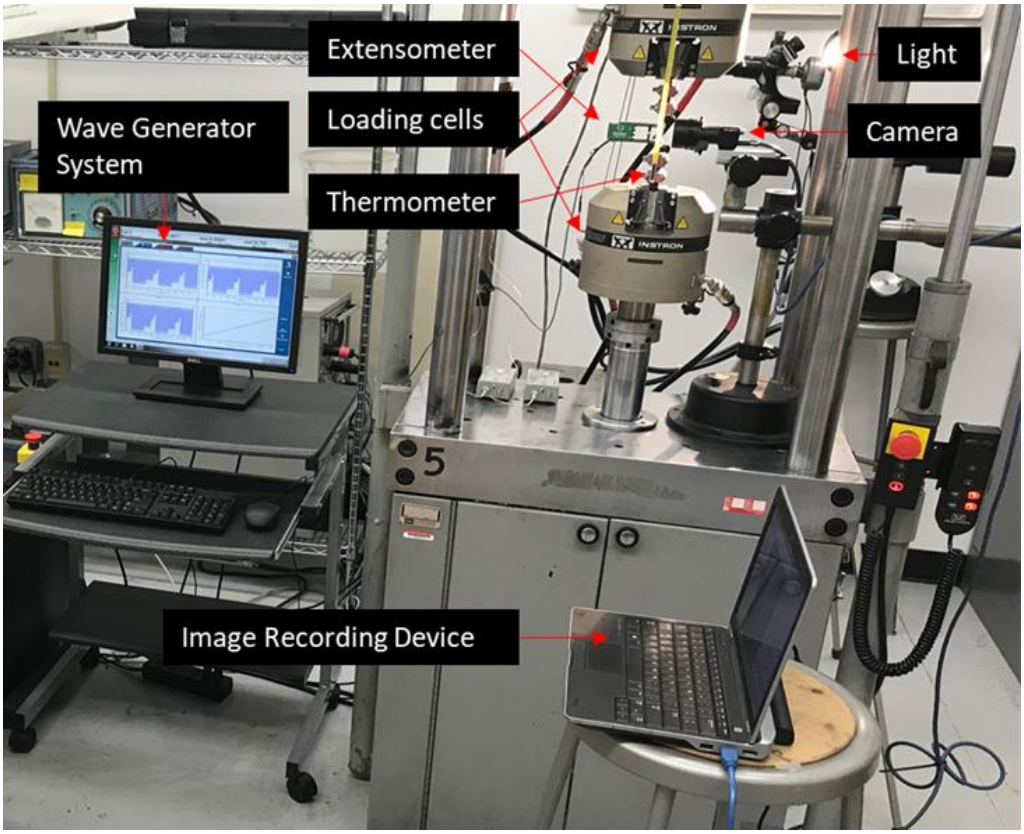

Figure 4-4 - Experimental setup

4.4.3. Digital image correlation

Specimens were prepared before each test by applying speckle pattern around the notch area. Enamel spray paint was used for speckle pattern painting. Speckle pattern quality was checked at the time of painting. A desirable speckle pattern was achieved when the histogram of the speckles grayscale roughly followed a bell shape [30]. Figure 5 shows an example of a desirable speckle pattern used in this study. Images are recorded using an 8 [MP] Point Grey Flea3 sensor with 3.8-13 [mm] Fujinon lens. For each test, a set of 10 consecutive image were recorded as “Reference” image before any load was applied. During the tests, at fixed intervals, the specimen was unloaded and 10 consecutive images were recorded. These consecutive images were then averaged using ImageJ [31] software to minimize noises in image recording. Image averaging was done by averaging the intensity of pixels. The averaged images were used for DIC analysis. The intervals for unloading and image recording was 1,500 cycles for the tests with overload spectrum, 7,500 cycles for test with HCF spectrum, 40 blocks for programmed loading spectrum and 5 blocks for variable amplitude loading spectrum.

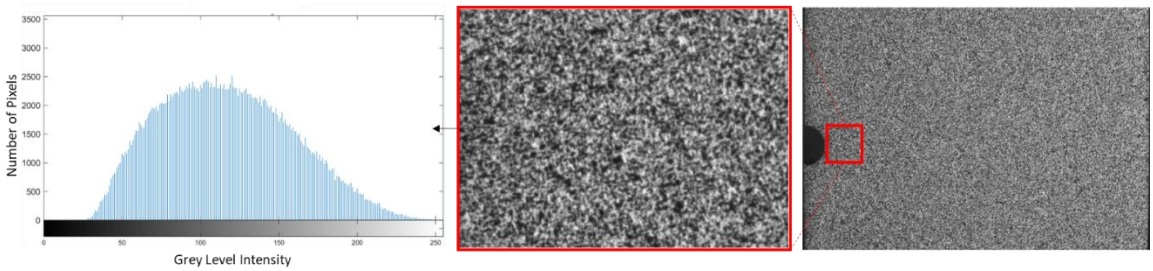

Figure 4-5 - An example of a desirable speckle pattern. Full image (right), AOI (center) and histogram of speckle pattern in contour area (left)

4.5. Results and discussion

Plastic deformation is consisted of plastic strain in axial (parallel to applied load), transvers and shear directions. Hence, the evolution of plastic deformation during fatigue tests is a combination of evolution of strain in all directions. However, trend of change in each of these terms is different during the fatigue life. An effective strain measurement accounting for the change in all strain components, defined as Von Mises strain, is used in this study to measure the thermodynamic entropy generation. Von Mises strain is calculated as:

$$\varepsilon_{von} = \sqrt{\varepsilon_1^2 + \varepsilon_2^2 - \varepsilon_1 \varepsilon_2} \qquad (4)$$

in which ε_{von} is the Von Mises strain, ε_1 and ε_2 are principal strains calculated from axial, transverse and shear strains. Figure 6 shows change in ε_{xx} (transverse), ε_{yy} (axial) and ε_{von} strain maps at four instances before crack initiation in one of the tests with variable amplitude loading spectrum. Crack initiation occurred at load block 107, shortly after the last images were taken. Axial, transverse and shear strain in the AOI were used to calculate principal strains and consequently, Von Mises strains. Figure 6 depicts the trend of changes in axial and transverse strain maps. It is seen that in the first three rows, transverse strain has higher value on the average comparing to the axial strain. However, as the test evolves and gets closer to crack initiation, axial strain increases more and reaches higher values comparing to transverse strain. The values and trend of change in axial or transverse strain maps individually, does not depict the full effect of plastic deformation at the notch root. Meanwhile, Von Mises strain (shown in the third column) can effectively depict the effect of both strain maps. The first three Von Mises strain maps are mostly affected by transverse strain, but the final Von Mises strain map is mostly affected by axial strain map. Crack

initiation follows the highly concentrated strain at the notch, depicted by ε_{yy} and ε_{von} in the fourth row. It is only shortly before crack initiation that plastic strain lobes appear in ε_{yy} and consequently in ε_{von}. Changes in the axial strain map is most significant at the time of crack initiation.

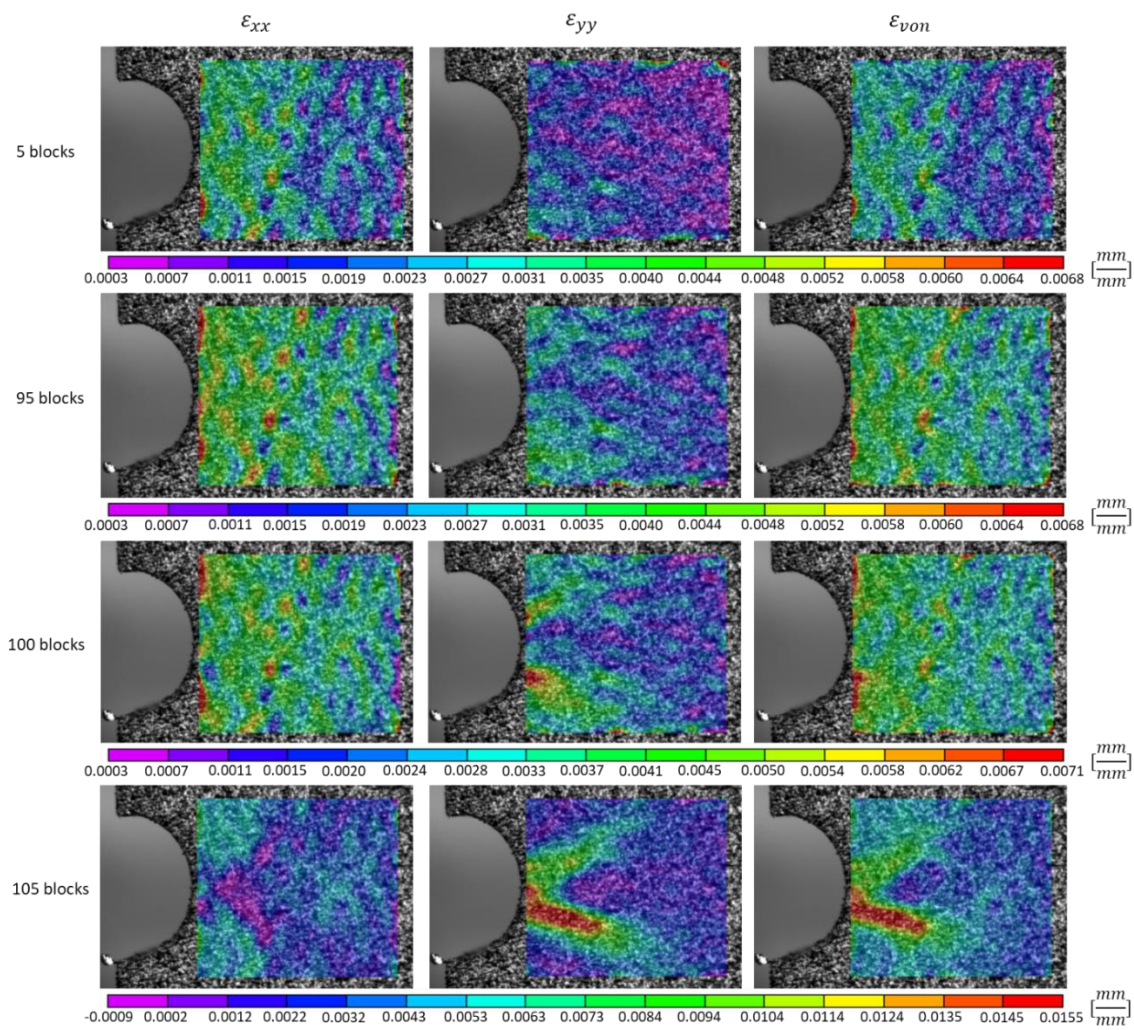

Figure 4-6 - Change in transverse (first column), axial (second column) and Von Mises (third column) strain maps in cycles leading to crack initiation. First row shows results after 40 block, second row after 95 blocks, third row after 100 blocks and fourth row shows results after 105 blocks of loading are applied.

The effect of overload cycle on the plastic deformation and consequently thermodynamic entropy is further studied in the tests with overload spectrum. In these tests, in addition to images taken every 1,500 cycles at zero load, images were also taken at 10% maximum

load before and after applying the overload. Therefore, for this specific loading spectrum, in addition to the change of plastic strain determined when no load is applied, change of total strain at 10% maximum load before and after application of an overload was also studied. Overload cycles are expected to increases the fatigue life of material [2] due to residual compressive stress and crack closure effect [32] in micro-cracks. Figure 7 shows the results for Von Mises plastic strain and the effect of overload cycle on the Von Mises total strain. Dotted lines indicate an overload cycle and the arrow on the dotted line show the change in total strain before and after an overload is applied.

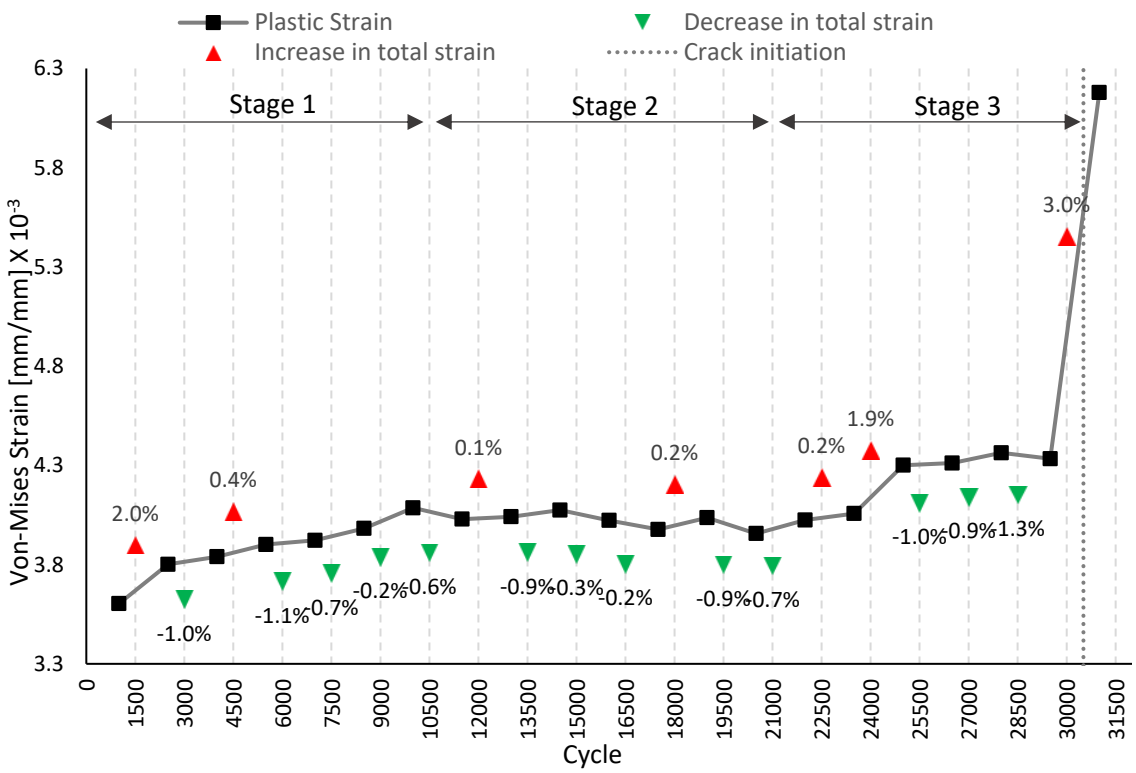

Figure 4-7 – Von Mises plastic and change in total strain before and after overload application at the notch root in an overload spectrum test

The overload effect is the subject of many studies in literature, addressing different aspects, such as its influence in notched specimen [33] [34], in biaxial fatigue loading [35] and the role of each mechanism and their interaction on crack growth retardation [36]. However,

these discussions are out of the scope of this study. Here, we are focused on the effect of periodic overload on plastic strain measured at the notch and consequently change in thermodynamic entropy and thermodynamic entropy generation. Figure 7 shows the overall trend of plastic strains is increasing, as expected, but it includes several points where it decreases due to the overload cycle. Results suggests that overload cycles affect the plastic strain differently at different stages of the fatigue life. In the first stage, after a major increase in total strain due to the first overload cycle [37], the total strain mainly decreases after the overload is applied, resulting in a decrease in the plastic strain accumulation rate. In the second stage, overload cycles are mostly associated with decrease in total strain. The decrease in the total strain cause a decrease in the overall value of the plastic strain. This is attributed to effect of crack closure that causes perturbation in micro-crack growth [38] and generation of compressive residual stress [39]. An increase in fatigue life is attributed to the decrease in the plastic strain values in this stage. In the third stage, there is an inflection point where the overload cycles are associated with detrimental effects on fatigue life due to large increases in total strain and an acceleration in the growth rate of plastic strain. In this stage, although overload cycles result in arresting the major micro-crack, they are also associated with nucleation of new deflected micro-cracks [36] that accumulate and result in a macro-crack initiation (a 0.25 [mm] crack), following a large increase in total strain at cycle 30,000. It is also important to note that the variability in the overload effects on the change in total strain is reflective of the stochastic nature of the fatigue process.

Thermodynamic entropy generation in the AOI (control volume), following Equation 2, is always a non-negative value. However, the decrease in the plastic strain values and

consequently thermodynamic entropy is a result of the entropy passing the control volume boundaries. Regarding to the second law of thermodynamic, entropy of a system is consisted of the entropy passing its boundaries and entropy generation within the boundary. Overload cycle generates residual compressive stresses at the notch. The effect of overload is seen as entropy passing the boundaries of control volume and change the entropy value of the control volume. Depending on the fatigue life expended, it can be a negative value, resulting in negative entropy generation measured (as in stage 2) or a positive value increasing the entropy generation and accelerating damage as in final stage of fatigue life leading to crack initiation. Therefore, all changes in entropy measurement follow the second law of thermodynamics.

Thermodynamic entropy measurement in most of the available literature is based on hysteresis energy calculated from global strain measurements [7], [11], [12], [40]–[44] using load frame or extensometer attached to specimen. However, use of global strain measurement may lead to large errors [45]. In fatigue loading, crack initiation follows plastic strain generation and development in high stress concentration areas (e.g. notches). These areas are small relative to the specimen geometry and therefore, local measurements would be able to better gauge the irreversible damage in these areas. Figure 8 shows the comparison in thermodynamic entropy measurement per unit volume in one test, using three different measurements approaches: (1) use of load frame data, (2) a LVDT extensometer, and (3) DIC data. Load frame data consists of the actuator position values and reflects energy dissipation from the whole volume of specimen except grip area. The LVDT extensometer records energy dissipation of a volume with 25 mm X 18 mm area and specimen thickness (3.175 [mm]). Entropy generation using global measurements is

calculated by measurement of hysteresis energy divided by temperature. Relative to the load frame, the extensometer provides more local information about the energy dissipation at the notch. However, comparing to the DIC strain measurements, the extensometer measurements are global. Hysteresis area measured using the global strain measurements are mostly affected by axial strain. Therefore, in order to provide a better comparison between global and local strain measurements, the local thermodynamic entropy measurement (DIC data) reported in Figure 8 only uses ε_{yy} values.

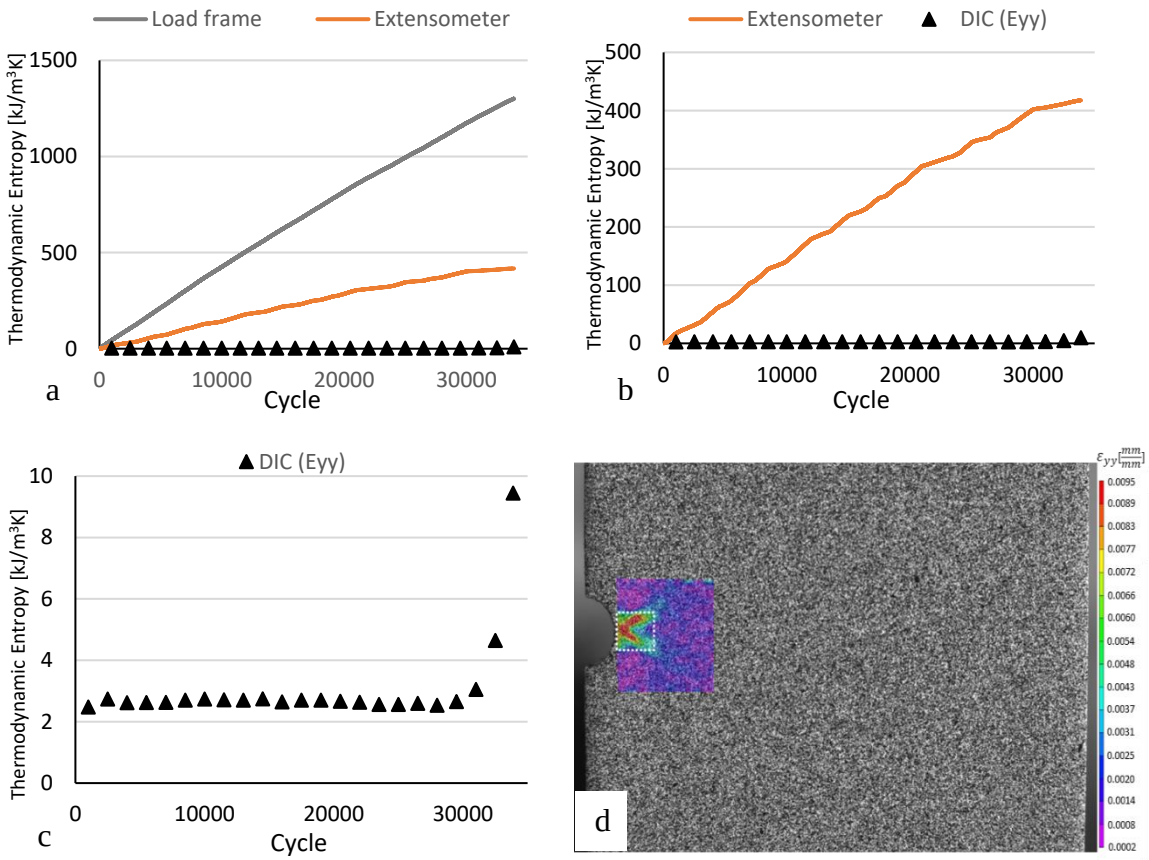

Figure 4-8 - Thermodynamic entropy generation measurement comparison using load frame data, extensometer and DIC data (a), extensometer and DIC data (b), DIC data (c) and the plastic strain lobes around the notch at the time of crack initiation (d). Measurement are carried out until crack initiation. Plastic strain values in the selected rectangle (d) are used for DIC measurement.

Figure 8 shows that the thermodynamic entropy generation using these different measurement approaches could vary by orders of magnitude. However, strain measurements using extensometer are shown to yield better plastic strain results comparing to use of cross-head positions (load frame) [45]. Thermodynamic entropy at crack initiation time measured from extensometer shown to yield similar values as reported in Liakat and Khonsari [44]. To accurately measure the entropy generation due to plastic deformation, only the amount of hysteresis energy that contribute to plastic deformation should be considered. Part of hysteresis energy that dissipated through heat (convention and radiation) does not damage material and should be neglected [7]. Wong and Kirby [26] reported that in low cycle fatigue tests of aluminum 6061-T6 until crack initiation, 85-95% of hysteresis energy absorbed by material is dissipated in form of heat. Also, it is shown by Knysh and Korkolis [46] that heat conduction and radiation increase with plastic deformation. Therefore, a careful attention to the contribution of different terms of hysteresis area is needed when global measurements are used to measure the hysteresis energy and subsequently thermodynamic entropy generation. However, DIC directly measures the plastic deformation on the material and can be readily used to calculate entropy generation due to plastic deformation.

To measure the thermodynamic entropy independent of the specimen geometry, the value calculated from Equation 3 is divided by contour area and specimen thickness. The result is thermodynamic entropy per unit volume or volumetric thermodynamic entropy. Although it is independent of the specimens' geometry, it depends on the contour area selected for plastic deformation measurements. Plastic deformation around the notch root is highly non-linear and concentrated at the center of the notch. Deformation decrease as

distance from the notch root increases. Therefore, the measurement of plastic deformation in the contour area is directly related to the entropy measurement per unit volume. In order to accurately measure thermodynamic entropy due to plastic deformation, contour area should cover the plastic deformation at the notch root at the time of crack initiation. Selection of a large contour area results in lower values for thermodynamic entropy per unit volume while selection of a small contour area might result in failure to capture all plastic deformations at crack initiation. Therefore, contour area should be selected to adequately cover all plastic deformations at the time of crack initiation in all tests. However, cyclic plastic zone size calculation is not a trivial task and depends on the loading spectrum [47]. In this work, a study on the plastic deformation at crack initiation showed that a square contour with 1.5 mm2 area can adequately capture plastic deformation at crack initiation in all tests. Figure 9 shows the contour area on last DIC image available before crack initiation in one of the variable amplitude loading tests. It is seen that the contour area covers the plastic deformation adequately.

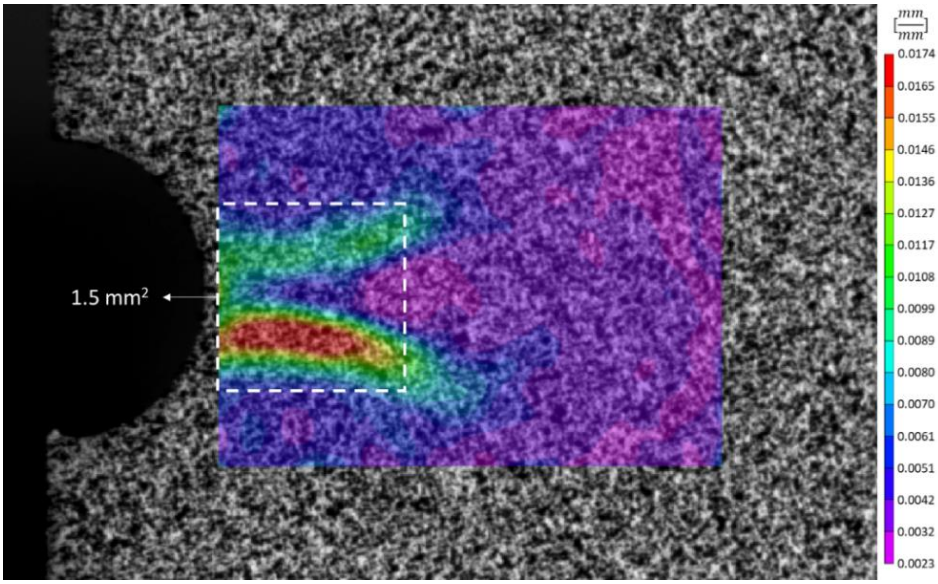

Figure 4-9 - Contour area on Von Mises strain at the notch root

Crack initiation follows damage accumulation during fatigue life of materials and happens when damage (thermodynamic entropy) reaches a specific level of entropic endurance. Figure 10 shows the fatigue damage accumulation rate of four different tests by volumetric entropy generation per cycle/block versus normalized fatigue life leading to crack initiation. Results show that the volumetric entropy generation rate is dependent on the loading spectrum and follows different rates at different points in fatigue life. However, at the end of fatigue crack initiation life, the rate increases substantially in all cases. The increase in damage rate at the final stages of fatigue crack initiation life is dependent on the damage rates preceding it. For instance, in case of HCF spectrum, the rate increase at the end of the test is smaller comparing to other spectrums. It suggests that the longer fatigue life resulted in damage accumulations with smaller rates to build up enough damage that result in crack initiation. Therefore damage rate increases less comparing to other loading spectrums. This is in contrast to other loading spectrums. Fluctuating stresses defined by other loading spectrums result in residual compressive stress at the notch, and therefore decrease in plastic strain. This results in generation of negative values for damage rate. However, it is observed that in these cases, the damage rate increases more substantially at the end of fatigue life. Therefore, negative values for damage rate should not always be inferred as a sign for longer life, but may be viewed as a sign for more severe damage generation in cycles leading to crack initiation.

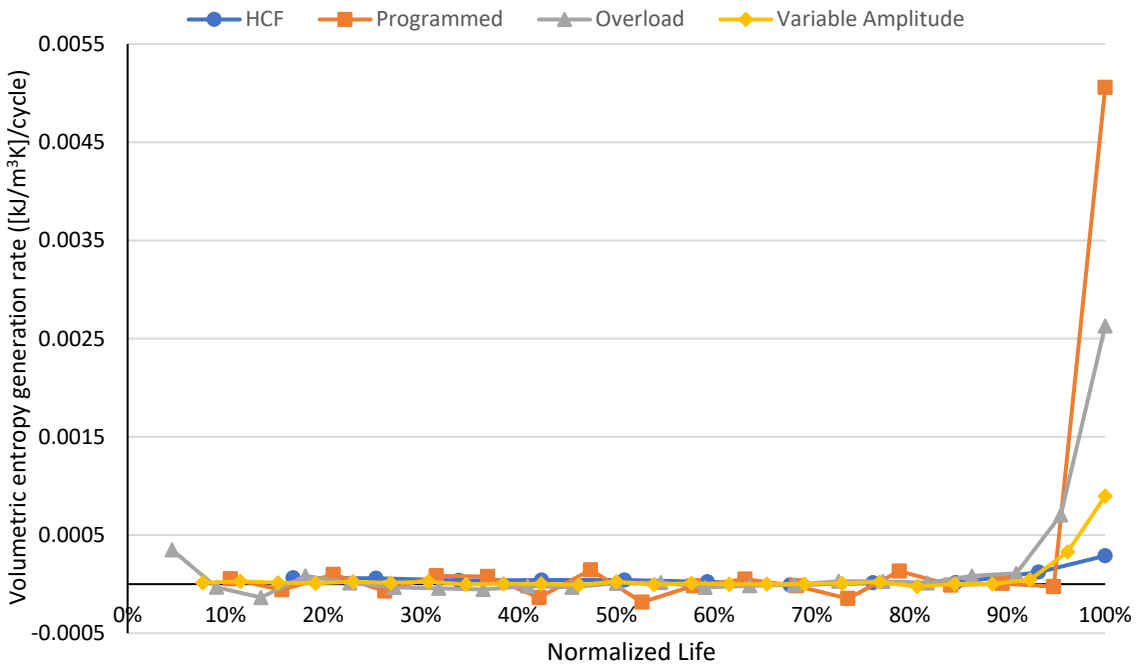

Figure 4-10 - Thermodynamic Entropy Generation rate until crack initiation at different loading spectrums.

Although volumetric entropy generation rate is found to be dependent on the loading conditions, it is expected that regardless of the loading spectrum and test duration, crack initiation happen at specific entropic endurance level [48]. Figure 11 shows the thermodynamic entropy per unit volume measured at the time of fatigue crack initiation. These measurements reflect the entropy generation due to plastic deformation measured in the last DIC image available. It is important to mention that since the DIC images are taken in the intervals explained earlier, the last DIC image available before crack initiation happens at different cycles in different tests. This resulted in some variability of volumetric thermodynamic entropy measured in different tests. However, the variability in final thermodynamic entropy value is small especially with regard to the wide range of time to crack initiation and loading spectrum in different tests.

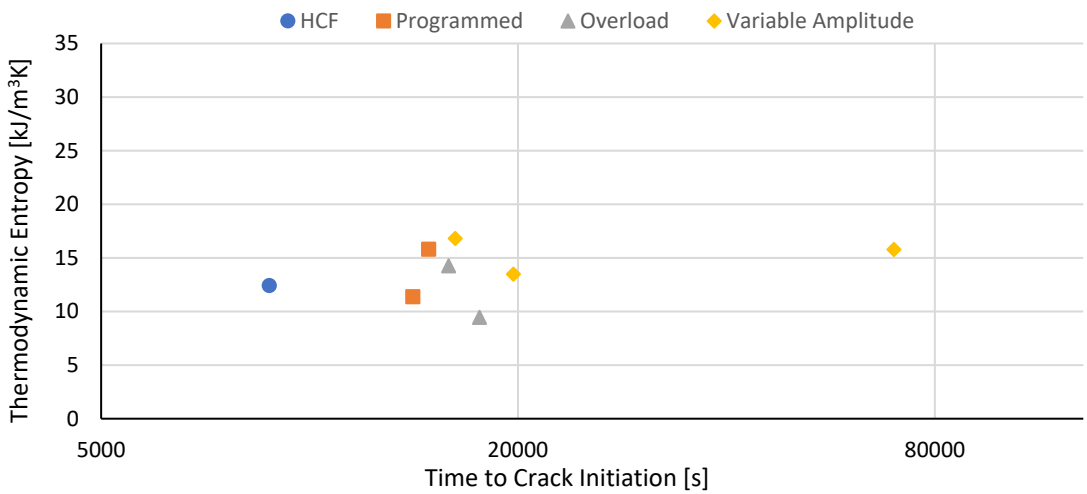

Figure 4-11 - Thermodynamic Entropy before crack initiation in different tests as a function of time to crack initiation.

Figure 11 show that regardless of the different damage accumulation rates, the final volumetric thermodynamic entropy reaches an entropic endurance level at the time of crack initiation. Therefore, it is seen that regardless of the loading conditions, the damage accumulation rate, the number of cycles to crack initiation, the frequency of test and room temperature, crack initiation happens when the thermodynamic entropy value reaches the endurance level. Statistical analysis of the thermodynamic entropy endurance levels shows that their variability reasonably follows a Weibull distribution. Figure 12 shows the distribution fit to data with 95% confidence level lines.

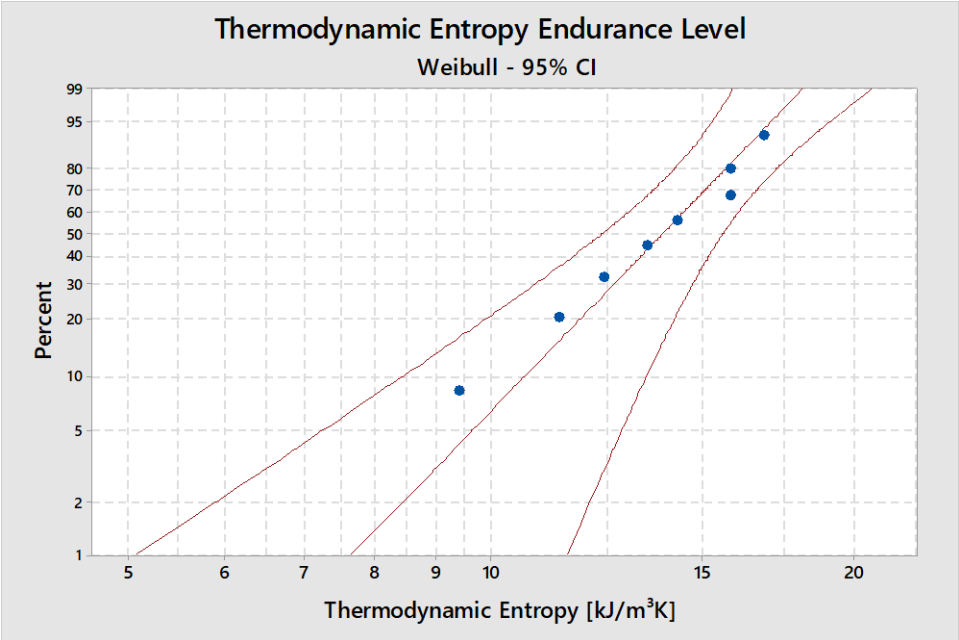

Figure 4-12 - Weibull distribution fit on volumetric entropic endurance level

The entropic endurance level as described by a Weibull probability distribution rather than a deterministic value can better account for the stochastic nature of fatigue life. The shape and scale parameters of the distribution are found as 7.1 and 14.64 respectively. This distribution describes a median value of 13.9 [kJ/m^{3}K] for the entropy endurance level in this material.

4.6. Conclusions

The study results presented in this paper examines the ability of DIC to measure the thermodynamic entropy generation due to plastic deformation in fatigue crack initiation. Eight fatigue experiments on notched dog-bone aluminum alloy specimens using four widely different loading spectrum, including overload cycles are performed. DIC is used to analyze the evolution of strain at the notch root due to the loading spectrum. For the periodic application of overloads, there were three stages observed for the fatigue process: (1) a decrease in the growth rate of the plastic strain, (2) an overall decrease in the plastic

strain, and (3) an inflection point where acceleration of the growth of plastic strain leads to crack initiation. A modification of Clasius-Duhem inequality was then introduced to convert the DIC measurements to thermodynamic entropy values to determine the criteria for crack initiation independent of the loading spectrum. Thermodynamic entropy generation per unit volume due to plastic deformation is measured near the notch area where the crack is formed. The thermodynamic entropy measurement due to plastic deformation using DIC is compared to global measurements (extensometer and cross-head position values). It is concluded that entropy generation due to plastic deformation accounts for a portion of the hysteresis energy. Care must be taken when hysteresis energies are used to determine thermodynamic entropy generations. Volumetric entropy generation (damage) rate is found to be dependent on the loading spectrum. However, regardless of the damage rate, time to crack initiation, loading spectrum, test frequency and temperature, crack initiation happened at a specific entropic endurance level. The entropic endurance level at the time crack initiation is introduced in form of a Weibull distribution. The scatter in the endurance level roots in two reasons: stochastic nature of fatigue life and availability of DIC image at the time of crack initiation. This distribution instead of a deterministic value can better assess fatigue life of the material before crack initiation and statistically estimate the remaining life. Higher frequency of image recording, specifically around the time of crack initiation can decrease the uncertainty of the entropic endurance distribution. The volumetric entropy endurance level method used in combination with strain-life analysis can help to effectively predict crack initiation, especially near the expected fatigue life, and support policies to repair, replace or retain components based on their remaining useful life estimation.

4.7. References

[1] Md. T. A. Ansari, K. K. Singh, and M. S. Azam, "Fatigue damage analysis of fiber-reinforced polymer composites—A review," *J. Reinf. Plast. Compos.*, vol. 37, no. 9, pp. 636–654, May 2018.

[2] Julie A Bannantine, Jess J. Comer, and James L. Handrock, *Fundamentals of metal fatigue analysis*, 90 vols. Englewood Cliffs, NJ: Prentice hall, 1990.

[3] S. A. Barter, L. Molent, and R. J. H. Wanhill, "Typical fatigue-initiating discontinuities in metallic aircraft structures," *Int. J. Fatigue*, vol. 41, pp. 11–22, Aug. 2012.

[4] M. D. Sangid, "The physics of fatigue crack initiation," *Int. J. Fatigue*, vol. 57, pp. 58–72, Dec. 2013.

[5] A. Imanian and M. Modarres, "A thermodynamic entropy-based damage assessment with applications to prognostics and health management," *Struct. Health Monit.*, vol. 17, no. 2, pp. 240–254, Mar. 2018.

[6] M. D. Bryant, M. M. Khonsari, and F. F. Ling, "On the thermodynamics of degradation," *Proc. R. Soc. Math. Phys. Eng. Sci.*, vol. 464, no. 2096, pp. 2001–2014, Aug. 2008.

[7] C. Basaran and S. Nie, "An Irreversible Thermodynamics Theory for Damage Mechanics of Solids," *Int. J. Damage Mech.*, vol. 13, no. 3, pp. 205–223, Jul. 2004.

[8] M. Amiri and M. M. Khonsari, "On the Role of Entropy Generation in Processes Involving Fatigue," *Entropy*, vol. 14, no. 1, pp. 24–31, Dec. 2011.

[9] M. Amiri and M. Modarres, "An Entropy-Based Damage Characterization," *Entropy*, vol. 16, no. 12, pp. 6434–6463, Dec. 2014.

[10] A. Kahirdeh and M. M. Khonsari, "Energy dissipation in the course of the fatigue degradation: Mathematical derivation and experimental quantification," *Int. J. Solids Struct.*, vol. 77, pp. 74–85, Dec. 2015.

[11] M. Naderi and M. M. Khonsari, "Thermodynamic analysis of fatigue failure in a composite laminate," *Mech. Mater.*, vol. 46, pp. 113–122, Mar. 2012.

[12] M. Naderi, M. Amiri, and M. M. Khonsari, "On the thermodynamic entropy of fatigue fracture," *Proc. R. Soc. Math. Phys. Eng. Sci.*, vol. 466, no. 2114, pp. 423–438, Feb. 2010.

[13] B. Pan, K. Qian, H. Xie, and A. Asundi, "Two-dimensional digital image correlation for in-plane displacement and strain measurement: a review," *Meas. Sci. Technol.*, vol. 20, no. 6, p. 062001, Jun. 2009.

[14] T. C. Chu, W. F. Ranson, and M. A. Sutton, "Applications of digital-image-correlation techniques to experimental mechanics," *Exp. Mech.*, vol. 25, no. 3, pp. 232–244, Sep. 1985.

[15] H. A. Bruck, S. R. McNeill, M. A. Sutton, and W. H. Peters, “Digital image correlation using Newton-Raphson method of partial differential correction,” *Exp. Mech.*, vol. 29, no. 3, pp. 261–267, Sep. 1989.

[16] M. Grédiac, “The use of full-field measurement methods in composite material characterization: interest and limitations,” *Compos. Part Appl. Sci. Manuf.*, vol. 35, no. 7–8, pp. 751–761, Jul. 2004.

[17] L. Chevalier, S. Calloch, F. Hild, and Y. Marco, “Digital image correlation used to analyze the multiaxial behavior of rubber-like materials,” *Eur. J. Mech. - ASolids*, vol. 20, no. 2, pp. 169–187, Mar. 2001.

[18] D. M. McGowan, D. R. Ambur, T. G. Hanna, and S. R. McNeill, “Evaluating the Compressive Response of Notched Composite Panels Using Full-Field Displacements,” *J. Aircr.*, vol. 38, no. 1, pp. 122–129, Jan. 2001.

[19] S. V. Lomov *et al.*, “Full-field strain measurements for validation of meso-FE analysis of textile composites,” *Compos. Part Appl. Sci. Manuf.*, vol. 39, no. 8, pp. 1218–1231, Aug. 2008.

[20] G. Nicoletto, G. Anzelotti, and E. Riva, “Mesoscopic strain fields in woven composites: Experiments vs. finite element modeling,” *Opt. Lasers Eng.*, vol. 47, no. 3–4, pp. 352–359, Mar. 2009.

[21] J. Payne, G. Welsh, R. J. Christ Jr., J. Nardiello, and J. M. Papazian, “Observations of fatigue crack initiation in 7075-T651,” *Int. J. Fatigue*, vol. 32, no. 2, pp. 247–255, Feb. 2010.

[22] J. D. Carroll, W. Abuzaid, J. Lambros, and H. Sehitoglu, “High resolution digital image correlation measurements of strain accumulation in fatigue crack growth,” *Int. J. Fatigue*, vol. 57, pp. 140–150, Dec. 2013.

[23] J. Carroll, W. Abuzaid, J. Lambros, and H. Sehitoglu, “An experimental methodology to relate local strain to microstructural texture,” *Rev. Sci. Instrum.*, vol. 81, no. 8, p. 083703, Aug. 2010.

[24] Z. Zhao, M. Ramesh, D. Raabe, A. M. Cuitiño, and R. Radovitzky, “Investigation of three-dimensional aspects of grain-scale plastic surface deformation of an aluminum oligocrystal,” *Int. J. Plast.*, vol. 24, no. 12, pp. 2278–2297, Dec. 2008.

[25] B. Wisner and A. Kontsos, “In situ monitoring of particle fracture in aluminium alloys,” *Fatigue Fract. Eng. Mater. Struct.*, vol. 41, no. 3, pp. 581–596, Mar. 2018.

[26] A. K. Wong and G. C. Kirby, “A hybrid numerical/experimental technique for determining the heat dissipated during low cycle fatigue,” *Eng. Fract. Mech.*, vol. 37, no. 3, pp. 493–504, Jan. 1990.

[27] *Vic-2D*. Version 6.0.6. Build 455 Correlated Solutions, Inc.

[28] C. Lane, R. L. Burguete, and A. Shterenlikht, “An Objective Criterion for the Selection of an Optimum DIC Pattern and Subset Size,” in *Proceedings of the XIth international congress and exposition*, 2008, pp. 1–9.

[29] N. Iyyer, S. Sarkar, R. Merrill, and N. Phan, “Aircraft life management using crack initiation and crack growth models – P-3C Aircraft experience,” *Int. J. Fatigue*, vol. 29, no. 9–11, pp. 1584–1607, Sep. 2007.

[30] Y. L. Dong and B. Pan, “A Review of Speckle Pattern Fabrication and Assessment for Digital Image Correlation,” *Exp. Mech.*, vol. 57, no. 8, pp. 1161–1181, Oct. 2017.

[31] M. D. Abràmoff, P. J. Magalhães, and S. J. Ram, “Image processing with ImageJ.,” *Biophotonics Int.*, vol. 11, no. 7, pp. 36–42, 2004.

[32] E. Salvati, H. Zhang, K. S. Fong, X. Song, and A. M. Korsunsky, “Separating plasticity-induced closure and residual stress contributions to fatigue crack retardation following an overload,” *J. Mech. Phys. Solids*, vol. 98, pp. 222–235, Jan. 2017.

[33] D. DuQuesnay, “Notch fatigue behaviour as influenced by periodic overloads,” *Int. J. Fatigue*, vol. 17, no. 2, pp. 91–99, Feb. 1995.

[34] C. Topper, “The influence of variable amplitude loading on crack closure and notch fatigue behaviour,” *Int. J. Fatigue*, vol. 19, no. 5, pp. 389–400, May 1997.

[35] M. Mokhtarishirazabad, P. Lopez-Crespo, B. Moreno, A. Lopez-Moreno, and M. Zanganeh, “Optical and analytical investigation of overloads in biaxial fatigue cracks,” *Int. J. Fatigue*, vol. 100, pp. 583–590, Jul. 2017.

[36] E. Salvati, S. O’Connor, T. Sui, D. Nowell, and A. M. Korsunsky, “A study of overload effect on fatigue crack propagation using EBSD, FIB–DIC and FEM methods,” *Eng. Fract. Mech.*, vol. 167, pp. 210–223, Nov. 2016.

[37] M. Funk and J. Bär, “Influence of crack initiation on short crack propagation and cyclic lifetime of AA 7475-T761,” *Procedia Struct. Integr.*, vol. 13, pp. 279–284, 2018.

[38] F. Yusof, P. Lopez-Crespo, and P. J. Withers, “Effect of overload on crack closure in thick and thin specimens via digital image correlation,” *Int. J. Fatigue*, vol. 56, pp. 17–24, Nov. 2013.

[39] P. Lopez-Crespo, M. Mostafavi, A. Steuwer, J. F. Kelleher, T. Buslaps, and P. J. Withers, “Characterisation of overloads in fatigue by 2D strain mapping at the surface and in the bulk: 2D Strain Mapping of Overloads,” *Fatigue Fract. Eng. Mater. Struct.*, vol. 39, no. 8, pp. 1040–1048, Aug. 2016.

[40] V. Ontiveros, M. Amiri, A. Kahirdeh, and M. Modarres, “Thermodynamic entropy generation in the course of the fatigue crack initiation: Thermodynamic Entropy Generation in the Course of the Fatigue Crack Initiation,” *Fatigue Fract. Eng. Mater. Struct.*, vol. 40, no. 3, pp. 423–434, Mar. 2017.

[41] T. Temfack and C. Basaran, “Experimental verification of thermodynamic fatigue life prediction model using entropy as damage metric,” *Mater. Sci. Technol.*, vol. 31, no. 13, pp. 1627–1632, Oct. 2015.

[42] M. Naderi and M. M. Khonsari, “A thermodynamic approach to fatigue damage accumulation under variable loading,” *Mater. Sci. Eng. A*, vol. 527, no. 23, pp. 6133–6139, Sep. 2010.

[43] M. Amiri, M. Naderi, and M. M. Khonsari, “An Experimental Approach to Evaluate the Critical Damage,” *Int. J. Damage Mech.*, vol. 20, no. 1, pp. 89–112, Jan. 2011.

[44] M. Liakat and M. M. Khonsari, “Entropic characterization of metal fatigue with stress concentration,” *Int. J. Fatigue*, vol. 70, pp. 223–234, Jan. 2015.

[45] H. B. Motra, J. Hildebrand, and A. Dimmig-Osburg, “Assessment of strain measurement techniques to characterise mechanical properties of structural steel,” *Eng. Sci. Technol. Int. J.*, vol. 17, no. 4, pp. 260–269, Dec. 2014.

[46] P. Knysh and Y. P. Korkolis, “Determination of the fraction of plastic work converted into heat in metals,” *Mech. Mater.*, vol. 86, pp. 71–80, Jul. 2015.

[47] B. Ould Chikh, A. Imad, and M. Benguediab, “Influence of the cyclic plastic zone size on the propagation of the fatigue crack in case of 12NC6 steel,” *Comput. Mater. Sci.*, vol. 43, no. 4, pp. 1010–1017, Oct. 2008.

[48] A. Imanian and M. Modarres, “Thermodynamics as a fundamental science of reliability,” *Proc. Inst. Mech. Eng. Part O J. Risk Reliab.*, vol. 230, no. 6, pp. 598–608, Dec. 2016.

Chapter 5: Fatigue crack initiation prognostics based on thermodynamic and information entropy using dynamic Bayesian network[1]

5.1. Abstract

Components are designed to endure a specific time or cycles before failure. The initial life analysis at the design stage is performed based on available, physics-based models. However, when the component is in-service, constant health monitoring and updating the estimation of remaining useful life (RUL) becomes a crucial task in component reliability assessment. Updating the RUL usually depends on data collected during the operation of the component, using one or more non-destructive testing (NDT) techniques that result in a large dataset. The correlation of the collected data to infer the damage state plays an essential role in RUL estimation. In this study, two NDT techniques, namely acoustic emission (AE) and digital image correlation (DIC), are used to collect data during fatigue tests on dog-bone aluminum alloy specimens until crack initiation, under multiple loading conditions. Information entropy of the AE signals and thermodynamic entropy measured using DIC are used to estimate and update the RUL using a Bayesian updating approach. The state process model and observation models are developed and implemented in a joint particle filter for damage prognostics and RUL estimation.

[1] The full-text of this chapter is to appear in the Proceedings of 67th Annual Reliability & Maintainability Symposium (RAMS), May 24-27 2021, Orlando, Florida.

5.2. Introduction

Ensuring safe operation and avoiding catastrophic failure is a pillar in all industries. Reliability assessment of structures plays a vital role in confidently resuming operation. These reliability assessments usually include periodic scheduled inspections that are discrete, expensive, labor-intensive, and slow. In case of airframes, these inspections require grounding and downtime that results in a considerable increase (by as much as 50%) in the operational cost [1]. One of the inspection goals is to detect and measure fatigue-induced cracks. Fatigue is one of the primary degradation mechanisms in structures, and avoiding fatigue failures by estimating remaining useful life (RUL) is a must to ensure safety. Recently, the aerospace industry is moving toward using structural health monitoring (SHM) techniques to detect defects and damages that reduce the need for routine maintenance, minimizes human intervention and increases the reliability in damage detection. These techniques seek to exploit the interpretation of high volumes of data collected by sensors during the operational life of a component. Hence, the periodically scheduled maintenance strategy is aimed to be replaced by condition-based monitoring. Health prognostics heavily depend on data acquisition, data interpretation methods, and RUL prediction techniques. The data acquisition is usually performed through one of the available non-destructive testing (NDT) techniques such as acoustic emission (AE) and digital image correlation (DIC). The use of these NDT techniques, especially AE, results in large databases that require careful interpretation and analysis. Conventional methods to analyze the collected data are usually based on assumptions and methods that depend on experimental conditions, resulting in limited applications. However, recent research is moving toward developing more general methods for data

interpretation based on a fundamental concept, i.e., entropy [2], to expand the application of these NDT techniques and improve reliability assessments. Entropy is a measure of irreversibility or uncertainty within a quantity and has recently gained much attention in the detection and measurement of damage in components under fatigue loading. Entropy, as a damage index, has shown promising results [3].

Techniques for RUL estimation usually heavily depend on data-driven modeling [4]. Purely data-driven modeling that lacks the integration of the underlying degradation process typically falls short in reliable estimations. Meanwhile, solely relying on physics-based modeling fails to incorporate new information that becomes available while operating a component. Therefore, a hybrid method that integrates the advantages of both modeling approaches is highly plausible. Some examples of such integrations can be seen in the literature by using dynamic Bayesian modeling that incorporates new physical measurements to update belief regarding the damage state of a component [5]. These methods tend to infer the stochastic hidden damage state of a component based upon one or more observation measurements. After each update based on new observations, these models extrapolate the damage state to a given damage tolerance level and estimate the time it takes for the component to reach the level, i.e., RUL. Some examples of successful applications of dynamic Bayesian updating in RUL estimations in literature are the following: A Bayesian regression analysis to estimate parameters in fatigue crack growth tests based on information entropy measurement [6], a Bayesian regression to estimate parameter in corrosion-fatigue testing based on thermodynamic entropy [7], particle filtering framework to measure the crack length in fatigue testing based on information

entropy and other Lamb signal parameters [8], and a joint particle filtering to estimate RUL based on Young's modulus and AE energy measurement [9].

Recently, authors have shown the applicability of using DIC in thermodynamic entropy measurement and introduced the entropic endurance threshold in aluminum alloy specimens until crack initiation and showed its independence on loading condition [10]. Furthermore, authors have developed a method to detect crack initiation in the material using information entropy of AE signals, independent of loading condition [11]. In this paper, a study is done on developing a framework based on Bayesian updating for RUL estimation of components based on the two entropic measurements. This study discusses a possible state process and observation model and shows their application on data available from four fatigue tests.

5.3. Methods

Each section here briefly covers the equations used for thermodynamic entropy and information entropy and the results acquired. For more information on each of the subjects and the loading conditions, readers are referred to the original publication. In the dynamic Bayesian updating section, the implemented particle filtering approach is briefly discussed.

5.3.1. Thermodynamic entropy

The application of thermodynamic entropy in fatigue damage measurement is initially formulated based on continuum damage mechanics, using the first and the second law of thermodynamics [12]. The crux of using it as a damage index in fatigue testing stems from the fact that fatigue is an irreversible cumulative damage. An alternative formulation (Eq.

1) for measurement of the thermodynamic entropy on the specimen surface is proposed by authors [10] that utilizes DIC strain measurements on the surface.

$$S = \sigma_y \frac{d}{T} A_{contour} \varepsilon_{avg} \quad (1)$$

In Equation 1, S is thermodynamic entropy, σ_y is yield stress of the material, d is specimen thickness, T is its temperature (in Kelvin), $A_{contour}$ is the area of interest where DIC measurement is performed and ε_{avg} is the average strain in the area of interest. The results from applying the equation on tests with different loading conditions revealed that an entropic endurance threshold, regardless of loading condition, could be described at which crack initiation happens. However, the change in thermodynamic entropy during the loading was found to be dependent on the loading condition. Figure 1 shows the trend in the thermodynamic entropy generation rate in four different tests with varying conditions of loading. Details about the loading conditions can be found in [10]. The rate of thermodynamic entropy generation depends on the loading condition. Therefore, the entropy generation rate cannot be readily and directly used to estimate RUL in a given test. To use the thermodynamic entropy measurements for RUL estimation in predictive modeling, an observation model should be defined to relate the entropy measurement to damage state of the component.

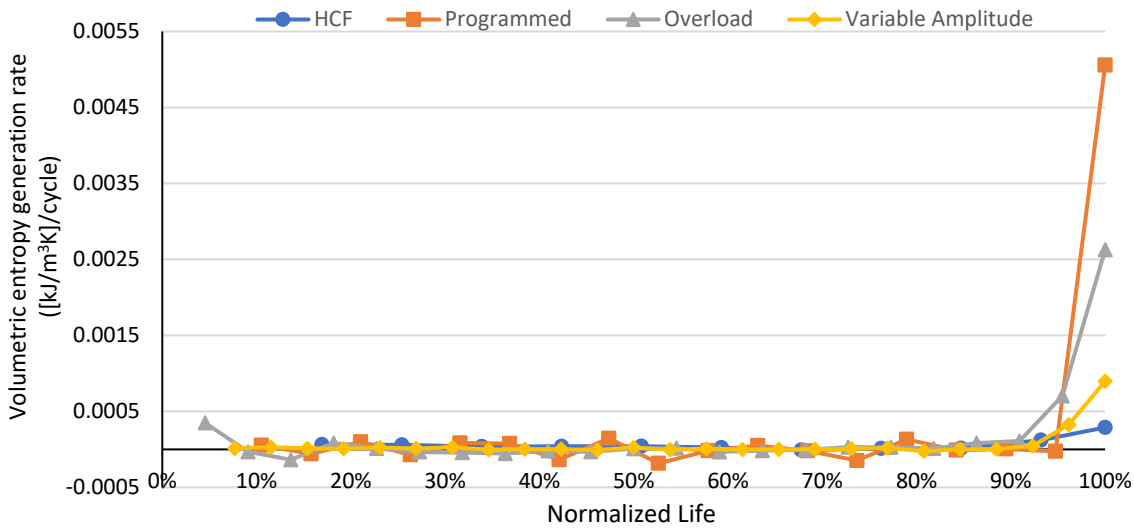

Figure 5-1 - Thermodynamic Entropy Generation rate until crack initiation at different loading spectrums. [10]

5.3.2. Information entropy

Information entropy is a measure of uncertainty or information content of the probability distribution of a random variable. Recently a number of studies have shown the benefits of using information entropy of AE signals in comparison to conventional parameters, including a study by authors [11]. In the study, Shannon [13] information entropy (Eq. 2) is used to measure the information content of AE signal waveforms emitted during the fatigue tests.

$$I = c\sum_{i=1}^{n} P(X_i)\ln(1/P(X_i)) \quad (2)$$

In Equation 2, I is information entropy, c is a constant considered to be unity, $X_i = \{x_1, x_2, \dots, x_n\}$ is the random variable (voltage values in waveforms) and $P(X_i)$ is the probability distribution of the random variable.

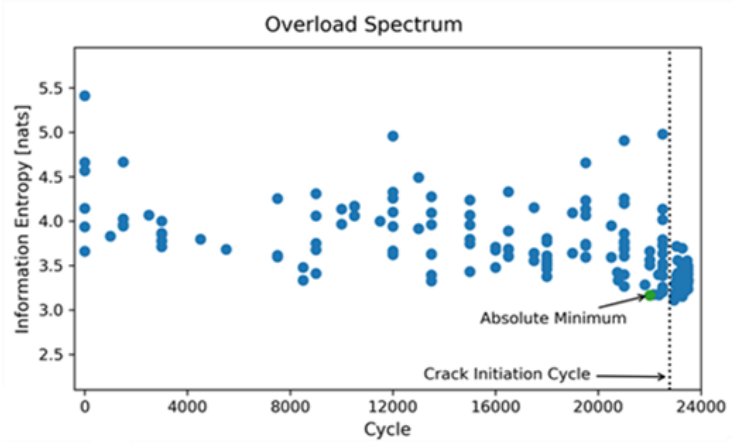

Figure 5-2 - Information entropy of valid signals in each channel for Overload spectrum. [11]

It is found that a threshold in information entropy exists at which crack initiation is imminent. The threshold does not depend on loading condition and can be used to detect crack initiation. Figure 2 shows information entropy values and marks the minimum value (the entropic endurance threshold) in a test with "overload" loading condition. As it is seen in the figure, the trend in information entropy values does not follow any specific trajectory. This implies that the information entropy trend cannot be readily used in RUL estimation and requires an observation model to translate the entropy measurements to entropy indexes.

5.3.3. Dynamic Bayesian updating

The prognostics and RUL estimation of structures in hybrid frameworks is usually done through updating the belief regarding damage state through Bayesian updating techniques. There are multiple techniques based on the Bayesian updating that can be used. Particle filtering (PF) technique, as a widely accepted Bayesian updating method, is used in this study. The PF technique works based on two models, a state processing model which governs the degradation process and moves the state in time, and an observation model

which translates new measurements to observations that can be used to update the state model.

Consider the state of a component at time k is described by x_k. A state function is defined as f, which represents the state evolution in time as in:

$$x_k = f(x_{k-1}, \omega_{k-1}) \quad (3)$$

in which, ω_k is the noise, representing the uncertainty around the degradation state. In PF, a defined number of particles representing a set of possible states are assumed at each time step and assigned a weight. These particles with their associated weights are moved through time using the state function. An observation function h is defined that translates damage state measurements as they become available to observations z_k:

$$z_k = h(x_k, \mu_k) \quad (4)$$

in which μ_k is the uncertainty in measurements. At any instance which observation of the damage state becomes available, the weights of particles in a state variable are updated using the Bayesian updating in Eq. 5. This Equation updates the probability density function (PDF) of the possible states and adjust the particle weights accordingly.

$$p(x_k|z_{1:k}) = \frac{p(z_k|x_k).p(x_k|z_{1:k-1})}{p(z_k|z_{1:k-1})} \quad (5)$$

One main drawback of the PF approach is that it does not update the state process model. This results in requiring a state model with known parameters which is not usually available, specifically in cases such as fatigue processes that have inherent stochastic behaviors. To address this issue, more sophisticated dynamic particle filtering techniques are proposed in the literature to update the parameters of the state model [14]. One such

technique is called the kernel-smoothing based approach [15] and is implemented in this study. This approach offers a simultaneous estimation of (degradation) state and the unknown parameters in the (degradation) state model. In this approach, in addition to the state model, the parameter vector of the state model, θ, is also updated when an observation becomes available, using the following equation:

$$\theta_{k-1} = \theta_{k-1}\sqrt{1-h^2} + \hat{\theta}_{k-1}\left(1-\sqrt{1-h^2}\right) \quad (6)$$

$$\theta_k = \theta_{k-1} + N\left(0, h^2 V(\theta_{k-1})\right) \quad (7)$$

in which $h \epsilon [0,1]$ is called kernel parameter. The parameter vector updating is a two-step process, including shrinkage (Eq. 6) and perturbation (Eq. 7), in which the kernel parameter determines the degree of shrinkage. After updating the damage state and the parameters of the damage state model, the mean-time-to-failure (MTTF) is estimated by moving the system state through state function to a specified damage tolerance threshold using:

$$MTTF = \sum_{i=1}^{N} t_f^{(i)} . w^{(i)} \quad (8)$$

In Eq. 8, i represents a particle and $w^{(i)}$ represents the weight of the particle and $t_f^{(i)}$ represent the time (or cycle) at which the particle reaches the damage tolerance threshold. The RUL is then measured by subtracting elapsed life at the time of measurement from the MTTF.

5.4. State process and observation models

The dependence of thermodynamic entropy generation rate on the loading condition and the sporadic changes in information entropy values during a test makes it very difficult to define a RUL estimation technique solely based on their trend. Meanwhile, each of the

measures provides invaluable information regarding the crack initiation time, independent of the loading condition. Therefore, two models, i.e. the state process model and observation model, are defined in this section to move the damage state through time and estimate RUL, and translate entropic measurements into entropic indexes that are then used to update the state model.

5.4.1. State process model

The state process model (degradation model) in this study is sought to be physically measurable damage that can be measured within a fatigue test. Therefore, a widely used measure, (Young's) modulus reduction, is considered in this study as the "true damage". Modulus reduction is measurable in fatigue tests and is expected as the natural response of a component during fatigue loading that results in crack initiation. The damage index is defined with:

$$D(n) = \frac{E_0 - E(n)}{E_0 - E_f} \quad (9)$$

in which E_0 is the initial modulus of a healthy component, E is the modulus in each cycle (n) and E_f is the modulus at the crack initiation. The damage index starts from 0 and reached to 1 at the time of crack initiation. The state process model is defined based on the damage index using the mathematical function proposed by Mao and Mahadevan [16]:

$$D^*(n) = q\left(\frac{n}{N_f}\right)^{m_1} + (1-q)\left(\frac{n}{N_f}\right)^{m_2} \quad (10)$$

in which q, m_1, m_2 are material dependent parameters of the equation, N_f is the crack initiation cycle, and n is the cycle at which the damage index is measured. Eq. 10 is proposed originally to measure damage based on modulus reduction in composite

materials. However, because of the intrinsic flexibility of the function to fit any three-stage curve with concave, constant and convex stages (or vice versa), it has been successfully used in case of crack initiation in metallic materials as well [9]. Change of the damage index and state model in one test is shown in Figure 3.

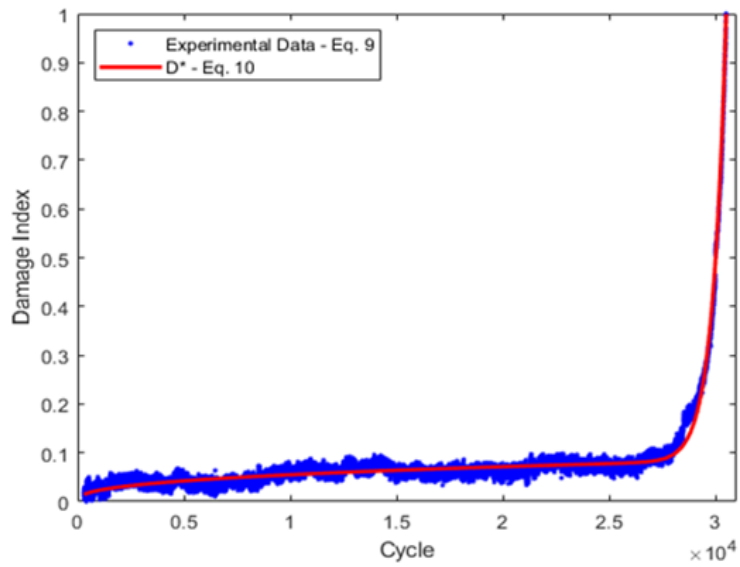

Figure 5-3 - Modulus reduction, experimental result (Eq. 9) and model based on Eq. 10

5.4.2. Observation model

The observation model is defined to translate entropy measurements to entropy indexes that can be used to update the damage state. Since the behavior of each entropy measurement is different through the fatigue life, each requires a unique observation model. The proposed observation models for thermodynamic entropy (D_S) and information entropy (D_I) are:

$$D_S(\mathrm{n}) = \frac{S(n) - S_{min}}{\hat{S} - S_{min}} \quad (11)$$

$$D_I(\mathrm{n}) = \frac{I_{max} - I(n)}{I_{max} - \hat{I}} \quad (12)$$

The subscript min and max refer to the minimum and maximum value in a given test and the hat over the parameter refers to its expected value (mean) of the corresponding entropy distribution at the time of crack initiation. The entropy distribution is defined on the entropic endurance threshold reported in earlier studies [10], [11]. The value of S_{min} is equal to the first measurement of thermodynamic entropy. The value of I_{max} is found during the test. Usually, the I_{max} happens in the beginning of a fatigue test. Figure 4 shows the results of applying the state and observation models. The advantage of using expected values of entropic endurance threshold in the observation functions is their independence to the loading conditions; hence the observation functions also become independent of loading conditions.

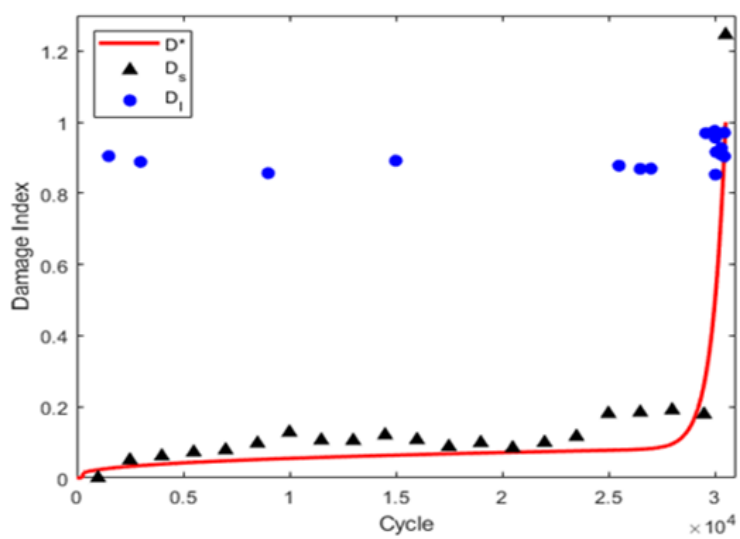

Figure 5-4 - State and observation models in a fatigue test

Both entropy indexes in Eq. 11 and 12 reach a value of ~1 at the time of crack initiation. However, D_I shows a two-stage health state in which the index indicates a potential imminent crack initiation only when it passes a specific threshold. A sensitivity analysis on the threshold level shows an appropriate threshold level of $D_I = 0.85$. Only the values over this threshold are shown in Fig. 4. It can be seen that there are some instances which

D_I passes the threshold, but the crack initiation is not imminent. This low accuracy in detection is reflected in the PF framework by a high uncertainty value (μ_k in Eq. 4). On the other hand, D_S is a multi-stage health state and the information provided by it is useful during all states of the test.

Figure 5 shows the overall framework and the relation of parameters[2].

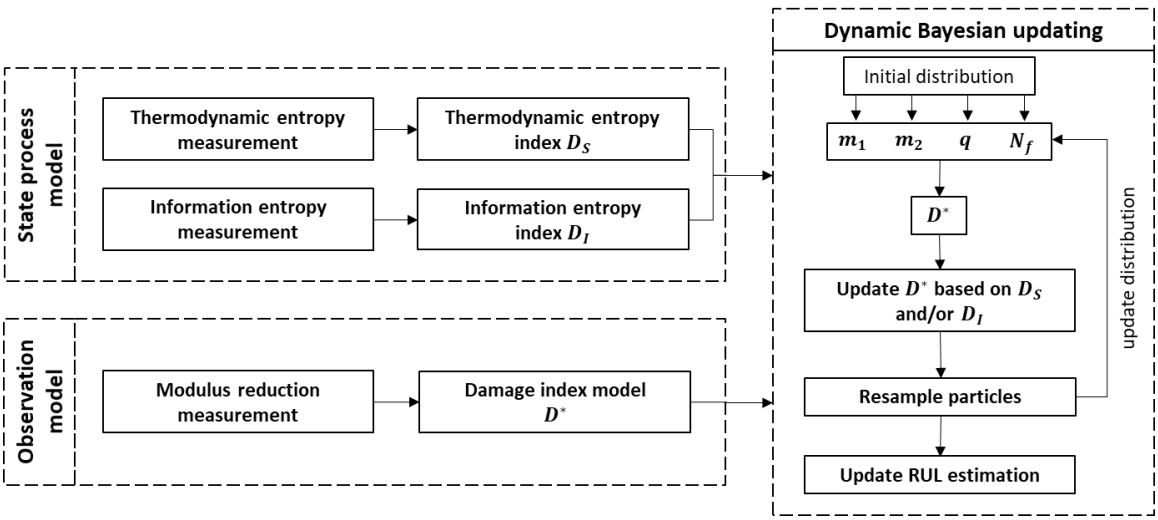

Figure 5-5 - Framework

5.5. Results and discussion

Thermodynamic and information entropy of 4 tests with three different loading conditions are used as case studies. In order to measure damage state of each particle at k time step, the state process model (Eq. 10) is discretized into small enough Δn using [9]:

$$D_k^* = D_{k-1}^* + \left.\frac{\Delta D^*}{\Delta n}\right|_{k-1} \times \Delta n \times e^{\omega_k} \quad (13)$$

[2] This figure does not appear in the published paper.

in which D_{k-1}^{*} is the damage state at the previous time step and $\frac{\Delta D^{*}}{\Delta n}$ is the derivative of the damage state with respect to cycle at the last time step, and the stochastic behavior is represented by e^{ω_k}. Equation 13 can be further written as in:

$$D_k^{*} = D_{k-1}^{*} + \left[\frac{m_1 \times q}{N_f} \times \left(\frac{n}{N_f}\right)^{m_1-1} + \frac{m_2 \times (1-q)}{N_f} \times \left(\frac{n}{N_f}\right)^{m_2-1}\right]_{k-1} \times \Delta n \times e^{\omega_k} \quad (14)$$

Equation 14 is used as the state function in the particle filtering framework in this study. The parameter vector $\theta_k = \left[m_1, m_2, N_f, q\right]_k$ is updated according to the kernel-smoothing process explained by Equations 6 and 7 whenever an update is available. The initial values for the parameter vector are assigned using a uniform distribution and prior knowledge, as reported in Table 1. For each parameter and the damage state, a number of 1000 particles is used, resulting in a total of 5000 particles for each test. The noise in the state process model and observation models are presented by a normal distribution $N(0, \omega_k)$ and $N(0, \mu_k)$ respectively. The variance of the normal distributions is assigned as the mean squared error (MSE) of the index (D^{*}, D_S or D_I) and the true damage (D). The damage tolerance level is set to 0.95 in all tests, indicating that higher values of damage are considered a failure. This value specifies the damage level from which the RUL is measured. The results of the PF and parameters convergence with their 90% confidence intervals (CI) in Test 4 is shown in Figure 5. The 90% CI is shown as a colored area.

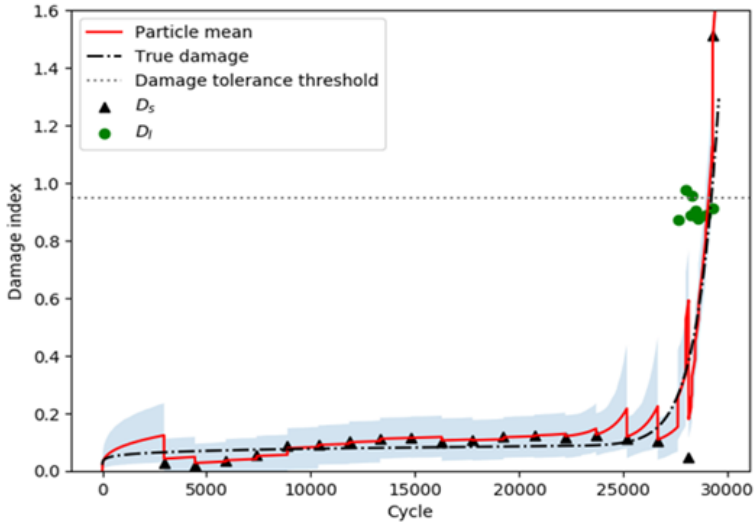

Figure 5-6 - Particle filter result

It is seen that in Figure 5, the true damage is within the 90% CI at any given time. The observation model noise (μ_k) for the thermodynamic entropy index has a lower value comparing to the information entropy index that results in a heavier impact in particle weight updating. The updated trajectory of parameters is depicted in Figure 6.

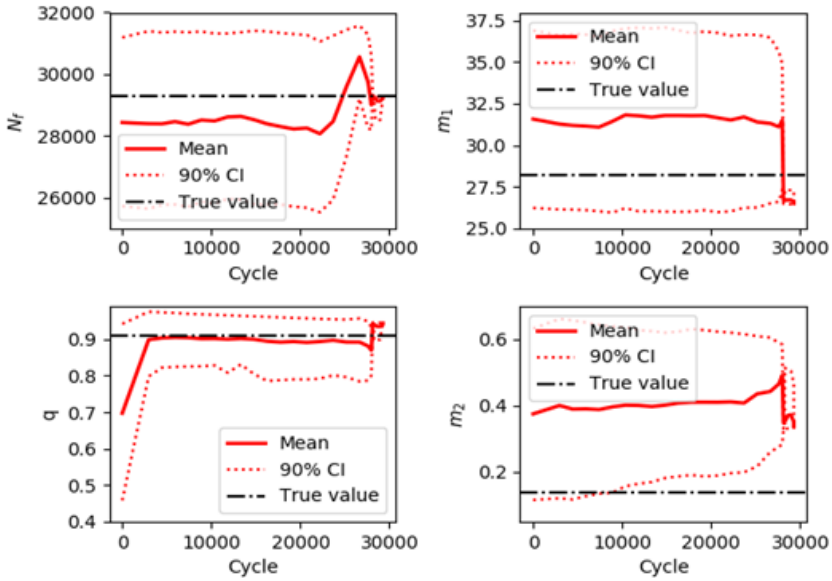

Figure 5-7 - Parameter vector update trajectory

It is seen that in the last update of parameters, confidence bounds merge to the mean, and all converge to one value. This is because the thermodynamic index at the time of crack

initiation is much higher than previous ones, which results in the resampling step to resample very few particles. Therefore, all of the new samples are generated from very similar or the same particles. It should be noted that since the true damage increases slowly for most of the component life, the particle filter algorithm converges gradually to the true values of the parameters. However, as soon as tests approach the end life, several information entropy damage indexes become available, and a substantial change in thermodynamic entropy damage index is seen; consequently, the PF effectively updates particles. Therefore, initial estimations, i.e., prior distributions for parameters, play an important role in the overall performance of the particle filtering framework. After each update to the parameter vector, the RUL is estimated using Eq. 8. The performance of the RUL estimation in the test is shown in Figure 7.

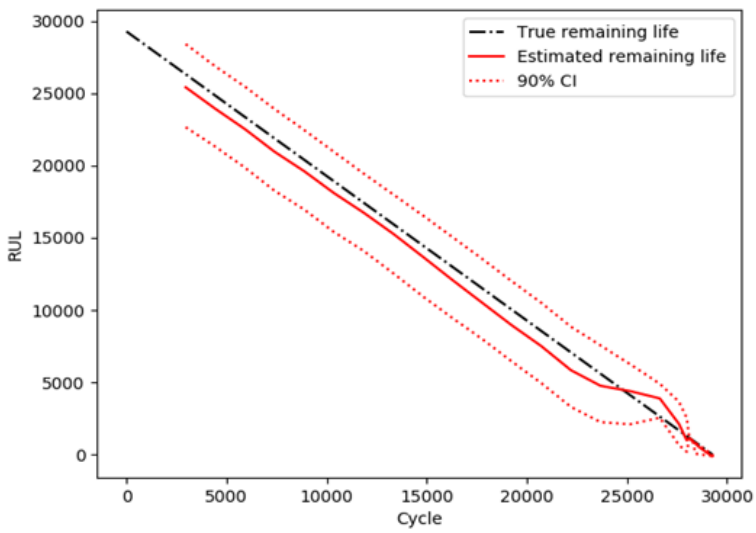

Figure 5-8 - RUL estimation

The true RUL stays within the 90% CI during the whole test and converges to the true value at the end of the life. The crack initiation cycle estimate is also shown in Figure 8. It can be seen how the distribution of estimations starts with a wide range and shrinks around the true value as more observations become available. The results of applying the

framework in different tests, the initial values, the converged values, and the errors are reported in Table 1. For each test PF is run multiple times with the same initial values and the reported results are the average of runs.

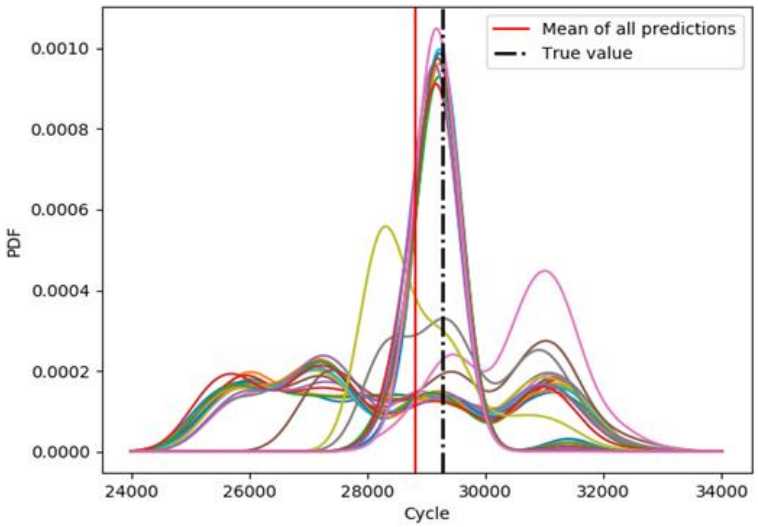

Figure 5-9 - Crack initiation estimation distribution

It is aimed to choose the same initial distribution for parameters in all tests. As it can be seen in Table 1, parameters q and m_2 have the same initial values in all tests, and N_f is the same in 3 tests. However, the value for m_2 is initialized in each test differently according to its true value. Although the parameters of Eq. 10 are expected to be material-dependent, the fitting procedure showed some differences in some of them, specifically, m_1. Perhaps due to the intrinsic stochasticity of fatigue problems, there is also stochasticity in the parameters. Nevertheless, the initial values for the parameters must be selected carefully. Especially in cases with a lower number of observations, an educated guess for the initial values is a must to ensure high accuracy in RUL estimations. The "# observation" in the Table refers to available entropy indexes in the test and their types. The average error shown in the table describes the average error in the estimation of the parameter. A negative value in error indicates underestimation. The average error in RUL estimation reports the

difference in the estimated crack initiation cycle and the true value once an observation becomes available. For instance, Test 1 on average makes a conservative estimation for the crack initiation cycle with an error of -846 cycles. Most of the tests resulted in conservative estimations for RUL within acceptable ranges.

Table 5-1 - PF results

Test #	Loading Condition	# Observations (S + I)	Parameter	Initial Distribution	Final Converged Value	True Value	Average Error	Average Error in RUL Estimation (cycles)
1	Overload	20 + 16	N_f	$\boldsymbol{U}$ (25000,32000)	31522	30514	-2.81%	-864
			q	$\boldsymbol{U}$ (0.4,0.99)	0.75	0.92	-25.69%	
			m_1	$\boldsymbol{U}$ (43,56)	50.06	48.03	3.69%	
			m_2	$\boldsymbol{U}$ (0.05,0.7)	0.22	0.38	-24.67%	
2	HCF	11 + 8	N_f	$\boldsymbol{U}$ (81000,88000)	87482	86279	-1.35%	-1567
			q	$\boldsymbol{U}$ (0.4,0.99)	0.77	0.75	4.08%	
			m_1	$\boldsymbol{U}$ (49,62)	54.18	56.98	-2.85%	
			m_2	$\boldsymbol{U}$ (0.05,0.7)	0.51	0.24	93.08%	
3	Programmed	18 + 5	N_f	$\boldsymbol{U}$ (25000,32000)	28253	27871	3.97%	1134
			q	$\boldsymbol{U}$ (0.4,0.99)	0.93	0.93	-1.14%	
			m_1	$\boldsymbol{U}$ (25,38)	31.28	35.23	-9.79%	
			m_2	$\boldsymbol{U}$ (0.05,0.7)	0.37	0.54	-23.06%	
4	Programmed	19 + 8	N_f	$\boldsymbol{U}$ (25000,32000)	29964	29272	-0.38%	-141
			q	$\boldsymbol{U}$ (0.4,0.99)	0.91	0.91	-2.38%	
			m_1	$\boldsymbol{U}$ (25,38)	33.46	28.2	15.09%	
			m_2	$\boldsymbol{U}$ (0.05,0.7)	0.49	0.14	218.19%	

The use of entropy indexes as observation in this framework increases its flexibility and applications, mainly due to the independence of the entropy from experimental conditions. More elaborated observation functions, damage index, and increased number of entropy measurements in a test can further improve the accuracy of this framework. A desirable improvement in the observation model (Eq. 11 and 12) would use the entropy endurance distribution rather that the expectation value of the distribution.

5.6. Conclusion

The use of entropy as a damage indicator in degradation processes such as fatigue is very promising. In this paper, we have briefly reviewed recent findings regarding the use of

thermodynamic and information entropy in detecting crack initiation. Although these entropic measurements provide invaluable information regarding crack initiation time, they cannot be directly used to estimate RUL of a component. This paper introduces an observation and state process model to implement the entropy measurements within a dynamic Bayesian updating framework. A joint Particle Filter framework is then defined based on kernel-smoothing to estimate the RUL and parameter of the state process model. The framework is applied to four tests with different loading conditions, and results are presented. The results show the ability of the proposed framework to estimate RUL in all tests with acceptable error. Possible improvements to the framework are explained and can be implemented in the definition of state and observation models. The significant advantage of this framework is its independence to loading condition that can provide hybrid data-driven and physics-based maintenance decisions, leading to further increase in the safety and reliability of components while decreasing the costs associated with scheduled periodic maintenance.

5.7. References

[1] A. P. Mouritz, *Introduction to Aerospace Materials*. Reston, VA: Woodhead Publishing, 2012.

[2] A. Imanian and M. Modarres, "Thermodynamics as a fundamental science of reliability," *Proceedings of the Institution of Mechanical Engineers, Part O: Journal of Risk and Reliability*, vol. 230, no. 6, pp. 598–608, Dec. 2016.

[3] H. Yun and M. Modarres, "Measures of Entropy to Characterize Fatigue Damage in Metallic Materials," *Entropy*, vol. 21, no. 8, p. 804, Aug. 2019.

[4] Y. Lei, N. Li, L. Guo, N. Li, T. Yan, and J. Lin, "Machinery health prognostics: A systematic review from data acquisition to RUL prediction," *Mechanical Systems and Signal Processing*, vol. 104, pp. 799–834, May 2018.

[5] M. Rabiei and M. Modarres, “A recursive Bayesian framework for structural health management using online monitoring and periodic inspections,” *Reliability Engineering & System Safety*, vol. 112, pp. 154–164, Apr. 2013.

[6] M. Chai, Z. Zhang, Q. Duan, and Y. Song, “Assessment of fatigue crack growth in 316LN stainless steel based on acoustic emission entropy,” *International Journal of Fatigue*, vol. 109, pp. 145–156, Apr. 2018.

[7] A. Imanian and M. Modarres, “A thermodynamic entropy-based damage assessment with applications to prognostics and health management,” *Structural Health Monitoring*, vol. 17, no. 2, pp. 240–254, Mar. 2018.

[8] S. F. Karimian, R. Moradi, S. Cofre-Martel, K. M. Groth, and M. Modarres, “Neural Network and Particle Filtering: A Hybrid Framework for Crack Propagation Prediction,” *arXiv:2004.13556 [eess, stat]*, Apr. 2020, Accessed: May 24, 2020. [Online].

[9] E. Rabiei, E. L. Droguett, and M. Modarres, “A prognostics approach based on the evolution of damage precursors using dynamic Bayesian networks,” *Advances in Mechanical Engineering*, vol. 8, no. 9, p. 168781401666674, Sep. 2016.

[10] S. F. Karimian, H. A. Bruck, and M. Modarres, “Thermodynamic entropy to detect fatigue crack initiation using digital image correlation, and effect of overload spectrums,” *International Journal of Fatigue*, vol. 129, p. 105256, Dec. 2019.

[11] S. F. Karimian, M. Modarres, and H. A. Bruck, “A new method for detecting fatigue crack initiation in aluminum alloy using acoustic emission waveform information entropy,” *Engineering Fracture Mechanics*, vol. 223, p. 106771, Jan. 2020.

[12] C. Basaran and S. Nie, “An Irreversible Thermodynamics Theory for Damage Mechanics of Solids,” *International Journal of Damage Mechanics*, vol. 13, no. 3, pp. 205–223, Jul. 2004.

[13] Shannon, Claude Elwood., “A Mathematical Theory of Communication,” *Bell system technical journal*, vol. 27, no. 3, pp. 379–423, 1948.

[14] X. Liu, W. Zhang, X. Liu, W. Dai, and G. Fu, “A Novel RLS-KS Method for Parameter Estimation in Particle Filtering-Based Fatigue Crack Growth Prognostics,” *IEEE Access*, vol. 7, pp. 156764–156778, 2019.

[15] Y. Hu, P. Baraldi, F. Di Maio, and E. Zio, “A particle filtering and kernel smoothing-based approach for new design component prognostics,” *Reliability Engineering & System Safety*, vol. 134, pp. 19–31, Feb. 2015.

[16] H. Mao and S. Mahadevan, “Fatigue damage modelling of composite materials,” *Composite Structures*, vol. 58, no. 4, pp. 405–410, Dec. 2002.

Chapter 6: Acoustic emission signal clustering in CFRP laminates using a new feature set based on waveform analysis and information entropy analysis[1]

6.1. Abstract

Acoustic Emission (AE) for structural health monitoring of fiber-reinforced polymers (FRP) has been under extensive study in past decades. Many of the available methods rely on using the conventional features of AE signals for clustering. These clusters are then related to a specific failure mechanism based on their behaviors. The conventional AE features are derived from a portion of the signal waveform that passes through a pre-determined threshold and is heavily affected by attenuation. Therefore, recent studies on AE are more focused on waveform analysis. A key parameter when analyzing the waveform distribution is the selection of appropriate bin width. This study discusses the choice of an optimum bin width for waveform analysis. This parameter is then shown to be well correlated to the conventional threshold-dependent features of AE signals. The bin width is then used as a time-domain representation of the waveform and is used with the peak frequency for signal clustering. A series of tensile tests are performed on cross-ply and quasi-isotropic carbon FRP (CFRP) specimens. The results show that AE signal clustering using these features outperform clustering performance using conventional AE features. This approach is shown to divide signals into two clusters; a cluster with matrix dominated signals and a cluster with fiber dominated signals. The information entropy of

[1] The full-text of this chapter has been published in the journal of Composite Structures, 113987, 2021. https://doi.org/10.1016/j.compstruct.2021.113987

signals in each cluster is evaluated and compared to the information entropy of noise signals.

6.2. Introduction

The use of Fiber Reinforced Polymer (FRP) laminates such as Carbon FRP (CFRP) has increased widely in different industries over the past decades. These materials offer high stiffness, high strength, high corrosion resistance, and long fatigue life at a lower weight ratio comparing to metallic counterparts. However, damage and failure mechanisms in FRP laminates are a more complex phenomenon. This usually utilizes large safety factors that cause overdesigning and stems from our lack of full comprehension of the governing damage mechanisms [1]. The damage mechanisms in FRP laminates are matrix cracking, fiber/matrix debonding, delamination, fiber breakage, and fiber pull-out. The sequence of damage mechanisms, their effect on each other, and the ultimate failure depend on parameters such as fiber types [2], matrix type [3], stacking sequence [4], and unidirectional or woven laminate [5] among others. It is the synergy between these mechanisms that leads to final failure [6]. Several non-destructive testing (NDT) techniques are proposed in the literature for structural health monitoring (SHM) and failure prevention of these materials [7], [8]. Among the available NDT techniques, the unique advantages of acoustic emission (AE) have gained increased attention [9]. The AE is a highly sensitive and passive technique that detects activity inside the material. This technique only requires small sensors that capture transient elastic waves emitted due to damage in the materials under stress.

The use of AE on composites dates back to the 1970s, focusing on the detection of damage onset [10]. Since then, the use of AE has expanded, and the correlation of signal features

to different damage mechanisms is discussed in the literature [11]. The relation between AE signals and damage mechanisms assumes that each damage mechanism emits a specific signal type. Signals are then clustered based on similarity measures to reveal the natural structure of the data through unsupervised clustering techniques [12] or supervised learning [13]. The clusters are then assigned to a specific damage mechanism based on their features. A comparison of three damage classification techniques is reported by McCrory et al. [14]. In [14], AE signals recorded in a buckling test on cross-ply CFRP are clustered using Artificial Neural Network (ANN), Unsupervised Waveform Clustering (UWC), and Measured Amplitude Ratio (MAR). In the ANN technique, five time-domain (rise-time, counts, absolute energy, duration, and amplitude) and three frequency-domain (average frequency, central frequency, and peak frequency) features of AE signals are used in the self-organizing map (SOM) before the k-mean algorithm clusters them. In UWC, waveforms are used as input to a principal component analysis (PCA) and clustered with the k-mean technique. In MAR, the ratio of energy in the flexural wave (A_0) and extensional wave (S_0) is used. The results show the ability of the MAR technique to discriminate delamination signals and the advantage of UWC and ANN in detecting more clusters.

Sawan et al. [15] compared four unsupervised techniques of k-means, hierarchical, fuzzy c-mean, and Gaussian mixture distribution (GMD) on an artificial database and showed GMD could provide better results. The authors then used the technique to cluster AE signals on open-hole CFRP specimens in tensile and four-point bending tests. Six time-domain (amplitude, rise-time, energy, counts, duration, and the ratio of amplitude to rise-time) and three frequency-domain (peak frequency, frequency centroid, and average

frequency) features of AE signals were selected for clustering. They argue that numerical techniques used for finding an optimum number of clusters might not always identify the right number of distinct clusters. Sause et al. [16] studied the best selection of AE features for clustering and used AE signals emitted from cross-ply CFRP in four-point bending tests. A total of 12 frequency-domain features are extracted from AE signals, and an exhaustive search is performed combining all possible combinations of 5 to 12 features. Results show that a five-feature set including three partial powers, peak frequency, and weighted peak frequency outperforms other candidates. Azadi et al. [17] studied the effect of loading rate on failure mechanisms of cross-ply open-hole CFRP specimens using AE signals. Tensile tests were initially performed on pure resin and fiber, and the frequency range was measured. AE signals of tensile tests on specimens were clustered based on wavelet packet transform and fuzzy c-mean, using the measured frequency range, four time-domain parameters (rise-time, count, energy, and amplitude), and two frequency-domain parameters (average frequency and peak frequency), respectively. They concluded that matrix cracking and debonding are associated with a frequency range of 100 – 420 [kHz], while fiber breakage is related to frequencies of 420 – 500 [kHz].

The selection of AE features for clustering purposes is not usually explicitly discussed; however, amplitude and peak frequency are the most used in the literature [18]. There is a general agreement on these parameters in the literature about their correlation to specific damage mechanisms. For instance, Gutkin et al. [19] report AE signal clustering in tensile and double cantilever beam (DCB) test on CFRP specimens with different layups. Four time-domain features (amplitude, energy, rise time, and duration) and peak frequency are used in a SOM with the k-mean clustering. The result shows that each failure mechanism

is associated with a specific peak frequency range; with matrix related mechanisms (matrix cracking, delamination, and fiber/matrix debonding) showing a peak frequency ranges of less than 300 [kHz] and fiber related mechanisms (fiber failure and fiber pull-out) with ranges higher than 400 [kHz] in peak frequency. Liu et al. [20] report the tensile test result on CFRP specimens with two layups of cross-ply and quasi-isotropic. The controlling damage mechanisms in each layup and the amplitude values related to them are reported. The higher amplitude range (above 70 [dB]) is related to fiber-pull out and fiber failure. In contrast, the lower range of amplitudes is related to matrix cracking and delamination. Although there is a general agreement in the literature on the association of damage mechanisms to specific amplitude and peak frequency ranges, some question their accuracy [21], [22]. It is also argued that frequency centroid might be a better feature than peak frequency to describe the AE source [23].

Conventional AE features are extracted from portions of the recorded waveform that exceeds a pre-determined threshold and is known as a “hit”. The derived time-domain and some frequency-domain features (such as average frequency), which are frequently used in clustering, are dependent on the threshold setting. Threshold-dependent features tend to be more affected by signal attenuation [24] and the signal attenuation in composite materials is not always negligible [25]. Hence, the recorded signal features become dependent on propagation and sensor acquisition capabilities. Godin et al. [26] study focuses on sensor type and effect of propagation on AE features. Although the shape and characteristics of AE signals directly depend on the source mechanism, it is shown in the paper how the choice of AE sensor, the distance of the sensor to source location, and attenuation can affect the AE signatures. Furthermore, it is shown how the selection of

irrelevant features can inversely affect the clustering performance. Hence it argues that AE features are dependent on the experimental setup, and a comparison of the AE results under different conditions should be performed carefully. The selection of conventional AE features for signal representation depends mainly on the experience rather than the effectiveness of the features themselves and results in an inevitable loss of information [27]. However, a feature extraction method based on waveform can mitigate the disadvantages associated with conventional threshold-dependent features.

Recent studies on the use of AE are focused on waveform analysis that mitigates the effect of threshold setting. Zhensheng et al. [27] present a new feature representation of AE signals based on the similarity of the probability distribution of raw waveforms when AE amplitudes are lower than environmental noise. Their paper proposes similarity measurements of waveforms based on their probability distribution to detect relevant AE signals from noises. The authors show the effectiveness of using the AE waveform in contrast to threshold-dependent parameters of the same signals. Xu et al. [28] argue that the selection of AE features and extraction of the features from AE signals play a vital role in pattern recognition. They state that the relevant features should be informative and non-redundant, and applicable under various environmental conditions. They perform a clustering based on waveform analysis by decomposing signal waveform based on wavelet packet decomposition. Another waveform analysis method that has recently gained attention is information entropy [29]. Information entropy measures the uncertainty within a distribution, and in the case of AE signals, it measures the uncertainty of a distribution associated with a signal waveform. Chai et al. [30] used the information entropy of AE signals measured in stainless steel specimens and reported similar evaluation of cumulative

values for entropy as for energy and count. Sauerbrunn et al. [31] report a better correlation of the entropy values to damage in aluminum materials. Burud and Kishen [32] discuss AE entropy's application on concrete and introduce it as an additional dimension to AE features. The recent review paper [1] on the characterization of laminated composites using acoustic emission suggests more focus on using techniques that directly evaluate signals waveforms such as information entropy.

The effort to select an efficient clustering technique and the use of SOM or PCA to improve the performance of clustering, among other efforts, are discussed in the literature. These and some of the other common "user's dilemma" for clustering are discussed by Jain [33]. However, the more crucial task in clustering is choosing the right feature extraction methods that identify the underlying structure of the data [33]. In this study, we focus on the selection of an appropriate bin width when dealing with waveform analysis and demonstrate the effectiveness of such a choice in waveform analysis. We also explore the correlation of the bin width to conventional AE features. The bin width is then used as a time-domain representative feature to cluster AE signals, and the results are compared to clustering with conventional AE features. The clustered signals have been explored in detail, and their information entropy values are examined. The information entropy of the signal waveforms is regarded as a new feature and its behavior in different clusters is studied and compared to noise signals. The proposed method is applied on AE signals recorded in a series of tensile tests on open-hole CFRP specimens with two different layups and three different geometries.

6.3. Experiments

6.3.1. Materials, geometry, and manufacturing

The material used for this study is CFRP. Two laminated sheets, each following a specific layup, are used for this study. The layups are Cross-Ply (CP) with a sequence of $[0/90]_{4s}$ and Quasi-Isotropic (QI) with a sequence of $[45/90/-45/0]_{2s}$. Both sheets have 16 plies, with each ply made up of high-performance unidirectional pre-preg sheets. The CP laminate is made with Toray T300 fibers [34] and toughened Toray 2500 epoxy resin with a 35% resin volume density. The QI sheet is made with Toray T700G fibers [34] and Toray 2510 pre-preg system [35] with a 65% fiber volume density.

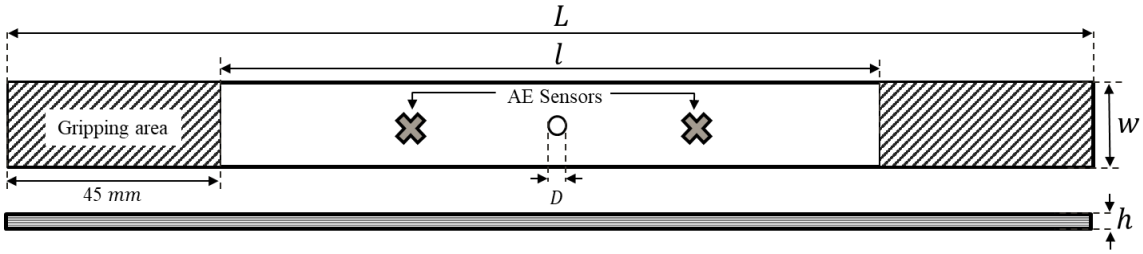

Figure 6-1 - Specimens geometry

All the specimens are cut from the same CP and QI laminates. The geometry selected for this study is rectangular open-hole with three different dimensions. Figure 1 shows the overall geometry. In this Figure, L is the overall specimen length, including gripping area, l is the gauge length, h is specimen thickness, w is specimen width, D is the hole diameter, and w/D and D/h are specific ratios for each specimen type. Specimens are named after their layup, with the third geometry called Quasi-Isotropic Scaled (QIS). Table 1 summarizes dimensions for all the specimen types and compares them to the ASTM D5766 standard. The CP specimens follow the ASTM standard, while QI and QIS specimens have different dimensions. QI specimens were decreased in width to increase the stress

concentration around the hole, which better follows the industrial test standards [36]. The QIS geometry follows the geometry of the specimen in [37] with the length increased to avoid excessive noise recording in AE sensors. Aluminum tabs were used at the grip area with the length of the grip area is kept constant at 45 [mm]. All the CP and QIS specimens are cut out of the original sheet using a CNC Routing machine, while QI specimens are cut out of the sheet using a water-jet cutting.

Table 6-1 - Specimens dimensions

	$L\ [\boldsymbol{mm}]$	$l\ [\boldsymbol{mm}]$	$\boldsymbol{h}\ [\boldsymbol{mm}]$	$w\ [\boldsymbol{mm}]$	$D\ [\boldsymbol{mm}]$	w/D	D/h
ASTM D5766	150 - 300	150 - 300	2 - 4	--	--	6	1.5 - 3.0
CP	270	180	3	36	6	6	2
QI	270	180	2.3	30	6	5	2.6
QIS	230	140	2.3	18	3.6	5	1.6

6.3.2. Mechanical responses and failure modes

All the specimens were tested vertically under tensile loading until the fracture with a cross-head displacement rate of 0.5 $[mm/min]$. A servo-hydraulic material testing system (MTS) machine retrofitted with an Instron 8800 controller was used to perform the tests. Tests were monitored around the hole using an 8 [MP] Point Grey Flea3 sensor with a 3.8-13 [mm] Fujinon lens. Figure 2 shows the typical stress-strain curve for each of the specimen geometries. It is seen that the CP specimens have higher tensile strength comparing to quasi-isotropic specimens. QI and QIS specimens show a very similar response as expected.

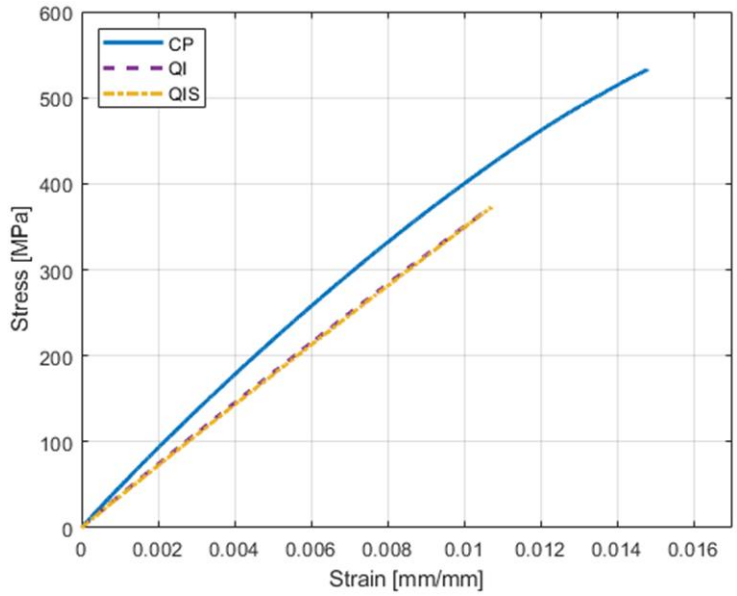

Figure 6-2 - Typical stress-strain curve for specimens

Table 2 summarizes the tensile test results of all the specimens and the number of tests for each geometry. The average value for tensile strength, modulus, and tensile strain with their corresponding coefficient of variation (CV) for each specimen geometry is reported in the table.

Table 6-2 - Summary of tensile test results (and their corresponding CV)

	σ_u [MPa]	E [GPa]	ε_u [%]	Number of specimens
CP	517.30 (2.68%)	46.05 (1.27%)	1.31% (8.54%)	6
QI	341.22 (7.34%)	37.12 (0.73%)	0.97% (8.06%)	5
QIS	337.08 (7.57%)	37.27 (1.87%)	0.94% (8.53%)	5

Figure 3 shows the typical failure mode in each of the geometries. The dominant failure mode observed in CP specimens is a brittle failure, while a pull-out is the dominant failure mechanism in QI and QIS specimens. The brittle failure is mainly associated with matrix cracking around the hole in the width to the free edges, followed by fiber failure. The pull-out failure is mainly associated with crack generation tangential to the hole in the 45-degree

direction and failure in the hole area between the layers that causes fibers in the 0-degree ply to fail at various locations close to the hole and layers to pull out.

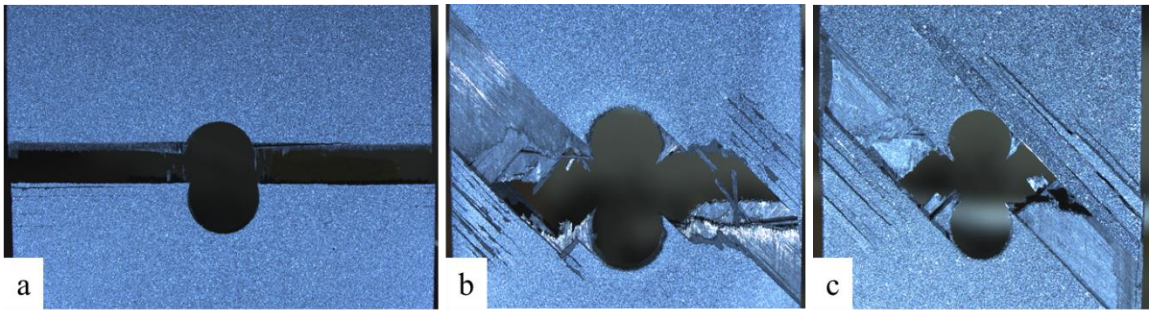

Figure 6-3 - Failure modes in CP (a), QI (b), and QIS (c) specimens

6.3.3. AE setup

Two AE wideband (WD) differential sensors from Physical Acoustics Corporation (MISTRAS Group, Princeton Junction, NJ) on a PCI-2 board, with an operating frequency range of 125 – 1000 [kHz] and a resonance frequency of 450 [kHz] were used to record AE signals in these tests. Ultrasonic gel couplant was used on the AE sensor's surface to improve attachment and signal recordings. Sensors were placed approximately 25 [mm] away from the hole in all specimens and vinyl tape was used for attachment. Signals were passed through a 40 [dB] pre-amplifier before reaching the data acquisition module. The Physical Acoustics AEwin software (Physical Acoustic Corporation, Version E5.60, MISTRAS Group, Princeton Junction, NJ, 2007) was used to record AE signals. The band-pass filter was set to 1 [kHz] – 3 [MHz]. The statistics of AE signals recorded for each specimen type is shown in Table 3. The effect of specimen geometry on the number of emitted signals is evident from the table.

Table 6-3 - AE signal statistics in all tests

Specimen type	Average number of signals in a test	The standard deviation of signals in a test
CP	4743	1163
QI	734	378
QIS	163	92

6.4. AE signal analysis

6.4.1. AE signals and waveforms

In AE testing, a threshold is set to only keep relevant signals and avoid noise signals from being recorded. The appropriate threshold in this study using a simple test [24] was found to be 50 [dB]. Signals that pass the threshold are damage related and recorded in the dataset. Recorded signals are defined by timing parameters peak definition time (PDT), hit definition time (HDT), hit lockout time (HLT), and max duration. The PDT defines the time window that signal amplitude and rise time are measured. This parameter is set to determine the true peak of the AE waveform. HDT is set to determine the end of a signal. A signal is considered complete when no voltage value passes the threshold level within the HDT time window. The HLT is set to prevent the reflection and late-time arriving parts of a signal to be recorded. During HLT, no signals are recorded and the previously recorded signal is transferred to memory. Max duration sets the maximum duration of a signal if no time window with HDT value can be detected in which no voltage value passes the threshold. These parameters are essential in determining a signal and directly influence the quality of the AE dataset recorded for a test, and are used in determining conventional AE features. The values for the timing parameters in this study are followed by the AEWin software manual suggestions, literature [38], and based on pencil lead break (PLB) tests. They are selected as 60 [μs], 100 [μs], 300 [μs], and 200 [ms] for PDT, HDT, HLT, and

max duration, respectively. To minimize the chance of missing any emitted signal, the HLT value is set to its minimum. A sample waveform showing the timing parameters and some conventional AE features is shown in Figure 4. In the Figure, HLT appears as a series of zero value voltages with a dashed line after the HDT window in the waveform.

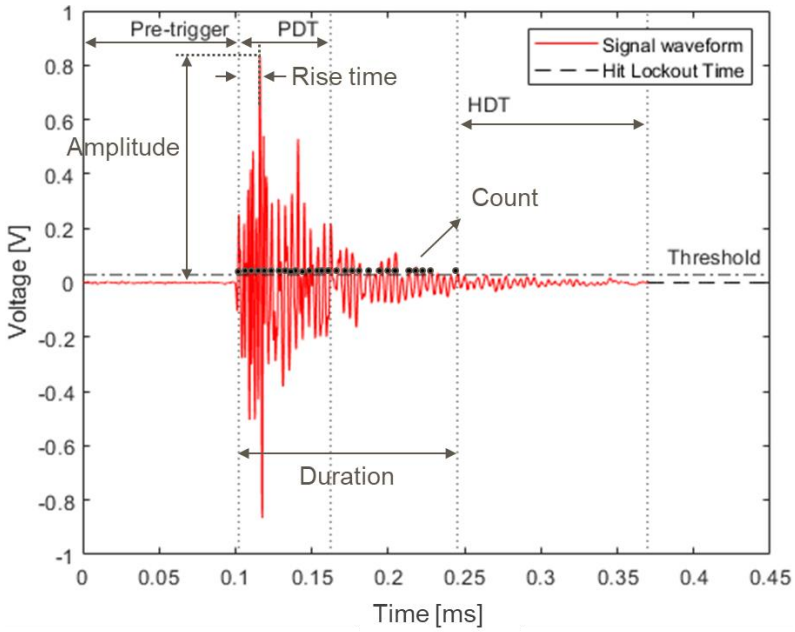

Figure 6-4 - AE waveform and timing parameters

The waveform generation of a signal follows a different set of parameters. Waveforms are time-domain depictions of a signal, generated based on the sampling rate, hit length, and pre-trigger time. Sample rate describes the number of voltage samples per second from a signal. A sampling rate of 2 [MHz] or higher is suggested for waveform analysis of CFRP materials [27] and a 5 [MHz] sampling rate is frequently used [2], [39]. A sampling rate of 5 [MHz] is selected for this study. The hit length determines the data points recorded for a waveform and is set to 10,240 (10k) in this study. Pre-trigger determines the time window recorded in a waveform before the first threshold passing event occurs. The value for the pre-trigger in this study is considered equal to the HDT parameter, 100 [μs]. Since the

waveform values in this time window are below the threshold, they have low voltage values. If a large time window is dedicated to them, it impacts the distribution of the waveform and consequently waveform entropy measurement, and might compromise the signal waveform depiction. The value selected for the pre-trigger parameter in this study is shorter than the default value suggested by the software (256 [μs]). The combination of these three parameters defines a waveform.

It should be noted that the selection of these parameters should ensure that a signal can be fully depicted by its waveform. For instance, the current waveform parameter setting results in a 2048 [μs] waveform. Therefore, signals with longer durations cannot be fully depicted with their waveform. The selection of these parameters should be made carefully. PLB tests were done in this study to confirm the selection of these parameters. In all of the tensile test AE dataset, on average, only 0.6% of signals were associated with longer durations that could be captured entirely by the waveform settings. However, even in those signals, the main event of the signal is recorded in the waveform and mostly, the reflections are left out of the waveform. Figure 5 shows a waveform of one of the PLB tests. It can be seen that the selected timing parameters fully captured the signal waveform and the PDT window correctly detected the highest voltage value.

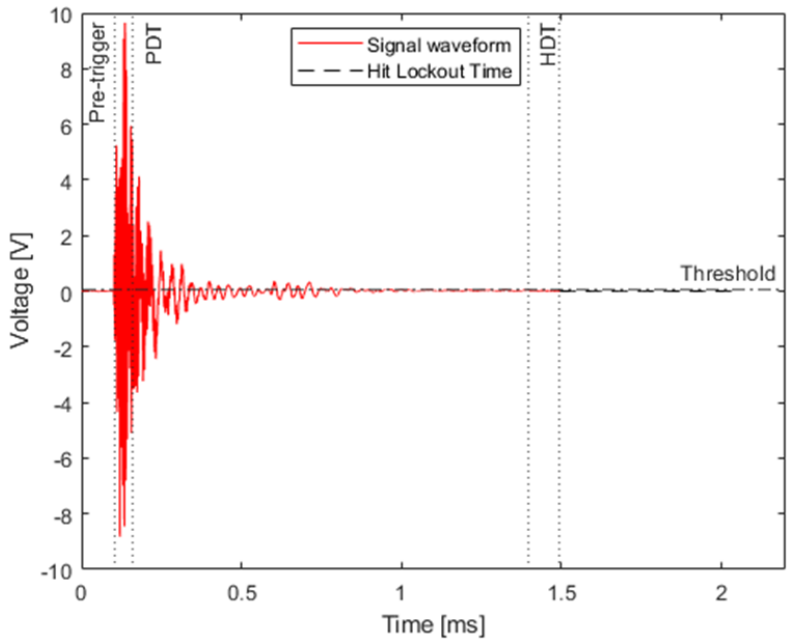

Figure 6-5 - PLB test signal

AE signals in this study are recorded in two independent sensors. The time it takes for one signal to travel from one sensor to other (delta-T) is measured on all specimens before applying any load. This value is then used to remove all the signals that arrived from other locations rather than the hole area. Only the signals passed the delta-T filtering (valid signals) are used for analysis in this study. Valid signals recorded in CP, QI, and QIS specimens will be referred to as CP, QI, and QIS datasets.

6.4.2. Bin width selection

The waveform information entropy measurement, as will be discussed in the next section, depends on defining a proper distribution for the voltage values in the waveform. The histogram is a desirable choice. It is a convenient and widely accepted distribution to reveal the underlying density of a variable. The assignment of a histogram to a signal waveform requires the selection of an appropriate bin width. However, the choice of bin width is usually overlooked. Bin width selection is an essential step in generating a histogram,

which refines the distribution and affects the entropy measurement. An ideal bin width should reveal the essential structure of the data while avoiding too much detail. The selection of an appropriate bin width to generate a histogram for a variable is studied in the literature by Scott [40] and further expanded by Wand [41]. In the context of waveform analysis, the bin width is usually selected as a fixed value based on the resolution of the AE data acquisition system [27], [29], [30]. The appropriate bin width for a waveform is referred to as the optimum bin width in this study and is calculated based on Equations 1 and 2. The use of optimum bin width in information entropy measurement is discussed in the literature [24]. It is suggested to use an average value of the optimum bin width of all signals in Aluminum alloys. This approach was useful in Aluminum alloys since the material was homogenous and the source of all AE signals were similar. In CFRP, however, the AE source varies depending on the damage mechanism and can be the fiber, matrix, or interface. It is widely accepted and assumed that each damage mechanism has a specific type of waveform. Therefore, the distribution for each waveform should be generated using the optimum bin width of the waveform. The optimum bin width of a waveform is calculated using Scott's [40] equation:

$$b_n = k\delta n^{-1/3} \qquad (1)$$

in which k is a constant, given as $k = 3.49$, δ is the standard deviation of the voltage values in a waveform, and n is the number of data points in the waveform. This equation has the inherent assumption that the underlying distribution follows a Gaussian distribution. To correct this assumption, two correction coefficients based on the difference in skewness and kurtosis are used that are shown in Equation 2:

$$b_{Opt} = b_n \times C_{sk} \times C_{kur} \qquad (2)$$

in which C_{sk} and C_{kur} are the correction coefficients for skewness and kurtosis difference, respectively, given in Scott [40]. The optimum bin width for each waveform is a time-domain parameter and is independent of the threshold setting. Figure 6 shows the correlation coefficient of widely used AE features in time- and frequency-domain to the optimum bin width in each dataset. These values are calculated for each test in a dataset and the average values in all tests of the datasets are shown in the figure.

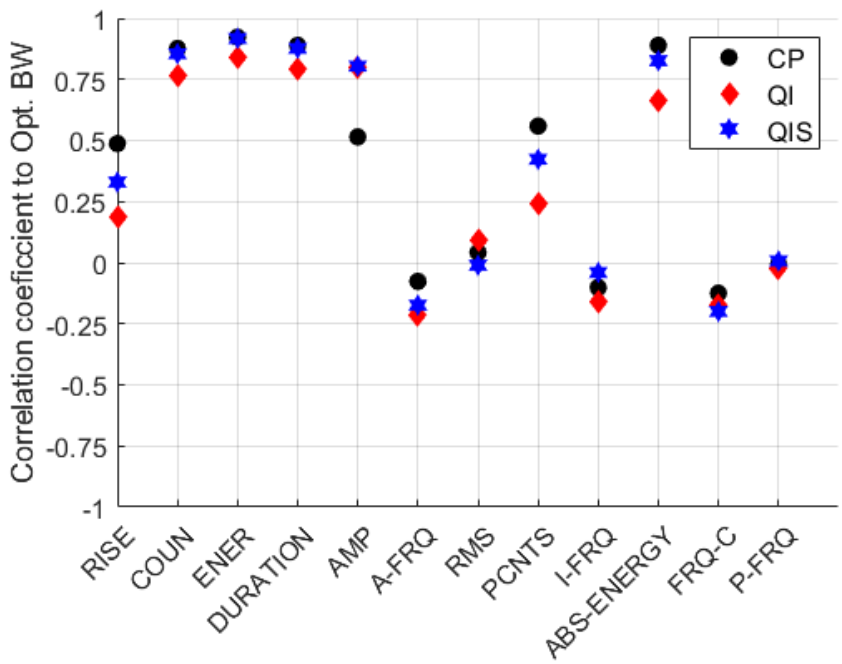

Figure 6-6 - Average correlation coefficient of optimum bin width to AE features in CP, QI, and QIS datasets.

It is seen that while the time-domain features generally show a high correlation coefficient, the optimum bin width is almost independent of frequency-domain features. Widely used AE features such as count, energy, duration, and amplitude show a very high correlation coefficient to the optimum bin width. This suggests that it can be used as a threshold-independent feature for time-domain representation when clustering. The use of optimum bin width in clustering would prevent data-redundancy from incurring by having a strong

correlation to various highly used time-domain features and preventing the repetition of using linearly related features, such as count and duration.

6.4.3. Waveform information entropy measurement

Information entropy is a measure of uncertainty or missing information [42] of the distribution of a random variable. The information entropy described by Shannon [43] defines a method of measuring the uncertainty of a discrete distribution. The assumption is that all values of the random variable are assigned with a probability of less than or equal to one and the summation of all the probability values in the random variable equals one. The random variable in our case is the voltage values in a waveform. The histogram of the random variable satisfies the requirements of Shannon entropy assumptions and it is used in this study as the non-parametric distribution of the voltage values. The Shannon entropy is defined by Equation 3:

$$I = -c \sum_{i=1}^{n} P(V_i) \ln(P(V_i)) \qquad (3)$$

In which $V_i = \{v_1, v_2, \dots, v_n\}$ is the random variable, $P(V_i)$ is the probability distribution of the voltage at the ith histogram bin, I is the information entropy, and c is a constant considered to be unity in this study. The unit of AE information entropy used in this study is 'nats' since in Equation 3 the natural logarithm is used. According to information entropy, uniform distributions have the highest information entropy since no value is preferred. Meanwhile, biased distributions have lower information entropy (or missing information) since some values are associated with higher probabilities. As discussed in the previous section, the choice of bin width plays an important role in developing a histogram. An ideal bin width would reveal the true shape of the underlying distribution of

the random variable, while a larger and a smaller bin width would result in simplification or too detailed histograms, respectively. Figure 7 shows the effect of bin width selection on the histogram and the information entropy value of a signal.

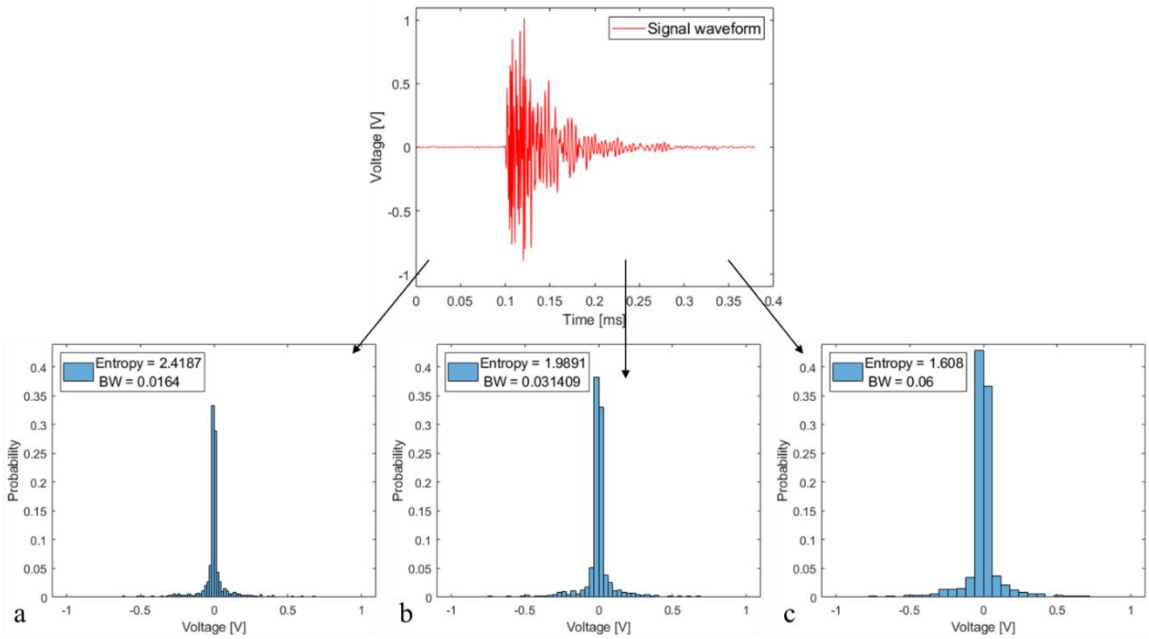

Figure 6-7 - Effect of bin width selection in probability distribution and entropy measurement. Bin width of 0.0164 and entropy of 2.4187 [nats] (a), optimum bin width of 0.0314 and entropy of 1.9891 [nats] (b) and bin width of 0.06 and entropy 1.608 [nats] (c)

In Figure 7-a, the average value of the optimum bin width of all signals in the test is used to construct the probability distribution and measure the entropy. In contrast, 7-b uses the optimum bin width value for the signal to construct the histogram and measure the entropy. Figure 7-c shows a subjectively chosen larger bin width value for comparison. The difference in probability distribution and entropy measurement can be easily seen. The result of bin width selection in entropy measurements of waveforms as a function of signals amplitude in a test is shown in Figure 8.

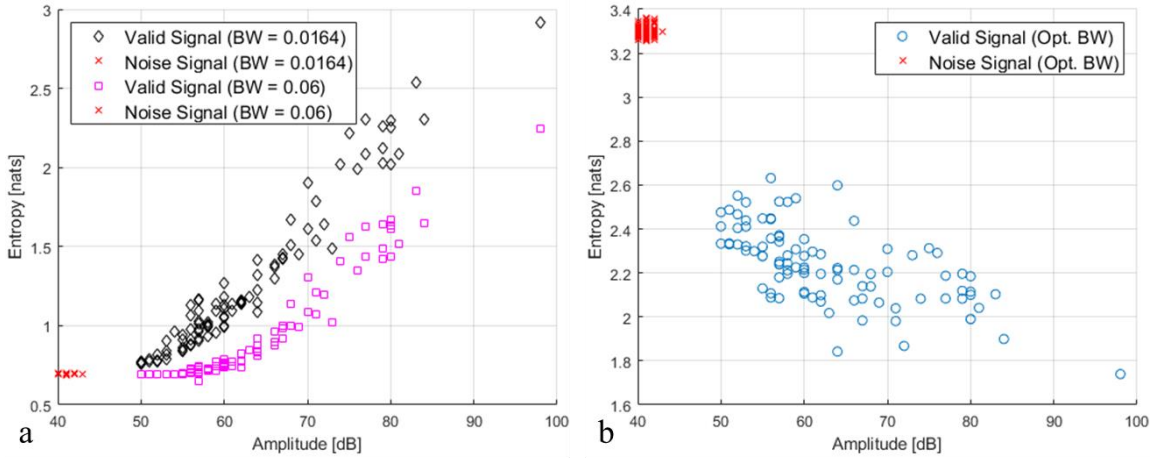

Figure 6-8 - Effect of fixed bin width (a) and optimum (variable) bin width (b) on entropy values of valid and noise signals.

In Figure 8-a, the entropy measurement using two fixed bin widths are shown. The smaller bin width is equal to the average of the optimum bin width in all signals in the test and corresponds to Figure 7-a. The larger bin width corresponds to the subjectively chosen bin width and corresponds to Figure 7-c. It is seen that in Figure 8-a, the change of bin width value results in a shift in the entropy values of the valid signals while the same trend is seen. This is in contrast with Figure 8-b, in which the optimum bin width of each signal waveform is used to measure the entropy of the waveform. It is seen that the trend of entropy values changes. The entropy values of the noise signals recorded before applying any load are also shown in the Figure. In 8-b, noise signals show higher entropy values comparing to valid signals, indicating that they are associated with higher uncertainties, while valid signals show lower uncertainties, indicating they carry more information.

The selection of the bin width directly affects the waveform analysis. In CFRP laminates, the AE source varies depending on the damage mechanism and originates in different materials. Therefore, a fixed value of bin width is not a desirable choice. The bin width for a waveform is proposed to be selected based on the waveform itself. This method results

in a variable bin width value called optimum bin width. The selection of the optimum bin width to measure entropy is compared with entropy measurement using a fixed bin width value. The results show that the trend of entropy values changes dramatically when the optimum bin width is used, and it better follows the definition of information entropy; noise signals show higher entropies, indicating higher uncertainties and valid signals show lower entropy values, indicating higher information content and lower missing information. The optimum bin width is also shown to be well correlated to conventional time-domain features of AE signals. This behavior results in redundancy reduction when clustering and makes it a potential candidate to present time-domain properties of AE signals. In the following section, signal clustering based on the optimum bin width as the time-domain representative of a waveform, and peak frequency, as the frequency domain representative, is explored.

6.5. Pattern recognition

As stated in the introduction, the pattern recognition in AE signals and correlation to different damage mechanisms is discussed in the available literature. The most widely used clustering technique in laminated composites is k-means [1]. Data representation in clustering techniques is one of the most important factors that influence performance. AE signal representation is usually performed through AE features in time-domain [2], frequency domain [16], or a combination [19] of them. The selection of AE features for clustering is not regulated and is unclear. Most of the time-domain features used are threshold-dependent and are highly affected by sensor/source distance, among others.

Meanwhile, techniques based on waveform analysis can minimize the effect of the threshold [1]. The crucial task in identifying the underlying clusters in a dataset is the right

feature extraction method [33]. Therefore, the features selected for clustering in this study are based on waveform analysis and are independent of the threshold setting: the optimum bin width and peak frequency. Optimum bin width is the signal representation in the time-domain. It is shown to strongly correlate with conventional AE features used in literature, and peak frequency is widely used as a frequency-domain feature in literature. The k-means clustering technique is used in this study and the clustering performance of the proposed feature set is compared to the proposed features in literature. Silhouette [44] values are used for clustering performance measurements, and Davis-Boulding [45] index is used to confirm the clustering performance compared to other feature sets. Clusters are then analyzed and are related to the underlying damage mechanisms based on their sequence and characteristics.

6.5.1. k - means

In terms of AE signal analysis, the k-means clustering techniques partitions a set of $AE = \{AE_i\},\ i = 1,2,\dots,n$ input signals collected in a test, with d-dimensional features, to k clusters with $C = \{c_1,\dots,c_K\}$ centroids, by minimizing the input distances to the centroids. The algorithm is performed by [46]:

1- Randomly choosing cluster centroid c_i.

2- Compute the distance of each input points $x_{1,\dots,n}$ to the cluster centers $c_{1,\dots,k}$ and assign them to the nearest cluster.

3- Recalculate the location of cluster centers to minimize the (Euclidean) distance of inputs to the centers using Equation 4:

$$d(x,c) = (x-c)(x-c)' \qquad (4)$$

4- Compute the average of the observations in each cluster to obtain new cluster centroids.

5- Repeat steps 2 through 4 until the cluster assignment does not change.

There are two phases in the third step of the algorithm: batch update and online update. In the first phase, batch update, each iteration consists of reassigning points to their nearest clusters' centroid, all at once, followed by recalculation of cluster centroids. The second phase, online update, consists of reassignment of inputs individually if it reduces the sum of distances and recalculation of cluster centroids after each reassignment. The performance of this method depends on the initial centroid selection.

One of the drawbacks of the k-means clustering algorithm is the requirement of knowing the number of clusters. To address it, a set of candidate cluster numbers k are usually selected and used in the clustering algorithm. For each k, a predetermined criterion is set to find the best candidate. Silhouette value [44] is selected in this study to measure the performance of each k. The Silhouette value for each point measures the similarity of the point to the points in its cluster comparing to the points in other clusters using Equation 5 [46]:

$$S_i = \frac{b_i - a_i}{\max(a_i, b_i)} \qquad (5)$$

in which a_i is the average distance from the ith point to the other points in the same cluster as i, and b_i is the minimum average distance from the ith point to points in a different cluster, minimized over clusters. The Silhouette value ranges from -1 to 1 and a value of 0.6 or greater indicates a good similarity.

6.5.2. Clustering results

In this study, for each set of AE features, an exhaustive search is performed to select the optimum number of clusters k. The possible number of clusters examined are $k \in [2,10]$ and the Silhouette value is used to measure the performance of clustering given a k. The following steps are taken to find the optimum k given AE features:

1- AE features are used to cluster AE signals in a test using all possible k values and the corresponding Silhouette value is recorded.

2- The previous step is repeated 10 times (to avoid local minima) and the Silhouette values are recorded and mean values are measured.

3- Previous steps repeated for all tests in a dataset.

4- Results are averaged and the k with the highest Silhouette value is selected as the optimum number of clusters for the AE feature set and dataset (CP, QI, or QIS).

These steps are taken for all the tests in a dataset for each AE feature set. Figure 9 shows these steps for the feature set peak frequency and optimum bin width in the QI dataset.

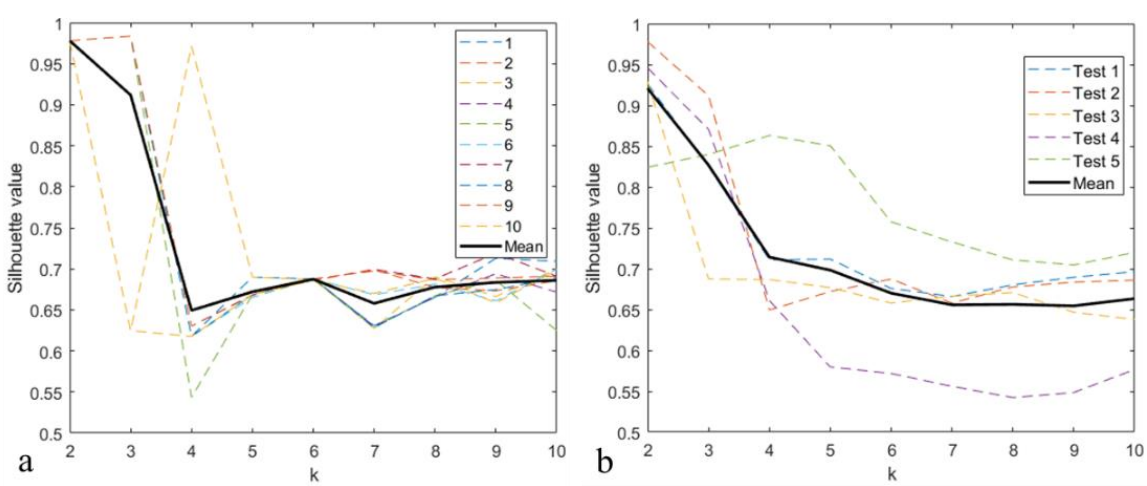

Figure 6-9 - Clustering steps 1 and 2 (a) and steps 3 and 4 (b) in QI dataset.

Figure 9-a shows steps 1 and 2 in which clustering using all the possible values of k is repeated 10 times in a specific test and Silhouette values are averaged. Figure 9-b shows steps 3 and 4 in which the average values in all tests in a dataset are compared and the average is measured to select the optimum number of clusters for the dataset given the feature set.

The performance of the proposed feature set is compared to other feature sets in literature. Table 4 shows the feature sets used in this study and their performance results in each dataset, and Figure 10 shows the result of clustering performance. Cluster similarity in all feature sets is also compared using the Davis-Bouldin (DB) index to verify the Silhouette values. The DB index measures the average distance of a point in each cluster to the cluster centers. Therefore, a lower value is an indication of better performance.

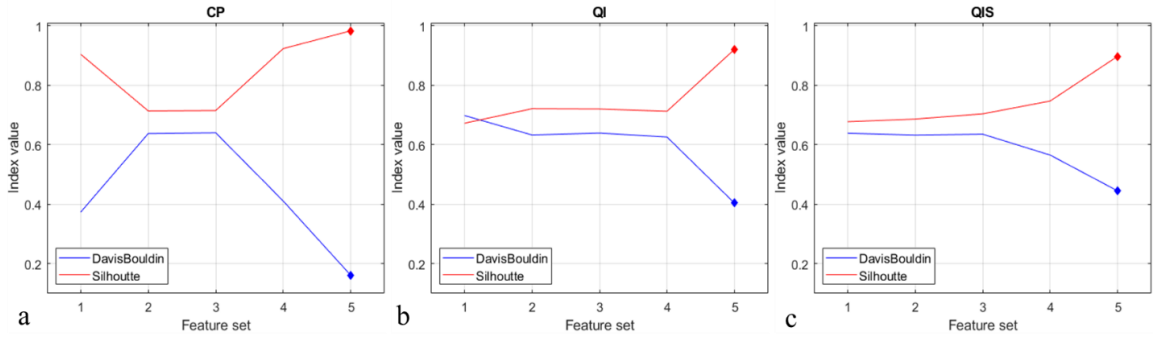

Figure 6-10 - Clustering performance of feature sets in CP (a), QI (b), and QIS (c) datasets measured by Silhouette and DB indexes.

The result of the proposed feature set in Figure 10 is shown with a solid Dimond. It is seen that while all the feature sets show good clustering performances (Silhouette value greater than 0.6), both indexes show a higher performance for the proposed feature set. However, the results explained in Table 4 show a discrepancy in the number of clusters selected for QI and QIS datasets. It is expected that QI and QIS datasets show the same number of

clusters since both have the same layup but different geometries. However, QIS is slightly preferred to have 3 clusters by Silhouette values. This is further discussed in the next part.

Table 6-4 - AE feature sets and clustering performance

Reference	AE Features	Feature set #	Mean Silhouette value			Number of clusters		
			CP	QI	QIS	CP	QI	QIS
Gutkin et al. [19]	Rise time - Energy - Duration - Amplitude - Peak Frequency	1	0.904	0.672	0.677	2	2	4
Ameur et al. [2]	Rise time - Duration - Amplitude - Counts to Peak - Absolute Energy	2	0.714	0.721	0.686	3	2	2
Haggui et al. [3]	Rise time - Energy - Duration - Amplitude - Counts to Peak	3	0.715	0.72	0.704	3	2	2
Saeedifar et al. [18]	Amplitude - Peak Frequency	4	0.923	0.712	0.747	2	2	3
Proposed	Optimum Bin Width - Peak Frequency	5	0.983	0.921	0.897	2	2	3

6.5.3. Delamination related signals

To further study the difference in the number of clusters in QI and QIS datasets, Test 3 in the QIS dataset is examined in more detail. The loading profile of the test is shown in Figure 11. As shown by the figure, this test involves a drop in loading profile near the failure strength. This drop is characterized by failure of the off-axis plies (45° plies) and transferring all the load-bearing to the on-axis plies (0° plies) [47] and causes delamination in the specimen. However, before the delamination can grow until it reaches the grips, the partial delamination allows some plies to pull-out from between each other at the point of fiber failure [37]. This behavior is notably seen in this test, while other QIS tests do not clearly show such behavior. Figure 11 shows the entropy values and signal clusters. It is notable that, as shown in Figure 11-b, cluster 2 appears immediately after the load drop.

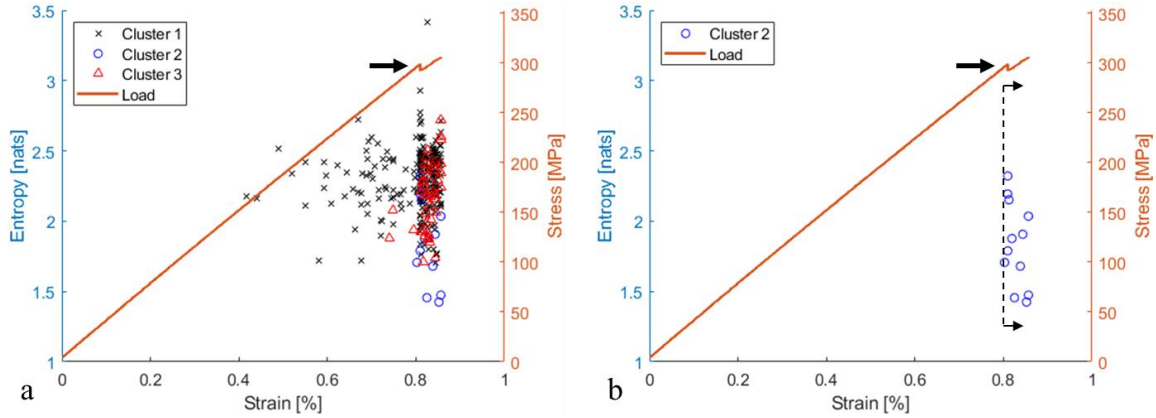

Figure 6-11 – Stress-strain curve of Test 3 in QIS dataset, showing entropy values of signals in all clusters (a) and cluster 2 (b)

Signals in cluster 2 are further examined in terms of their peak frequency, bin width (optimum bin width will simply be called bin width from here on), and waveform shapes. Figure 12 shows the results. The number of signals in this cluster is small in comparison to the other clusters. These signals are associated with low peak frequency values, similar to cluster 1, while showing large bin width values.

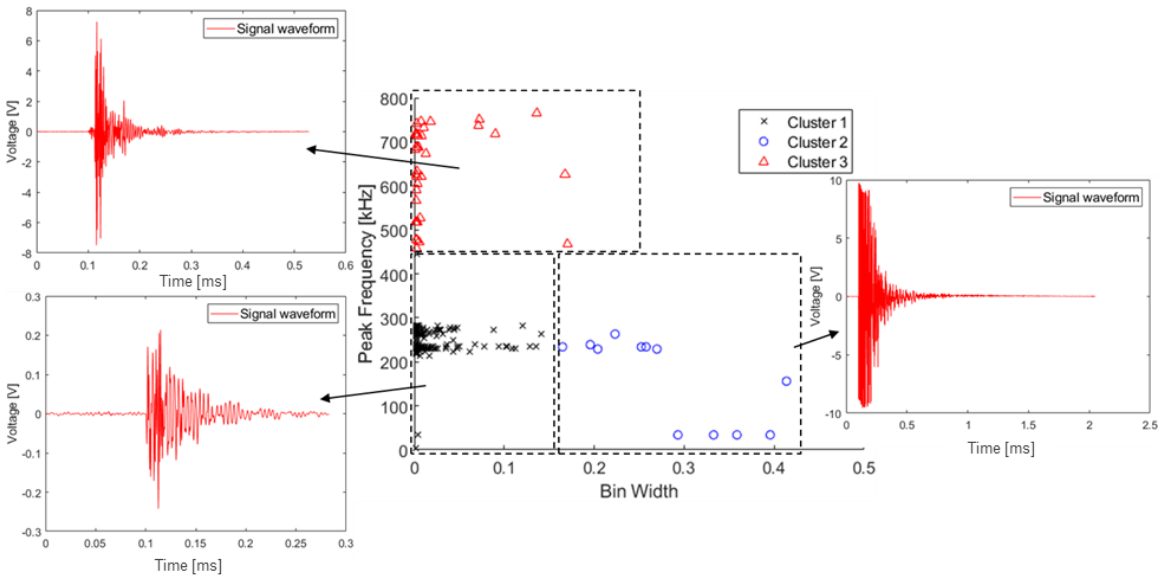

Figure 6-12 - Peak frequency versus bin width of signals in all clusters in Test 3 of QIS dataset and their typical waveform shapes (duration of signal waveform shown varies).

A typical waveform of the signals for each cluster is also shown in Figure 12. The waveforms in cluster 2 are associated with multiple spikes with high voltage values in a short span at the beginning, while waveforms in other clusters are related to single spikes. While the amplitude of signals in other clusters has a wide range, signals in cluster 2 are associated with high amplitudes. These signals are related to delamination. To study and compare signal waveforms of cluster 2, all QIS tests were examined in detail.

Figure 13 shows the results for Test 2 and Test 4 in QIS dataset. The waveform analysis of the signals in cluster 2 shows that in Test 2, only one of the signals can be related to delamination. However, none of the signals of cluster 2 in Test 4 show such a waveform shape. The similarity of the peak frequencies of cluster 1 and cluster 2, and the higher bin width values of delamination signals observed in Test 3, suggests that these two clusters can be combined. The delamination signals can be detected as signals in the combined clusters with bin width values larger than a threshold. The threshold is found to approximately be 0.17. Therefore, signal clustering based on the proposed features (feature set 5) can successfully cluster signals into 2 clusters and detect delamination signals within cluster 1 with bin width values larger than 0.17. Furthermore, in the QIS dataset, the selection of 2 clusters results in an average Silhouette value of 0.86, which is still higher than other feature sets in Table 4. This finding is tested on signals in all datasets and results for one test in each dataset are shown in Figure 14.

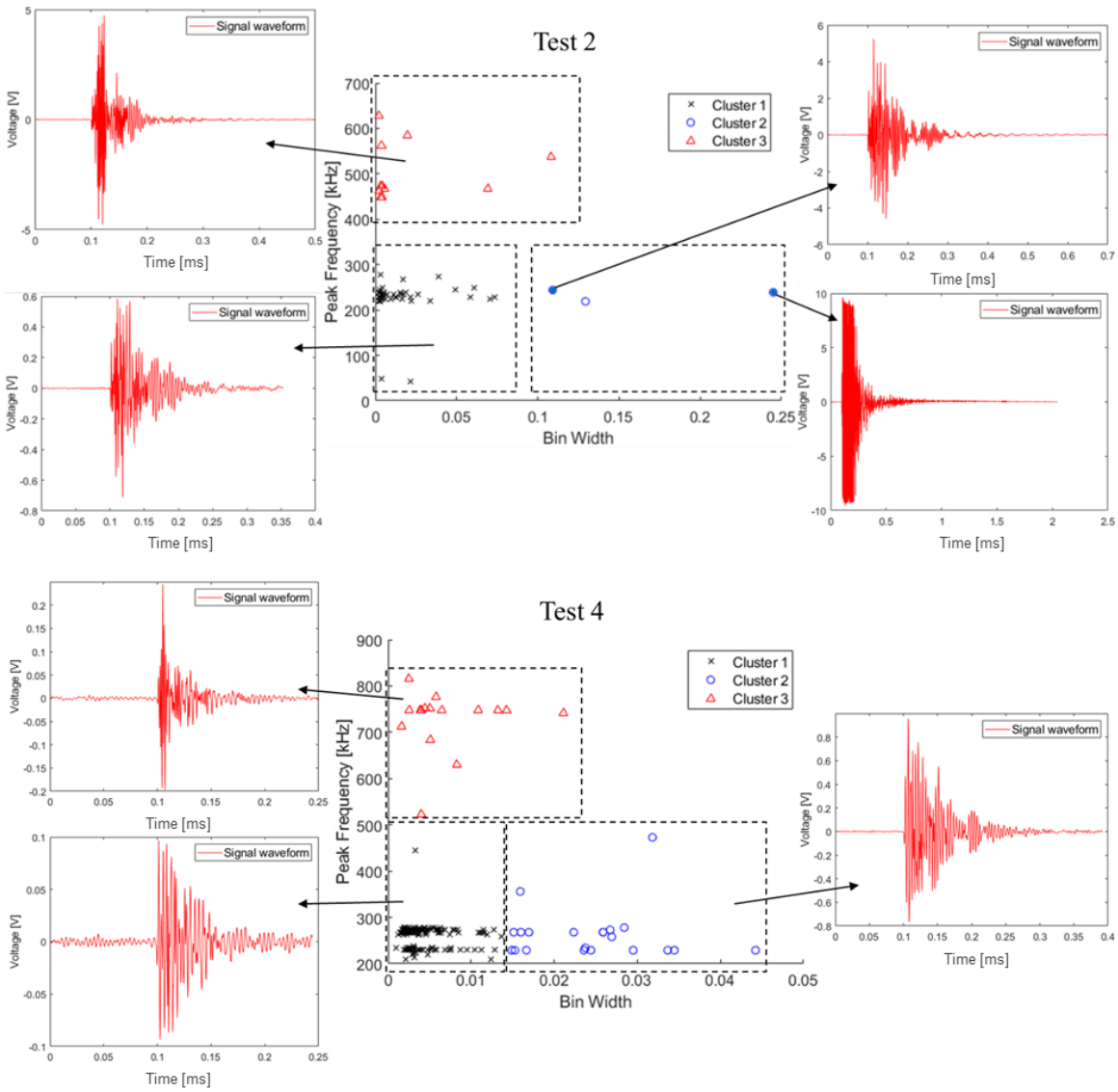

Figure 6-13 – Peak frequency versus bin width in QIS Test 2 (top) and Test 4 (bottom) and the waveforms of signals in each cluster (duration of signal waveform shown varies).

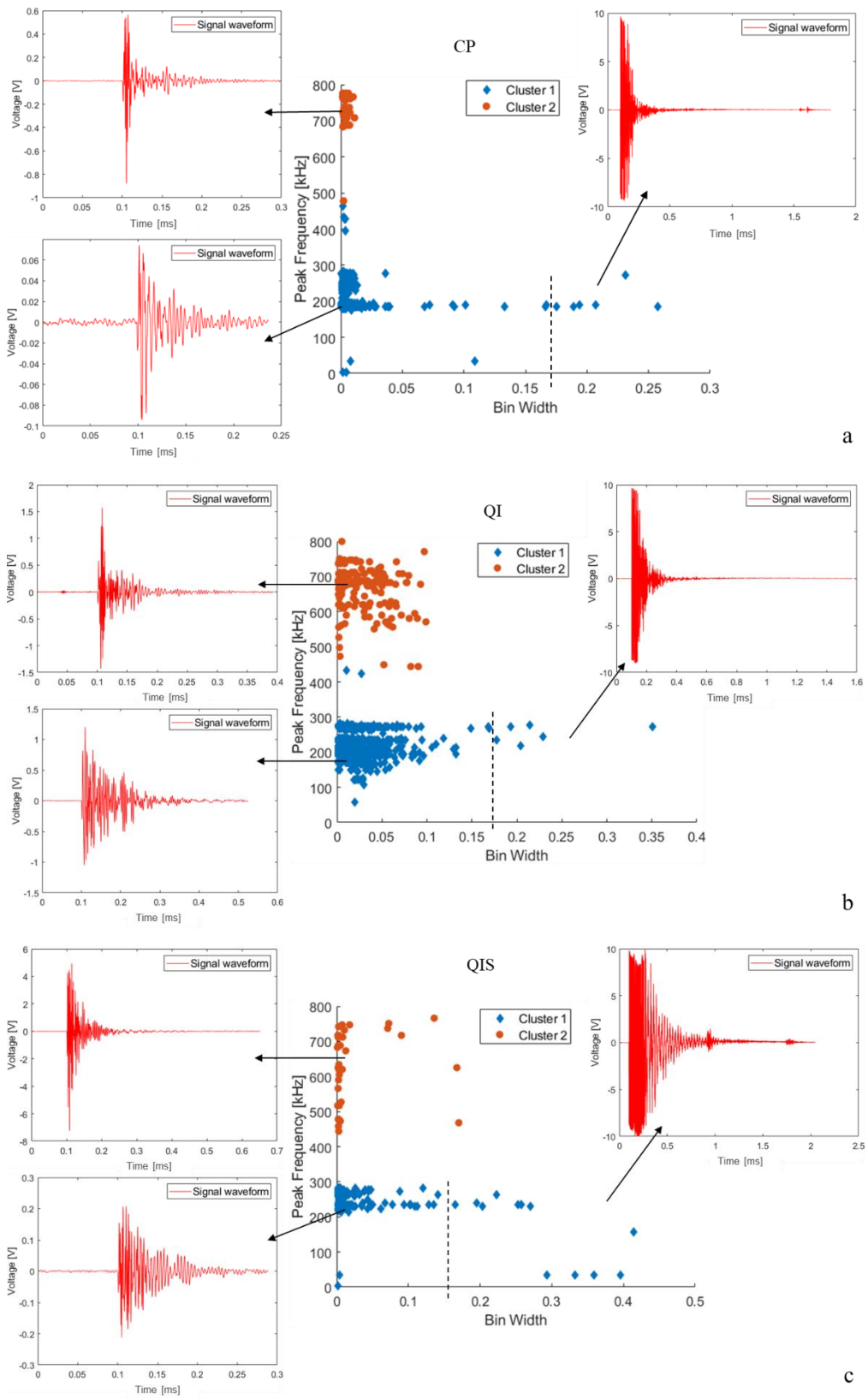

Figure 6-14 - Signal clusters in CP (a), QI (b), and QIS (c) datasets, typical waveforms, and delamination waveforms (duration of signal waveform shown varies).

The delamination related signals are mostly observed in larger specimens. In the QIS dataset, only two tests show this type of signal, while in almost all tests of CP and QI specimens, this type of signal is observed. However, the number of these signals is small in the QI dataset and negligible in the CP dataset compared to other signals. In QIS specimens, the lower cross-section area results in lower stress redistribution chances to cause delamination.

6.5.4. Cluster analysis

The signal clustering results show that regardless of specimen geometry or layup, the clustering based on peak frequency and bin width consistently cluster signals to two clusters with similar characteristics. Cluster 1 in all specimens is associated with peak frequency below 400 [kHz], and cluster 2 is associated with peak frequencies higher than that. Figure 15 shows the distribution of peak frequency in each cluster in one of the tests from each dataset. It is seen that cluster 1 is mostly associated with lower peak frequency values between 0 [kHz] to 400 [kHz], while cluster 2 is associated with peak frequencies of 400 [kHz] to 800 [kHz].

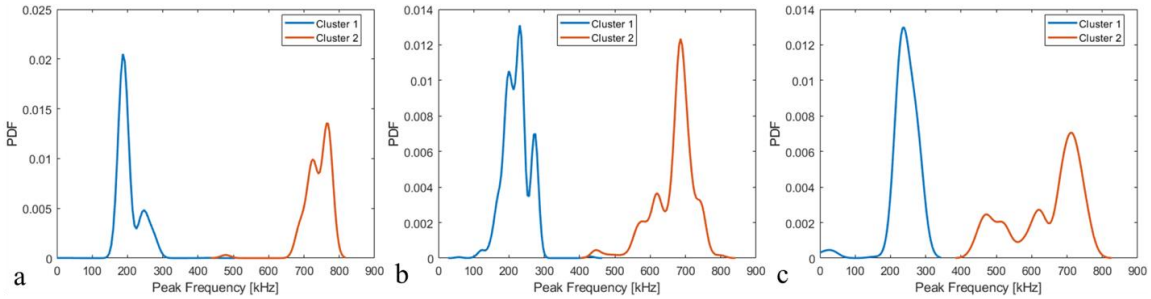

Figure 6-15 - Peak frequency distribution (probability density function – PDF) of the clusters in one of the tests in CP (a), QI (b), and QIS (c) datasets.

The distribution of clusters concerning the load values is shown in Figure 16. This Figure shows that cluster 1 precedes cluster 2 and generally, lower load values are associated with cluster 1.

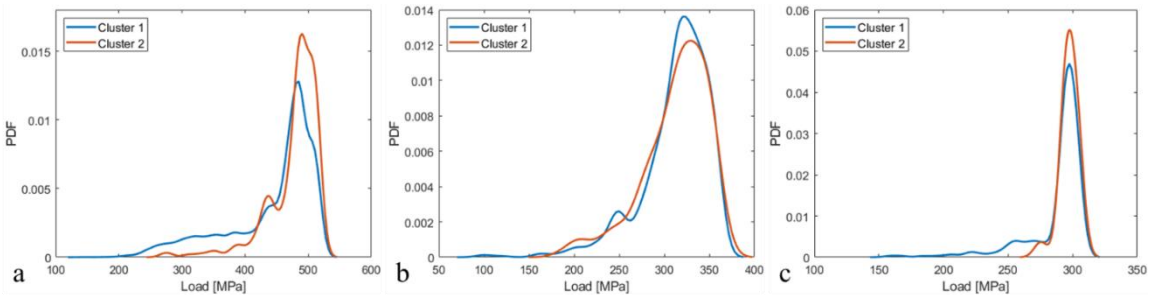

Figure 6-16 - Load distribution (probability density function – PDF) of the clusters in one of the CP (a), QI (b), and QIS (c) tests and their appearing sequence.

Lower peak frequencies are repeatedly related to matrix related damages in literature [1] while higher peak frequencies are attributed to fiber-related damages. Therefore, based on the peak frequency, and the consistent sequence of their appearance with respect to the load values, cluster 1 is attributed to matrix dominated signals and cluster 2 is attributed to fiber dominated signals. Matrix dominated refer to signals with matrix cracking, fiber/matrix debonding and delamination damage mechanisms, and fiber dominated refer to signals with fiber breakage and fiber pull-out damage mechanisms.

6.6. Waveform entropy

The waveform information entropy of signals in both clusters is studied in more detail in this section. First, entropy values of the valid signals in the two clusters are compared to entropy values of noise signals. This comparison describes a range of entropy values in noise and valid signals. Next, the trend of entropy changes in tests, the correlation of entropy values to signal amplitudes, and the distribution of entropy values in each cluster are studied.

6.6.1. Noise signals

Noise signals are the type not generated from the material and are attributed to environmental causes. There are three types of noise signals studied here. The first type is the noise signals recorded at the beginning of tests with the specimen attached to the load cell and no load applied. The threshold is set to a minimum in this case and the purpose of recording these signals is to find an appropriate threshold setting to avoid recording noise signals in a test. The second type of noise signals is recorded before a test and with a proper threshold setting. These signals' amplitude is at the border of the threshold that might pass it. These signals happen sporadically in some tests. The third type of noise signals are associated with amplitude close to the threshold and pass it during the test. These signals (second and third type) are only recorded in the AE sensor close to the actuator that is more susceptible to external noises due to load frame vibrations and hydraulic pressure. Signals in the second and third categories are removed from the AE datasets when techniques such as delta-T filtering are applied. However, to characterize their waveform and compare them to valid signals, their entropy values are studied. Figure 17 shows the typical noise waveforms and their entropy values compared to entropy values of valid signals in a test.

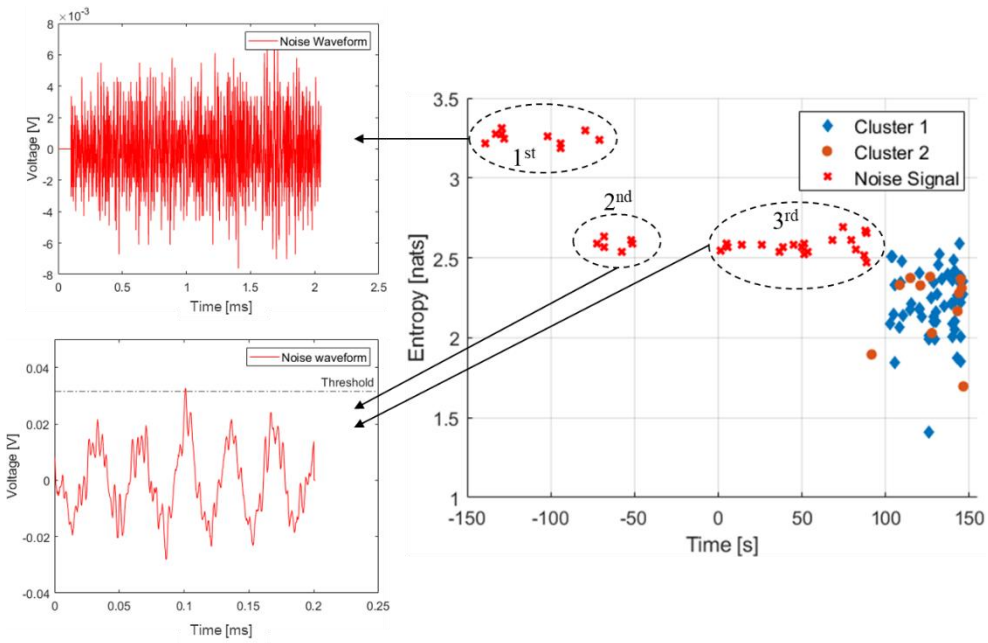

Figure 6-17 - Comparison of the noise signal waveforms and entropy to valid signals

In Figure 17, negative time values associated with the first and second types of noise signals indicate that they are recorded before the test starts. The waveform of the signals in the first type of noise differs significantly from the other two types. The reason is the threshold that is set to minimum, causing timing parameters HDT not to affect. These signals show the highest entropy values. The entropy values for other noise signals are lower than the first type but still are in the higher range of entropy values comparing to the entropy of the valid signals. The similar entropy values in noise signals indicate the similarity in the probability distribution of the underlying waveform and the waveforms. This is in contrast to the entropy values of valid signals and hence their underlying waveform and probability distributions. This behavior is expected and also reported in the literature [27].

6.6.2. Valid signals

The typical trend for waveform entropy of valid signals for one of the tests in each dataset is shown in Figure 18. The loading profile and the signal clusters are also shown in the

figure. It is observed that while waveform entropy of signals in cluster 1 is more centered around specific values, signals in cluster 2, in general, show a higher range of entropy values.

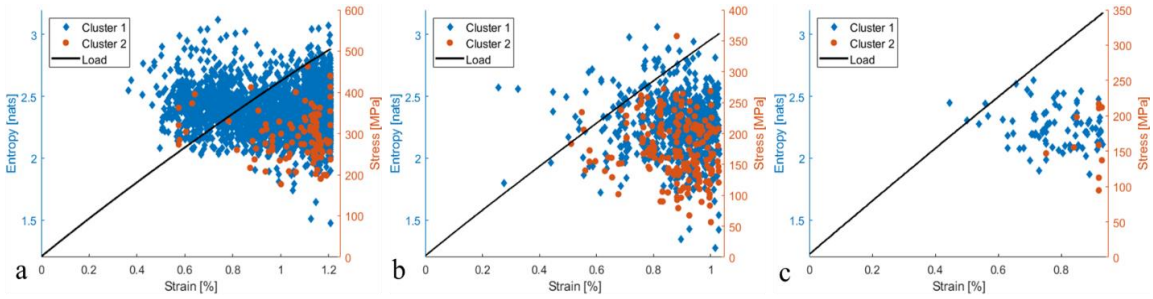

Figure 6-18 - Waveform entropy of valid signals in one test within CP (a), QI (b), and QIS (c) dataset.

Test data represented in Figure 18 show that near the failure time, several signals with low entropy values appear. This behavior is observed in most of the tests in all datasets. These signals tend to be associated with cluster 2. This is expected since this cluster is associated with fiber dominated failures. The delamination-related signals in cluster 1 were also shown to have low entropy values. This suggests that generally, lower entropy values are associated with more severe damage events.

6.6.3. Entropy analysis

To better characterize the behavior of entropy values and their relation to the failure mechanisms, Figure 19 shows the overall behavior of entropy values as a function of amplitude for one test of each dataset. Test data shown in Figure 19 are the same data used in Figure 18.

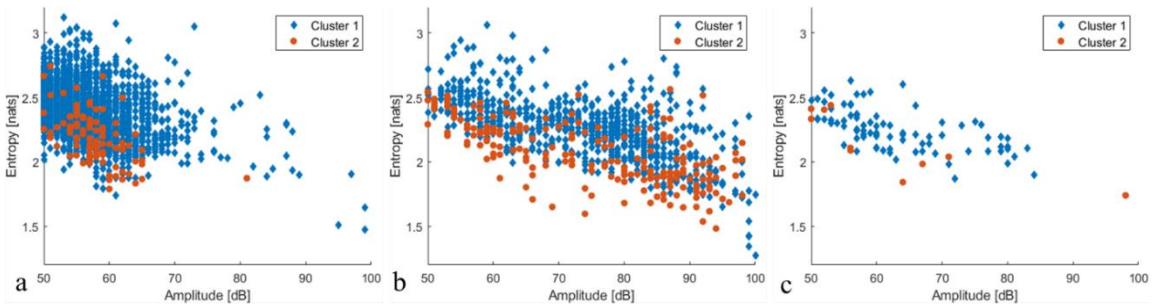

Figure 6-19 - Waveform entropy values of the tests shown in Figure 16 as a function of amplitude in CP (a). QI (b) and QIS (c) dataset.

Figure 19 shows a decreasing trend for entropy values as a function of amplitude. Higher amplitude signals are associated with more severe damages [1]. Therefore, the trend further verifies that lower entropy values are associated with more severe damage events. Figure 20 shows the distribution of entropy values in each cluster. The distribution of entropy values shows that cluster 2 is generally associated with lower entropy values. This is consistent with the conclusion that cluster 2 is representing fiber dominated signals. Figure 20 shows the results for the same tests, as shown in Figure 18.

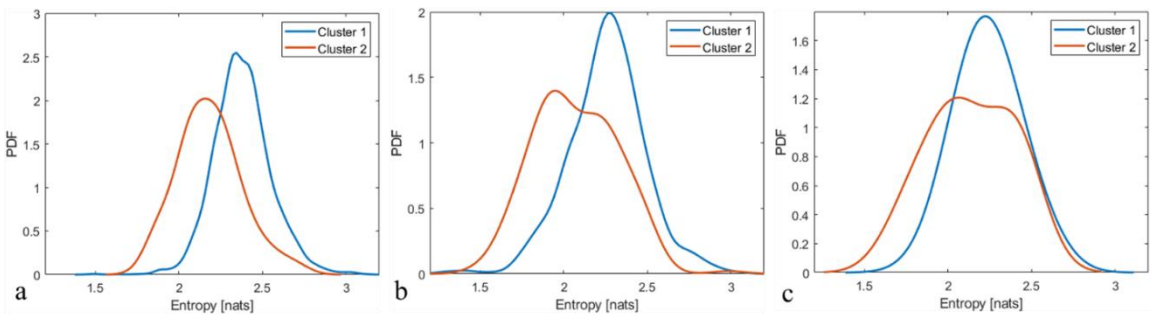

Figure 6-20 - Distribution (probability density function – PDF) of the waveform entropy values in each cluster of the tests shown in Figure 16 in CP (a), QI (b), and QIS (c) dataset.

6.7. Conclusion

The timing and waveform recording parameters play an essential role in the quality of the AE dataset. While some suggestions for timing parameters based on materials are available in the literature, the waveform parameters are not discussed as much. The values for

sampling rate, hit length, and pre-trigger should be selected carefully. Specifically, the pre-trigger value plays an important role in waveform analysis. Since the voltage values recorded in the period are lower than the threshold value, it directly impacts the bin width measurement, waveform distribution, and entropy measurement. Therefore, a pre-trigger value equal to the HDT value for CFRP laminate is suggested in this study.

The selection of bin width to generate a probability distribution for waveforms is usually overlooked. The common practice is the subjectively selected fixed bin width for all the signals. Due to the nature of AE signal sources in FRP materials, selecting a fixed bin width for waveform analysis of all signals does not seem proper. In this study, the bin width for each waveform is selected based on the waveform characteristics and the results are compared to the fixed bin width selection approach. The bin width value is independent of the threshold setting and is measured based on the Scotts equation using all the voltage values in a waveform. This feature is strongly correlated with the conventional time-domain threshold-dependent features of AE signals and used as a time-domain representation of the waveform in clustering. The bin width and peak frequency are used as a new feature set for AE signal clustering. The results show that the proposed feature set can successfully cluster signals into matrix and fiber dominated clusters. Delamination related signals are included in the matrix dominated cluster and characterized by larger bin widths than a suggested value of 0.17. Possible improvement in clustering might be achieved if frequency centroids or partial power frequencies are used instead of peak frequency. The entropy shows to be a robust discriminator of noise signals from valid signals. Noise signals show the highest entropy values, while the entropy decreases as a function of amplitude. This suggests that AE signals due to more severe damages such as

fiber breakage and delamination are associated with lower entropy values. Low entropy values appeared near the failure point in tests and can be regarded as final failure signatures.

6.8. References

[1] M. Saeedifar and D. Zarouchas, "Damage characterization of laminated composites using acoustic emission: A review," *Composites Part B: Engineering*, vol. 195, p. 108039, Aug. 2020, doi: 10.1016/j.compositesb.2020.108039.

[2] M. Ben Ameur *et al.*, "Investigation and identification of damage mechanisms of unidirectional carbon/flax hybrid composites using acoustic emission," *Engineering Fracture Mechanics*, vol. 216, p. 106511, Jul. 2019, doi: 10.1016/j.engfracmech.2019.106511.

[3] M. Haggui, A. El Mahi, Z. Jendli, A. Akrout, and M. Haddar, "Static and fatigue characterization of flax fiber reinforced thermoplastic composites by acoustic emission," *Applied Acoustics*, vol. 147, pp. 100–110, Apr. 2019, doi: 10.1016/j.apacoust.2018.03.011.

[4] E. H. Saidane, D. Scida, M. Assarar, and R. Ayad, "Damage mechanisms assessment of hybrid flax-glass fibre composites using acoustic emission," *Composite Structures*, vol. 174, pp. 1–11, Aug. 2017, doi: 10.1016/j.compstruct.2017.04.044.

[5] H. Q. Ali, I. Emami Tabrizi, R. M. A. Khan, A. Tufani, and M. Yildiz, "Microscopic analysis of failure in woven carbon fabric laminates coupled with digital image correlation and acoustic emission," *Composite Structures*, vol. 230, p. 111515, Dec. 2019, doi: 10.1016/j.compstruct.2019.111515.

[6] A. P. Vassilopoulos and T. Keller, *Fatigue of fiber-reinforced composites*. London ; New York: Springer, 2011.

[7] P. Duchene, S. Chaki, A. Ayadi, and P. Krawczak, "A review of non-destructive techniques used for mechanical damage assessment in polymer composites," *Journal of Materials Science*, Jan. 2018, doi: 10.1007/s10853-018-2045-6.

[8] A. Poudel, S. S. Shrestha, J. S. Sandhu, T. P. Chu, and C. G. Pergantis, "Comparison and analysis of Acoustography with other NDE techniques for foreign object inclusion detection in graphite epoxy composites," *Composites Part B: Engineering*, vol. 78, pp. 86–94, Sep. 2015, doi: 10.1016/j.compositesb.2015.03.048.

[9] F. Dahmene, S. Yaacoubi, M. El Mountassir, N. Bendaoud, C. Langlois, and O. Bardoux, "On the modal acoustic emission testing of composite structure," *Composite Structures*, vol. 140, pp. 446–452, Apr. 2016, doi: 10.1016/j.compstruct.2016.01.003.

[10] B. Wang, S. Zhong, T.-L. Lee, K. S. Fancey, and J. Mi, "Non-destructive testing and evaluation of composite materials/structures: A state-of-the-art review," *Advances in*

Mechanical Engineering, vol. 12, no. 4, p. 168781402091376, Apr. 2020, doi: 10.1177/1687814020913761.

[11] C. Barile, C. Casavola, G. Pappalettera, and V. P. Kannan, "Application of different acoustic emission descriptors in damage assessment of fiber reinforced plastics: A comprehensive review," *Engineering Fracture Mechanics*, vol. 235, p. 107083, Aug. 2020, doi: 10.1016/j.engfracmech.2020.107083.

[12] L. Li, S. V. Lomov, X. Yan, and V. Carvelli, "Cluster analysis of acoustic emission signals for 2D and 3D woven glass/epoxy composites," *Composite Structures*, vol. 116, pp. 286–299, Sep. 2014, doi: 10.1016/j.compstruct.2014.05.023.

[13] N. Godin, S. Huguet, R. Gaertner, and L. Salmon, "Clustering of acoustic emission signals collected during tensile tests on unidirectional glass/polyester composite using supervised and unsupervised classifiers," *NDT & E International*, vol. 37, no. 4, pp. 253–264, Jun. 2004, doi: 10.1016/j.ndteint.2003.09.010.

[14] J. P. McCrory *et al.*, "Damage classification in carbon fibre composites using acoustic emission: A comparison of three techniques," *Composites Part B: Engineering*, vol. 68, pp. 424–430, Jan. 2015, doi: 10.1016/j.compositesb.2014.08.046.

[15] H. A. Sawan, M. E. Walter, and B. Marquette, "Unsupervised learning for classification of acoustic emission events from tensile and bending experiments with open-hole carbon fiber composite samples," *Composites Science and Technology*, vol. 107, pp. 89–97, Feb. 2015, doi: 10.1016/j.compscitech.2014.12.003.

[16] M. G. R. Sause, A. Gribov, A. R. Unwin, and S. Horn, "Pattern recognition approach to identify natural clusters of acoustic emission signals," *Pattern Recognition Letters*, vol. 33, no. 1, pp. 17–23, Jan. 2012, doi: 10.1016/j.patrec.2011.09.018.

[17] M. Azadi, H. Sayar, A. Ghasemi-Ghalebahman, and S. M. Jafari, "Tensile loading rate effect on mechanical properties and failure mechanisms in open-hole carbon fiber reinforced polymer composites by acoustic emission approach," *Composites Part B: Engineering*, vol. 158, pp. 448–458, Feb. 2019, doi: 10.1016/j.compositesb.2018.09.103.

[18] M. Saeedifar, M. A. Najafabadi, D. Zarouchas, H. H. Toudeshky, and M. Jalalvand, "Clustering of interlaminar and intralaminar damages in laminated composites under indentation loading using Acoustic Emission," *Composites Part B: Engineering*, vol. 144, pp. 206–219, Jul. 2018, doi: 10.1016/j.compositesb.2018.02.028.

[19] R. Gutkin, C. J. Green, S. Vangrattanachai, S. T. Pinho, P. Robinson, and P. T. Curtis, "On acoustic emission for failure investigation in CFRP: Pattern recognition and peak frequency analyses," *Mechanical Systems and Signal Processing*, vol. 25, no. 4, pp. 1393–1407, May 2011, doi: 10.1016/j.ymssp.2010.11.014.

[20] P. F. Liu, J. K. Chu, Y. L. Liu, and J. Y. Zheng, "A study on the failure mechanisms of carbon fiber/epoxy composite laminates using acoustic emission," *Materials & Design*, vol. 37, pp. 228–235, May 2012, doi: 10.1016/j.matdes.2011.12.015.

[21] F. E. Oz, N. Ersoy, and S. V. Lomov, “Do high frequency acoustic emission events always represent fibre failure in CFRP laminates?,” *Composites Part A: Applied Science and Manufacturing*, vol. 103, pp. 230–235, Dec. 2017, doi: 10.1016/j.compositesa.2017.10.013.

[22] F. E. Oz, N. Ersoy, M. Mehdikhani, and S. V. Lomov, “Multi-instrument in-situ damage monitoring in quasi-isotropic CFRP laminates under tension,” *Composite Structures*, vol. 196, pp. 163–180, Jul. 2018, doi: 10.1016/j.compstruct.2018.05.006.

[23] E. Maillet, C. Baker, G. N. Morscher, V. V. Pujar, and J. R. Lemanski, “Feasibility and limitations of damage identification in composite materials using acoustic emission,” *Composites Part A: Applied Science and Manufacturing*, vol. 75, pp. 77–83, Aug. 2015, doi: 10.1016/j.compositesa.2015.05.003.

[24] S. F. Karimian, M. Modarres, and H. A. Bruck, “A new method for detecting fatigue crack initiation in aluminum alloy using acoustic emission waveform information entropy,” *Engineering Fracture Mechanics*, vol. 223, p. 106771, Jan. 2020, doi: 10.1016/j.engfracmech.2019.106771.

[25] K. Ono, “Review on Structural Health Evaluation with Acoustic Emission,” *Applied Sciences*, vol. 8, no. 6, p. 958, Jun. 2018, doi: 10.3390/app8060958.

[26] N. Godin, P. Reynaud, and G. Fantozzi, “Challenges and Limitations in the Identification of Acoustic Emission Signature of Damage Mechanisms in Composites Materials,” *Applied Sciences*, vol. 8, no. 8, p. 1267, Jul. 2018, doi: 10.3390/app8081267.

[27] Z. Yang, W. Yan, L. Jin, F. Li, and Z. Hou, “A novel feature representation method based on original waveforms for acoustic emission signals,” *Mechanical Systems and Signal Processing*, vol. 135, p. 106365, Jan. 2020, doi: 10.1016/j.ymssp.2019.106365.

[28] D. Xu, P. F. Liu, and Z. P. Chen, “A waveform clustering method for damage mode identification for composite laminates under hygrothermal environment,” *Engineering Fracture Mechanics*, vol. 239, p. 107290, 2020, doi: 10.1016/j.engfracmech.2020.107290.

[29] F. T. Santo, T. P. Sattar, and G. Edwards, “Validation of Acoustic Emission Waveform Entropy as a Damage Identification Feature,” *Applied Sciences*, vol. 9, no. 19, p. 4070, Sep. 2019, doi: 10.3390/app9194070.

[30] M. Chai, Z. Zhang, and Q. Duan, “A new qualitative acoustic emission parameter based on Shannon’s entropy for damage monitoring,” *Mechanical Systems and Signal Processing*, vol. 100, pp. 617–629, Feb. 2018, doi: 10.1016/j.ymssp.2017.08.007.

[31] C. Sauerbrunn, A. Kahirdeh, H. Yun, and M. Modarres, “Damage Assessment Using Information Entropy of Individual Acoustic Emission Waveforms during Cyclic Fatigue Loading,” *Applied Sciences*, vol. 7, no. 6, p. 562, May 2017, doi: 10.3390/app7060562.

[32] N. Burud and J. C. Kishen, “Damage detection using wavelet entropy of acoustic emission waveforms in concrete under flexure,” *Structural Health Monitoring*, p. 147592172095709, Sep. 2020, doi: 10.1177/1475921720957096.

[33] A. K. Jain, “Data clustering: 50 years beyond K-means,” *Pattern Recognition Letters*, vol. 31, no. 8, pp. 651–666, Jun. 2010, doi: 10.1016/j.patrec.2009.09.011.

[34] “Toray Composite Materials America, Inc.” https://www.toraycma.com/page.php?id=27 (accessed Nov. 30, 2020).

[35] “Toray Composite Materials America, Inc.” https://www.toraycma.com/page.php?id=661 (accessed Nov. 30, 2020).

[36] O. J. Nixon-Pearson and S. R. Hallett, “An experimental investigation into quasi-static and fatigue damage development in bolted-hole specimens,” *Composites Part B: Engineering*, vol. 77, pp. 462–473, Aug. 2015, doi: 10.1016/j.compositesb.2015.03.051.

[37] O. J. Nixon-Pearson and S. R. Hallett, “An investigation into the damage development and residual strengths of open-hole specimens in fatigue,” *Composites Part A: Applied Science and Manufacturing*, vol. 69, pp. 266–278, Feb. 2015, doi: 10.1016/j.compositesa.2014.11.013.

[38] M. Kharrat, E. Ramasso, V. Placet, and M. L. Boubakar, “A signal processing approach for enhanced Acoustic Emission data analysis in high activity systems: Application to organic matrix composites,” *Mechanical Systems and Signal Processing*, vol. 70–71, pp. 1038–1055, Mar. 2016, doi: 10.1016/j.ymssp.2015.08.028.

[39] M. Kharrat, V. Placet, E. Ramasso, and M. L. Boubakar, “Influence of damage accumulation under fatigue loading on the AE-based health assessment of composite materials: Wave distortion and AE-features evolution as a function of damage level,” *Composites Part A: Applied Science and Manufacturing*, vol. 109, pp. 615–627, Jun. 2018, doi: 10.1016/j.compositesa.2016.03.020.

[40] D. W. Scott, “On optimal and data-based histograms,” *Biometrika*, vol. 66, no. 3, pp. 605–610, 1979.

[41] M. P. Wand, “Data-Based Choice of Histogram Bin Width,” *The American Statistician*, vol. 51, no. 1, pp. 59–64, 1997.

[42] A. Ben-Naim, “Entropy, Shannon’s Measure of Information and Boltzmann’s H-Theorem,” *Entropy*, vol. 19, no. 2, p. 48, Jan. 2017, doi: 10.3390/e19020048.

[43] Shannon, Claude Elwood., “A Mathematical Theory of Communication,” *Bell system technical journal*, vol. 27, no. 3, pp. 379–423, 1948.

[44] P. J. Rousseeuw, “Silhouettes: A graphical aid to the interpretation and validation of cluster analysis,” *Journal of Computational and Applied Mathematics*, vol. 20, pp. 53–65, Nov. 1987, doi: 10.1016/0377-0427(87)90125-7.

[45] D. L. Davies and D. W. Bouldin, “A Cluster Separation Measure,” *IEEE Trans. Pattern Anal. Mach. Intell.*, vol. PAMI-1, no. 2, pp. 224–227, Apr. 1979, doi: 10.1109/TPAMI.1979.4766909.

[46] “The MathWork Inc, Matlab. Matlab R2020a user’s manual.” 2020.

[47] B. G. Green, M. R. Wisnom, and S. R. Hallett, “An experimental investigation into the tensile strength scaling of notched composites,” *Composites Part A: Applied Science and Manufacturing*, vol. 38, no. 3, pp. 867–878, Mar. 2007, doi: 10.1016/j.compositesa.2006.07.008.

Chapter 7: Acoustic emission signal waveform information entropy analysis in open-hole CFRP laminates under fatigue loading[1]

7.1. Abstract

Acoustic Emission (AE) is one of the most well-known non-destructive testing (NDT) techniques and its use on fiber-reinforced polymers (FRP) has been under extensive study in the past decades. Most of the available methods rely on using the conventional features of AE signals for analysis. However, conventional AE features are derived from a portion of the signal waveform that passes through a pre-determined threshold and is heavily affected by attenuation. Therefore, recent studies on AE are more focused on waveform analysis. An AE waveform analysis technique that has recently gained attention is Shannon's information entropy. This study discusses the analysis of the information entropy of the AE signals emitted during tensile fatigue testing of open-hole carbon FRP (CFPR) specimens. A signal clustering based on waveforms' characteristics is performed. Results show that AE waveform entropy is a robust time-domain feature that can discriminate signals independent of threshold setting. It is observed that signals with high information entropy values are related to fatigue crack surface fretting, while signals with low entropy are mostly related to severe fatigue damage cases.

7.2. Introduction

The industrial use of composite materials has been increasing steadily over the past three decades. In composites, two or more components are combined to achieve properties

[1] The full-text of this chapter forms a paper currently (i.e., April 2021) submitted to the Materials Evaluation journal.

superior to each of them individually. These materials offer a wide variety of properties regarding their constituent parts and manufacturing processes. Some of their properties and characteristics have motivated industries, such as the aerospace industry, to replace conventional metallic alloys with composites. Uses of the fiber-reinforced polymer (FRP) laminated composites have been the most pervasive due to their superior stiffness, strength, corrosion resistance, density, and fatigue life. The ability to exploit the full potential of lightweight FRP laminated composite structures has been hindered by a lack of a methodology for non-destructively testing (NDT) and quantifying fatigue damage independent of the conditions under which structures are used. Fatigue damage is a complex problem in FRP materials. A variety of damage mechanisms such as matrix cracking, fiber/matrix debonding, delamination, and fiber breakage are present in FRP laminated composites [1]. These damage mechanisms happen in different length scales and the synergy between them ultimately leads to fracture.

The use of various NDT techniques for damage assessment in polymer composites is reviewed by Duchene et al. [2]. The application of NDT techniques to characterize damage evolution shows that Acoustic Emission (AE) can detect all the failure mechanisms. AE is a well-known NDT technique that has been used extensively on composites [3]–[5]. This technique only requires small sensors that detect activity inside the material. Structural changes and internal redistribution of stress within the material result in energy release. Part of this energy is released in the form of AE signals [6]. The use of the AE technique on FRP composite materials under fatigue loading has already been addressed, such as in references [7]–[11]. The size of the AE signal dataset that generates as a result of a fatigue test, specifically in carbon FRP (CFRP) materials, is usually in the order of million signals

[12]. This makes uses of the technique challenging [13]. Additionally, the dependence of damage progression on laminate layup [14], [15] requires careful selection of layup to draw general conclusions.

Studies based on AE typically use a combination of signal features such as count, rise time, energy, duration, peak frequency, and amplitude for analysis [5]. However, some of these features are derived from a portion of the signal waveform that passes through a pre-determined threshold and is adversely affected by the wave propagation medium and attenuation characteristics [16]. This is significantly more pronounced in fatigue damage assessment as the progression of damage causes wave distortion and increases the signal attenuation [17]. Techniques based on AE waveform analysis have the potential to mitigate the effect of threshold setting on AE analysis [18]. For instance, Ebrahimkhanlou et al. [19] have recently proposed a deep-learning framework that automatically extracts features of the AE waveform and performs source localization. The effectiveness of their framework is shown on an actual fuselage panel.

An AE waveform analysis technique that recently has gained attention is Shannon information entropy [20], [21]. AE waveform information entropy relies on the information content of the distribution of emitted AE signals (described by the waveforms). Comparing to the conventional features, AE waveform information entropy is a more integral measure of information content in a signal and eliminates the effect of threshold on analysis. It uses the signal distribution characteristics to measure the information content of the signal. Consequently, it quantifies damage, independent of conventional AE signal features, which depend on experimental and loading conditions. Chai et al. [22] used the AE information entropy and showed that the cumulative energy, counts, and entropy evolve similarly with

time. Sauerbrunn et al. [23] suggested that waveform information entropy would be a better index of damage than count and energy. Recently, this paper's authors [24] have shown that AE entropy can be used to detect crack initiation in fatigue loading of aluminum specimens.

In this study, information entropy is used to characterize AE signal waveforms emitted from open-hole CFRP specimens under tensile fatigue loading. Fatigue loading follows a step-stress method to shorten the fatigue life and consequently reduce the volume of AE signals. Several fatigue loadings were employed, and the resulting AE signals were clustered based on their waveform characteristics in time- and frequency-domains. Finally, AE waveform entropy values were studied and compared to the fatigue damage index.

7.3. Experimental procedure

7.3.1. Material, geometry, layup, and failure mode

Specimens used in this study are cut using a CNC Routing machine from the same sheet of CFRP material. The laminated sheet follows a layup sequence of $[45/90/-45/0]_{2s}$ with a total of 16 plies. Each ply is made up of high-performance unidirectional pre-preg sheets with Toray T700G fibers [25] and Toray 2510 pre-preg system [26] with a 65% fiber volume density. Figure 1 shows the geometry of the specimens, their dimensions, and AE sensor placement. Compared to the ASTM D5766 standard, specimens were decreased in width to increase the stress concentration around the hole, which better follows the industrial test standards [27]. The selected geometry follows the geometry of the specimen in [28] with the length increased to avoid excessive noise recording in the AE sensors. Aluminum tabs with a 45° angle at the tip were used over at the gripping area. Tests were monitored around the hole using an 8 [MP] Point Grey Flea3 sensor with a 3.8-13 [mm]

Fujinon lens. Figure 2 shows the experimental setup and failure mode in two specimens at the time of fracture. The failure mode is a pull-out failure, similar to the tensile failure mode, but with more presence of delamination.

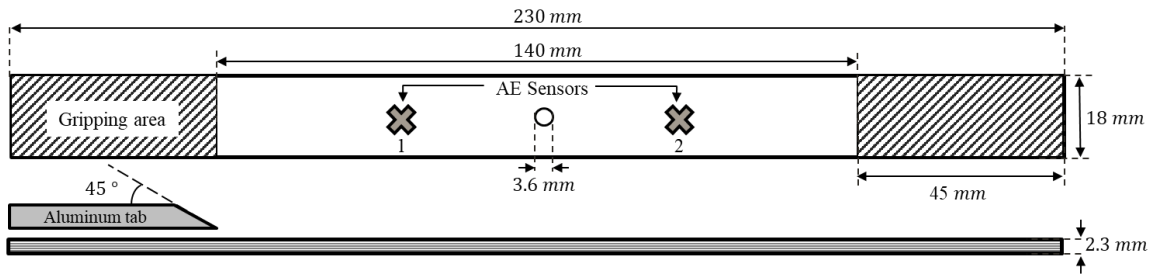

Figure 7-1 - Specimen geometry and dimensions

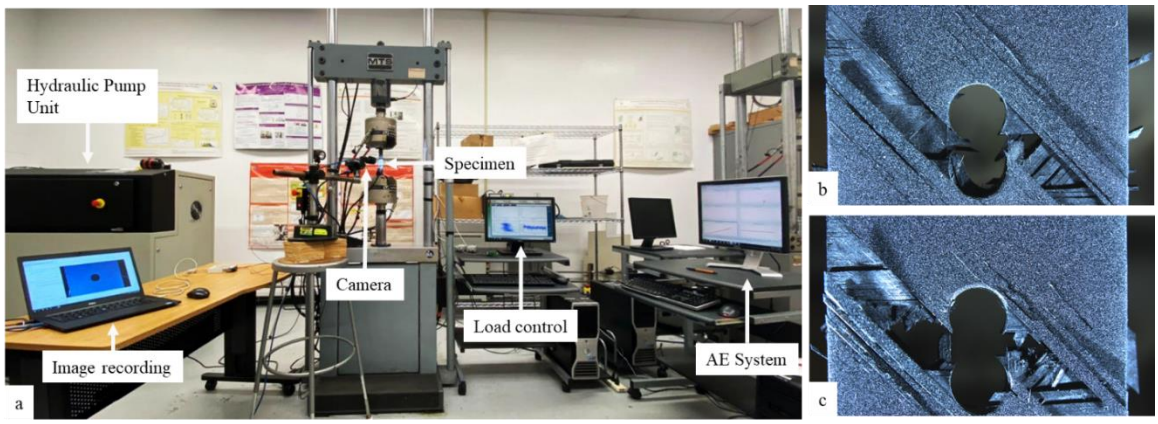

Figure 7-2 - Tests setup (a) and failure modes in tests T06 (b) and T07 (c)

7.3.2. Loading conditions

A servo-hydraulic material testing system (MTS) machine retrofitted with an Instron 8800 controller was used to perform the tests. All the specimens were fatigued with a step-stress loading condition. At each loading step, specimens were fatigued for a predetermined number of cycles, and then the test was paused, and the specimens were temporarily unloaded. Upon reloading, a quasi-static loading rate of 0.2 [kN/s] was applied until the mean desired stress of the next step was achieved. All fatigue loadings were performed at a stress ratio of 0.1 and a frequency of 10 [Hz]. Figure 3-a shows the loading procedure in the tests. Each loading interval consisted of a loading step of 2,500 cycles, and the stress

level was increased every two loading intervals. Figure 3-b shows the σ_{max} of the loading intervals for the five different loading conditions used in this study. Tests were performed and continued until fracture. The tests' loading profiles, failure cycles and σ_{max} at the failure cycle are listed in Table 1.

7.3.3. AE setup

Two AE wideband (WD) differential sensors from Physical Acoustics Corporation (MISTRAS Group, Princeton Junction, NJ) on a PCI-2 board, with an operating frequency range of 125 – 1000 [kHz] and a resonance frequency of 450 [kHz], were used to record AE signals. Ultrasonic gel couplant was used on the AE sensors' surface to improve attachment and signal recordings. Sensors were placed approximately 25 [mm] away from the hole, and the vinyl tape was used for attachment. Signals were passed through a 40 [dB] pre-amplifier before reaching the data acquisition module. The Physical Acoustics AEwin software (Physical Acoustic Corporation, Version E5.60, MISTRAS Group, Princeton Junction, NJ, 2007) was used to record AE signals. The band-pass filter was set to 1 [kHz]–3 [MHz]. The time it takes for one signal to travel from one sensor to other (delta-T) was measured on all specimens before applying any load. This value was then used to remove all the signals that arrived from locations other than the hole area. Only the signals that passed the delta-T filtering (i.e., valid signals) are used for analysis in this study. Table 2 shows the statistics of the total number of signals recorded in both sensors, the number of signals recorded in Sensor 2 (Channel 2), and the valid signals that passed the delta-T filtering and are used in the analysis.

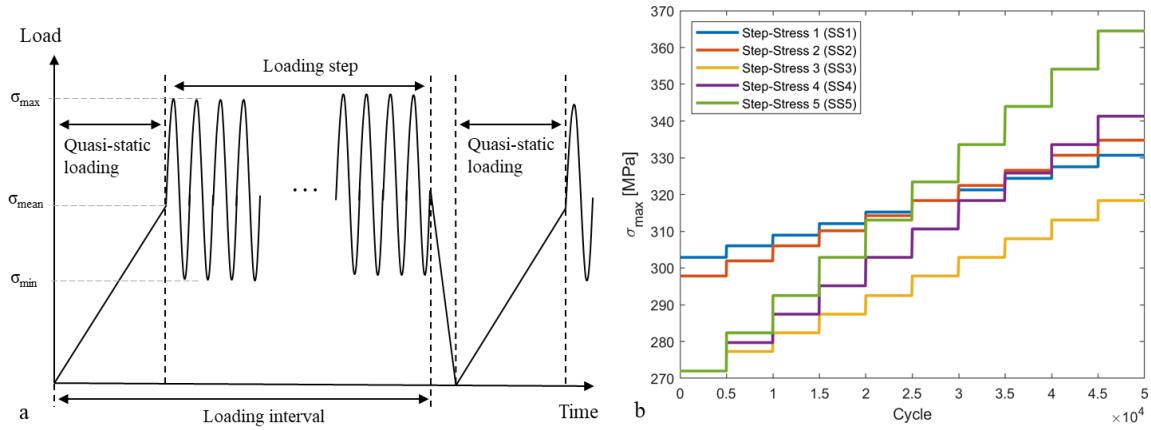

Figure 7-3 - Loading sequence (a) and step stress values (b)

Table 7-1 - Tests loading condition and failure cycles

Tests #	Loading profile	Failure cycle	σ_{max} at failure [MPa]
T01	SS1	99,437	361
T02	SS2	90,570	371
T03	SS3	108,556	379
T04	SS3	72,627	344
T05	SS4	20,402	303
T06	SS4	71,277	380
T07	SS4	65,805	372
T08	SS5	40,241	354
T09	SS5	50,621	374
T10	SS5	71,865	415

Table 7-2 - Statistics of the AE signals in all tests

Tests #	Total # of signals in a test	# of signals in Ch2	# of valid signals in Ch2
T01	3,843,597	1,610,028	347,300
T02	3,957,967	1,781,724	403,202
T03	4,092,357	1,905,710	640,202
T04	3,032,376	1,123,312	286,888
T05	966,549	352,120	99,278
T06	4,231,685	1,752,735	451,556
T07	2,905,889	1,066,363	229,392
T08	1,667,890	737,857	165,867
T09	1,679,587	754,616	160,070
T10	4,326,064	2,043,722	423,202

As shown in Table 2, AE signals for each test generated a large dataset to be carefully analyzed. Data from both channels are used for delta-T filtering. However, only the signals recorded in Channel 2 (Ch2) were used for analysis. This sensor was placed further from the actuator and thus was less prone to noises caused by high-pressure hydraulic fluid vibrations.

7.3.4. AE signals and waveforms

AE signals in this study were measured by applying a threshold of 52 [dB]. This threshold value was found by mounting specimens to the load frame and measuring background AE signal amplitudes, while no load was applied. Signals are defined by timing parameters peak definition time (PDT), hit definition time (HDT), hit lockout time (HLT), and max duration. The values for the timing parameters in this study are followed by the AEWin software manual suggestions, reference [29], and based on the pencil lead break (PLB) tests. They were selected as 60 [μs], 100 [μs], 300 [μs], and 200 [ms] for PDT, HDT, HLT, and max duration, respectively. To minimize the chance of missing any emitted signal, the HLT value was set to its minimum. A sample waveform showing the timing parameters and some conventional AE features is shown in Figure 4. In this figure, the HLT appears as a series of zero voltages with a dashed line following the HDT window in the waveform.

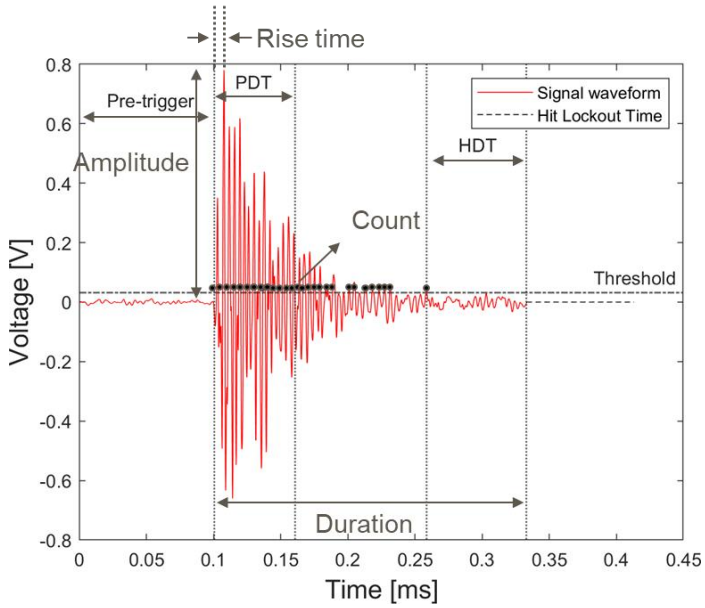

Figure 7-4 – A sample AE waveform, timing parameters, and some time-domain features

The waveform of a signal is generated based on the sampling rate, pre-trigger time, and hit length. A sampling rate of 2 [MHz] or higher is suggested for waveform analysis of CFRP materials [30] and a 5 [MHz] sampling rate is frequently used [17], [31]. A sampling rate of 5 [MHz] was selected for this study. The value for the pre-trigger in this study is equal to the HDT parameter, 100 [µs]. The hit length determines the data points recorded for a waveform. It was initially set to 10,240 (10k) data points that resulted in a waveform with a maximum duration of 2048 [µs]. However, after the preliminary analysis of the first two tests showed the presence of longer signals, the hit length was increased to the maximum allowable value of 15,360 (15k) data points. This change resulted in waveform recording of signal with durations up to 3072 [µs]. The initial waveform settings resulted in missing to record the full waveforms of an average of 1.45% of valid signals in the first two tests. However, the increase in hit length resulted in recording the full waveforms in almost all valid signals of the rest of the tests. All the signals with partial waveforms are removed from the analysis.

7.4. Method

7.4.1. Fatigue damage index

The fatigue damage index is measured based on dynamic modulus reduction and modeled with the Mao-Mahadevan [32] equation. The modulus is measured during fatigue loading using Equation 1:

$$E = \frac{F_{max}\, L}{\delta\, A} = \frac{F_{max}}{\varepsilon\, A} \qquad (1)$$

in which L is the gauge length (shown in Figure 1), and A is the gross cross-section area, neglecting the hole. F_{max} is the maximum load in the cycle, and δ is the specimen extension as the maximum load. Note that the modulus measurement based on tensile loading at the beginning of loading intervals shows lower values. This is due to the material's response to the loading rate, in which a higher loading rate results in higher strength with lower strain values (higher modulus) and vice versa [33]. This is further discussed in [34] and [35]. The fatigue damage index is defined using Equation 2:

$$D(n) = \frac{E_0 - E(n)}{E_0 - E_f} \qquad (2)$$

in which E_0 is the initial modulus of a healthy component, E is the modulus in each cycle n and E_f is the final modulus measurement before fracture. The damage index is modeled using the Mao-Mahadevan [32] shown by Equation 3:

$$D^*(n) = q\left(\frac{n}{N_f}\right)^{m_1} + (1-q)\left(\frac{n}{N_f}\right)^{m_2} \qquad (3)$$

in which q, m_1 and m_2 are material dependent parameters, N_f is the fracture cycle, and n is the cycle at which the damage index is measured. The modeled damage index is used as the damage index in this study. The result of applying Eq. 3 on the experimental data measured using Eq. 2 is shown in Figure 5. The damage index shows a three-stage fatigue life in which the rate of damage index is high in the first and last stage while the damage increase is gradual in the second stage.

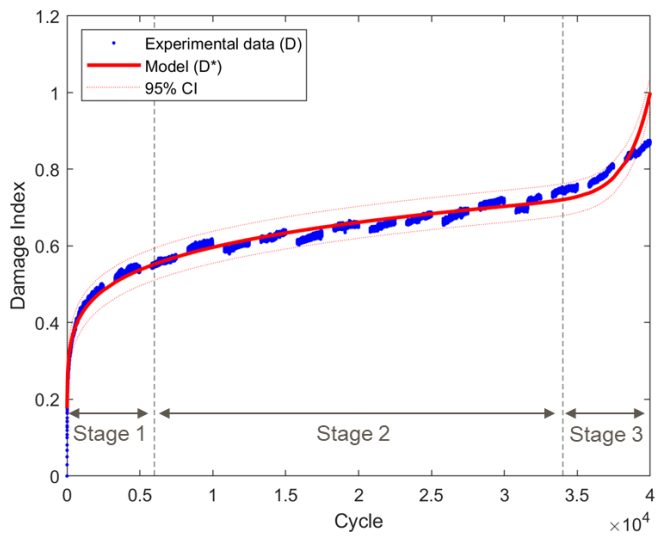

Figure 7-5 - Experimental and modeled damage index in T08

7.4.2. AE waveform analysis and information entropy measurement

The waveform of an AE signal is used to measure the information entropy based on Shannon [36] entropy:

$$I = c \sum_{i=1}^{n} P(V_i) \ln(1/P(V_i)) \qquad (4)$$

in which $V_i = \{v_1, v_2, \dots, v_n\}$ is the voltage values of the waveform (random variable), $P(V_i)$ is the probability distribution of the voltage, I is the information entropy, and c is a constant considered to be unity in this study. The unit of AE information entropy in this

study is 'nats' since Equation 4 uses the natural logarithm. According to the information entropy, uniform distributions have the highest information entropy since no value is preferred. Meanwhile, biased distributions have lower information entropy (or missing information) since some values are associated with higher probabilities. An inherent assumption in Eq. 4 requires that all values of the random variable are assigned with a probability of less than or equal to one, and the summation of all the probability values in the random variable equals one. Histogram of a random variable satisfies the requirements of Shannon entropy assumptions and is used in this study as the non-parametric distribution of the voltage values. The selection of an appropriate bin width to generate a histogram for a random variable is studied in the literature by Scott [37]:

$$b_n = k\delta n^{-1/3} \qquad (5)$$

where b_n is the appropriate bin width, k is a constant, given as $k = 3.49$, δ is the standard deviation of the random variable, and n is the number of data points in the random variable. This equation has the inherent assumption that the underlying distribution of the random variable follows a Gaussian distribution. To correct the assumption, two correction coefficients based on the difference in skewness and kurtosis of the actual distribution and Gaussian distribution are used:

$$b_c = b_n \times C_{sk} \times C_{kur} \qquad (6)$$

in which C_{sk} and C_{kur} are the correction coefficients for skewness and kurtosis difference, respectively, given in Scott [37], and b_c is the corrected bin width. The selection of a bin width to generate a histogram based on the signals' waveform rather than using a fixed bin width value for all signals is previously discussed by this paper's authors in [38]. It is

shown that this approach results in bin width to be a time-domain parameter that is independent of the threshold setting. The correlation coefficient of bin width to the time- and frequency-domain features of signals is shown in Figure 6.

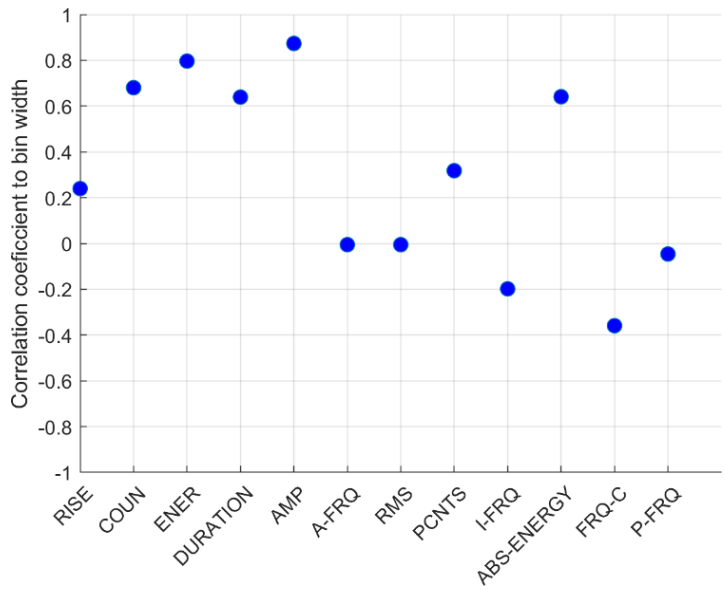

Figure 7-6 - Average correlation coefficient of AE signal features to bin width in all tests

The correlation coefficient of bin width in all tests is found, and the average values in all tests are shown in the figure. Figure 6 shows that while bin width is well correlated to frequently used time-domain features such as energy, duration, and amplitude, it is independent of frequency-domain features.

7.4.3. Signal clustering

AE signal clustering is performed based on k-means clustering. The k-means is the most widely used clustering technique in the AE analysis of laminated composites [18]. This technique partitions input signals with d-dimensional features to k clusters with $C = \{c_1, \dots, c_K\}$ centroids by minimizing the input distances of signals to these centroids. The metric used in this study for clustering is the Euclidean distance. The features used in clustering are bin width and peak frequency. As shown in Figure 6 and discussed in detail

by this paper's authors in [38], bin width is strongly correlated to the conventional time-domain features of AE signals, making it an excellent choice to present time-domain properties of AE signals and results in redundancy reduction. Also, peak frequency is a broadly accepted and commonly used parameter to represent the frequency-domain of signals. Therefore, bin width and peak frequency of signals are used for clustering. The possible number of clusters examined are $k \in [2,8]$ and the Silhouette value [39] is used to measure the performance of clustering given a choice of k. Davis Bouldin (DB) [40] values are also used for cluster performance measurement to verify Silhouette values. Features are normalized to the range of [0 1] before clustering, and the clustering procedure is repeated 10 times to avoid local minima. Figure 7 shows the optimum number of clusters.

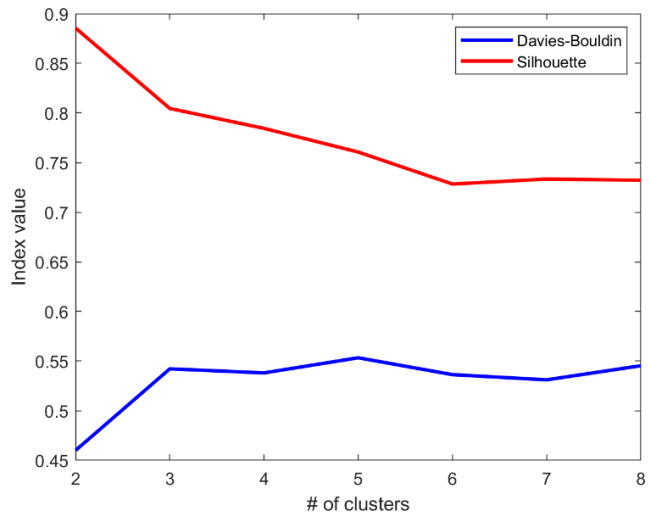

Figure 7-7 - Optimum number of clusters based on Silhouette and DB indexes.

The results shown in Figure 7 are the average of Silhouette and DB values for a cluster number in all tests. It is seen that similar to AE signals of the same material in tensile testing reported in [38], the optimum number of clusters is found to be 2.

7.5. Results and discussion

The AE signal clustering results from two tests are shown in Figure 8. As it is evident from the figure, there are two types of clustering observed in the dataset. A total of 4 tests show clusters displayed in Figure 8-a (type-a), in which clusters are distinctly separate considering the bin width values. However, 6 tests show clusters shown in Figure 8-b (type-b), in which clusters are distinctly separate with respect to their peak frequency range. To investigate this further, two more clustering feature sets were considered. In one, only peak frequency was used for clustering, and in the other, only the bin width values were employed. Comparison of the resulting clusters shows that for tests with type-a clustering, the bin width was the dominant feature, while in tests with type-b clustering, the dominant feature was the peak frequency.

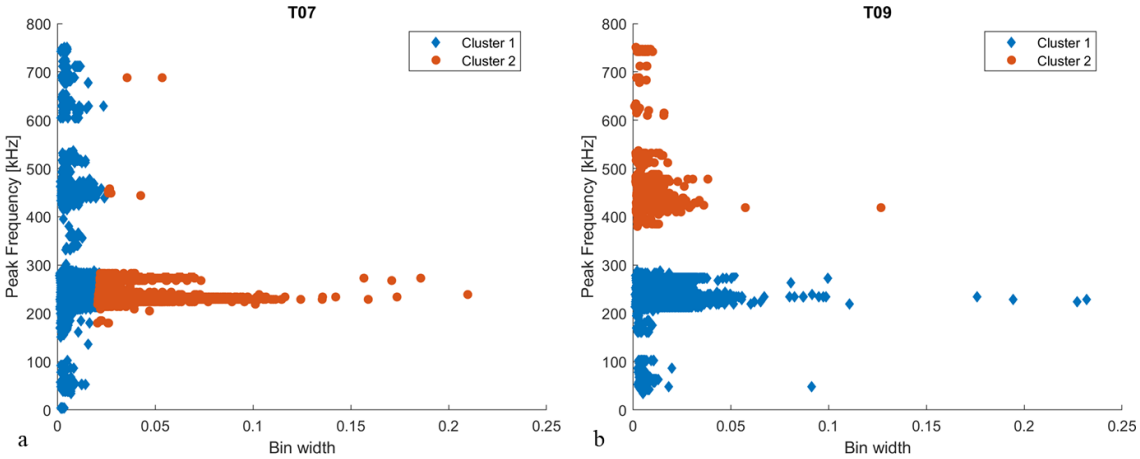

Figure 7-8 - Signal clustering results in T07 (a) and T09 (b)

The two types of clustering indicate that the time-domain and frequency-domain features are competing factors in clustering. Therefore, for the case fatigue test, it is not possible to correlate clusters to their underlying failure mechanisms based on the frequency range of a cluster [41]. This observation can be correlated to the fact that fatigue loading generates multiple stress concentrations and damages within a specimen. These factors can result in

failure mechanisms to emit signals with different signatures than the ones usually expected [42]. Nevertheless, regardless of the clustering type, the number of signals in Cluster 2, on average, is only about 8% of all the signals. Figure 9 shows the share of signals in each cluster for all the tests. In the remainder of the study, tests with type-a clustering were marked by an asterisk.

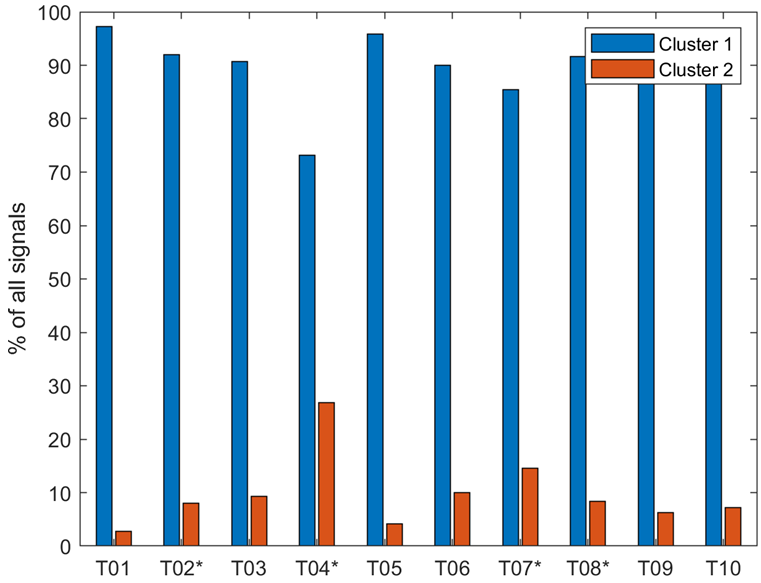

Figure 7-9 - Proportion of signals with respect to their cluster label

Figure 10 shows the trend of entropy values as a function of bin width in two tests and displays waveform shapes of some signals. It is seen that, as expected, the entropy values decrease as the bin width increases. There are two areas of the figure that were further explored. First, it was observed that signals with entropy values of 3 [nats] and higher mainly were associated with cluster 1. The typical waveform of some of these signals is displayed in Fig. 10. These waveforms show multiple spikes and appear to be related to matrix failure and generated due to crack surface fretting in fatigue loading. The peak frequency range for these signals is less than 300 [kHz]. Second, the signals with large bin width values were analyzed. The typical waveform of these signals is shown in Fig. 10.

Signals with similar waveforms and bin width values have previously been found in tensile tests and were related to delamination by the authors of this study [38]. These signals are associated with low entropy values and can be associated with either of the clusters. This association seems to be dependent on the clustering characteristics of the tests performed. The peak-frequency range for these signals is mainly within a narrow range of 225 - 275 [kHz].

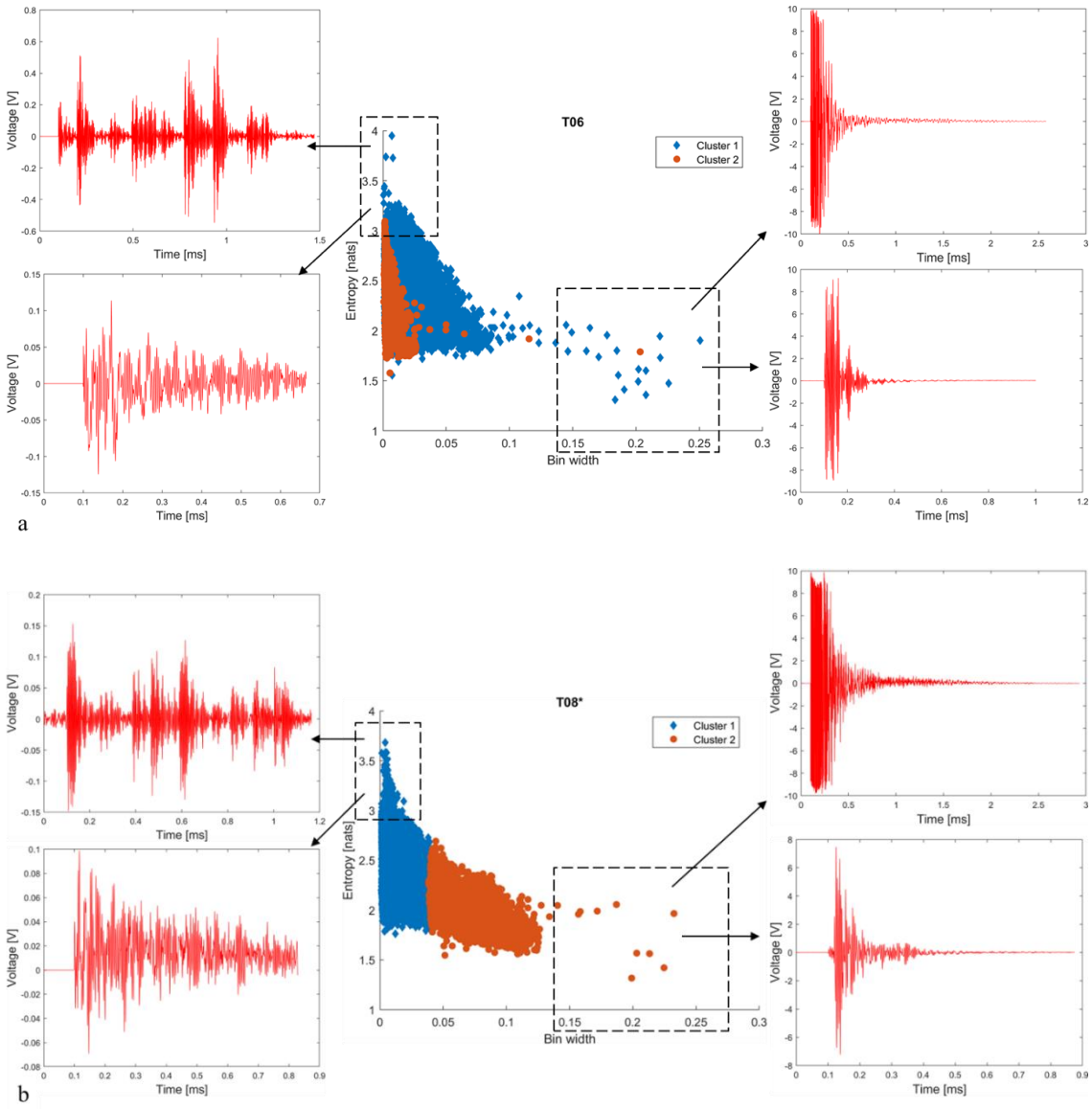

Figure 7-10 - Entropy of signals versus bin width values and the typical waveforms of signals in a region in T06 (a) and T08 (b)

Figure 11 shows the trend of entropy values in four different fatigue tests with the damage index shown on the right y-axis, and signals with large bin width are marked. Figure 11 shows that regardless of the classification type, signals in cluster 2 are associated with lower entropy values. The three-stage of fatigue life for the damage rate is marked with vertical dashed lines on the figures. It is seen that the large bin width signals are usually associated with large increases in the damage, indicating that they are associated with severe damage. Also, it is observed that entropy values reach lower values in the first and last stage of the fatigue life, where the damage rate (modulus reduction rate) is high. Therefore, low entropy values can be attributed to more severe damages to the material.

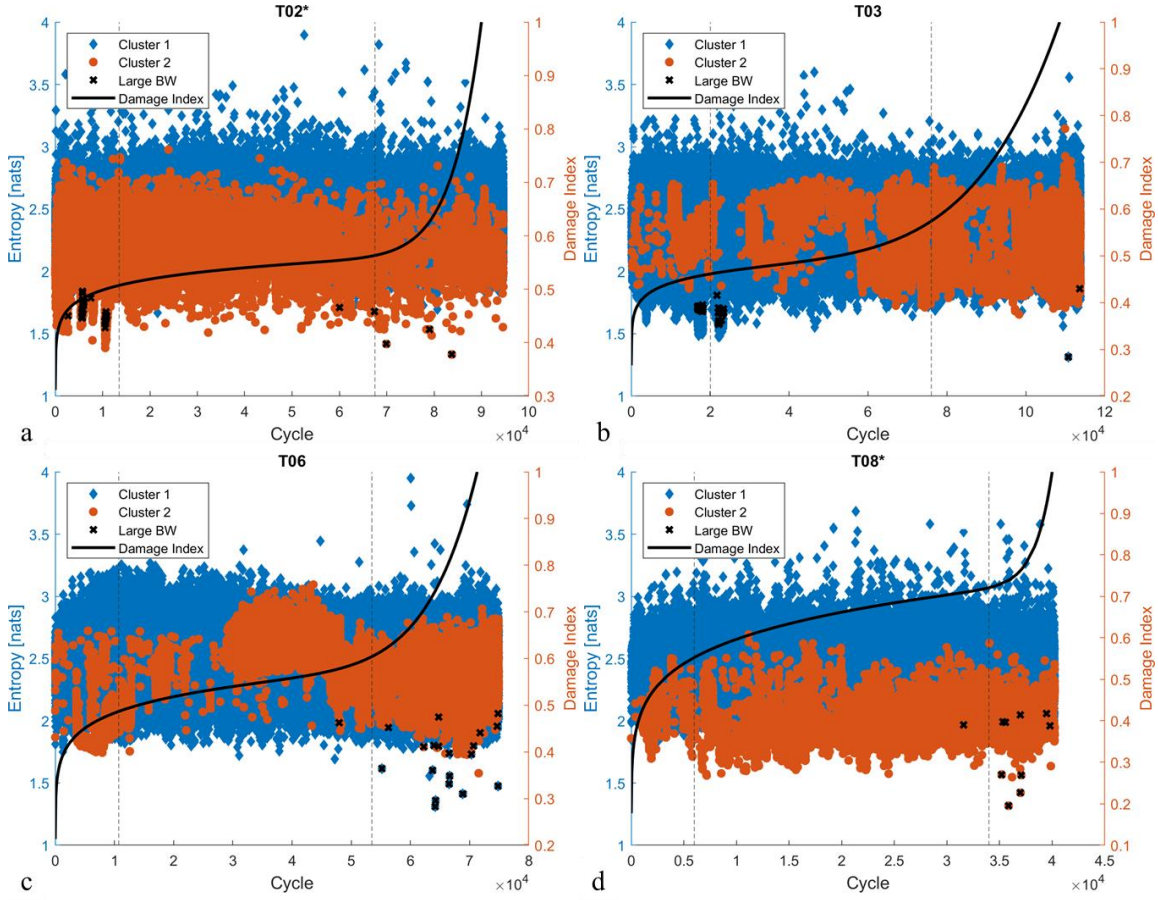

Figure 7-11 - Trend of entropy values during fatigue test and its relation to damage index in four tests of T02 (a), T03 (b), T06 (c), and T08 (d)

The distribution of entropy values with respect to their clusters is shown in Figure 12. This figure further confirms that signals in cluster 2 are associated with lower entropy values. Figure 13 shows the trend of entropy values as a function of signal amplitudes. It is observed that although signals with all amplitude can be associated with low entropy values, a general decreasing trend is seen. Furthermore, signals with amplitudes above 90 [dB], which are commonly associated with severe damages, are associated with low entropy values.

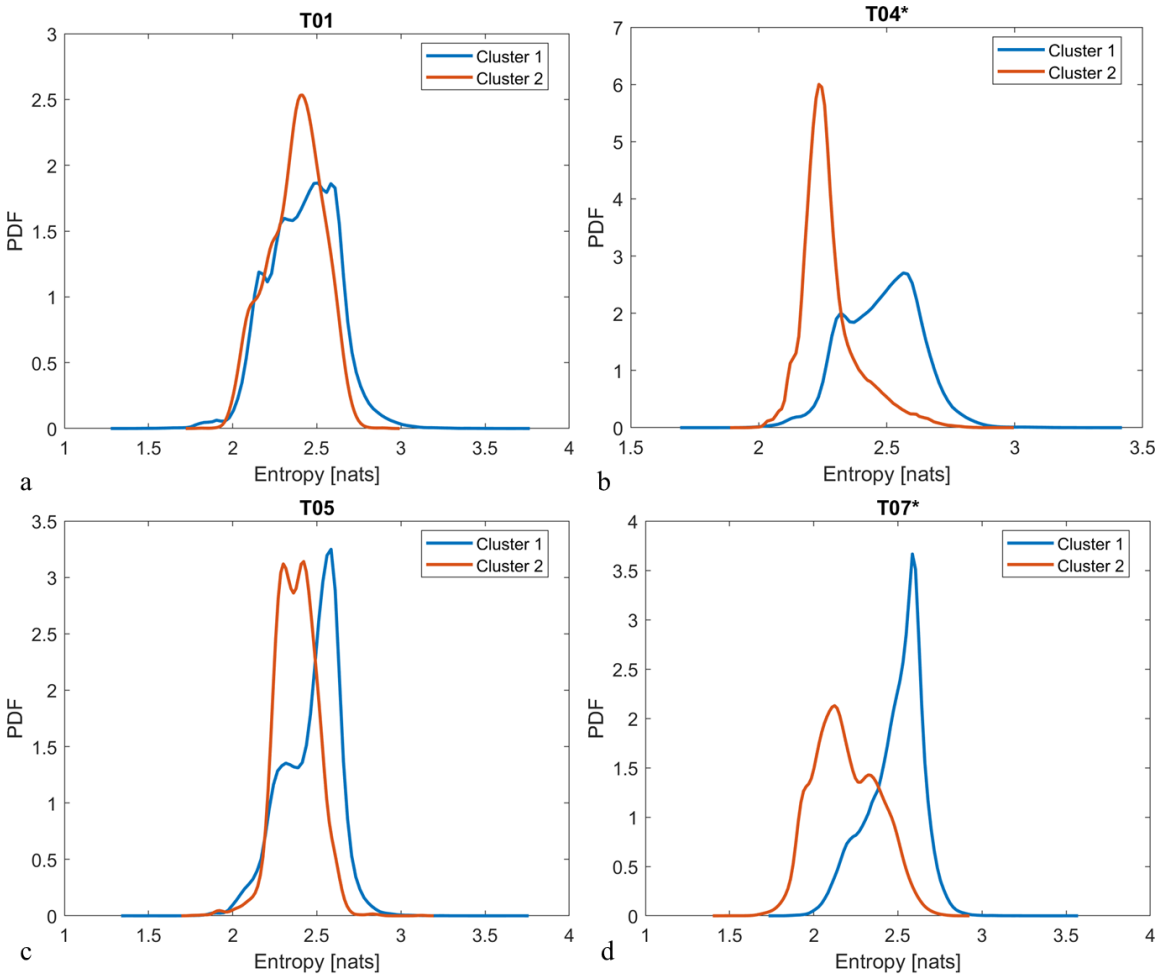

Figure 7-12 - Probability density function (PDF) of entropy values in each cluster in four tests of T01 (a), T04 (b), T05 (c), and T07 (d)

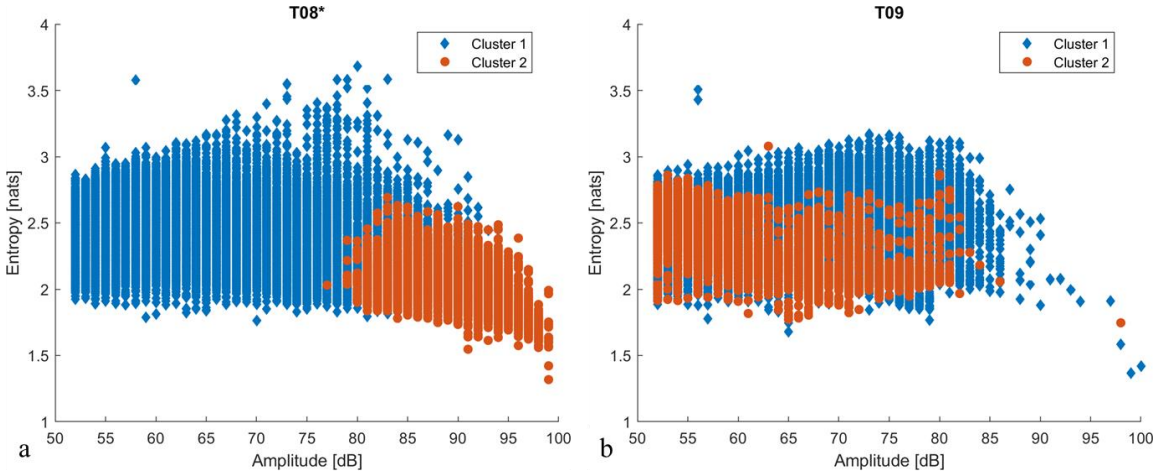

Figure 7-13 - Trend of entropy as a function of amplitude in tests T08 (a) and T09 (b)

7.6. Conclusion

This study shows the AE waveform entropy is a robust time-domain feature that can discriminate signals independent of the threshold setting. High entropy signals appear to have multiple spikes in their waveforms, typically expected from fatigue crack fretting. Conversely, lower entropy value signals, specifically signal with large bin widths, relate to more severe damages during the fatigue life. Regardless of the signal clustering, this paper shows that signals with large bin width values are associated with low entropy values, which appear when the damage index rate is at its peak. Therefore, the emergence of these signals can be interpreted as a high damage rate.

The competing effect of bin width and peak frequency in the resulting signal clusters in different tests are found as important characteristics. Accordingly, it was not possible to relate a specific cluster to a particular mechanism of damage. However, the number of signals in cluster 2 remained low in all tests, and the distribution of entropy values in the cluster was shown to cover a lower range of entropy values. Therefore, concerning the relation of the low entropy values and severe damages, it can be concluded that signals in

cluster 2 were mainly related to the fiber failure or interface failure (delamination) mechanisms. This cluster should be carefully observed as it better correlates with the final failure and fatigue life.

7.7. References

[1] A. P. Vassilopoulos, "The history of fiber-reinforced polymer composite laminate fatigue," *International Journal of Fatigue*, vol. 134, p. 105512, May 2020, doi: 10.1016/j.ijfatigue.2020.105512.

[2] P. Duchene, S. Chaki, A. Ayadi, and P. Krawczak, "A review of non-destructive techniques used for mechanical damage assessment in polymer composites," *Journal of Materials Science*, Jan. 2018, doi: 10.1007/s10853-018-2045-6.

[3] Y. Wang *et al.*, "Study on Multifractal Characteristics of Acoustic Emission Sequence of Concrete with Different Steel Fiber Content under Uniaxial Tension," *Materials Evaluation*, vol. 78, no. 9, pp. 1045–1054, Sep. 2020, doi: 10.32548/2020.me-04135.

[4] A. Jayababu, V. Arumugam, B. Rajesh, and C. Suresh Kumar, "Damage Characterization in Glass/Epoxy Composite Laminates under Normal and Oblique Planes of Cyclic Indentation Loading with AE Monitoring," *Materials Evaluation*, vol. 79, no. 1, pp. 61–77, Jan. 2021, doi: 10.32548/2021.me-04126.

[5] C. Barile, C. Casavola, G. Pappalettera, and V. P. Kannan, "Application of different acoustic emission descriptors in damage assessment of fiber reinforced plastics: A comprehensive review," *Engineering Fracture Mechanics*, vol. 235, p. 107083, Aug. 2020, doi: 10.1016/j.engfracmech.2020.107083.

[6] A. Kahirdeh and M. M. Khonsari, "Energy dissipation in the course of the fatigue degradation: Mathematical derivation and experimental quantification," *International Journal of Solids and Structures*, vol. 77, pp. 74–85, Dec. 2015, doi: 10.1016/j.ijsolstr.2015.06.032.

[7] M. Haggui, A. El Mahi, Z. Jendli, A. Akrout, and M. Haddar, "Static and fatigue characterization of flax fiber reinforced thermoplastic composites by acoustic emission," *Applied Acoustics*, vol. 147, pp. 100–110, Apr. 2019, doi: 10.1016/j.apacoust.2018.03.011.

[8] M. Bourchak, I. Farrow, I. Bond, C. Rowland, and F. Menan, "Acoustic emission energy as a fatigue damage parameter for CFRP composites," *International Journal of Fatigue*, vol. 29, no. 3, pp. 457–470, Mar. 2007, doi: 10.1016/j.ijfatigue.2006.05.009.

[9] R. Unnthorsson, T. Runarsson, and M. Jonsson, "Acoustic emission based fatigue failure criterion for CFRP," *International Journal of Fatigue*, vol. 30, no. 1, pp. 11–20, Jan. 2008, doi: 10.1016/j.ijfatigue.2007.02.024.

[10] D. Tsamtsakis, M. Wevers, and P. de Meester, “Acoustic Emission from CFRP Laminates during Fatigue Loading,” *Journal of Reinforced Plastics and Composites*, vol. 17, no. 13, pp. 1185–1201, Sep. 1998, doi: 10.1177/073168449801701304.

[11] W. Roundi, A. El Mahi, A. El Gharad, and J.-L. Rebiere, “Acoustic emission monitoring of damage progression in Glass/Epoxy composites during static and fatigue tensile tests,” *Applied Acoustics*, vol. 132, pp. 124–134, Mar. 2018, doi: 10.1016/j.apacoust.2017.11.017.

[12] T. Loutas, N. Eleftheroglou, and D. Zarouchas, “A data-driven probabilistic framework towards the in-situ prognostics of fatigue life of composites based on acoustic emission data,” *Composite Structures*, vol. 161, pp. 522–529, Feb. 2017, doi: 10.1016/j.compstruct.2016.10.109.

[13] D. D. Doan, E. Ramasso, V. Placet, S. Zhang, L. Boubakar, and N. Zerhouni, “An unsupervised pattern recognition approach for AE data originating from fatigue tests on polymer–composite materials,” *Mechanical Systems and Signal Processing*, vol. 64–65, pp. 465–478, Dec. 2015, doi: 10.1016/j.ymssp.2015.04.011.

[14] F. E. Oz, M. Mehdikhani, N. Ersoy, and S. V. Lomov, “In-situ imaging of inter- and intra-laminar damage in open-hole tension tests of carbon fibre-reinforced composites,” *Composite Structures*, vol. 244, p. 112302, Jul. 2020, doi: 10.1016/j.compstruct.2020.112302.

[15] W. Roundi, A. El Mahi, A. El Gharad, and J.-L. Rebière, “Experimental and numerical investigation of the effects of stacking sequence and stress ratio on fatigue damage of glass/epoxy composites,” *Composites Part B: Engineering*, vol. 109, pp. 64–71, Jan. 2017, doi: 10.1016/j.compositesb.2016.10.044.

[16] K. Ono, “Review on Structural Health Evaluation with Acoustic Emission,” *Applied Sciences*, vol. 8, no. 6, p. 958, Jun. 2018, doi: 10.3390/app8060958.

[17] M. Kharrat, V. Placet, E. Ramasso, and M. L. Boubakar, “Influence of damage accumulation under fatigue loading on the AE-based health assessment of composite materials: Wave distortion and AE-features evolution as a function of damage level,” *Composites Part A: Applied Science and Manufacturing*, vol. 109, pp. 615–627, Jun. 2018, doi: 10.1016/j.compositesa.2016.03.020.

[18] M. Saeedifar and D. Zarouchas, “Damage characterization of laminated composites using acoustic emission: A review,” *Composites Part B: Engineering*, vol. 195, p. 108039, Aug. 2020, doi: 10.1016/j.compositesb.2020.108039.

[19] A. Ebrahimkhanlou, M. B. Schneider, B. Dubuc, and S. Salamone, “A Deep Learning Framework for Acoustic Emission Sources Localization and Characterization in Complex Aerospace Panels,” *Materials Evaluation*, p. 10, 2021, doi: 10.32548/2021.me-04179.

[20] R. Unnthorsson, T. P. Runarsson, and M. T. Jonsson, “AE Entropy for the Condition Monitoring of CFRP Subjected to Cyclic Fatigue,” *Journal of Acoustic Emission*, vol. 26, pp. 262–269, 2008.

[21] H. Yun and M. Modarres, “Measures of Entropy to Characterize Fatigue Damage in Metallic Materials,” *Entropy*, vol. 21, no. 8, p. 804, Aug. 2019, doi: 10.3390/e21080804.

[22] M. Chai, Z. Zhang, and Q. Duan, “A new qualitative acoustic emission parameter based on Shannon’s entropy for damage monitoring,” *Mechanical Systems and Signal Processing*, vol. 100, pp. 617–629, Feb. 2018, doi: 10.1016/j.ymssp.2017.08.007.

[23] C. Sauerbrunn, A. Kahirdeh, H. Yun, and M. Modarres, “Damage Assessment Using Information Entropy of Individual Acoustic Emission Waveforms during Cyclic Fatigue Loading,” *Applied Sciences*, vol. 7, no. 6, p. 562, May 2017, doi: 10.3390/app7060562.

[24] S. F. Karimian, M. Modarres, and H. A. Bruck, “A new method for detecting fatigue crack initiation in aluminum alloy using acoustic emission waveform information entropy,” *Engineering Fracture Mechanics*, vol. 223, p. 106771, Jan. 2020, doi: 10.1016/j.engfracmech.2019.106771.

[25] “Toray Composite Materials America, Inc.” https://www.toraycma.com/page.php?id=27 (accessed Nov. 30, 2020).

[26] “Toray Composite Materials America, Inc.” https://www.toraycma.com/page.php?id=661 (accessed Nov. 30, 2020).

[27] O. J. Nixon-Pearson and S. R. Hallett, “An experimental investigation into quasi-static and fatigue damage development in bolted-hole specimens,” *Composites Part B: Engineering*, vol. 77, pp. 462–473, Aug. 2015, doi: 10.1016/j.compositesb.2015.03.051.

[28] O. J. Nixon-Pearson and S. R. Hallett, “An investigation into the damage development and residual strengths of open-hole specimens in fatigue,” *Composites Part A: Applied Science and Manufacturing*, vol. 69, pp. 266–278, Feb. 2015, doi: 10.1016/j.compositesa.2014.11.013.

[29] M. Kharrat, E. Ramasso, V. Placet, and M. L. Boubakar, “A signal processing approach for enhanced Acoustic Emission data analysis in high activity systems: Application to organic matrix composites,” *Mechanical Systems and Signal Processing*, vol. 70–71, pp. 1038–1055, Mar. 2016, doi: 10.1016/j.ymssp.2015.08.028.

[30] Z. Yang, W. Yan, L. Jin, F. Li, and Z. Hou, “A novel feature representation method based on original waveforms for acoustic emission signals,” *Mechanical Systems and Signal Processing*, vol. 135, p. 106365, Jan. 2020, doi: 10.1016/j.ymssp.2019.106365.

[31] M. Ben Ameur *et al.*, “Investigation and identification of damage mechanisms of unidirectional carbon/flax hybrid composites using acoustic emission,” *Engineering Fracture Mechanics*, vol. 216, p. 106511, Jul. 2019, doi: 10.1016/j.engfracmech.2019.106511.

[32] H. Mao and S. Mahadevan, “Fatigue damage modelling of composite materials,” *Composite Structures*, vol. 58, no. 4, pp. 405–410, Dec. 2002, doi: 10.1016/S0263-8223(02)00126-5.

[33] M. Azadi, H. Sayar, A. Ghasemi-Ghalebahman, and S. M. Jafari, “Tensile loading rate effect on mechanical properties and failure mechanisms in open-hole carbon fiber reinforced polymer composites by acoustic emission approach,” *Composites Part B: Engineering*, vol. 158, pp. 448–458, Feb. 2019, doi: 10.1016/j.compositesb.2018.09.103.

[34] D. Lee, H. Tippur, and P. Bogert, “Quasi-static and dynamic fracture of graphite/epoxy composites: An optical study of loading-rate effects,” *Composites Part B: Engineering*, vol. 41, no. 6, pp. 462–474, Sep. 2010, doi: 10.1016/j.compositesb.2010.05.007.

[35] X. Li, M. Saeedifar, R. Benedictus, and D. Zarouchas, “Damage Accumulation Analysis of CFRP Cross-Ply Laminates under Different Tensile Loading Rates,” *Composites Part C: Open Access*, p. 100005, Jul. 2020, doi: 10.1016/j.jcomc.2020.100005.

[36] Shannon, Claude Elwood., “A Mathematical Theory of Communication,” *Bell system technical journal*, vol. 27, no. 3, pp. 379–423, 1948.

[37] D. W. Scott, “On optimal and data-based histograms,” *Biometrika*, vol. 66, no. 3, pp. 605–610, 1979.

[38] S. F. Karimian and M. Modarres, “Acoustic emission signal clustering in CFRP laminates using a new feature set based on waveform analysis and information entropy analysis,” *Composite Structures*, p. 113987, Apr. 2021, doi: 10.1016/j.compstruct.2021.113987.

[39] P. J. Rousseeuw, “Silhouettes: A graphical aid to the interpretation and validation of cluster analysis,” *Journal of Computational and Applied Mathematics*, vol. 20, pp. 53–65, Nov. 1987, doi: 10.1016/0377-0427(87)90125-7.

[40] D. L. Davies and D. W. Bouldin, “A Cluster Separation Measure,” *IEEE Trans. Pattern Anal. Mach. Intell.*, vol. PAMI-1, no. 2, pp. 224–227, Apr. 1979, doi: 10.1109/TPAMI.1979.4766909.

[41] F. E. Oz, N. Ersoy, and S. V. Lomov, “Do high frequency acoustic emission events always represent fibre failure in CFRP laminates?,” *Composites Part A: Applied Science and Manufacturing*, vol. 103, pp. 230–235, Dec. 2017, doi: 10.1016/j.compositesa.2017.10.013.

[42] R. Gutkin, C. J. Green, S. Vangrattanachai, S. T. Pinho, P. Robinson, and P. T. Curtis, “On acoustic emission for failure investigation in CFRP: Pattern recognition and peak frequency analyses,” *Mechanical Systems and Signal Processing*, vol. 25, no. 4, pp. 1393–1407, May 2011, doi: 10.1016/j.ymssp.2010.11.014.

Chapter 8: Structural health monitoring in open-hole CFRP laminates under fatigue loading based on thermodynamic entropy analysis[1]

8.1. Abstract

Structural health monitoring of composite laminates has been studied in the past decades. Many empirical and analytical approaches have been proposed in the literature. Recently, thermodynamic entropy-based techniques have gained more attention, because they have the potential for removing the dependency of the common approaches on experimental conditions in order to provide an independent measure of damage. This study applies the thermodynamic entropy concepts, and measures the entropy generation due to damage in step-stress tensile fatigue loadings. Several tests are performed on open-hole CFRP laminates, and mechanical and temperature responses are recorded. This allows for the energy dissipation associated with thermal and mechanical mechanisms that contribute to entropy generation to be carefully isolated and measured. Furthermore, the damage associated with residual plastic deformation is measured on the surface using the full-field deformation technique known as Digital Image Correlation (DIC). Experimental results indicate that although the trajectory of plastic deformation, internal damage evolution, and heat conduction energy dissipation drastically differ in different tests, the final entropy

[1] The full-text of this chapter is currently (i.e., April 2021) prepared to submit to the 13th International Workshop on Structural Health Monitoring (IWSHM), December 7-9 2021, Stanford University, CA.

generation values at the time of fracture converge to a critical value, which is known as the "entropy endurance limit" or "fatigue fracture entropy (FFE)".

8.2. Introduction

The use of composites in industry has been increasing steadily over the past decades. Fiber-reinforced polymer (FRP) composites have been the most pervasive due to their superior stiffness, strength, corrosion resistance, fatigue life, and density relative to conventional lightweight metals. There are many advantages to using composites, including the ability to easily tailor their design through laminate architectures to meet specific performance requirements, making them highly desirable as both primary and secondary structures. However, structural components are prone to degradation, and catastrophic failures may occur if they are not properly maintained. Fatigue is a major cause of failure in structural components [1]. Fatigue failure occurs due to fluctuating loads at much lower levels than the nominal strength of the components. During operation, the fatigue-induced changes in component materials, referred to as "damage", accumulate and ultimately result in failure. Fatigue damage is a complex problem in composite materials. Vassilopoulos [2] provides a history of fiber-reinforced polymer composite laminate fatigue. There are various potential damage mechanisms, such as matrix cracking, fiber/matrix debonding, delamination, and fiber breakage present in FRP laminated composites. The synergy between these mechanisms ultimately leads to catastrophic failure. Fatigue life analysis and remaining useful life estimations using conventional methods usually require use of complex equations that suffer from intrinsic epistemic uncertainties. Furthermore, small deviations between specimen properties can result in considerable deviation from the initial prediction. Liu and Mahadevan [3] propose a probabilistic fatigue life prediction that aims

to reduce some of the uncertainties. Other papers have also proposed different uncertainty reduction approaches [4]. However, these approaches are complex and require consideration of many contributing factors [5], in addition to the effect of loading conditions on fatigue analysis of composite laminates [6].

Recently, the development of novel approaches for characterizing composites' fatigue behavior based on thermodynamic entropy analysis has emerged [7]. As a state function, thermodynamic entropy is inherently independent of the damage accumulation path and provides the potential to characterize fatigue damage independent of the loading condition. Examples of it are shown in [8], [9], and the entropy use in structural health monitoring and remaining useful life estimation is demonstrated in [10]. Fatigue damage is an irreversible process that dissipates energy and thus generates entropy. This irreversibility and entropy generation can be measured from detected thermal and mechanical energies dissipated while the system undergoes fatigue. While the plastic energy dissipation through hysteresis loop measurement has been used to predict fatigue damage accumulation [11], [12], such predictions and their applications can be further improved in an entropy framework. In this case, the contributing mechanisms of the hysteresis loop must be studied further, and the variables participating in entropy generation should be isolated. The contributing energy dissipation mechanisms in hysteresis loop and their interaction depend on the material and loading condition. A previous study by the authors [13] has shown the potential of crack initiation detection based on thermodynamic analysis using non-destructive testing (NDT) techniques that include digital image correlation (DIC) analysis. The use of NDT techniques on composite laminates have been extensively shown in the literature [14], specifically by relying on temperature analysis [15], [16] and DIC [17]–

[20]. DIC is a full-field strain measurement technique and is used in this study to estimate the plastic deformation energy in fatigue loading.

The use of thermodynamic entropy as a damage index stems from the fact that fatigue damage is irreversible. Thermodynamic entropy has the potential to combine different energy dissipations mechanisms and present them under one unique value. This is a valuable property that broadens it applications and offers life prediction techniques independent of loading condition. This is because a change in the loading condition would change energy dissipations. Energy dissipation property is promising in composite laminates due to the complexity of damage progression, the mechanisms for energy dissipation, activation of such mechanisms, and the synergy between multiple damage mechanisms that accelerate fatigue failure. Therefore, in this study all the participating energy dissipation mechanisms in entropy generation are carefully identified and measured during step-stress tensile fatigue testing. The loading conditions follow different starting points and stress-step sizes. The energy dissipations from different mechanisms are then used to quantify the entropy generation and identify a critical value associated with catastrophic fatigue failure.

8.3. Experimental procedure

In this section, the material, geometry, manufacturing of the specimens, and the dominant failure mode are first described. Then, descriptions of the loading conditions, DIC and temperature measurements explanations are provided.

8.3.1. Materials, geometry, manufacturing, and failure mode

A laminated sheet made of carbon FRP (CFRP) with the layup sequence of $[45/90/-45/0]_{2s}$ is used for this study. Each ply of the laminate is made with Toray T700G fibers [21] and Toray 2510 pre-preg system [22] with a 65% fiber volume density. All the specimens are cut from the same sheet using a CNC Routing machine. The specimens follow an open-hole rectangular geometry. Figure 1 shows the geometry of specimens and the dimensions. Figure 2 shows the experimental setup and failure mode in two specimens at fracture. The fatigue fracture failure mode is pull-out failure, similar to the tensile failure mode, but with more presence of delamination.

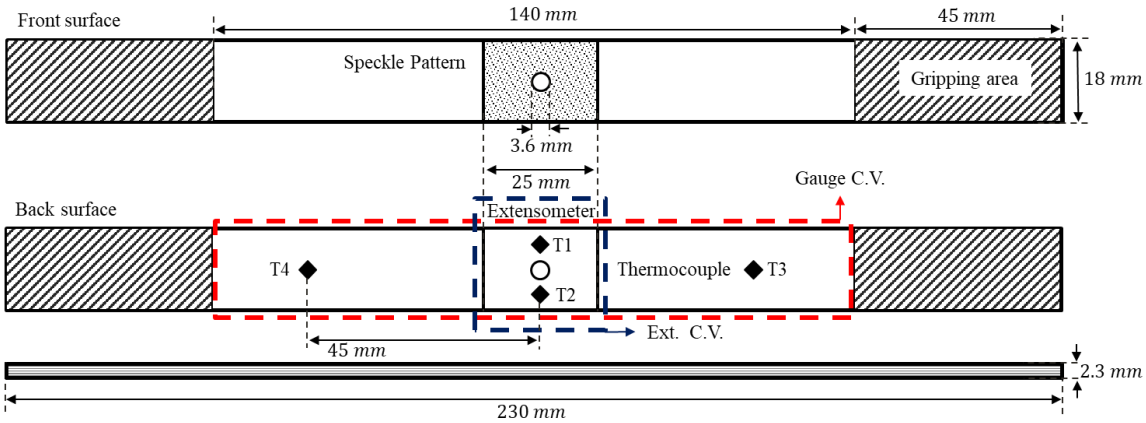

Figure 8-1 - Specimen geometry, sensor placement and control volumes

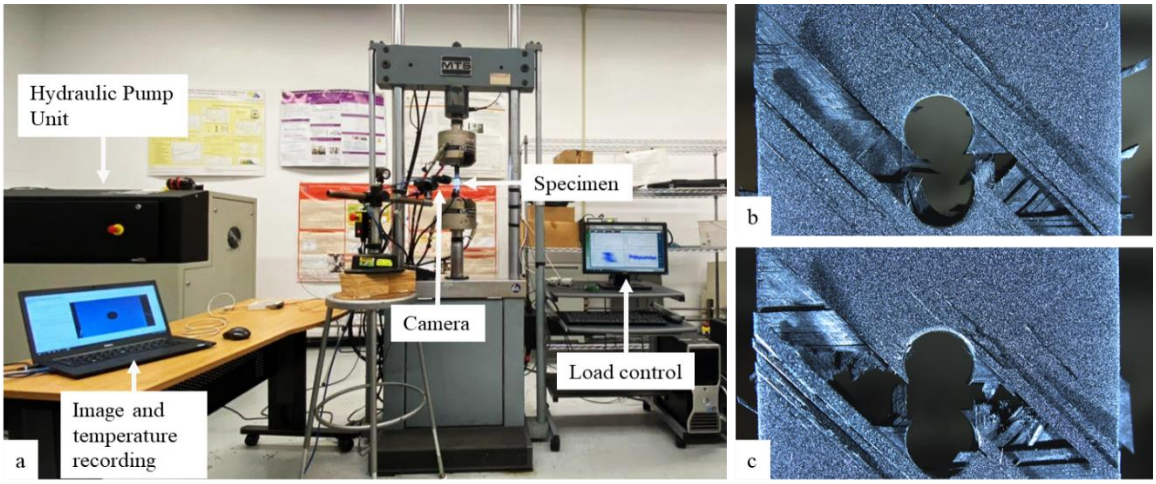

Figure 8-2 - Experimental setup (a) and pull-out fracture failure mode in two tests (b and c).

8.3.2. Loading condition and data acquisition

A step-stress tensile fatigue loading condition was used in this study. At each loading step, specimens were fatigue for a predetermined number of cycles, and then the test was paused. At the pause, specimens were unloaded and images for DIC analysis were taken. Upon reloading, specimens were loaded quasi-statically with a loading rate of 0.2 [kN/s] until the mean stress of the next step. All fatigue loadings were performed at a stress ratio of 0.1 and a frequency of 10 [Hz]. Figure 3-a shows the loading procedure in the tests. Each loading interval includes a loading step of 2,500 cycles and the stress level was increased every two loading intervals. Figure 3-b shows the σ_{max} of the loading intervals for the different loading conditions used in this study. Tests were continued until fracture. Test number, their loading profile, failure cycle and σ_{max} at the failure cycle is reported in Table 1.

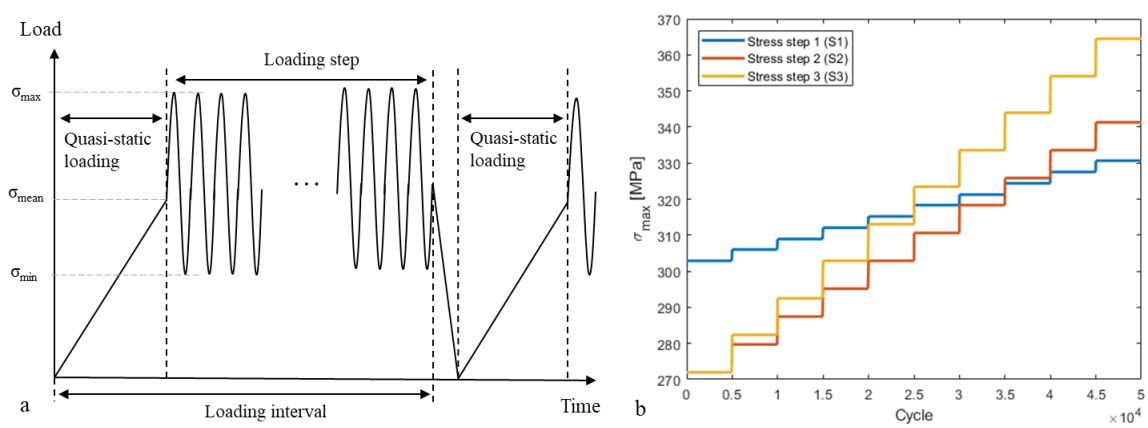

Figure 8-3 - Loading procedure (a) and different stress-steps in loading each condition (b)

Table 8-1 - Tests summary

Tests #	Loading profile	Failure cycle	σ_{max} at failure [MPa]
T1	S1	99,437	361
T2	S2	71,277	380
T3	S2	65,805	372
T4	S3	40,241	354
T5	S3	50,621	374
T6	S3	71,865	415

A servo-hydraulic material testing system (MTS) machine retrofitted with an Instron 8800 controller was used to perform the tests and record the mechanical response of the specimens. In addition to the servo-hydraulic machine, a linear variable differential transformer (LVDT) extensometer is attached to the back surface of the specimens to record local response (Figure 1). Specimens were speckle patterned on the front surface. Tests were monitored around the hole using an 8 [MP] Point Grey Flea3 sensor with a 3.8-13 [mm] Fujinon lens. For each test, a set of 5 consecutive images were recorded as the "Reference" image before any load was applied. At the unloading intervals, the specimen was unloaded and five consecutive images were recorded. These consecutive images were then averaged to minimize noises in image recording. Image averaging was done by averaging the intensity of pixels. The averaged images were used for DIC analysis. The temperature profile of specimens was recorded using four thermocouples attached to the back surface, as shown in Figure 1. Temperature data of these sensors are used to determine the heat transfer from specimens. Material properties of density, specific heat, heat conduction coefficient and heat radiation emissivity are reported in Table 2 [22], [23].

Table 8-2 - Material properties

$\rho\ [kg/m^3]$	$c\ [J/kgK]$	$k\ [W/mK]$	ε
1517	752	9.6	0.85

8.4. Thermodynamic entropy analysis

Thermodynamic entropy generation in fatigue testing is derived based on continuum damage mechanics presented in [24]. The entropy generation rate is defined by Equation 1:

$$\dot{S} = \frac{1}{T}\left(\sigma : \dot{\varepsilon}_p - A_k \dot{V}_k - \frac{1}{T}\dot{q} \cdot \nabla T\right) \geq 0 \qquad (1)$$

in which $\dot{S}$ is the entropy generation rate, T is the absolute temperature, σ is the stress, $\dot{\varepsilon}_p$ is the plastic strain, $\dot{V}_k$ is the change rate of any internal variable, A_k is the thermodynamic forces associated with the internal variable, $\dot{q}$ is the thermal flux and ∇T is the temperature gradient. Therefore, entropy generation defined by Eq. (1) consists of contributions from three dissipative energies: entropy generation due to plastic deformation $\frac{1}{T}\left(\sigma : \dot{\varepsilon}_p\right)$, entropy generation due to the evolution of internal variables $\frac{1}{T}\left(A_k \dot{V}_k\right)$, and entropy generation due to heat conduction $\frac{1}{T}\left(\frac{1}{T}\dot{q} \cdot \nabla T\right)$. It is important to emphasize that heat conduction is the only heat dissipation mechanism that participates in entropy generation. The share of each of the three energy dissipation mechanisms contributing part in entropy generation depends on the material. For instance, while energy dissipation due to internal damage is negligible in metallic materials [24], it can account for as much as 50% of energy dissipation in composite laminates [25].

The contribution of energy dissipation for each mechanism is measured separately in this study and the relation between the three terms of Equation 1 is defined based on the hysteresis loop measurement. The hysteresis loop energy is explained in Equation 2:

$$H = E_{damage} + E_{plastic} + Q_{dissipation} \qquad (2)$$

In this equation E_{damage} describes the internal damage energy consumed by the specimen that is used to grow cracks and delamination, $E_{plastic}$ is the energy used for plastic deformation and $Q_{dissipation}$ is the heat dissipation due to temperature difference on the specimen and surroundings. Heat dissipation can be further described by the summation of

heat transfer due to conduction, convection and radiation. Each of which is shown by the following Equations:

$$Q_{dissipation} = Q_{cond} + Q_{conv} + Q_{rad} \tag{3}$$

$$q_k = \left[\frac{\left(k\, A_{cross-section}\, \frac{T_a - T_b}{\Delta x_{a-b}}\right)}{V_{C.V.}}\right] \times 1/f_{temp} \tag{4}$$

$$q_h = \left[\frac{\left(h\, A_{surf}\, (T_s - T_{amb})\right)}{V_{C.V.}}\right] \times 1/f_{temp} \tag{5}$$

$$h = 1.42\, \left(\frac{T_s - T_{amb}}{L}\right)^{0.25} \tag{6}$$

$$q_r = \left[\frac{\epsilon\, \sigma_{SB}\, A_{surf}\, \left({T_s}^4 - {T_{amb}}^4\right)}{V_{C.V.}}\right] \times 1/f_{temp} \tag{7}$$

where q_k is the conduction heat transfer and k is the heat conduction coefficient reported in Table 2, q_h is the heat convection, h is the convection coefficient calculated using empirical Equation 6, T_s is surface temperature and T_{amb} is ambient temperature, q_r is the radiation heat transfer, ϵ is the emissivity value reported in Table 2, σ_{SB} is the Stefan-Boltzmann coefficient. Equations 3-7 are used to measure the heat transfer whenever temperature data are available. In order to transfer heat dissipation units from $[W]$ to $[{}^{J}/_{m^3}]$, their values are divided by the temperature acquisition rate that is $f_{temp} = 2\ [Hz]$ and $V_{C.V.}$, the volume of their control volume (C.V.). A different approach to measure the heat dissipation for a loading interval is the use of cooling rate [26]. In this method, fatigue

loading is paused suddenly and the cooling rate is measured. This rate is then translated to heat dissipation using Equation 8:

$$\rho \,.\, c \,.\, \left.\frac{\partial T_s}{\partial t}\right|_{t=t_*^+} = -\,Q = -(Q_{cond} + Q_{conv} + Q_{rad}) \qquad (8)$$

where ρ is specimen density (Table 2), c is the specimen specific heat (Table 2), $\left.\frac{\partial T_s}{\partial t}\right|_{t=t_*^+}$ is the slope of temperature change at the pause, and Q is the heat dissipation that is the summation of heat conduction, convection and radiation. In order to convert the heat dissipation energy for the loading step, Q should be divided by $f_{test} = 10\,[Hz]$ and multiplied by the number of cycles in the loading step. Figure 4 shows the temperature profile and measurement of the cooling rate for a loading interval in a test. The initial decreasing and monotonic increase are due to unloading and quasi-static loading in a loading interval.

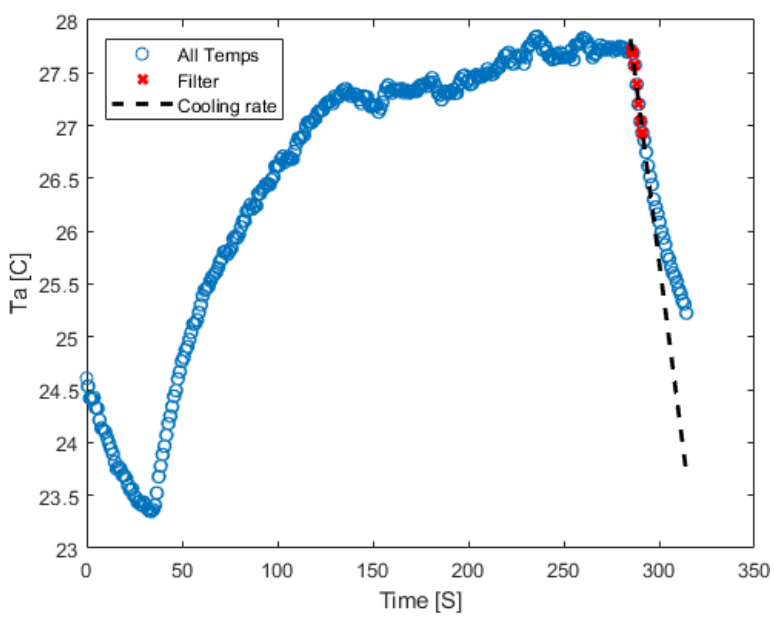

Figure 8-4 - Cooling rate measurement based on the temperature profile

The plastic damage energy is measured using the residual plastic strain values from DIC analysis on the surface. For this purpose, strain values generated by DIC analysis are measured and averaged around the hole area and used in Equation 9:

$$E_{plastic} = \sigma_y \, \varepsilon_{avg} \qquad (9)$$

in which σ_y is the tensile strength of the material measured as $\sigma_y = 337\ [MPa]$ and ε_{avg} is the average residual plastic strain on the surface at the time of measurement. The area of interest (AOI) for DIC analysis and strain measurements is local to the hole area. In order to minimize the effects of crack growth and pseudo-compression values sometimes appearing on the surface as a result of large cracks and lack of accurate correlations, a total number of 16 virtual extensometer within the AOI are used to measure the strain values in loading direction (ε_{yy}). These extensometers are distributed such that 6 cover each side of the hole and 4 cover the hole area. The extensometers showing negative values are removed from averaging. Figure 5 shows the strain map and virtual extensometer placement in a test.

Looking back at Equation 2, we can see that on the right-hand side, all the variables can be measured except the internal damage energy. On the left-hand side, we can measure the hysteresis loop using the stress-strain curves during fatigue loading. Therefore, the internal damage energy can be found by subtracting the left-hand side of Eq. 2 with the measured heat dissipation and plastic deformation energy on the right-hand side. However, it should be made sure that the C.V. used for measurements are consistent. There are two C.V.s assumed in this study that are shown in Figure 1. The larger C.V. is named Gauge C.V. and covers the whole gauge area of the specimen and the smaller C.V. is called Ext. C.V.

which covers only covers the more local area around the hole that is covered by the extensometer. The interaction between the C.V.s and their effect on the data analysis is further discussed in the next section.

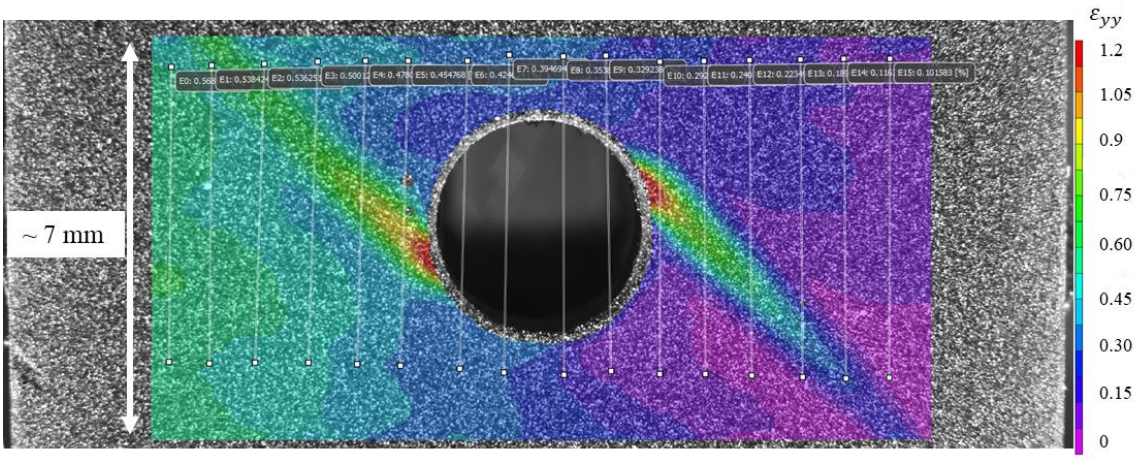

Figure 8-5 - Strain map around the hole area and virtual extensometers on surface

8.5. Experimental results and discussion

Based on geometric symmetry and the similarity of temperatures recorded in thermocouples near the hole (T1 and T2) and temperatures recorded in thermocouples near the grips (T3 and T4) shown in Figure 1, these temperatures are averaged and used as T_a and T_b based on the following:

$$T_a = \frac{T_1 + T_2}{2} \qquad (10)$$

$$T_b = \frac{T_3 + T_4}{2} \qquad (11)$$

The effect of this change in the variable is seen when the heat dissipation of the two C.V.s is compared. Figure 6-a shows the result of heat dissipation measurement based on Eq. 8 of a test for the two selected C.V.s. It is seen that the heat dissipation is higher in the Ext.

C.V. This is because the temperature profile is not uniform on specimens and the temperature around the hole area is considerably higher. When the Ext. C.V. is studied, its temperature is represented by T_a. In this case, the outer temperature for heat conduction measurement would be T_b. On the other hand, when Gauge C.V. is selected, the representative temperature would be the average of T_a and T_b and the grip temperature to measure the conduction heat transfer is considered to be equal to T_b. Figure 6-b shows the effect of heat dissipation measurement based on Eq. 4-7. This comparison further magnifies the effect of C.V. selection when measuring heat dissipation. This becomes especially important in the case of entropy measurement. As explained above, conduction heat transfer is the only portion of heat dissipation that participated in entropy generation. As seen in Figure 6-b, this heat dissipation mechanism is mostly impacted by the C.V. selection. The heat convection and heat radiation dissipation values are comparable and not heavily affected by the change of C.V., while heat conduction values are drastically changed. The Ext. C.V. is the fracture site. Therefore, conduction heat dissipation values of the Ext. C.V. should be used in entropy measurements.

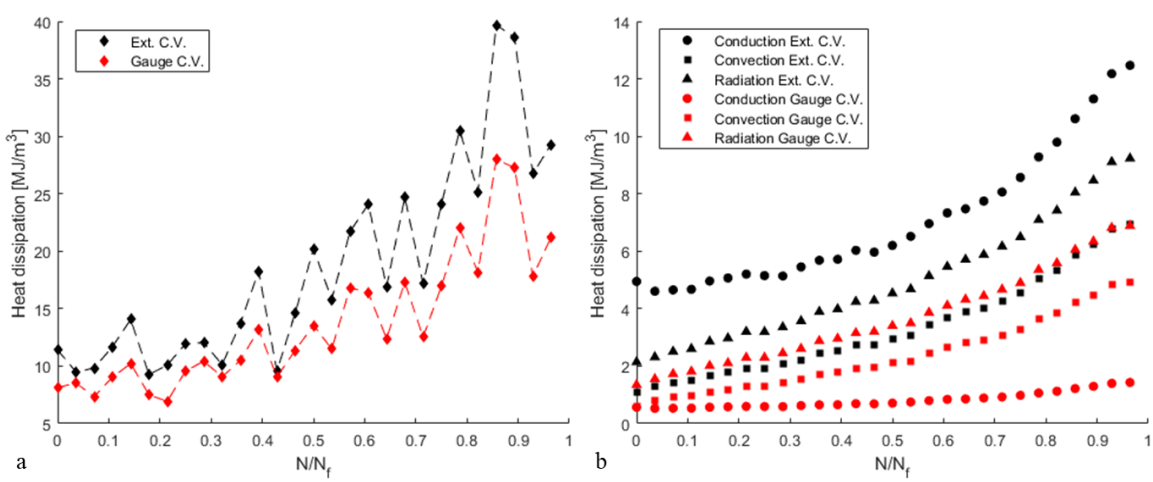

Figure 8-6 - Heat dissipation (Eq. 8) for Ext. and Gauge C.V. (a) and heat transfer mechanisms (Eq. 4-7) of the two C.V. (b) in T6.

The measurement of total energy dissipation based on hysteresis energy (Eq. 2) is also affected by the selection of C.V. When the larger C.V. (i.e., the Gauge C.V.) is considered, the hysteresis loop measurement uses the stress-strain data collected by the loading frame. Meanwhile, the hysteresis loop measurement for the Ext. C.V. is done based on the data collected in the extensometer. Figure 7-a shows how these two measurements (per cycle) compare in a test. As expected, hysteresis energy in Gauge C.V. is continuously higher than the one for Ext. C.V. This is due to the larger volume that it covers and consequently the higher energy consumed by the material. Although, when the trend of the two measurements is compared, it is seen that the hysteresis measurements by loading frame are more affected by the increase in stress in step-stress loading. Figure 7-b and 7-c show the trajectory of hysteresis measurements within a loading step. It is seen that while hysteresis measurements in Gauge C.V. stay at a constant level within a loading step and increase as the stress level of the following loading step increases (Figure 7-b), the hysteresis measurements by extensometer show an increase within a loading step, and are negligibly affected by stress increase of the following steps (Figure 7-c). The observation made in Figure 7 and comparing the hysteresis measurements and heat dissipation measurements in the Ext. C.V. suggests that we can assume the hysteresis measurements by extensometer is mostly affected by the internal and plastic deformation energies rather than heat dissipations. Therefore, Eq. 2 can be re-written as:

$$H_{Gauge\ C.V.} = \left[E_{damage} + E_{plastic}\right]_{Ext.\ C.V.} + \left[E_{damage} + E_{plastic}\right]_{Non-Ext.\ C.V.} + Q_{Ext.\ C.V.} + Q_{Non-Ext.\ C.V.} \quad (12)$$

And

$$H_{Ext.\ C.V.} = \left[E_{damage} + E_{plastic}\right]_{Ext.\ C.V.} \qquad (13)$$

in which $H_{Gauge\ C.V.}$ is the hysteresis energy measured by loading frame for the Gauge C.V., $H_{Ext.\ C.V.}$ is the hysteresis energy measured by extensometer for the Ext. C.V., and Q is the heat dissipations. Eq. 12 explains that the energy absorbed in the specimen (Gauge C.V.) is equal to the summation of energy dissipations in the Ext. C.V. and the rest of the specimen. Figure 8 displays how Eq. 12 is showing in a test.

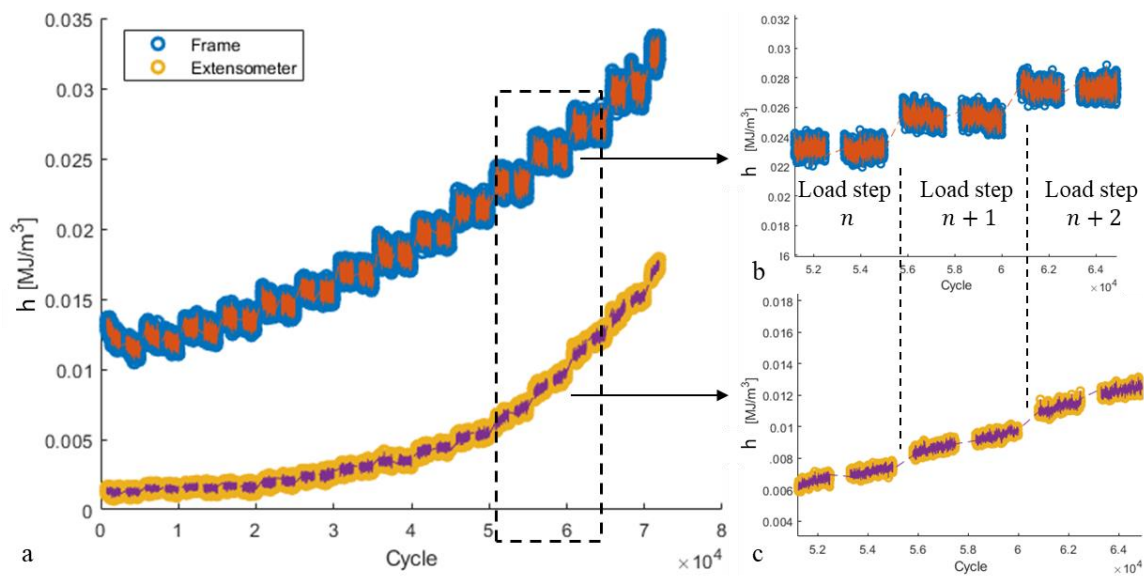

Figure 8-7 - Comparison of the hysteresis energy per cycle measured in Gauge C.V. vs. Ext. C.V. in T6

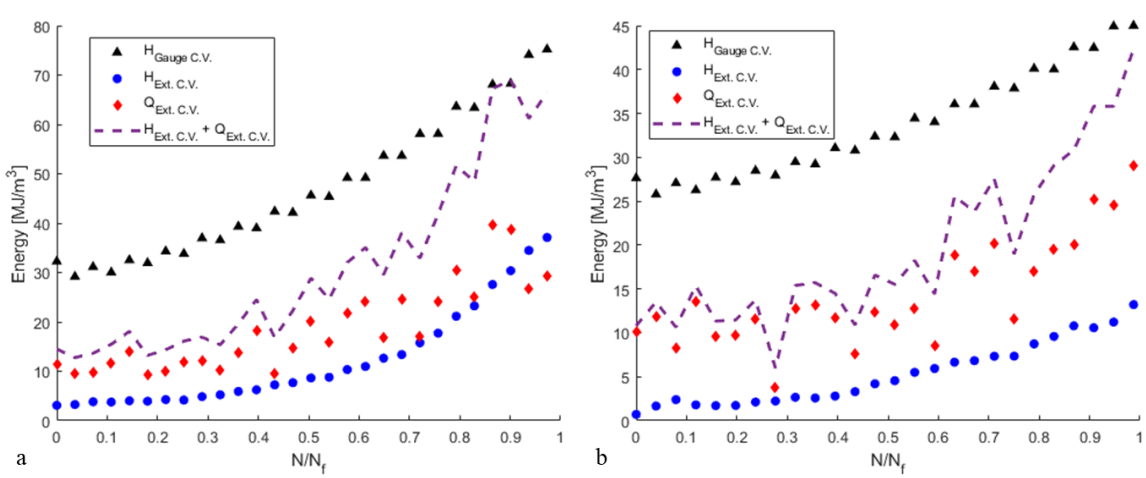

Figure 8-8 - Comparison of the hysteresis energy in Gauge C.V. with hysteresis energy and heat dissipation energy in Ext. C.V. in T6 (a) and T4 (b)

Figure 8 shows that the assumption made for the hysteresis values and the separations of the energies are valid. The area under the dashed line in the figure indicates the energies spent in the Ext. C.V. by both heat dissipation and hysteresis energy (i.e., plastic deformation energy and internal damage energy) and the rest would show the energies consumed by the rest of the specimen. It shows that in the beginning, energy consumption by the specimen is more uniform and the absorbed energy is distributed more evenly in the specimen. However, as we get closer to the fracture failure, a higher share of the energy that enters Gauge C.V. is consumed in the Ext. C.V. that leads the final fracture at the hole. The figure also shows how the hysteresis energy trend in Ext. C.V. (plastic and internal damage energy) is compared to the heat dissipation energy.

With regard to the fracture location of the specimen that falls in the Ext. C.V., the entropy generation in tests can be measured using the following equation:

$$S = \sum_{load\ steps} \frac{1}{T_{a\_avg}} [H + Q_{cond}]_{Ext.\ C.V.}$$

$$= \sum_{load\ steps} \frac{1}{T_{a\_avg}} [E_{damage} + E_{plastic} + Q_{cond}]_{Ext.\ C.V.} \quad (14)$$

in which S is the cumulative entropy generation, T_{a_avg} is the average temperature in a loading step, H is hysteresis energy of the Ext. C.V. that is the summation of $E_{damage} + E_{plastic}$ in the C.V., Q_{cond} is the conduction heat transfer from the Ext. C.V. and the summation is over all loading steps. Figure 9 shows the final entropy generation values reached in different tests at the time of fracture. It is seen that entropy converges to a mean

value of 1.13 [$^{MJ}/_{m^3K}$]. This value is called "entropy endurance limit" or "fatigue fracture entropy (FFE)", and it is similar to the values previously reported [8], [9].

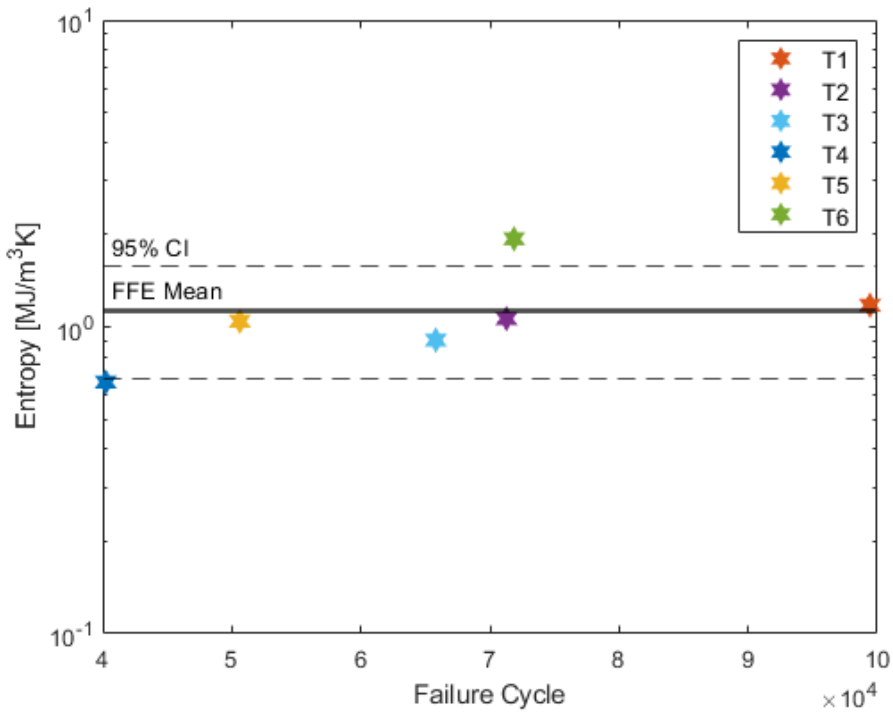

Figure 8-9 - Fatigue fracture entropy (FFE) of all tests at their failure cycle, and the mean and 95% confidence interval for FFE

The values reported in the figure are measured using hysteresis energy and heat conduction energy of the Ext. C.V. In order to further study the effect of dissipation energies in entropy generation, the hysteresis values can be further divided into plastic deformation energy and internal damage energy as shown in Eq. 13. The plastic deformation energy can be estimated using locally measured strains near the hole using the DIC technique and based on Eq. 9. Therefore, the share of internal damage energy can also be estimated. Figure 10 shows the energy dissipation trend for each component separately and compares them in three different tests. The trend for temperature values and entropy generation is also shown in the figure.

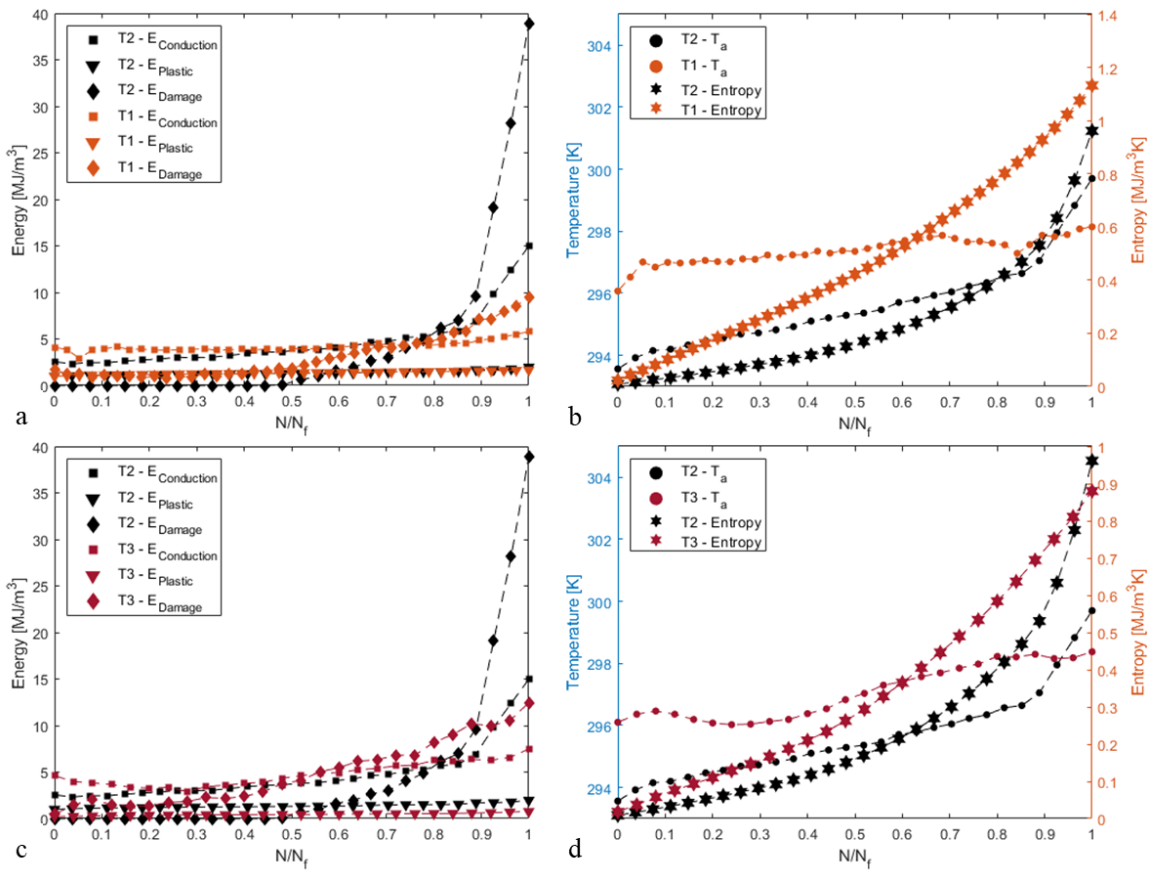

Figure 8-10 – Comparison of energy dissipation mechanisms participating in entropy generation in tests T1 and T2 (a) and T2 and T3 (c) and comparison of the temperature increase and entropy generation trend in tests T1 and T2 (b) and T2 and T3 (d).

Figure 10-a shows the energy dissipation and 10-b shows the mean temperature change and entropy generation trend in two tests of T1 and T2 that are fatigued using loading conditions of S1 and S2. It is seen that although the energy dissipations by each mechanism, temperature increase and entropy generation trend are different throughout each test, they both have reached fracture failure when their final cumulative entropy has reached the FFE value. Figure 10-c and 10-d compare the tests of T2 and T3. It is seen that although the loading conditions of the tests shown are identical, the mechanism of energy dissipation differs substantially. It is also seen that due to the brittle characteristic of CFRP materials, as expected, the share of plastic deformation is small in comparison to damage energy.

Also, the share of internal damage increases as the tests progress. In the beginning, the share of this variable is usually small and heat conduction plays the main role in entropy generation. However, its share increases exponentially as the test progress and becomes the largest energy dissipation mechanism.

8.6. Conclusion

Thermodynamic entropy generation in laminated open-hole CFRP specimens is studied in this paper. In particular, the contributions of each energy dissipation mechanism have been characterized through careful measurements of each variable. It is shown that when measuring entropy, the selection of a control volume should be made very carefully. This selection would affect the measurement of heat conduction dissipation that directly influences the entropy generation measurement. Energy dissipation due to plastic deformation is estimated using the DIC technique and is very sensitive to measurement conditions. The amount of energy dissipation due to internal damage is also estimated, so the interaction between energy dissipation mechanisms could be explained.

It is shown that regardless of loading condition and substantial difference in energy dissipation trajectories, the final fracture under tensile fatigue loading in specimens occurs when the cumulative thermodynamic entropy generation reaches the entropy endurance limit or FFE value of 1.13 $[{}^{MJ}/_{m^3K}]$. This value and the trajectory of the participating parameters can be used in structural health monitoring of CFRP composite laminates and provide indications of final failure before a catastrophic event occurs.

8.7. References

[1] Md. T. A. Ansari, K. K. Singh, and M. S. Azam, "Fatigue damage analysis of fiber-reinforced polymer composites—A review," *Journal of Reinforced Plastics and Composites*, vol. 37, no. 9, pp. 636–654, May 2018, doi: 10.1177/0731684418754713.

[2] A. P. Vassilopoulos, "The history of fiber-reinforced polymer composite laminate fatigue," *International Journal of Fatigue*, vol. 134, p. 105512, May 2020, doi: 10.1016/j.ijfatigue.2020.105512.

[3] Y. Liu and S. Mahadevan, "Probabilistic fatigue life prediction of multidirectional composite laminates," *Composite Structures*, vol. 69, no. 1, pp. 11–19, Jun. 2005, doi: 10.1016/j.compstruct.2004.04.012.

[4] A. Shirazi and A. Varvani-Farahani, "A Stiffness Degradation Based Fatigue Damage Model for FRP Composites of (0/θ) Laminate Systems," *Appl Compos Mater*, vol. 17, no. 2, pp. 137–150, Apr. 2010, doi: 10.1007/s10443-009-9099-1.

[5] P. Alam, D. Mamalis, C. Robert, C. Floreani, and C. M. Ó Brádaigh, "The fatigue of carbon fibre reinforced plastics - A review," *Composites Part B: Engineering*, vol. 166, pp. 555–579, Jun. 2019, doi: 10.1016/j.compositesb.2019.02.016.

[6] N. Post, S. Case, and J. Lesko, "Modeling the variable amplitude fatigue of composite materials: A review and evaluation of the state of the art for spectrum loading," *International Journal of Fatigue*, vol. 30, no. 12, pp. 2064–2086, Dec. 2008, doi: 10.1016/j.ijfatigue.2008.07.002.

[7] A. Imanian and M. Modarres, "A thermodynamic entropy-based damage assessment with applications to prognostics and health management," *Structural Health Monitoring*, vol. 17, no. 2, pp. 240–254, Mar. 2018, doi: 10.1177/1475921716689561.

[8] M. Naderi and M. M. Khonsari, "Thermodynamic analysis of fatigue failure in a composite laminate," *Mechanics of Materials*, vol. 46, pp. 113–122, Mar. 2012, doi: 10.1016/j.mechmat.2011.12.003.

[9] M. Naderi and M. M. Khonsari, "On the role of damage energy in the fatigue degradation characterization of a composite laminate," *Composites Part B: Engineering*, vol. 45, no. 1, pp. 528–537, Feb. 2013, doi: 10.1016/j.compositesb.2012.07.028.

[10] B. Mohammadi and A. Mahmoudi, "Developing a new model to predict the fatigue life of cross-ply laminates using coupled CDM-entropy generation approach," *Theoretical and Applied Fracture Mechanics*, vol. 95, pp. 18–27, Jun. 2018, doi: 10.1016/j.tafmec.2018.02.012.

[11] K. Momenkhani, S. Sarkani, and D. L. Jones, "Development and Application of a Model Using Center of Gravity of Hysteresis Loops to Predict Fatigue Damage

Accumulation in Fiber-reinforced Plastic Laminates," *Journal of Composite Materials*, vol. 39, no. 6, pp. 557–575, Mar. 2005, doi: 10.1177/0021998305047101.

[12] S. Giancane, F. W. Panella, and V. Dattoma, "Characterization of fatigue damage in long fiber epoxy composite laminates," *International Journal of Fatigue*, vol. 32, no. 1, pp. 46–53, Jan. 2010, doi: 10.1016/j.ijfatigue.2009.02.024.

[13] S. F. Karimian, H. A. Bruck, and M. Modarres, "Thermodynamic entropy to detect fatigue crack initiation using digital image correlation, and effect of overload spectrums," *International Journal of Fatigue*, vol. 129, p. 105256, Dec. 2019, doi: 10.1016/j.ijfatigue.2019.105256.

[14] B. Wang, S. Zhong, T.-L. Lee, K. S. Fancey, and J. Mi, "Non-destructive testing and evaluation of composite materials/structures: A state-of-the-art review," *Advances in Mechanical Engineering*, vol. 12, no. 4, p. 168781402091376, Apr. 2020, doi: 10.1177/1687814020913761.

[15] A. Poudel, K. R. Mitchell, T. P. Chu, S. Neidigk, and C. Jacques, "Non-destructive evaluation of composite repairs by using infrared thermography," *Journal of Composite Materials*, vol. 50, no. 3, pp. 351–363, Feb. 2016, doi: 10.1177/0021998315574755.

[16] R. Steinberger, T. Valadasleitao, E. Ladstatter, G. Pinter, W. Billinger, and R. Lang, "Infrared thermographic techniques for non-destructive damage characterization of carbon fibre reinforced polymers during tensile fatigue testing," *International Journal of Fatigue*, vol. 28, no. 10, pp. 1340–1347, Oct. 2006, doi: 10.1016/j.ijfatigue.2006.02.036.

[17] S. Giancane, F. W. Panella, R. Nobile, and V. Dattoma, "Fatigue damage evolution of fiber reinforced composites with digital image correlation analysis," *Procedia Engineering*, vol. 2, no. 1, pp. 1307–1315, Apr. 2010, doi: 10.1016/j.proeng.2010.03.142.

[18] J. Montesano, M. Selezneva, M. Levesque, and Z. Fawaz, "Modeling fatigue damage evolution in polymer matrix composite structures and validation using in-situ digital image correlation," *Composite Structures*, vol. 125, pp. 354–361, Jul. 2015, doi: 10.1016/j.compstruct.2015.02.035.

[19] R. Ambu, F. Aymerich, and F. Bertolino, "Investigation of the effect of damage on the strength of notched composite laminates by digital image correlation.," *The Journal of Strain Analysis for Engineering Design*, vol. 40, no. 5, pp. 451–461, 2005.

[20] A. Khechai, A. Tati, B. Guerira, A. Guettala, and P. M. Mohite, "Strength degradation and stress analysis of composite plates with circular, square and rectangular notches using digital image correlation," *Composite Structures*, vol. 185, pp. 699–715, Feb. 2018, doi: 10.1016/j.compstruct.2017.11.060.

[21] "Toray Composite Materials America, Inc." https://www.toraycma.com/page.php?id=27 (accessed Nov. 30, 2020).

[22] "Toray Composite Materials America, Inc." https://www.toraycma.com/page.php?id=661 (accessed Nov. 30, 2020).

[23] A. Adibekyan, E. Kononogova, C. Monte, and J. Hollandt, "Review of PTB Measurements on Emissivity, Reflectivity and Transmissivity of Semitransparent Fiber-Reinforced Plastic Composites," *Int J Thermophys*, vol. 40, no. 4, p. 36, Apr. 2019, doi: 10.1007/s10765-019-2498-0.

[24] C. Basaran and S. Nie, "An Irreversible Thermodynamics Theory for Damage Mechanics of Solids," *International Journal of Damage Mechanics*, vol. 13, no. 3, pp. 205–223, Jul. 2004, doi: 10.1177/1056789504041058.

[25] E. Kristofer Gamstedt, O. Redon, and P. Brøndsted, "Fatigue Dissipation and Failure in Unidirectional and Angle-Ply Glass Fibre/Carbon Fibre Hybrid Laminates," *Key Engineering Materials*, vol. 221–222, pp. 35–48, Dec. 2001, doi: 10.4028/www.scientific.net/KEM.221-222.35.

[26] G. Meneghetti, "Analysis of the fatigue strength of a stainless steel based on the energy dissipation," *International Journal of Fatigue*, vol. 29, no. 1, pp. 81–94, Jan. 2007, doi: 10.1016/j.ijfatigue.2006.02.043.

Chapter 9: Conclusions, Contributions and Recommendations

9.1. Conclusions

This dissertation developed new methods to detect fatigue damage and assess fatigue life in metallic (i.e., aluminum alloy) and FRP laminated composites (i.e., CFRP) using measurements from two NDT techniques: AE and DIC. Methodologies were developed to convert the NDT measurements into information entropy and thermodynamic entropy generated by fatigue damage, and correlate these entropies with the cumulative amount of fatigue damage to predict fatigue life. Experimental results supported developing these methods and were used to validate the results and the developed models. The research results mainly concluded that:

9.1.1. AE and information entropy-related conclusions

- Information entropy of AE signal waveforms exhibits little dependence on the spatial location of the measurement, unlike threshold-dependent features of AE signal such as count and energy.
- The minimum value of information entropy of AE signal waveforms precedes the formation of a fatigue macrocrack in aluminum materials, independent of the loading conditions.
- The critical role of bin width selection is an essential step in generating a histogram from an AE signal waveform, and consequently, measuring its information entropy, and is usually overlooked. Bin width selection based on the previous work by Scotts [1] proved to be useful.

- In aluminum materials, the appropriate bin width for the AE waveform histogram is found to be a fixed value equal to the average bin width of all valid signals.
- In FRP materials, due to the nature of AE signal sources, selecting a fixed bin width for waveform analysis of all signals does not seem proper. In this case, the appropriate bin width for each waveform should be set individually based on the waveform characteristics.
- The bin width value of an AE signal waveform is independent of the threshold setting. This feature strongly correlates with the conventional time-domain threshold-dependent features of AE signals in CFRP laminated composites. It can be used as a time-domain representation of the waveform in clustering.
- The AE waveform information entropy is a robust time-domain feature that can discriminate signals in fatigue loading of FRP materials. High entropy signals are related to fatigue crack fretting. Conversely, low entropy value signals with large bin widths relate to more severe damages during the fatigue life.
- Signals with large bin width values are associated with low entropy values and appear when the fatigue damage index rate in CFRP laminated composites is at its peak. Therefore, the emergence of these signals can be interpreted as existence of a high damage rate.

9.1.2. DIC and thermodynamic entropy-related conclusions

- In aluminum materials in which plastic deformation accounts for the highest portion of the hysteresis energy, the DIC technique can be successfully used to measure thermodynamic entropy on the surface.

- The thermodynamic entropy generation rate is found to be dependent on the loading spectrum. However, regardless of the damage rate, time to crack initiation, loading spectrum, test frequency and temperature, crack initiation in aluminum materials occurs at a nearly constant entropic endurance level or FFE value of 13.9 $[{}^{kJ}/_{m^3K}]$.
- Concerning the high non-linearity in thermal and strain maps in fatigue testing on materials, the selection of a control volume for thermodynamic entropy measurement should be made very carefully. This selection mainly affects the measurement of heat conduction dissipation that directly influences the thermodynamic entropy measurement and is more pronounced in CFRP laminated composites.
- Regardless of the loading condition and substantial difference in energy dissipation trajectories, the final fracture in CFRP laminated composites under tensile fatigue loading occurs when the cumulative thermodynamic entropy generation reaches the entropic endurance limit or FFE value of 1.13 $[{}^{MJ}/_{m^3K}]$.

9.1.3. Fatigue life estimation-related conclusion

- The use of information entropy and thermodynamic entropy within a dynamic Bayesian updating framework results in accurate estimations of RUL independent of fatigue loading conditions.

9.2. Contributions

The major contributions are as follows:

1. Development and validation of a novel approach to use AE waveform information entropy for fatigue damage detection and life assessment in both metallic and FRP laminated composites.
2. Development of new techniques for appropriate bin width selection to more appropriately measure the information entropy of the detected fatigue-related AE signal waveforms.
3. Development of new approaches to using the DIC technique in thermodynamic entropy measurement in both metallic and FRP composite materials.
4. Assessment of the thermodynamic entropic endurance limits in both metallic and FRP composite materials with detail entropy generation trajectories.
5. Development of a framework for RUL estimation based on the information entropy and thermodynamic entropy.

9.3. Recommendations for future research

Based on the results of this research the recommendations for future works are summarized as:

- Study the characteristics and the ranges of AE waveform information entropy related to different fatigue damage mechanisms in FRP laminated composites and the effect of fatigue damage on the information entropy values.
- Development of AE signal waveform decomposition and noise reduction methods based on information entropy in fatigue damage analysis.

- Use of maximum entropy principle for representing AE waveform to find information entropy values to further decrease the effect of AE signal attenuation.
- Use of the Kullback–Leibler divergence and maximum relative entropy principles for AE waveform distribution analysis and their applications for fatigue failure detections.
- Investigations of the information entropy values associated to the strain map measurement using DIC technique.
- Study of the relationship between the two entropic indices used in this study and explanation of their theoretical relation in the context of fatigue damage assessment.
- Calculation of the thermodynamic entropy using a higher frequency of DIC image recordings to decrease the uncertainty of the entropic endurance distribution.
- Inclusion of uncertainties associated with the distribution of information entropy and thermodynamic entropy at the time of failure in RUL estimations.
- Applications of more sophisticated machine learning techniques such as the Convolutional Neural Network for online thermodynamic entropy and information entropy measurement, and data fusion, to achieve real-time RUL estimations.
- Study the detection of failure mechanisms and their progression in unbalanced laminated composites, fasteners and joints.
- Investigate the effects of resin rich areas in laminated composites.

9.4. Reference

[1] D. W. Scott, “On optimal and data-based histograms,” *Biometrika*, vol. 66, no. 3, pp. 605–610, 1979.